

REALISTIC MULTI-ORBITAL SYSTEMS

Correlated Adatoms on Surfaces

Dissertation
zur Erlangung des Doktorgrades
des Fachbereichs Physik
der Universität Hamburg



vorgelegt von
J. Roberto S. Mozara

2021

Gutachter der Dissertation: Prof. Dr. Alexander I. Lichtenstein
Prof. Dr. Michael Potthoff

Prüfungskommission: Prof. Dr. Alexander I. Lichtenstein
Prof. Dr. Michael Potthoff
Prof. Dr. Peter Schmelcher
PD Dr. Jens Wiebe
Jun.-Prof. Dr. Frank Lechermann

Vorsitzender der Prüfungskommission: Prof. Dr. Peter Schmelcher

Datum der Disputation: 15.10.2021

Vorsitzender des Fach-Promotionsausschusses: Prof. Dr. Wolfgang Hansen

Leiter des Fachbereichs Physik: Prof. Dr. Günther H. W. Sigl

Dekan der MIN-Fakultät: Prof. Dr. Heinrich Graener

Kurzfassung

J. Roberto S. Mozara

Realistische Multi-Orbitale Systeme – Korrelierte Adatome auf Oberflächen

Die vorwiegend angewandten experimentellen Techniken in der Oberflächenwissenschaft, die Rastertunnelmikroskopie und -spektroskopie, haben einen Präzisionsgrad erreicht, sodass die Ergebnisse zu ihrer Erklärung die Entwicklung neuer theoretischer Herangehensweisen erfordern. Die experimentelle Präzision erlaubt mittlerweile eine detaillierte Auflösung sowohl der physikalischen und chemischen Zusammensetzung als auch der spektralen Eigenschaften von Oberflächen. Während vereinfachten Modelle ein erstes qualitatives Verständnis der physikalischen Vorgänge erlauben, erfordert die experimentelle Auflösung der orbitalen und spektralen Substrukturen eine realistische theoretische Darstellung des zu untersuchenden physikalischen Systems und eine numerisch exakte Lösung der entsprechenden Modelle. Die vorliegende Arbeit entwickelt eine Kombination aus *ab initio* Dichtefunktionaltheorie und dem Vielteilchen-Anderson-Modell, um korrelierte Adatome, Moleküle und Nanosysteme auf Substratoberflächen darzustellen, und bündelt beide Herangehensweisen und deren Kombination sowohl in einen weitergehenden theoretischen und physikwissenschaftlichen Kontext als auch in den gegenwärtigen Stand der Forschung ein. Die Entwicklung des *ab initio* Vielteilchenmodells und die numerische Herangehensweise zu seiner Lösung wird um die Anwendung auf drei bestimmte Oberflächensysteme, von denen zwei vorher experimentell untersucht wurden, herum angeordnet.

Die Tantaloxidoberfläche Ta(001)-p(3×3)-O wird gegenwärtig im Hinblick auf den Kondo-Effekt auf supraleitenden Oberflächen, welcher zu den sogenannten Yu-Shiba-Rusinov-Zuständen führt, untersucht. Die geometrische und quantenchemische Komplexität dieser Substratoberfläche erlaubt das Zusammenspiel von Adsorbaten an verschiedenen Positionen, jeder in seinem eigenen Kondo-Zustand. Die vorliegende Arbeit untersucht die Ta(001)-p(3×3)-O-Oberfläche mithilfe der Dichtefunktionaltheorie und identifiziert sowohl ihre elektronische und quantenchemische Struktur als auch ihre spektralen Eigenschaften. Da ihre relevanten Adsorptionsmechanismen für einzelne und mehrere Atome bis heute noch nicht geklärt worden sind, wird die Dichtefunktionaltheorie um die Einbeziehung der van-der-Waals-Wechselwirkungen erweitert, die sich als wichtig für die Stabilität und für spezielle Anordnungen von Adsorbaten auf verschiedenen Oberflächen erwiesen haben.

Aufgrund der zwei-dimensionalen Geometrie von Oberflächensystemen führt die Symmetriebrechung nicht nur zu einer ausgeprägten Kristallfeldaufspaltung und richtungsabhängigen Hybridisierung der Adatomorbitale, sie führt auch zu einer anisotropen Coulomb-Wechselwirkungsmatrix. Diese wird wichtiger auf Substraten mit Pseudolücken, da die reduzierte Zustandsdichte am Fermi-niveau die lokalen Wechselwirkungen auf den Adatomen die Physik bei niedrigen Energien dominieren lässt. Die vorliegende Arbeit betrachtet Co-Adatome auf Graphen und löst numerisch das entsprechende *ab initio* Anderson-Modell mithilfe von zeitkontinuierlichem Quanten-Monte-Carlo und der kürzlich entwickelten Methode der stochastischen Optimierung. Die Coulomb-Wechselwirkungsanisotropie wird innerhalb der eingeschränkten Random-Phase-Approximation ermittelt, welche allerdings zeigt, dass auch auf Substraten mit Pseudolücken die lokalen Wechselwirkungen nicht viel stärker als die Hybridisierung sein müssen. Ihre Prävalenz kann allerdings von der

Selbstenergie in Bereichen niedriger Energie abgelesen werden, welche eine Restrukturierung der orbitalen Beiträge aufgrund der Symmetriebrechung offenbart.

Das System aus einem Co-Adatom auf Cu(111) stellt einen Benchmark für den multi-orbitalen Kondo-Effekt von Übergangsmetallen auf Metalloberflächen dar. Die spektrale Signatur ist eine Resonanz am Fermi-Niveau, deren Breite durch die Kondo-Temperatur bestimmt wird, welche die Mitte des Übergangsbereichs zu dem Effekt markiert und entweder theoretisch aus numerischen Lösungen oder experimentell durch Anfitten mit Fano- oder Frotta-Linien extrahiert werden kann. Der Kondo-Effekt in multi-orbitalen Systemen ist das Resultat einer komplizierten Überlagerung von Spin- und orbitalen Beiträgen. Platziert man das Co-Adatom neben einer symmetriebrechenden Cu-Kette, so erscheinen zusätzliche Kristallfeldaufspaltungen und Anisotropien in der Hybridisierung, welche zu einem modifizierten differentiellen Leitfähigkeitsspektrum führen. Die vorliegende Arbeit analysiert drei spezifische $\text{CoCu}_n/\text{Cu}(111)$ -Systeme, indem die entsprechenden Anderson-Modelle gelöst und weiterhin *ab initio* differentielle Leitfähigkeitsspektren berechnet werden, welche direkt mit den experimentellen Ergebnissen verglichen werden können. Die Analyse führt nicht nur zu einer quantitativen Übereinstimmung zwischen Theorie und Experiment, sondern kann sowohl die multi-orbitalen Kondo-Szenarien identifizieren als auch die Kondo-Temperaturen extrahieren, was durch Anfitten an experimentelle Daten oder innerhalb vereinfachter Beschreibungen mit einem einzelnen Orbital möglich war.

Schlagwörter: Tantal, Oxidoberfläche, Superstruktur, Rekonstruktion, orbitale Hybridisierung, freies Elektronenpaar, Rastertunnelmikroskopie, Rastertunnelspektroskopie, Dichtefunktionaltheorie, van der Waals-Wechselwirkung, Cobalt, Graphen, Adatom, korreliertes Elektronensystem, eingeschränkte Random-Phase-Approximation, Anderson-Modell, Quanten-Monte-Carlo, analytische Fortsetzung, Anisotropie, Kupferoberfläche, Streumechanismus, multi-orbitaler Kondo-Effekt

Abstract

J. Roberto S. Mozara

Realistic Multi-Orbital Systems – Correlated Adatoms on Surfaces

The most widely used experimental techniques in surface science, scanning tunnelling microscopy and spectroscopy, have attained at a degree of sophistication, that their findings demand the development of new theoretical approaches for their explanation. Nowadays the experimental precision allows for a detailed resolution of the physical and chemical composition of surfaces as well as of their spectral properties. While simplified models provide a first qualitative understanding of physical effects, the experimental resolution of orbital and spectral substructures call for a realistic theoretical representation of the physical systems under consideration and for a numerically exact solution of the associated models. The present thesis develops a combination of *ab initio* density functional theory and the many-body Anderson impurity model to represent correlated adatoms, molecules, and nanosystems on substrate surfaces, and embeds both approaches and their combination into a wider theoretical and physics science context as well as into the current state of research. The development of the *ab initio* many-body model and the numerical approach for its solution will be drawn around their application on three particular surface systems, of which two of them have been experimentally investigated beforehand.

The tantalum oxide surface Ta(001)-p(3×3)-O is currently under consideration as regards the Kondo effect on superconducting surfaces, which result in the so-called Yu-Shiba-Rusinov states, and the geometric and quantum-chemical complexity of the substrate surface allows for the interplay of adsorbates at various locations, each being in a different Kondo state. The present thesis examines the Ta(001)-p(3×3)-O surface by means of density functional theory, and identifies its electronic and quantum-chemical structure as well as its spectral properties. As its relevant adsorption mechanisms for single and several atoms is to date not well understood, the density functional analysis is extended as to account for van der Waals interactions, which have been observed to be important for the stability and for specific arrangements of adsorbates on several surfaces.

Due to the two-dimensional geometry of surface systems, symmetry breaking not only leads to a pronounced crystal field splitting and directionally dependent hybridization of adatom orbitals, but also leads to an anisotropic Coulomb interaction matrix. These become more important in pseudo-gapped substrates because the reduced density of states at the Fermi level renders the local interactions on the adatom dominating the low-energy physics. The present thesis considers Co adatoms on graphene and numerically solves the corresponding *ab initio* Anderson impurity model by means of continuous-time quantum Monte Carlo and the recently developed stochastic optimization method. The Coulomb interaction anisotropy is determined within the constrained random phase approximation, which shows that also on pseudo-gapped substrates the local interactions may be not much stronger than the hybridization. Yet, their prevalence can be observed from the low-energy region of the self-energy, which reveals a restructuring of its orbital contributions due to symmetry breaking.

The system of a Co adatom on Cu(111) provides a benchmark for the multi-orbital Kondo effect of transition metal atoms on metallic surfaces. The spectral signature is a

resonance feature at the Fermi level with a width determined by the Kondo temperature, which marks the middle of the cross-over scale of the effect and can be extracted either theoretically from numerical solutions, or experimentally by fitting with Fano or Frotal lines. In multi-orbital systems the Kondo state is the result of a complicated superposition of spin and orbital contributions. Placing the Co adatom next to a symmetry-breaking Cu chain, additional crystal field splittings and hybridization anisotropies appear, which lead to a modified differential conductance spectrum. The present thesis analyses three specific $\text{CoCu}_n/\text{Cu}(111)$ systems by means of solving their corresponding Anderson impurity models and of further deriving *ab initio* differential conductance spectra, which can be directly compared to experimental results. The analysis not only leads to a quantitative agreement between theory and experiment, but can also identify the multi-orbital Kondo scenarios and extract Kondo temperatures, which was not possible by fitting to experimental data or within simplified single-orbital descriptions.

Key words: tantalum, oxide surface, superstructure, reconstruction, orbital hybridization, lone pair, scanning tunnelling microscopy, scanning tunnelling spectroscopy, density functional theory, van der Waals interaction, cobalt, graphene, adatom, correlated electron system, constrained random phase approximation, Anderson impurity model, quantum Monte Carlo, analytical continuation, anisotropy, copper surface, scattering mechanism, multi-orbital Kondo effect

Contents

| | | |
|----------|--|------------|
| 1 | Introduction | 1 |
| 2 | DFT and the Ta(001)-p(3×3)-O surface | 7 |
| 2.1 | Density functional theory | 11 |
| 2.1.1 | The Hohenberg-Kohn theorems and the Kohn-Sham solution | 11 |
| 2.1.2 | The exchange-correlation functional | 14 |
| | The local density approximation | 15 |
| | The generalized gradient approximation | 16 |
| 2.1.3 | Spin in DFT | 17 |
| 2.1.4 | Hubbard- U in DFT | 20 |
| 2.2 | Scanning tunnelling microscopy and the Tersoff-Hamann model | 24 |
| 2.3 | Context of the Ta(001)-p(3×3)-O surface | 27 |
| 2.4 | “An atomically thin oxide layer on the elemental superconductor Ta(001) surface” | 33 |
| 2.5 | Van der Waals forces in DFT: The Tkatchenko-Scheffler method | 50 |
| 2.5.1 | The iterative Hirshfeld algorithm | 52 |
| 2.5.2 | Self-consistent screening of dispersion coefficients | 53 |
| 2.6 | Application of the TS method to the Ta(001)-p(3×3)-O surface | 54 |
| 2.6.1 | Oxygen adsorption and tantalum reconstruction again | 54 |
| 2.6.2 | Hirshfeld charges and polarization | 57 |
| 2.6.3 | Dispersion coefficients | 59 |
| 3 | QMC solution of the AIM and the Co/graphene system | 63 |
| 3.1 | The GW approximation | 70 |
| 3.1.1 | The spectral function | 75 |
| 3.1.2 | The constrained random phase approximation | 77 |
| 3.2 | The Anderson impurity model | 79 |
| 3.2.1 | DFT+AIM | 82 |
| 3.3 | The continuous-time quantum Monte Carlo method | 84 |
| 3.4 | The stochastic optimization method | 88 |
| 3.5 | Context of the Co/graphene system | 91 |
| 3.6 | “Cobalt adatoms on graphene: Effects of anisotropies on the correlated electronic structure” | 100 |
| 4 | Multi-orbital Kondo Effect of CoCu$_n$/Cu(111) systems | 113 |
| 4.1 | The Kondo effect in multi-orbital systems | 122 |

| | | |
|----------|---|------------|
| 4.2 | Crystal Field Theory | 126 |
| 4.3 | Many-Electron Operators | 128 |
| 4.4 | Asymmetry factors in multi-orbital systems | 131 |
| 4.5 | The Kondo Hamiltonian from scaling | 135 |
| 4.5.1 | The Schrieffer-Wolff transformation | 136 |
| 4.5.2 | Poor man's scaling | 139 |
| 4.5.3 | Orbital Kondo effect | 141 |
| 4.6 | Kondo effect of Co adatoms at Cu chains | 141 |
| 4.6.1 | Experimental results | 143 |
| 4.6.2 | DFT+AIM setup | 144 |
| 4.6.3 | Derivation of the differential conductance | 145 |
| 4.6.4 | Analysis of orbital contributions | 149 |
| 4.6.5 | Analysis of orbital Kondo peaks | 150 |
| 4.6.6 | Estimation of temperature dependence | 152 |
| 4.6.7 | Comparison of double countings | 153 |
| 4.6.8 | Analysis of symmetry breaking | 153 |
| 4.6.9 | Comparison to one-orbital model | 156 |
| 4.6.10 | Summary | 157 |
| 5 | Summary and Outlook | 159 |
| | Bibliography | 163 |
| | Acronyms | 195 |
| | List of Figures | 199 |
| | List of Tables | 201 |
| | Appendix | 203 |
| A | Beyond spin-DFT and DFT+U | 203 |
| A.1 | Current in DFT | 203 |
| A.2 | Relativistic DFT | 207 |
| B | The PAW formalism and the SOC | 215 |
| C | Luttinger-Ward functional and the DC correction | 219 |
| C.1 | Exact DC correction | 219 |
| C.2 | Relation between DMFT and the AIM via the Luttinger-Ward functional . . | 221 |
| | Publications | 223 |

CHAPTER 1

Introduction

The electron on which forms and worlds are built,
Leaped into being, a particle of God.
A spark from the eternal Energy spilt,
It is the Infinite's blind minute abode.

In that small flaming chariot Shiva rides.
The One devised innumerably to be;
His oneness in invisible forms he hides,
Time's tiny temples of eternity.

Atom and molecule in their unseen plan
Buttress an edifice of strange oneness,
Crystal and plant, insect and beast and man, –
Man on whom the World-Unity shall seize,

Widening his soul-spark to an epiphany
Of the timeless vastness of Infinity.

Sri Aurobindo (1938) [[Sri72](#)]

Man has been trying to understand and deploy condensed matter systems according to his growing capabilities based on his cerebral and cultural status during the course of evolution. Guided by intuitions and by means of mental reasoning, in the last few centuries he has developed the enormously sophisticated and successful framework provided by the combination of experimental and theoretical physics. Based on quantum theory we nowadays have a theoretical framework at hand which promises a complete understanding of condensed matter systems and their properties. Alongside with experimental results from the late 19th and the 20th century, quantum theory has been based on reductionist avenues and led to the resolution of condensed matter systems into its constituents and the relations between them. In terms of the most fundamental verified physical theories of today, condensed matter systems can be identified as many-body objects composed of a huge amount of participating atoms, which can be described by [quantum electrodynamics \(QED\)](#) of bound states [[Eng02](#)]. The intricacies which often arise in the description of many-body systems are the result of the mutual interactions between its constituents, out of which cooperative or resonant phenomena may emerge. These are often difficult to reproduce theoretically, especially if one is interested in microscopic sourcing and description rather than in phenomenological heuristics. But the efforts pay off, since back again at the material scale, the condensed states of matter and the many-body cooperations themselves

arise as being fundamental as the underlying interactions between its constituents from which they are derived [And72].

Condensed matter systems comprise ionic cores (the nuclei) and electrons which both interact via the electromagnetic field. For the consideration of the electronic structure alone, the ionic motions can be disentangled and treated separately (Born-Oppenheimer approximation; see for example [Sch13]). One may perform a structural relaxation (for example within [density functional theory \(DFT\)](#), see Ref. [Bit06] and references therein, but also within its extensions [Leo08]), in which the actual ionic equilibrium structure can be obtained by including back-reaction effects of the electronic structure on the spatial ionic configuration. Furthermore, the vibrational motion of the ions about their equilibrium positions can be included within [DFT](#) and its extensions, and leads to coupling of the electrons to the corresponding [quasi-particles \(QPs\)](#) called phonons.

Assuming for now the ions residing at their equilibrium positions, the electrons move in the external potential given by the ionic lattice, and usually one describes the electromagnetic interaction between the electrons via the photon field, while the electrons are coupled to the ions via their electrostatic potential [Eng02]. The electrostatic Coulomb interaction between the electrons themselves (as part of the electromagnetic interactions) can be derived in the Coulomb gauge from the longitudinal part of the electromagnetic field, and it appears accompanied by the current-current interaction (the transversal part) needed to restore causality (the Coulomb interaction is instantaneous) and involving the magnetic interaction in the system (see Ref. [Kle09] and Appx. A.2). These interactions are at the basis of all condensed matter systems and, according to their importance, may or may not be included in theoretical and computational approaches for their description.

The most widely used computational approach to materials is [DFT](#) which is based on the [Hohenberg-Kohn \(HK\)](#) theorems [Hoh64] (Sec. 2.1.1). Hohenberg and Kohn proved that the ground state of an interacting electron system can be found by the minimization of an energy functional depending on the electronic density alone which is in one-to-one correspondence with the external potential built up by the ionic lattice. While the electrostatic density-density Coulomb interaction (the Hartree term) and the exchange term can be taken into account exactly, the drawback of [DFT](#) is the approximation to the correlation energy needed to establish the bijective [Kohn-Sham \(KS\)](#) mapping of the interacting electron system to an auxiliary non-interacting system, both represented in terms of densities [Koh65].

If the exchange and correlation interactions are relevant for the material under study, [DFT](#) must be extended by some theory going beyond its approximations. The class of materials containing atoms with open d or f shells show a peculiar interplay between the delocalization of electrons over the ionic lattice due to their kinetic energy, which is well described by [DFT](#), and the localization due to strong Coulomb attraction by the ionic centres and the subsequent electronic Coulomb repulsion between the electrons. These interactions leads to strong correlations between the localized electrons [Geo04]. Expressing the electronic quantum fields in terms of creation and annihilation operators, the Hubbard model can naturally be derived from the above outlined [QED](#) Hamiltonian (Appx. A.2 and Ref. [Hub63]; before any approximation made by [DFT](#)), and it reflects the Coulomb correlations, their strength, and the competition between localization and delocalization

directly, while the exchange interaction is already included in second quantization due to the inherent Fermi statistics.

The *local* electronic correlations can be accounted for by means of a self-consistent embedding of the **Anderson impurity model (AIM)** (Sec. 3.2) into the Hubbard model within the **dynamical mean-field theory (DMFT)** approach [Geo92; Geo96; Met89; Vol12]. The **AIM** singles out a correlated site of the ionic lattice and describes its correlations exactly, while the self-consistency condition incorporates the effects of the other correlated sites in a **mean-field (MF)**, though dynamical, approximation. Non-local interactions between the electrons, on the other hand, are difficult to describe and there exist, even conceptually, diverse approaches. The **GW approximation (GWA)** and the **random phase approximation (RPA)** remain in the continuous energy band picture of the electronic system traversing the ionic lattice, and while they account properly for the non-local correlations, those are admitted to be rather weak only (Sec. 3.1). To such weak interactions belong the **van der Waals (vdW)** forces which result from correlations between distant density fluctuations (Sec. 2.5). Another perspective is provided by **extended DMFT (EDMFT)** [Bie03; Hel11; Sun02] or the dual-fermion and dual-boson approaches [Rub12; Rub09], which all rely on the picture of electrons hopping between discrete localized orbitals and interacting locally as well as non-locally. While the combination of their corresponding equations would yield a complete representation of the extended Hubbard model containing fermionic as well as bosonic **degrees of freedom (DOF)**, computational solutions in these approaches always resort to some kind of approximation and often still remain highly demanding. An exhaustive computational description of strongly correlated systems taking into account non-local effects thus remains one of the most challenging tasks in condensed matter theory, despite many efforts and numerous established approaches.

The extension of **DFT** by **DMFT** to include local electronic correlations is accomplished by a projection procedure of the continuous DFT energy bands onto the discrete localized orbitals placed at the correlated sites of the material under consideration. In this way one obtains *ab-initio* parameters of an **AIM**, which in turn provides the basis for a self-consistent description of the Hubbard model (Subsec. 3.2.1). The relevant computational efforts for the solution of the Hubbard model within **DMFT** go into the solution of the **AIM**, and one of the most widely used approaches is the **quantum Monte Carlo (QMC)** evaluation of the partition function for the eventual computation of the **Green's function (GF)** or higher-order correlation functions (Sec. 3.3). The **GF** encodes the relevant spectral information which can be compared with experimental data. – The **double counting (DC)** problem results from a difficulty to represent the many-body correlations which are already contained in the **DFT** approach in terms of the **AIM** variables, though such a representation is needed for not to overdetermine the correlations and to subtract them during the transition from **DFT** to the **AIM**. As the **DC** problem was present in the **DFT+AIM** approach to the systems investigated in the present thesis, Appx. C provides a short account of its recently established precise definition within the **Luttinger-Ward (LW)** functional approach.

Two classes of correlated materials in terms of geometry can be described with this way of going beyond the **DFT** approach. First, one may have a single or a set of correlated adatoms, molecules or nanosystems which are placed on a substrate with particular physical properties. Such an introduction of inhomogeneities on clean surfaces provides one further

functionalization of materials for industrial applications. These surface systems can be represented and efficiently described by the [AIM](#) alone. The second class is given by bulk systems for which a self-consistency description has to be supplemented to the [AIM](#) as to let it describe a material being represented by the Hubbard model.

New experimental results demand the application of these material-specific approaches to correlated materials for their theoretical substantiation. Clearly, the number of different correlated materials as well as the number of effects and emergent phenomena which can be addressed by the [DFT+AIM](#) or the [DFT+DMFT](#) approaches are very large. The present thesis aims to develop the [DFT+AIM](#) framework for the description of correlated [transition metal \(TM\)](#) adatoms on metallic surfaces along three experimentally realized systems. The experimental setups and techniques are described in the publications included or will to some extent be explained in the main text of the thesis. The theoretical basics and computational techniques, and the physical effects which can be addressed within the [DFT+AIM](#) approach are discussed more extensively, although still in an intermediate detailedness: this is because the eventual aim of the present thesis is the presentation of a particular central theme within the [DFT+AIM](#) approach - the realistic description of the multi-orbital Kondo effect on correlated adatoms (Chpt. 4) -, which needs quite a few of ingredients with themselves having vast and profound theories behind them. For example, the Kondo effect is one of the fundamental resonant phenomena in correlated many-body systems which is connected to [Fermi liquid \(FL\)](#) theory and the scaling approach (introductory part to Chpt. 4 and Sec. 4.5, respectively).

The second chapter begins its presentation by developing [DFT](#) (Sec. 2.1), followed by a short account of [scanning tunnelling microscopy \(STM\)](#) (Sec. 2.2), which is one important experimental technique of surface science. The main text develops [DFT](#) as used in the projects reported on, that is, from its basics to its extensions for inclusion of the spin (Subsec. 2.1.3) and the [MF](#) approximation to the Coulomb interaction (Subsec. 2.1.4), while a further extension to current- and relativistic [DFT](#) is provided in the appendix (Appx. A). In this way [DFT](#) is embedded successively into larger contexts and eventually connected to relativistic [QED](#). At the time of writing the tantalum-oxide surface Ta(001)-p(3×3)-O is being investigated extensively by the research group of J. Wiebe and R. Wiesendanger at the Institute for Nanostructure and Solid State Physics of the University of Hamburg. Sec. 2.3 provides an embedding of the Ta(001)-p(3×3)-O surface into the current state of research, and Sec. 2.4 presents the publication which resulted from a joint collaboration and reports on the experimental and [DFT](#) characterization of this surface. The publication is followed by a study on [vdW](#) forces in [DFT](#) and their application on the same surface. It is not only about a further characterization of the Ta(001)-p(3×3)-O surface itself: the current belief is that the adatom adsorption structure, as, for example, reported in Ref. [Cor17], depends on [vdW](#) forces.

The third chapter describes the [DFT+AIM](#) approach (Subsec. 3.2.1) and its [continuous-time quantum Monte Carlo \(CTQMC\)](#) solution (Sec. 3.3) followed by a published application of the techniques on the system of a cobalt adatom on graphene (Co/graphene; Secs. 3.5 and 3.6). The new feature with respect to the [AIM](#) the chapter is going to describe is the consideration of the realistic Coulomb interaction matrix as determined from the [constrained RPA \(cRPA\)](#) (Subsec. 3.1.2). Owing to the geometric symmetry breaking

a surface induces on the adatom, the local Coulomb interaction strength is smaller on orbitals pointing towards the surface compared to ones in other directions, because then screening is more efficient. For the Co/graphene system the effects of anisotropy on the electronic structure were minor, but the self-energy shows considerable differences to the case in which the Coulomb interaction matrix has been rotationally averaged. Any physical properties extracted from the self-energy will thus be affected by the screening anisotropy.

The fourth chapter has the multi-orbital Kondo effect as its topic. The exposition sets out with a general overview on **FL** theory with the aim to provide the basic ideas for an understanding of the emergence of the Kondo effect. **FL** theory connects two different **ground states (GSs)** by an adiabatic switching-on of the (Coulomb) interactions and eventually describes the, possibly strongly, interacting electron system in terms of weakly interacting **QPs**. The discussion is complemented by a further exposition of the scaling approach which provides a microscopic picture of the Kondo effect in terms of an effective antiferromagnetic interaction between the magnetic moments of the adatom and the conduction electrons in the substrate (Sec. 4.5). In contrast to **FL** theory, the scaling approach leaves the Coulomb interaction strength unchanged and works on the hybridization by successively integrating out the high-energy **DOF**, thereby obtaining the low-energy effective Kondo model. Two further ingredients are necessary to understand the **QMC** solution of a realistic **AIM** in the Kondo regime: First, with the help of the **many-electron (ME)** operator approach (Sec. 4.3) one can track the microscopic transitions of the adatom between its eigenstates due to hybridization events and determine the associated Kondo scenario of the system under consideration. Second, in experiments the Kondo effect manifests itself as a spectral resonance feature near the Fermi level; for comparison between theory and experiment one obtains the Kondo resonance from the **QMC** solution to the corresponding **AIM** by derivation of the differential conductance (Sec. 4.4). – The rest of the chapter contains the application of the **DFT+AIM** approach to the system of a cobalt adatom on the copper surface supporting an additional copper chain (CoCu_n/Cu(111); Sec. 4.6), a system which is currently at experimental investigation in the group of A. Weismann and R. Berndt at the Institute of Experimental and Applied Physics of the Christian Albrechts University (CAU) of Kiel. Their finding was that the usual Kondo effect of the Co/Cu(111) system was modified by placing the Co adatom next to a Cu chain. The **DFT+AIM** approach was able to identify the hybridization anisotropy induced by the chain as the source for the modified spectral resonance feature, and to provide a complete understanding of the underlying multi-orbital Kondo effect.

CHAPTER 2

DFT and the Ta(001)-p(3×3)-O surface

The set of condensed matter systems considered in research can be roughly divided into two interconnected subareas: the real materials which are investigated experimentally and one might seek to describe by theoretical and computational means, and the simplified and abstract model-like systems which ought to focus on the most relevant properties of the often very complex real materials. In principle, the computational description of real materials refers to obtaining its physical, for example, thermodynamic and energetic properties, often via its partition function or associated thermodynamic potentials like the energy. The mathematical investigation and computational description of model-like systems, on the other hand, refers to the exploration of its physical properties under simplified conditions and of techniques for their retrieval. Both subareas, the real materials and the model systems, are mutually beneficial: most of the advanced techniques employed to describe real materials were first developed for the solution of model systems and subsequently extended to material-specific higher-dimensional parameter spaces, while the ideas for construction of model systems mostly were born during investigations of real materials. The present thesis focusses on the material-specific approaches.

In second quantization, the simplest many-body Hamiltonian describing interacting electrons in the external potential of a fixed ionic lattice is given by

$$\hat{H} = \sum_{\sigma} \int d\mathbf{r} \hat{\psi}_{\sigma}^{\dagger}(\mathbf{r}) \left[-\frac{1}{2} \Delta + V_{\text{ext}}(\mathbf{r}) - \mu \right] \hat{\psi}_{\sigma}(\mathbf{r}) + \frac{1}{2} \sum_{\sigma\sigma'} \int d(\mathbf{r}, \mathbf{r}') \hat{\psi}_{\sigma}^{\dagger}(\mathbf{r}) \hat{\psi}_{\sigma'}^{\dagger}(\mathbf{r}') V_{\text{el-el}}(\mathbf{r} - \mathbf{r}') \hat{\psi}_{\sigma'}(\mathbf{r}') \hat{\psi}_{\sigma}(\mathbf{r}). \quad (2.1)$$

Here, $V_{\text{ext}}(\mathbf{r})$ is the external ionic potential and μ the chemical potential, and the electrons interact via the Coulomb law: $V_{\text{el-el}}(\mathbf{r} - \mathbf{r}') = 1/|\mathbf{r} - \mathbf{r}'|$. Natural atomic units with $\hbar = c = m = 1$ are used [Sza96]. As such, the Hamiltonian in Eq. (2.1) is the full non-relativistic time-independent Hamiltonian for an electron system in an external potential.

Mathematically one can describe the electronic system in terms of a linear superposition of Slater determinants constructed of single orbitals [Dir26; Giu05; Hei26; Sch13; Sla29; Sza96]. All Slater determinants together provide a complete basis of the interacting many-body Hilbert space, while the orbitals involved in the determinants refer to an independent-electron description. This is the so-called full **configuration interaction (CI)** [Sza96]. The determinantal structure naturally incorporates the required antisymmetry of the many-body **wave function (WF)**, which leads to the so-called exchange interactions,

and the linear superposition of determinants possesses enough mathematical flexibility for the complete description of correlations. The **Hartree-Fock (HF)** approximation tries to approximate the many-body **GS** by one Slater determinant only, and while the exchange energy is thereby fully taken into account, the deviation of the **HF-GS** energy from the exact one is the correlation energy. Within the **CI** approach, the deviation may be minimized by taking into account a, possibly limited, superposition of Slater determinants. Other approaches, like quantum-mechanical perturbation theory or the **GF** formalism, try to include the correlations by other means. We will come back to that point in the next chapter.

The **HF** approximation is one possibility to reduce the **ME** problem to an effective one-electron problem, where the two-body interactions are represented by an average one-body potential seen by an electron in the averaged presence of all other electrons. This is in the spirit of **MF** approaches to many-body systems, and in case of **HF** theory amounts to the neglect of quantum fluctuations [Giu05]. This point will also be discussed together with the **GF** formalism in the next chapter (see introductory part to Chpt. 3).

The **HF** equation is an **eigenvalue (EV)** equation for the spin-orbitals which appear in the **HF-WF** (the Slater determinant):

$$h(\mathbf{r}_1)\chi_a(\mathbf{r}_1) + \sum_{b \neq a} \left[\int d\mathbf{r}_2 \frac{|\chi_b(\mathbf{r}_2)|^2}{|\mathbf{r}_1 - \mathbf{r}_2|} \right] \chi_a(\mathbf{r}_1) - \sum_{b \neq a} \left[\int d\mathbf{r}_2 \frac{\chi_b^*(\mathbf{r}_2)\chi_a(\mathbf{r}_2)}{|\mathbf{r}_1 - \mathbf{r}_2|} \right] \chi_b(\mathbf{r}_1) = \varepsilon_a \chi_a(\mathbf{r}_1). \quad (2.2)$$

Here, the subscript on the spin-orbitals denotes the spin and orbital indices. The first term on the l.h.s. contains the kinetic energy and the external one-body potential, and it is followed by the Hartree/Coulomb (the second) and the exchange (third) term. The Coulomb operator is local and multiplicative, while the exchange operator is non-local in **HF** theory and cannot be written in terms of a multiplicative factor for the **WF**. The Hartree and the exchange term comprise two-particle interactions, and while the former is repulsive, the latter is attractive and contributes to the binding structure of molecules and solids. According to Koopmans' theorem [Koo34; Sza96], the negative of the orbital energies which appear on the right-hand side of Eq. (2.2) can be considered as ionization energies. This, however, refers to some “frozen orbital” approximation due to the neglect of correlations and, mostly, because relaxation of spin-orbitals after ionization is not taken into account (removal of one electron from the N -electron **HF-WF** does not yield the **HF-WF** of the $(N - 1)$ -electron system). These shortcomings are overcome in going beyond the **HF** approximation, for example, in the **GF** approach (see introductory part to Chpt. 3).

A sophisticated computational description of real materials beyond the **HF** approximation becomes rapidly difficult because the Hilbert space dimension grows exponentially with the number of spin-orbitals and expansion coefficients (that is why **HF** calculations are mostly performed for limited quantum systems, such as atoms, molecules, and nanosystems). In contrast to that, the many-body **GS** and its physical properties are already determined by the electronic charge density, which is a function of just three variables. Thus, instead

of trying to built up a many-body **WF** and compute the material's properties out of it, one can use directly the charge density as the variable to be determined. The first step in this direction was done within the **Thomas-Fermi (TF)** model [Fer27; Tho27], which is a precursor to **DFT**. Thomas and Fermi found an expression for the kinetic energy of electrons in atoms in terms of the electronic density (in fact, the to-be-discussed **local density approximation (LDA)** of the kinetic energy of non-interacting electrons, here shown with natural constants),

$$T_s^{\text{TF}}[n] = \frac{3}{5} \int d\mathbf{r} \frac{\hbar k_F^2}{2m} n(\mathbf{r}), \quad (2.3)$$

while the ionic potential and the Hartree term retain their classical forms. They were able to calculate the energy of an atom, but atomic shell structures, Friedel oscillations, and chemical bonding cannot be found in the **TF** model [Giu05; Koh65; Tel62]. Furthermore, exchange due to the Pauli principle was not included (but then accomplished by Dirac [Dir30]), and correlations were not accounted for at all.

The **HF** theory and the **TF** model contain the mathematical structures relevant for the **DFT**. The **HF** Eq. (2.2) shows that the Coulomb and exchange operators which multiply the spin-orbitals depend on the spin-orbitals themselves, so that an iterative procedure has to be applied for its solution. There is thus a principle of self-consistency inherent to **HF** theory which carries over to **DFT** as well. And the charge density in the **TF** model is the variable for an energy functional which is to be minimized by the Rayleigh-Ritz method (the original papers by Thomas and Fermi solved the **EV** equations by other means, though [Fer27; Tho27]).

The result thus is that, instead of trying to built up directly a many-body **WF**, one can compute the material's properties by means of minimizing an energy functional which depends on the electronic density alone, and which formally contains all correlation effects from the outset. This is possible due to the **HK** theorems which include the bijective correspondence between the electronic density and the external ionic potential - while the rest of the energy functional containing electronic kinetic and interaction energies is universal (**HK** theorem I) -, and a variational principle (**HK** theorem II) [Hoh64]. The implementation of **DFT** is realized by the description of the interacting electron system in terms of an auxiliary non-interacting **KS** particle system as such that it yields the interacting **GS** electronic density [Koh65]. The mapping onto a **MF** one-electron problem is given by the effective **KS** potential $V_{\text{KS}}(\mathbf{r}) = V_{\text{ext}}(\mathbf{r}) + V_{\text{H}}(\mathbf{r}) + V_{\text{XC}}(\mathbf{r})$ comprising the potential of the ionic lattice, the Coulomb interaction on the Hartree level (the Hartree term), and the **exchange-correlation (XC)** potential. For the **XC** potential approximations have to be devised as it is unknown in general (an apparently fundamental circumstance despite the fact that the **GS** electronic density of the many-body system can in principle be represented exactly). The **KS** system is auxiliary and necessary for the **DFT** implementation only, for the electronic density may surely be represented by a **WF** and this might indeed be done in terms of the **KS** orbitals organized into a single Slater determinant (referring to the independent-electron point of view), but it is the electronic density and the total energy which are important for the description of the material's **GS** properties.

DFT has been applied to numerous and very different physical and chemical systems with a lot of success. These systems comprise atoms, molecules, solids, and compositions of those, for example, nanosystems of atoms and molecules on surfaces. In Sec. 2.4 the application of DFT to the Ta(001)-p(3×3)-O surface is presented, and in Sec. 2.5 the vdW extension detailed. Even though Ta(001)-p(3×3)-O is on the borderline between metallicity and insulating behaviour, and bonding is somewhat overestimated DFT (see Sec. 2.5), the results provide a very good starting point for the understanding of this oxide surface and the basis for future investigations. There are, however, classes of systems for which DFT yielded less satisfactory results, and that is mostly connected with the approximations to the XC term, which are necessary due the difficulty to represent correlations in terms of the electronic density. In the next Chpts. 3 and 4 correlations are accounted for by models which are based on a description dual to the density. But also in the approaches discussed there, DFT still yields the starting point for the inclusion of material-specific data.

The following sections introduce DFT and present the results of its application to the Ta(001)-(3×3)-O surface. With that they also detail the basis of all computations and further studies performed or reported on in the present thesis. – Sec. 2.1 presents a general derivation of DFT. This includes the outline of the HK theorems and their KS implementation (Subsec. 2.1.1); the discussion of the XC functional and the most common of its approximations (Subsec. 2.1.2); and the extension of DFT to include magnetism (Subsec. 2.1.3). Extensions to include the current density (Appx. A.1), and a further one for the relativistic domain (Appx. A.2) are provided in the appendix; non-relativistic DFT is hereby successively embedded into larger contexts, and finally derived from relativistic QED, explaining the emergence of spin and the spin-orbit coupling (SOC), and the form of the Coulomb interaction. The latter can also be introduced to DFT by an ad-hoc MF-like extension within DFT+U (Subsec. 2.1.4). – Sec. 2.2 describes STM and the corresponding theory for the interpretation of STM images on a basic level. Together with scanning tunnelling spectroscopy (STS), STM experiments are the ones mostly conducted for such systems as investigated in the present thesis. Not many STM experiments have been performed on adsorbates on graphene monolayers due to their difficult preparation, but the Ta(001)-(3×3)-O as well as the CoCu_n/Cu(111) systems (see Chpt. 4) discussed in the present thesis were investigated by STM. – Sec. 2.3 provides the general embedding of the Ta(001)-(3×3)-O system in the context of surface science and current research. – Sec. 2.4 finally exemplifies the application of DFT on the Ta(001)-(3×3)-O surface by presenting the publication as the result of the joint collaboration with the group of Dr. Jens Wiebe and Prof. Roland Wiesendanger. – Sec. 2.5 goes further, and extends DFT by the vdW interactions, which often happen to be relevant for the adsorbate-surface interaction and geometry. It includes a discussion on the iterative Hirshfeld (HI) algorithm to account for charge transfer (Subsec. 2.5.1), and on the self-consistent screening of dispersion coefficients (Subsec. 2.5.2). – Sec. 2.6 describes the application of vdW-DFT to the Ta(001)-(3×3)-O surface; this includes the structural modifications by the vdW interactions (Subsec. 2.6.1), a Hirshfeld charge and polarization analysis (Subsec. 2.6.2), and a discussion of the dispersion coefficients (Subsec. 2.6.3).

2.1 Density functional theory

We start the exposition of **DFT** by reformulating the **EV** problem for the Hamiltonian in Eq. (2.1), in terms of the **HK** minimum principle for an energy functional depending on the electronic density. Extensions to include the spin or current density, or to account better for the correlations, will be introduced in the next subsections after the **DFT** basics have been laid out, or in the appendix (Appx. A). **HF** theory has provided the ideas of self-consistency and **MF** theory to electronic systems, and **DFT** implements the idea of energy-functional minimization in the **HK** theorems via the **KS** equations, which can be seen analogous to the **HF** equations, but which extend them in taking into account correlations beyond the exchange term. These correlations can be considered further by a **MF**-like extension within **DFT+U**.

2.1.1 The Hohenberg-Kohn theorems and the Kohn-Sham solution

Hohenberg and Kohn [Hoh64] started their derivation of **DFT** by decomposing the Hamiltonian in Eq. (2.1) into three parts,

$$\hat{H} = \hat{T} + \hat{V}_{\text{ext}} + \hat{V}_{\text{el-el}}, \quad (2.4)$$

where the first part is the kinetic energy, the second part the external (and the chemical) potential, and the third part the electron-electron interactions. Formally, the interacting **GS** charge density is given by the expectation value

$$n(\mathbf{r}) = \langle \Psi_0 | \hat{\psi}^\dagger(\mathbf{r}) \hat{\psi}(\mathbf{r}) | \Psi_0 \rangle. \quad (2.5)$$

The **GS** given by the **WF** $|\Psi_0\rangle$ is assumed to be non-degenerate, but degenerate **GSs** can be considered as well [Sch13]. The expectation value renders the electronic density $n(\mathbf{r})$ being a functional of the external potential $V_{\text{ext}}(\mathbf{r})$. The **HK** theorem I states that the external potential $V_{\text{ext}}(\mathbf{r})$ can conversely be viewed as a unique functional of the electronic density $n(\mathbf{r})$. This bijection is clear in view of the universality of the other two terms in Eq. (2.4), $\hat{T} + \hat{V}_{\text{el-el}}$, which have the same form for all electronic systems, and the proof can be read in Ref. [Hoh64] and in all textbooks on **DFT**.

The external potential $V_{\text{ext}}(\mathbf{r})$ determines the Hamiltonian \hat{H} , and as $V_{\text{ext}}(\mathbf{r})$ is a functional of $n(\mathbf{r})$, $|\Psi_0\rangle$ is also a functional of $n(\mathbf{r})$. The two universal terms in Eq. (2.4) can then be used to define a universal density-dependent functional,

$$F[n] = \langle \Psi_0 | \hat{T} + \hat{V}_{\text{el-el}} | \Psi_0 \rangle. \quad (2.6)$$

The Hamiltonian expectation value $E_V[n] = \langle \Psi_0 | \hat{H} | \Psi_0 \rangle$ can now be decomposed into the universal part and the part containing the external potential,

$$E_V[n] = F[n] + \int d\mathbf{r} V_{\text{ext}}(\mathbf{r})n(\mathbf{r}), \quad (2.7)$$

and it depends parametrically on the external potential. The **GS** energy is obtained for the

GS density. The HK theorem II states that $E_V[n]$ is minimal for the GS density, that is,

$$E = \min_{n(\mathbf{r})} \left\{ F[n] + \int d\mathbf{r} V_{\text{ext}}(\mathbf{r})n(\mathbf{r}) \right\}. \quad (2.8)$$

We assume for now that all functional derivatives with respect to the density are admissible (see e.g. Ref. [Giu05] for a discussion of this point), and the variational principle leads to the equation

$$\frac{\delta F[n]}{\delta n(\mathbf{r})} = -V_{\text{ext}}(\mathbf{r}), \quad (2.9)$$

which again shows the bijective correspondence between the electronic density and the external potential (HK theorem I). The universal part of the functional is difficult to find as it contains the correlations, and no conclusive expression in terms of the density has been found until today.

Kohn and Sham set out for the computational realization of the HK theorems [Koh65]. To this end, the functional $F[n]$ is further decomposed into yet another universal functional and the Hartree energy,

$$F[n] = G[n] + \frac{1}{2} \int d(\mathbf{r}, \mathbf{r}') \frac{n(\mathbf{r})n(\mathbf{r}')}{|\mathbf{r} - \mathbf{r}'|}. \quad (2.10)$$

The Hartree term will be denoted by $E_H[n]$ in what follows. The functional $G[n]$ contains the kinetic energy and the correlations. According to the HK theorems, the kinetic energy for a non-interacting electron system, $T_s[n]$, is a unique functional of the density. Thus, all correlations in the system may be gathered into one XC functional $E_{\text{xc}}[n]$, so that

$$G[n] = T_s[n] + E_{\text{xc}}[n]. \quad (2.11)$$

The XC functional $E_{\text{xc}}[n]$ is defined by exactly that decomposition. While $T_s[n]$ is the kinetic energy of a non-interacting system, the particles still are subjected to the constraint that they yield the interacting density $n(\mathbf{r})$,

$$T_s[n] = \min_{\psi \rightarrow n(\mathbf{r})} \langle \psi | \hat{T} | \psi \rangle. \quad (2.12)$$

The kinetic energy for the auxiliary non-interacting KS system is in general different to the one for the interacting system. With all the definitions at hand, we are able to rewrite the energy functional as

$$E_V[n] = T_s[n] + E_{\text{ext}}[n] + E_H[n] + E_{\text{xc}}[n]. \quad (2.13)$$

The energy due to the external potential $E_{\text{ext}}[n]$, and the Hartree energy $E_H[n]$ do not depend on whether the electronic system is interacting or not as long as they have the interacting density as their variable. The minimum principle (HK theorem II) yields the

equation

$$\frac{\delta T_s[n]}{\delta n(\mathbf{r})} = -V_{\text{KS}}[n](\mathbf{r}), \quad (2.14)$$

where

$$V_{\text{KS}}[n](\mathbf{r}) = \frac{\delta(E_{\text{ext}}[n] + E_{\text{H}}[n] + E_{\text{xc}}[n])}{\delta n(\mathbf{r})}. \quad (2.15)$$

The **KS** potential $V_{\text{KS}}[n](\mathbf{r})$ is a local functional of the density. As the electronic system is described in terms of non-interacting particles moving in the **KS** potential, one is now able to define the **KS** equation

$$\left[-\frac{1}{2}\Delta + V_{\text{KS}}[n](\mathbf{r}) \right] \phi_{\alpha\sigma}(\mathbf{r}) = \varepsilon_{\alpha} \phi_{\alpha\sigma}(\mathbf{r}), \quad (2.16)$$

along with the condition that the **KS-WFs** combine to yield the interacting density

$$n(\mathbf{r}) = \sum_{\alpha=1}^N \sum_{\sigma} |\phi_{\alpha\sigma}(\mathbf{r})|^2, \quad (2.17)$$

which enters into the **KS** potential $V_{\text{KS}}[n](\mathbf{r})$. The index α comprises band, momentum, and possible some other indices; the momentum is assumed confined to the first **Brillouin zone (BZ)** (due to Bloch's theorem), the band index can be transformed to other orbitals if needed [Sch13]. As in **HF** theory, the **KS** equation needs to be solved iteratively until self-consistency is achieved, and one has eventually found the interacting **GS** density and the **GS** energy. The difference, though, is the complete locality of the **KS** operator, while the **HF** operator was non-local, but now all correlations are included (at least formally). After having obtained the solution and some rearrangements, the **GS** energy is given by

$$E = \sum_{\alpha=1}^N \varepsilon_{\alpha} - E_{\text{H}}[n] - \int d\mathbf{r} V_{\text{xc}}[n](\mathbf{r})n(\mathbf{r}) + E_{\text{xc}}[n]. \quad (2.18)$$

As in **HF** theory, the **GS** energy is not just the sum of the orbital energies, but modified by the interactions. As the **KS** system is an auxiliary system, neither the **EVs** nor the **WFs** are physical, even though they are often used like that, and we will do the same to project onto local orbitals and derive hybridization functions. There is, however, a proof showing that in metals the **EV** of the highest occupied **KS** orbital is the true Fermi level (in spite of the fact that the **KS** Fermi surface is not physical) [Giu05].

2.1.2 The exchange-correlation functional

The electron-electron interaction in Eq. (2.1) can be rewritten in terms of the density operator as [Sch13]

$$\hat{V}_{\text{el-el}} = \frac{1}{2} \int \frac{d(\mathbf{r}, \mathbf{r}')}{|\mathbf{r} - \mathbf{r}'|} [\hat{n}(\mathbf{r})\hat{n}(\mathbf{r}') - \delta(\mathbf{r} - \mathbf{r}')\hat{n}(\mathbf{r})]. \quad (2.19)$$

The **XC** functional is the difference

$$\begin{aligned} E_{\text{xc}}[n] &= \langle \Psi_0 | \hat{V}_{\text{el-el}} | \Psi_0 \rangle - E_{\text{H}}[n] \\ &= \frac{1}{2} \int \frac{d(\mathbf{r}, \mathbf{r}')}{|\mathbf{r} - \mathbf{r}'|} \langle \Psi_0 | [\hat{n}(\mathbf{r}) - n(\mathbf{r})] [\hat{n}(\mathbf{r}') - n(\mathbf{r}')] - \delta(\mathbf{r} - \mathbf{r}')n(\mathbf{r}) | \Psi_0 \rangle \\ &=: \frac{1}{2} \int d(\mathbf{r}, \mathbf{r}') \frac{n(\mathbf{r})n_{\text{xc}}[n](\mathbf{r}, \mathbf{r}')}{|\mathbf{r} - \mathbf{r}'|}. \end{aligned} \quad (2.20)$$

Integrating the expectation value in the integrand in the second line of Eq. (2.20) over \mathbf{r}' , one obtains the important sum rule

$$\int d\mathbf{r}' n_{\text{xc}}[n](\mathbf{r}, \mathbf{r}') = -1, \quad (2.21)$$

which leads to the interpretation of $n_{\text{xc}}[n](\mathbf{r}, \mathbf{r}')$ as describing an **XC** hole surrounding an electron due to exchange and correlation. In terms of the so-called pair correlation function $g[n](\mathbf{r}, \mathbf{r}')$, the **XC** hole can be written as

$$n_{\text{xc}}[n](\mathbf{r}, \mathbf{r}') = n(\mathbf{r}') (g[n](\mathbf{r}, \mathbf{r}') - 1), \quad (2.22)$$

and the expectation value of the electron-electron interaction takes on the form

$$\langle \Psi_0 | \hat{V}_{\text{el-el}} | \Psi_0 \rangle = \frac{1}{2} \int d(\mathbf{r}, \mathbf{r}') \frac{n(\mathbf{r})n(\mathbf{r}')g[n](\mathbf{r}, \mathbf{r}')}{|\mathbf{r} - \mathbf{r}'|}. \quad (2.23)$$

This equation makes the naming of $g[n](\mathbf{r}, \mathbf{r}')$ as pair correlation function obvious, and it describes the deformation of the Hartree energy to account for the full electron-electron interaction. The pair correlation function can also be calculated in **HF** theory, and using the **KS** orbitals, one may put it in direct analogy. The expression in terms of **KS** orbitals is the exchange-only approximation [Giu05].

The general form of the **XC** functional $E_{\text{xc}}[n]$ (i.e., for the **inhomogeneous electron gas** (**IHEG**)) is not known because the correlations cannot be expressed in terms of the density (at least up to now). It is possible, though, to extract the exchange term from $E_{\text{xc}}[n]$ [Koh65], which then has the same form as in **HF** theory, cf. Eq. (2.2), only with use of the **KS** orbitals. In the energy functional $E_V[n]$, this decomposition would yield a term

$$E_{\text{x}}[n] = -\frac{1}{2} \int d(\mathbf{r}, \mathbf{r}') \frac{n_1(\mathbf{r}, \mathbf{r}')n_1(\mathbf{r}', \mathbf{r})}{|\mathbf{r} - \mathbf{r}'|}, \quad (2.24)$$

with

$$n_1(\mathbf{r}, \mathbf{r}') = \sum_{\alpha\sigma} \phi_{\alpha\sigma}(\mathbf{r}) \phi_{\alpha\sigma}^*(\mathbf{r}'). \quad (2.25)$$

As the non-local nature of the exchange interaction renders the computational efforts rather high, the extraction of the exchange term is not incorporated in the DFT implementation used in the projects reported in the present thesis.

Already Hohenberg and Kohn [Hoh64] and Kohn and Sham [Koh65] used the XC functional for the homogeneous [homogeneous electron gas \(HEG\)](#) as a first approximation, and subsequently extended it by the gradient expansion in terms of the density. Both approximations were employed in the publications included in the present thesis, and are shortly described in the next two subsections.

The local density approximation

The HF equations are exactly solvable for an [HEG](#) [Sch13], and one obtains an exact expression for the exchange energy in terms of the density,

$$\varepsilon_x(n) = -\frac{3}{4} \left(\frac{3}{\pi}\right)^{1/3} n^{1/3} = -\frac{3}{4} \left(\frac{3}{2\pi}\right)^{2/3} \frac{1}{r_s}, \quad (2.26)$$

where the Wigner-Seitz radius defined by $n = (4\pi r_s^3/3)^{-1}$ was inserted. The correlation energy per electron for an [HEG](#) was computed via Monte Carlo by Ceperley and Alder [Cep80] in the parametrization of Perdew and Zunger [Per81],

$$\varepsilon_c(n) = \begin{cases} -0.1423 (1 + 1.0529\sqrt{r_s} + 0.3334 r_s)^{-1} & \text{for } r_s \geq 1, \\ -0.0480 + 0.0311 \ln(r_s) - 0.0116 r_s + 0.0020 r_s \ln(r_s) & \text{for } r_s < 1. \end{cases} \quad (2.27)$$

The XC energy per electron for the [HEG](#) is the sum of both terms, $\varepsilon_{xc}(n) = \varepsilon_x(n) + \varepsilon_c(n)$. Within the LDA, the XC energy per electron of the [IHEG](#) is approximated by the same expression, so that one obtains the XC functional

$$E_{xc}^{\text{LDA}}[n] = \int d\mathbf{r} \varepsilon_{xc}(n(\mathbf{r}))n(\mathbf{r}). \quad (2.28)$$

The XC potential in the LDA can then be obtained via functional derivation,

$$V_{xc}^{\text{LDA}}[n](r) = \frac{\delta E_{xc}^{\text{LDA}}[n]}{\delta n(\mathbf{r})}. \quad (2.29)$$

Comparing with Eq. (2.20), one can express the XC energy in the LDA in terms of the XC hole as

$$\frac{1}{2} \int d\mathbf{r}' \frac{n_{xc}^{\text{LDA}}[n](\mathbf{r}, \mathbf{r}')}{|\mathbf{r} - \mathbf{r}'|} = \varepsilon_{xc}(n(\mathbf{r})). \quad (2.30)$$

Apart from the factor of $\frac{1}{2}$, the expression on the left-hand side is the Hartree potential of the XC hole. However, it is obvious from Eq. (2.30) that its long-range behaviour is not the one of the Coulomb law, $\propto 1/|\mathbf{r}|$. This behaviour might lead to problems for chemical bonding as it depends strongly on the correct overlap of WFs [Sch13]. The known overestimation of bonding within the LDA is due to an incorrect logarithmic divergence in the high-density limit [Giu05], which is corrected by the generalization of the LDA described in the next subsection. In contrast to these deficiencies, the sum rule in Eq. (2.21) is satisfied, which is one reason for its successes.

The generalized gradient approximation

The LDA can be employed if the electronic density is sufficiently slowly varying, nearly behaving like an HEG, and it fails for strongly correlated systems. It can be considered as the lowest order within the expansion of the XC functional integrand in the gradients of the density [Hoh64; Sch13]. A slowly varying density can be defined as the one which changes only little within local Wigner-Seitz spheres (i.e., the density is rather high), so that an expansion of the integrand of the XC functional in the small quantity

$$x = \left(\frac{4\pi}{3}\right)^{1/3} r_s \frac{|\nabla n(\mathbf{r})|}{n(\mathbf{r})} = \frac{|\nabla n(\mathbf{r})|}{n^{4/3}(\mathbf{r})} \ll 1 \quad (2.31)$$

can be performed. This leads to the expression of the **gradient expansion approximation (GEA)**

$$E_{xc}[n] = E_{xc}^{\text{LDA}}[n] + \int d\mathbf{r} f(n(\mathbf{r})) \frac{|\nabla n(\mathbf{r})|^2}{n^{4/3}(\mathbf{r})}, \quad (2.32)$$

where higher order terms have been neglected. Written as such, it is already an extension away from the HEG to the IHEG, but still with a slowly varying density. A particular variant of the second order shown in Eq. (2.32) for spin-polarized systems was given by Rasolt and Geldart [Giu05; Ras86] having the form

$$E_{xc}^{\text{GEA},(2)}[n_{\uparrow}, n_{\downarrow}] = \frac{1}{2} \sum_{\sigma\sigma'} \int d\mathbf{r} B_{xc,\sigma\sigma'}(n_{\uparrow}(\mathbf{r}), n_{\downarrow}(\mathbf{r})) \nabla n_{\sigma}(\mathbf{r}) \cdot \nabla n_{\sigma'}(\mathbf{r}). \quad (2.33)$$

The major drawback of the GEA is the violation of the sum rule in Eq. (2.21). The **generalized gradient expansion (GGA)** is designed to satisfy the sum rule, and correct the LDA for the overbinding. The details are rather complex and a derivation together with relevant references can be found in Ref. [Giu05], a few details of which we will reflect shortly.

The XC functional in the GGA for the generally spin-polarized case assumes the form

$$E_{XC}^{\text{GGA}}[n_{\uparrow}, n_{\downarrow}] = \int d\mathbf{r} f(n_{\uparrow}(\mathbf{r}), n_{\downarrow}(\mathbf{r}), \nabla n_{\uparrow}(\mathbf{r}), \nabla n_{\downarrow}(\mathbf{r})). \quad (2.34)$$

Then it is subjected to the sum rule and the correct long-range behaviour, alongside with some other exact properties like various scaling behaviours (e.g., for the density)

and asymptotics (e.g., for the gradient). A derivation of $E_{\text{XC}}^{\text{GGA}}[n_{\uparrow}, n_{\downarrow}]$ was performed by Perdew, Burke, and Ernzerhof (PBE) [Per96], and it takes the form

$$E_{\text{XC}}^{\text{GGA}}[n_{\uparrow}, n_{\downarrow}] = \int d\mathbf{r} F_{\text{xc}}(r_s(\mathbf{r}), p(\mathbf{r}), s(\mathbf{r})) \varepsilon_{\text{x}}(n(\mathbf{r})) n(\mathbf{r}), \quad (2.35)$$

where $r_s(\mathbf{r})$ is the local Wigner-Seitz radius, $p(\mathbf{r})$ the local fractional spin-polarization, and $s(\mathbf{r})$ essentially the small quantity given in Eq. (2.31), that is, the normalized gradient. The reason for this form is the better knowledge of the exchange hole in the exchange-only GGA, and its exact knowledge in the LDA as the starting point for the derivation (i.e., $\varepsilon_{\text{x}}(n(\mathbf{r}))$ is given in Eq. (2.26)). The LDA is assumed in the limit $F_{\text{xc}}(r_s, p, s) \simeq F_{\text{xc}}(r_s, p, 0)$.

The PBE functional was used in the project on the Ta(001)-p(3×3)-O surface (Secs. 2.4 and 2.6). A precursor to PBE, the Perdew-Wang 91 (PW91) functional [Wan91], was used for Co/graphene (Sec. 3.6) and the CoCu_n/Cu(111) systems (Sec. 4.6). PW91 is based on expressions for the correlation energy in the RPA (Sec. 3.1), generalized from the HEG (i.e., the LDA) to slowly varying densities (the high-density limit $r_s \rightarrow 0$).

2.1.3 Spin in DFT

The magnetism of condensed matter systems can be described with DFT at different levels of sophistication, and we choose here to show spin-DFT on an intermediate level, that is, mostly for collinear magnetic states; non-collinearity can be introduced at the price of an index war. This version for DFT was mostly used throughout the projects reported in the present thesis, with use of the non-collinear extension only for a few checks. We shortly discuss other extensions (Appx. A), including the relativistic one, but describe details only for simplified models and rather present only some general physical considerations with regard to the ones mentioned in the introduction.

DFT was extended to spin-polarized systems by von Barth and Hedin [Bar72]. The starting point is the Pauli equation, which is the non-relativistic approximation to the Dirac equation (cf. last paragraph in Appx. A.2). The Hamiltonian includes an external electromagnetic potential (to ensure gauge invariance), and a magnetic field derived from the rotation of its vectorial part, $\mathbf{B} = \nabla \times \mathbf{A}$, and it acts in the Hilbert space of spinor states. In this way, the density variable becomes generalized to a 2×2 Hermitian matrix [Bih06]

$$n_{\sigma\sigma'}(\mathbf{r}) = \langle \Psi_0 | \hat{\psi}_{\sigma}^{\dagger}(\mathbf{r}) \hat{\psi}_{\sigma'}(\mathbf{r}) | \Psi_0 \rangle = [\underline{n}(\mathbf{r})]_{\sigma\sigma'}, \quad (2.36)$$

here, in the general non-collinear case, with $\sigma, \sigma' = +, -$. The KS potential as a functional derivative with respect to the density becomes a matrix as well, and the KS equations reads (cf. Eqs. (2.15) and (2.16))

$$\left[-\frac{1}{2} \Delta \mathbb{1}_2 + \underline{V}_{\text{KS}}[\underline{n}](\mathbf{r}) \right] \begin{pmatrix} \phi_{\alpha,+}(\mathbf{r}) \\ \phi_{\alpha,-}(\mathbf{r}) \end{pmatrix} = \varepsilon_{\alpha} \begin{pmatrix} \phi_{\alpha,+}(\mathbf{r}) \\ \phi_{\alpha,-}(\mathbf{r}) \end{pmatrix}, \quad (2.37)$$

where $\underline{1}_2$ denotes the 2×2 unity matrix. In terms of the **KS** orbitals, the density looks like

$$n_{\sigma\sigma'}(\mathbf{r}) = \sum_{\alpha=1}^N \phi_{\alpha\sigma}^*(\mathbf{r})\phi_{\alpha\sigma'}(\mathbf{r}), \quad (2.38)$$

and it consists of the charge and magnetization densities,

$$\underline{n}(\mathbf{r}) = \frac{1}{2} [n(\mathbf{r})\underline{1}_2 + \underline{\sigma} \mathbf{m}(\mathbf{r})], \quad (2.39)$$

with $\underline{\sigma}$ the vector of Pauli matrices. Both, the external potential $V_{\text{ext}}(\mathbf{r})$ and the **XC** potential $V_{\text{xc}}[n](r)$ appearing in the **KS** potential $V_{\text{KS}}[n](r)$ are of matrix form,

$$\underline{V}_{\text{ext}/\text{xc}}(\mathbf{r}) = V_{\text{ext}/\text{xc}}(\mathbf{r})\underline{1}_2 + \mu_{\text{B}}\underline{\sigma}\mathbf{B}_{\text{ext}/\text{xc}}(\mathbf{r}), \quad (2.40)$$

with $\mu_{\text{B}} = e\hbar/2mc = \frac{1}{2}$ the Bohr magneton in natural units. In this way, the **XC** potential incorporates correlations which are now changed by the presence of the external magnetic field (we will discuss this point shortly a few paragraphs below). An external electrostatic field changes the one of the ionic lattice and can be absorbed into $V_{\text{ext}}(\mathbf{r})$. In the general non-collinear case, that is, if the magnetic moments in the system are not aligned, Eq. (2.37) describes a set of coupled **KS** equations for the density components. In the collinear case, when all magnetic moments are aligned along a preferred direction, e.g. the one given by the external magnetic field, Eq. (2.37) goes over into two decoupled equations with components now indexed by $(+, -) = (\uparrow, \downarrow)$.

We shortly state the **XC** functional in the **local spin density approximation (LSDA)** for the collinear case [Sch13]. The one in the **spin-GEA** and **spin-GGA** have already been given in Subsec. 2.1.2, albeit in a general functional form. The **XC** functional in **LSDA** is

$$E_{\text{xc}}^{\text{LSDA}}[n_{\uparrow}, n_{\downarrow}] = \int d\mathbf{r} \varepsilon_{\text{xc}}(n(\mathbf{r}), p(\mathbf{r}))n(\mathbf{r}), \quad (2.41)$$

where $p(\mathbf{r}) = [n_{\uparrow}(\mathbf{r}) - n_{\downarrow}(\mathbf{r})]/n(\mathbf{r})$ is the fractional spin polarization. Like in the paramagnetic case for the **HEG**, one has the splitting $\varepsilon_{\text{xc}}(n, p) = \varepsilon_{\text{x}}(n, p) + \varepsilon_{\text{c}}(n, p)$. The exchange part is given by

$$\varepsilon_{\text{x}}(n(\mathbf{r}), p(\mathbf{r})) = -\frac{3}{8} \left(\frac{3}{\pi} \right) n^{1/3}(\mathbf{r}) \left[(1 + p(\mathbf{r}))^{4/3} + (1 - p(\mathbf{r}))^{4/3} \right], \quad (2.42)$$

and the correlation part was numerically determined by Ceperley and Alder [Cep80], and given in the parameterization of Vosko *et al.* [Vos80], it can be looked up in Ref. [Sch13].

Even without an external magnetic field it is sometimes beneficial to use **spin-DFT**, because then there are more **DOF** available for the determination of the electronic structure or the relaxed geometry. According to experience, **spin-DFT** sometimes yields larger adsorption heights for adatoms. In post-**DFT** calculations there might occur differences in the results based on magnetically or paramagnetically **DFT**-determined geometries. For example, the Co/graphene system (Sec. 3.6) was relaxed within **spin-DFT**, because

the accordingly larger Co adsorption height renders the screening of the local Coulomb interactions (computed by the to-be-discussed **cRPA**) by the graphene electrons weaker. Thus, the Coulomb interactions on adatoms come out stronger compared to the ones based on the paramagnetically relaxed geometry. But there often happens to result unphysical magnetic moments in the spin-DFT-optimized geometry, as the larger distance between adatom and surface seem to allow for spin excitations, which in generic cases without **SOC** do not exist (physically, the **SOC** is always present, but it is often smaller than most other scales in the system). In this case one has to take the average between the spin components to obtain paramagnetic quantities extracted from spin-DFT, or use paramagnetic DFT with the magnetically relaxed geometry. In general one has to be cautious with spin-DFT as there exist examples (like bulk Cr) for the sensitive dependence of the magnetic properties on the lattice constants, which in turn depend on the energy functional chosen [Bih06; Sin92] (see also Refs. [Bih00; Faw88; Kol02; Kol05; Sch16] on bulk Cr and Cr(001)). Whenever available, it is always worth to compare with experimental results.

The physics of a magnetically behaved system can be understood to some extent by observing the shift of the spin-up and spin-down portions of the **density of states (DOS)** with respect to each other (next to other spectral deviations away from the paramagnetic case). In the simple phenomenological interpretation of the Stoner model, the energy bands are just shifted with respect to each other, $\varepsilon_\sigma(\mathbf{k}) = \varepsilon(\mathbf{k}) + I\langle n_{-\sigma} \rangle$, where I is the Stoner exchange parameter. Any energy enhancement introduced by such a splitting is on the overall overcompensated by the reduction due to the exchange interaction (see also introduction to this chapter). The Stoner model can be obtained from the Hubbard model by the **MF** approximation, and is thus valid for weak correlations [Lic13]. (The Hubbard model can in principle be obtained from Eq. (2.1) by a tight-binding-like transformation to local orbitals which cover all sites, cf. Refs. [Kar13; Kor08; Kov10; Kun11], and is essentially the lattice version of the to-be-discussed **AIM** (Sec. 3.2)). For strongly correlated materials, on the other hand, the Hubbard model (at half-filling) is effectively the Heisenberg spin model. In systems where Coulomb localization and band delocalization are on a comparable scale, such as in **TM** systems, both, longitudinal (Stoner) and transverse (Heisenberg), magnetic fluctuations need to be considered equally within the Hubbard model. The Stoner parameter I can be identified with the exchange part of the (non-local) Coulomb interaction between two different sites, $J_{12} = \langle 12 | V_{\text{el-el}}(\mathbf{r}_1 - \mathbf{r}_2) | 21 \rangle$. Ref. [Lic13] also provides a review of how these quantities can be calculated from first principles.

While the Stoner model point of view can lead to an understanding of magnetism in **DFT**, it also makes its shortcomings apparent [Lic13]: **DFT** contains correlations only in the **MF** approximation (see Ref. [Coh08] for a more thorough assessment of the **DFT** limitations). Within the **GF** approach (Chpt. 3, and here especially in Appx. C.1), one can furthermore see by the equal-time nature of the formalism for **DFT** that collective excitations, such as plasmons and magnons (cf. Appx. A.1), are excluded from its description (but one may still describe them approximately, e.g., within the frozen magnon approximation [Ess11; Gro01]). (Cf. introductory part to Chpt. 4: Plasmons are quantized density oscillations (quasi-particles) which arise from the long-range part of the Coulomb interaction; magnons are analogous collective spin excitations.) The equal-time nature also excludes a notion of temperature beyond the Fermi distribution function, but thermal excitations (which

may generate plasmons and magnons) can lead to a reduction of the magnetic order in the system. Such matters can be met, for example, within **time-dependent DFT (TDFT)** which yields the exact response functions. However, due to its reliance on the random phase approximation, it is again valid only for rather weakly correlated systems such as aluminium and its plasmonic excitations. One possible solution to include strong correlations in real materials lies in a first consideration of the local correlations within an **AIM** (Chpt. 3), and then in a successive extension of that model, first by the self-consistency of **DMFT** (cf. Subsec. 3.2.1) [Geo92; Geo96; Met89; Vol12], and then by the dual-fermion and dual-boson approaches for the non-local correlations [Rub12; Rub09]; or first by the to-be-discussed **GWA** (Sec. 3.1), and then by some **EDMFT** [Bie03; Hel11; Sun02]. Non-local correlations can also be considered within real-space **DMFT** (rDMFT), in which the local correlations on several impurities represented by individual **AIMs** are connected via the **DMFT** self-consistency [Kub16; Tit12], as well as within **cluster DMFT** (cDMFT) [Har16; Nom14; Pot18]. There are many implementations and results of, and reviews on, the **DFT+DMFT** and related approaches, see Refs. [Ama08; Ani97b; Dan14; Geo04; Gull11; Hau10; Hel07; Hel08; Kot06; Lec06; Nek13; Pau19; Pav14; Pav11; Pou07; Tom12] for a selection. The present thesis will later focus on the local correlations without any self-consistency or anything beyond, that is, to the **DFT+AIM** approach for correlated adatoms (and nanostructures) on surfaces.

The concept of spin will be further embedded into the current- and spin-DFT in Appx. A.1, and more comprehensively derived from **QED** and **relativistic DFT (RDFT)** in Appx. A.2. In the non-relativistic limit one can observe that the spin is coupled to the electronic motion via the **SOC**. The electrons move through a lattice potential, or are localized in the vicinity of an adatom on the surface, so the motion and thus the magnetism is anisotropic. The concept of magnetic anisotropy will be discussed to some extent in Appx. B. As mentioned in Subsec. 3.2.1, the implementation details for the transition from **DFT** to the **AIM**, and to some extent for **DFT** itself as in its incarnation within the **Vienna *ab-initio* simulation package (VASP)** [Kre96], can be read in Refs. [Kar13; Kar11b] and Sec. 3.6. In Appx. B we will describe a very few **DFT** implementation details with regard to the magnetic anisotropy.

2.1.4 Hubbard- U in DFT

In principle, **DFT** fully describes the **GS** of the inhomogeneous electron system and takes into account all correlation effects. In practice, nobody knows how the **XC** functional for the inhomogeneous system looks like. Together with reduced delocalization and momentum, these inhomogeneities lead to localization of electrons, especially around nuclei having d - or f -shell valencies (Mott localization [Mot49; Mot37]) [Ani97a; Coc12]. Localization is accompanied by band narrowing, resulting in bands looking more like energy states, sometimes in insulating behaviour with gaps between energy bands around the Fermi level, and in discontinuities of the **XC** potential (which, however, are not reproduced in the **LDA** and **GGA** approximation) [Per17; Sei96]. Localized electrons happen to be strongly correlated, a situation which is not met properly by common **XC** functionals derived under conditions like slowly varying charge densities near the **HEG** limit. Furthermore, the **KS** formalism renders the **XC** potential being a multiplicative and **MF**-like term depending

on the density (and possibly its gradients). In these points the **HF** theory seems more precise and general in comparison to **DFT**; but via the hybrid functional approach the **HF** exchange interactions can be taken into account exactly in **DFT** [Bec93]; and **HF** theory does not contain correlations at all, as these pertain to a multi-determinantal description (full **CI** or some approximative approach to it). Like ordinary band theory, which itself emphasizes delocalization and metallicity, **HF** theory does not contain Mott physics.

The shortcomings were in particular seen for Mott insulators like the *3d*-**TM** oxides [Ani97a; Ani91b]. In Ref. [Ani91b] a first so-called **DFT+U** scheme was set up which used the Hubbard parameter U and the Stoner exchange parameter I (identified with the Hund’s rule exchange J), both calculated beforehand within **constrained DFT** (**cDFT**) (see Refs. [Ani91a; Coc05; Gun89]), in an augmentation of the **DFT** energy functional by a **MF**-like approximation to the Hubbard interaction term,

$$E_V[n] = E_V^{\text{DFT}}[n] + \frac{1}{2} \sum_{imm'\sigma} U(n_{im\sigma} - \bar{n}_i)(n_{im',-\sigma} - \bar{n}_i) + \frac{1}{2} \sum_{i,m \neq m',\sigma} (U - J)(n_{im\sigma} - \bar{n}_i)(n_{im'\sigma} - \bar{n}_i). \quad (2.43)$$

The index i runs over the correlated sites, and m, m' over the correlated orbitals. **DFT** is a **MF** approximation to the correlations, reflecting them in the Hartree and **XC** potential, both contained in $E_V^{\text{DFT}}[n]$. The second and third terms contain the deviations of the local occupations of the correlated shell around their **MF** values, $\bar{n}_i = \frac{1}{2(2l+1)} \sum_{m\sigma} n_{im\sigma}$. In this way, spin and orbital **DOF** are treated on an equal footing allowing for both, spin and orbital, polarizations. It should be noted that the occupation **EVs** are used instead of number operators for the Hubbard term, signifying that the **DFT+U** approach still is a (static) **MF** approach to the correlations (in contrast to **DMFT**). The reduction of the correlation strength in the third term implements the first Hund’s rule (it is $U > J > 0$).

A reorganization of the Coulomb interactions shown in Eq. (2.43) into the “direct” Hubbard term (i.e., occupations directly, and not their deviation around the **MF** value) and the so-called **DC** term was performed subsequently [Czy94; Sol94], opening up a more detailed assessment of the correlations in the **DFT+U** functional being used. The Hubbard term was then extended to fulfil invariance under unitary transformations of the local basis [Lie95], providing the possibility to include all Coulomb interaction terms and its convenient Slater parametrization in the spherically symmetric case. Finally, a simplified form of the functional has been proposed [Dud98], to be discussed below, and which has been used in the simulations reported in Secs. 2.4 and 2.6.

In general, the **DFT+U** functional is now decomposed into three terms [Coc12],

$$E_V^{\text{DFT+U}}[n] = E_V^{\text{DFT}}[n] + E^{\text{Hubbard}}[\{n_{imm'\sigma}\}] - E^{\text{DC}}[\{n_{i\sigma}\}], \quad (2.44)$$

where the second term contains the electronic interactions as in the Hubbard model (with occupation **EVs** and not the deviations from their **MF** value), and the third term the **DC** reflecting the correlations already present in **DFT**, but which are more appropriately accounted for by the Hubbard term. That means, the **DC** is the **DFT-MF** approximation to

the Hubbard term. The occupation matrices can be obtained from DFT via projections of the Bloch states (indexed by band n and momentum \mathbf{k}) onto atomic-like orbitals (indexed by site i and orbital m), weighted by the Fermi function,

$$n_{imm'\sigma} = \sum_{n\mathbf{k}} f_{n\mathbf{k}\sigma} \langle \psi_{n\mathbf{k}\sigma} | \phi_{im'} \rangle \langle \phi_{im} | \psi_{n\mathbf{k}\sigma} \rangle. \quad (2.45)$$

In terms of these, the Hubbard term in the full and unitary invariant form is given by

$$\begin{aligned} E^{\text{Hubbard}}[\{n_{imm'\sigma}\}] &= \frac{1}{2} \sum_{i, \{m\}, \sigma} [\langle m, m'' | \hat{V}_{\text{el-el}} | m', m''' \rangle n_{imm'\sigma} n_{im''m''', -\sigma} \\ &\quad + (\langle m, m'' | \hat{V}_{\text{el-el}} | m', m'' \rangle - \langle m, m'' | \hat{V}_{\text{el-el}} | m''', m' \rangle) n_{imm'\sigma} n_{im''m'''\sigma}]. \end{aligned} \quad (2.46)$$

Expanding the Coulomb potential $V_{\text{el-el}}(\mathbf{r} - \mathbf{r}') = 1/|\mathbf{r} - \mathbf{r}'|$ into spherical harmonics, one obtains

$$\langle m, m'' | \hat{V}_{\text{el-el}} | m', m''' \rangle = \sum_{k=0}^{2l} a_k(m, m', m'', m''') F^k, \quad (2.47)$$

where the summation has been limited to the case of one electronic shell with specific n and l . The angular Slater integrals are given by

$$a(m, m', m'', m''') = \frac{4\pi}{2k+1} \sum_{q=-k}^k \langle lm | \hat{Y}_{kq} | lm' \rangle \langle lm'' | \hat{Y}_{kq}^* | lm''' \rangle, \quad (2.48)$$

and the radial Slater integrals by

$$F^k = \int d(r, r') (rr')^2 R_{nl}^2(r) \frac{r_{\leq}^k}{r_{>}^{k+1}} R_{nl}^2(r') \equiv F^k(nl, nl). \quad (2.49)$$

These Slater integrals appear from representing the spherical harmonics in position space. Only F^0 , F^2 , F^4 are needed for d elements. For the spherically symmetric case, the Hubbard parameters can be extracted from the Coulomb interaction components via

$$\begin{aligned} U &= \frac{1}{(2l+1)^2} \sum_{mm'} \langle mm' | \hat{V}_{\text{el-el}} | mm' \rangle = F^0, \\ J &= \frac{1}{2l(2l+1)} \sum_{m \neq m'} \langle mm' | \hat{V}_{\text{el-el}} | mm' \rangle = \frac{F^2 + F^4}{14}. \end{aligned} \quad (2.50)$$

These reversely determine the Coulomb interaction in its rotationally invariant parameterization; a more thorough discussion on the Slater and other parameterizations can be found in Ref. [Kar13]. If the values U and J in Eq. (2.50) or the full (orbital-dependent)

Coulomb interaction matrix in Eq. (2.46) are known (e.g., from cDFT [Ani91a; Coc05; Gun89], or from cRPA and possible subsequent averaging, Subsec. 3.1.2, and Secs. 3.5 and 3.6), one knows in fact the screened Coulomb interaction. This is to be distinguished from the bare Coulomb interaction used in HF theory. One may note at this point that the Coulomb interaction from cRPA is actually frequency-dependent, and DFT+ U only takes into account its static part for the Hubbard term ($\omega = 0$; like most quantum impurity solvers, cf. Chpt. 3); in fact, DFT+ U is the static limit of the GWA (Sec. 3.1) [Coc12].

Finally, according to HF theory, the DC term accompanying the general Hubbard term given in Eq. (2.46) assumes the form [Coc12]

$$E^{\text{DC, FLL}}[\{n_{i\sigma}\}] = \frac{1}{2} \sum_i \left[U_i n_i (n_i - 1) - J_i \sum_{\sigma} n_{i\sigma} (n_{i\sigma} - 1) \right], \quad (2.51)$$

with $n_i = \sum_{m\sigma} n_{im\sigma}$ and $n_{i\sigma} = \sum_m n_{im\sigma}$. This is the so-called “fully localized limit (FLL)” which works well for more localized orbitals with strong correlations. The DC term is subtracted, so integer orbital occupations of 0 or 1 favouring the Mott localization are encouraged. For the other limit of more extended orbitals with rather metallic behaviour and weaker correlations, the “around MF (AMF)” limit given in Eq. (2.43) can be used. Together with the Hubbard term, the AMF functional encourages non-uniform occupations within the correlated orbitals. For Co/graphene (Sec. 3.6) the AMF limit was used as it performed best for this apparently weakly correlated system (the AMF limit was tested against the FLL). For the CoCu_n/Cu(111) systems (Sec. 4.6) both DC approaches were used according to the degree of delocalization of the correlated Co adatom in the different Cu(111) environments (Subsec. 4.6.7). Hybrid combinations of DC terms interpolating between these two limits are sometimes also beneficial [Coc12]. In Appx. C.1 the DC theory is placed in the general context of the Luttinger-Ward functional, where it receives its exact definition from a non-perturbative “intersection” of DFT and DMFT (or the AIM); that is, one has to represent the correlations within DFT in the variables of DMFT.

A few extensions of the DFT+ U functional are available. An important one is the so-called DFT+ U + V method based on the extended Hubbard model containing the inter-site Coulomb interactions [Coc12],

$$\hat{H}_V^{\text{Hubbard}} = \sum_{\langle i,j \rangle} V_{ij} \hat{n}_i \hat{n}_j, \quad (2.52)$$

where the sum runs over nearest-neighbour correlated sites (spin and orbital indices are implicit). The form given here allows for directional dependence of the interactions. Alongside with its suggested importance for high- T_c superconductivity (SC) ($U > 0$ and $V < 0$), magnetic and charge order, charge density waves (CDWs), spin density waves (SDWs), and other non-local properties of materials can be described by taking into account inter-site correlations. These considerations go along the ones on local and non-local correlations made in Subsec. 2.1.3 and Appx. A.1. For example, for the solution of extended Hubbard models, to which Eq. (2.52) contributes the non-local Coulomb interactions, one can extend the DMFT by the dual-boson approach [Rub12; Ste16b].

Retaining only the lowest order of the expansion in Eq. (2.48), $a_0(m, m', m'', m''') = \delta_{mm'} \delta_{m''m'''}$, one obtains the simplification of the full Hubbard term used within the **DFT+U** calculations for the Ta(001)-p(3×3)-O surface [Dud98]. The Hubbard and **DC** terms have the form

$$\begin{aligned} E^{\text{Hubbard}}[\{n_{imm'\sigma}\}] - E^{\text{DC}}[\{n_{i\sigma}\}] &= \frac{1}{2} \sum_i U_i [(\text{Tr}(\underline{n}_i))^2 - \text{Tr}((\underline{n}_i)^2)] \\ &\quad - \frac{1}{2} \sum_i U_i n_i (n_i - 1) \\ &= \frac{1}{2} \sum_i U_i \text{Tr}[\underline{n}_i (1 - \underline{n}_i)]. \end{aligned} \quad (2.53)$$

The trace runs over spin and orbital indices, and the third line shows that the rotational invariance of the original full Hubbard term (Eq. (2.46)) is maintained. No Hund's rule coupling J is contained in the formula (excluding non-collinear magnetic order, particular multi-orbital correlations, and its interplay with the **SOC** [Coc12]), but in Ref. [Dud98] the on-site Coulomb strength was actually denoted by $U_{\text{eff},i} = U_i - J_i$. In principle this might cause problems as, for example, the relation $U < J$ what was found to be relevant for the Fe magnetic moment of Fe-based **SCs** [Coc12]. For positive $U_{\text{eff},i}$, though, integer occupations are preferred and Mott localization is found.

For the Ta(001)-p(3×3)-O surface the **DFT+U** approach from Ref. [Dud98] was employed with U on oxygens, because their local interaction was found to be relevant when these are situated in **TM** environments (U on oxygen p shells is often comparable to U on **TM** d shells) [Nek00]. As the oxygen p shell is approximately filled when placed on the Ta(001) surface, the Hund's rule coupling J is less important and a single U_{eff} sufficient. Test calculations showed that U on tantalums around 1.0 eV (which lies within the range used in Ref. [Lan13]) does not change any results.

2.2 Scanning tunnelling microscopy and the Tersoff-Hamann model

The systems studied in the present thesis belong to the realm of surface science. One of the experiments to study surfaces and nanoparticles thereon is **STM** invented by Binnig *et al.* in 1982 [Bin82]. In the ideal setup, an atomically sharp metallic or **superconducting (SC)** tip is positioned above the surface, and the resulting tunnelling current is measured. A bias voltage between the tip and the surface can be applied additionally.

Usually tungsten, platinum or platinum/iridium tips are used for metallic tips; materials for **SC** tips include niobium and vanadium. In the **constant-current (CC)** mode, the bias voltage is fixed, while the tip is free to relax in the direction perpendicular (longitudinal) to the surface [Hes16]. The distance is controlled by a feedback loop containing a piezoelectric crystal, which expands linearly with the current crossing it, so that the tip height is adjusted accordingly and the bias-dependent surface topography can be assessed. Alternatively, the tip height can be fixed and the resulting tunnelling current measured while scanning through all lateral positions. Usual currents vary between 10 pA and 10 nA, and the longitudinal resolution is within 0.1 Å. As **STM** relies on an exponential dependence of the

tunnelling current with respect to the tip-to-surface distance, and is thus very sensitive to that distance, the whole setup has to be isolated from vibrations from within and without the laboratory by a vibration damper (see the book by Wiesendanger [Wie94] for technical details).

For the derivation of the tunnelling current, we follow Ref. [Giu14]. Bardeen provided the first derivation of the tunnelling current between two metal layers separated by a vacuum gap, which include the Fermi levels, the DOS, and the spatial overlap of the respective WFs [Bar61]. The tunnelling current between tip and surface is then given by an expression resembling first-order perturbation theory,

$$I(V, \mathbf{r}_t) = 2\pi \sum_{ij} f(E_{t,i} - E_{t,F}) [1 - f(E_{s,i} - E_{s,F})] |M_{ij}(\mathbf{r}_t)|^2 \delta(E_{t,i} - E_{s,j}), \quad (2.54)$$

where the tip Fermi level is offset from the one of the surface by the bias voltage V , $E_{t,F} = E_{s,F} + V$. The convention is such that a positive bias leads to a current flowing from the tip to the surface. To this end, the state i of the tip with energy $E_{t,i}$ must be occupied, which is indicated by the corresponding Fermi function, while the state j of the surface with energy $E_{s,j}$ must accordingly be unoccupied. The tunnelling matrix element at the position of the tip $M_{ij}(\mathbf{r}_t)$ was determined in Ref. [Bar61] as

$$M_{ij}(\mathbf{r}_t) = \frac{1}{2} \int d\mathbf{S} [\psi_{t,i}^*(\mathbf{r} - \mathbf{r}_t) \nabla \psi_{s,j}(\mathbf{r}) - \psi_{s,j}^*(\mathbf{r}) \nabla \psi_{t,i}(\mathbf{r} - \mathbf{r}_t)], \quad (2.55)$$

where \mathbf{S} is a surface separating tip and surface. The tunnelling matrix element $M_{ij}(\mathbf{r}_t)$ is the expectation value of the current operator, and $|M_{ij}(\mathbf{r}_t)|^2$ describes the interference of tip and surface WFs.

Under the assumption of a spherical tip apex, Tersoff and Hamann determined the tunnelling matrix element being proportional to the surface WF at the centre of the tip sphere [Ter85],

$$M_{ij}(\mathbf{r}_t) \propto \psi_{s,j}(\mathbf{r}_t). \quad (2.56)$$

Furthermore, DFT describes the GS at zero temperature where the Fermi functions become step functions. Using the tip DOS, $\rho_t(E) = \sum_i \delta(E - E_{t,i})$, the expression for the tunnelling current can be simplified to

$$I(V) \propto \int_{E_{s,F}}^{E_{s,F}+V} dE \rho_t(E) \sum_j |\psi_{s,j}(\mathbf{r}_t)|^2 \delta(E - E_{s,j}), \quad (2.57)$$

where the sum over states j yields the local DOS (LDOS) of the surface at the position of the tip, $\rho_s(\mathbf{r}_t, E)$. In the Tersoff-Hamann (TH) approach the tip is simplified as a spherical potential, that is, its WF has only the $l = 0$ angular moment. Higher moments (relevant for a large tip apex) can be included or modelled at the cost of the simple proportionality in Eq. (2.56), while one still may retain only the relevant $m = 0$ components (the others would give WF nodes against the surface). In practice one not only assumes an s -wave tip,

but also a constant DOS ρ_t , so that Eq. (2.57) becomes just the energy-integrated LDOS of the surface at the position of the tip. In the CC mode, the surface $\mathbf{r}_t = (x, y, z(x, y))$ is then the surface topography measured in STM experiments. The derivative of the tunnelling current $dI(V)/dV$ yields the LDOS of the surface at the position of the tip and at the particular bias voltage, $\rho_s(\mathbf{r}_t, V)$. In this way the local electronic structure can be measured directly via STM. Technically, the conductance dI/dV is measured by superimposing a modulation voltage V_{mode} , and the current is measured directly with a lock-in amplifier. The conductance is closely related to the result obtained via STS, in which the surface is scanned pixel by pixel, and at each lateral position one fixes the height of the tip and sweeps through the bias. Doing that procedure for several heights, one measures the three-dimensional vacuum LDOS of the surface.

Magnetic surfaces can be investigated by spin-polarized STM (SP-STM) and STS (SP-STs) [Pal12], in which spin-polarized currents are used to determine the magnetic structure of the surface. In Ref. [Pal12] the details of the tip electronic structure, the bias-dependent background, and the tip-derivative terms are included in the calculation of the conductance dI/dV . The background results from the derivative of the energy- and bias-dependent tunnelling probability $T(E, eV)$ in an extended version of Eq. (2.57),

$$I(V) \propto \int_{E_{s,F}}^{E_{s,F}+V} dE \rho_t(E) \rho_s(E) T(E, eV). \quad (2.58)$$

The theory was applied to a Cr monolayer on Ag(111) in the non-collinear Néel state at low temperatures, and while the background term was found to be proportional to the tunnelling current, the other two terms made up the details for the comparison to experimental tunnelling spectra. These and the magnetic asymmetries were additionally found to depend on the details of the tip electronic structure.

A simple understanding of the exponential dependence of the LDOS on the tip-to-surface distance can be obtained in a very simple model [Giu14], in which the surface-to-vacuum potential barrier is modelled by a step function of height $E_{s,F} + \phi$, where ϕ is the work function of the surface. Solving the longitudinal Schrödinger equation for electrons at the Fermi edge,

$$-\frac{\hbar^2}{2m} \frac{d\psi(z)}{dz} + (E_{s,F} + \phi)\psi(z) = E_{s,F}\psi(z), \quad (2.59)$$

one obtains $\psi(z) \propto \exp[-(2m\phi/\hbar^2)^{1/2}z]$. Using this result in Eq. (2.57), one can anticipate the exponential dependence of the tunnelling current on the tip-to-surface distance d , $I \propto \exp[-2(2m\phi/\hbar^2)^{1/2}d]$. Within the spherical approximation for the tip, having a radius of curvature R , the lateral resolution can be determined as $[2(R+d)\text{Å}]^{1/2}$ [Ter85]. If $R \gg d$, the resolution depends on the quality of the tip, while if $R \ll d$ (single-atom tip apex), it depends on the distance d . Another important issue is the longitudinal resolution (the 0.1 Å mentioned before) of contrast corrugations already for clean surfaces (e.g., the alternations of top and hollow positions, or CDWs), which also happens to have an exponential dependence on the tip-to-surface distance, like the tunnelling current itself.

The landscape of condensed matter systems is very large, showing an abundance of quantum-mechanical effects, and the situation for surface systems is no less complex. Often these show a diverse interplay of quantum-mechanical and quantum-chemical effects, which now can be directly accessed via the **STM** technique. At this point only two examples will be presented, before we go over to the case of the Ta(001)-p(3×3)-O surface which was investigated by a combination of **STM**, **STS**, and **DFT** (Sec. 2.4). As explained in Sec. 2.4, **DFT** provides us with a rather metallic interpretation of the Ta(001)-p(3×3)-O surface, albeit it points by various means to its insulating behaviour which was also seen by **STS**. The delocalized band picture of **DFT** thus still allows to access the quantum-chemical properties of surface systems. Chpt. 4 provides a generalization of **STM** theory to account for the correlations on nanosystems supported on surfaces.

STM provides a means for the real-space spectroscopy of surfaces and for a highly resolved measurement of their topography. A fascinating example of a quantum-mechanical effect is the delocalization of Co adsorbates on the Cu(110)-p(2×1)-O surface [Kin16] (albeit results were obtained with the related method of **atomic force microscopy (AFM)** [Bin86]). The surface charge density around the Co adatoms develops Friedel oscillations. These are generally seen around surface imperfections, and contain, for example, information on the Fermi surface nesting, as was explained along the Cr(001) surface (though, these Friedel oscillations are to be distinguished from **CDWs** (Appx. A.1)) [Kol02; Kol05]. Friedel oscillations can also mediate long-range interactions between adsorbates. Now, several Co atoms were placed on the Cu(110)-p(2×1)-O surface, and a complicated **potential energy surface (PES)** with maxima and minima emerged out of the interpenetrating Friedel oscillations. Placing yet another Co atom at a minimum of this **PES**, it transitions into a long-living delocalized state of ring-like form. While **AFM** was able to image this delocalized state of the Co adatom, **DFT** and a phenomenological construction of the long-range interaction based on the Friedel oscillations were able to reveal its origin. The authors of Ref. [Kin16] used the **DFT+U** method (Subsec. 2.1.4) to take into account correlations on localized Co adatoms, in conjunction with **vdW** forces, as these were found to be relevant already for the structure of the Cu(110)-O substrate [Bam13]. **VdW** forces in **DFT** and their application to the Ta(001)-p(3×3)-O surface are described in Secs. 2.5 and 2.6.

Like surface reconstructions and Friedel oscillations, **CDWs** (Appx. A.1) can also be detected via **STM**, an example being given by 2H-NbSe₂ showing a 3×3 superlattice [Hes16]. A great deal of research is now being pursued by the study of **TM** adsorbates on (conventional) **SC** surfaces, where they exhibit the **Yu-Shiba-Rusinov (YSR)** state (see Sec. 2.3 and references therein). A particular realization is given by Fe adatoms on the Ta(001)-p(3×3)-O surface. The rest of the present chapter is devoted to the electronic, structural, and quantum-chemical properties for the Ta(001)-p(3×3)-O surface.

2.3 Context of the Ta(001)-p(3×3)-O surface

The publication “An atomically thin oxide layer on the elemental superconductor Ta(001) surface” (Phys. Rev. Materials 3, 094801 (2019)) presented in the following section examines the O-reconstructed Ta surface Ta(001)-p(3×3)-O by means of **STM**, **STS**, and **DFT**. The pretreatment in the present section puts the Ta(001)-p(3×3)-O surface in place

of general surface science (O-chemisorbed **TM** surfaces) and current state of research (e.g., on Kondo physics on conventional **SCs**), and assesses the quality of the **DFT** approach to this surface.

There exist three main classes of oxygen compounds in terms of geometry and composition [Ste14]. There are the bulk, and the bulk-terminated binary, ternary, and quaternary oxides, of which the binary ones are particularly relevant for the present study as “parental compounds”, showing structural, physical, and chemical similarities with O-chemisorbed surfaces of the same or similar substrate-atomic species. The ternary and quaternary compounds comprise systems such as high- T_c **SCs**.

Finally, there are the O-chemisorbed surfaces themselves. Even though often being simple in their atomic composition, they show an abundance of physical effects, ranging from various substrate reconstructions and superstructure formations, to peculiar local quantum-chemical arrangements and long-range electronic effects. The introduction of individual or arranged inhomogeneities can further functionalize materials, an example being given by vacancies on the chlorine-terminated Cu(100) surface [Kal16]. Data points can be physically represented by the charge, spin, or positional state of a single atom or quantum dot. The authors of Ref. [Kal16] were able to store complex information in the positional arrangement of many inhomogeneities given by pairs of Cl atoms and vacancies.

In the case of Ta(001)-p(3×3)-O, a recent functionalization has been achieved by the adsorption of single Fe atoms on the surface [Cor17; Kam18; Kam21; Kam19]. The p(3×3)-O template which emerges during annealing provides various adsorption sites above and below the surface – even with different adsorption heights at the same lateral position. It further provides the basis for various arrangements of several Fe adatoms [Kam18; Kam21]. Magnetic adatoms interact with the substrate electrons via effective spin- and orbital-flip processes, which arise from the interplay of Coulomb localization and hybridization: The discrete adatom eigenstates are hybridized to the substrate electron bands (**AIM**, Sec. 3.2), and electrons can hop between adatom and substrate via hybridization events, thereby changing the spin and orbital state of the adatom during time, so that the local moment is effectively screened. This is the Kondo effect to be discussed in detail in Chpt. 4.

The properties of the adatom are determined by its valency, level splittings, and the characteristics of the local interactions. In particular, along with the suppression of two-valued orbital occupancies due to Coulomb localization, electrons in different orbitals will interact with each other, and pairs of electrons will interchange their spin. The properties of the substrate, on the other hand, can be very diverse. These may be geometric in nature, as, for example, in the $\text{CoCu}_n/\text{Cu}(111)$ systems with and without additional Cu chains next to the Co adatom 4.6, leading to different crystal field (level) splittings. Or these may be physical in nature, as, for example, if the **SOC** intertwining spin and orbital **DOF** is effective; often the **SOC** on the adatom is induced by the substrate. The influence of the substrate properties on the Kondo behaviour is nowadays of increased interest. In particular, the Kondo effect is sensitive to a reduced **DOS** near the Fermi level, as it needs enough states which provide electron hopping channels. For example, the pseudo-gap in graphene has the form of a Dirac cone near the Fermi level, which reduces the Kondo effect and makes it highly dependent on graphene doping, see Secs. 3.5 and 3.6 and references therein. For the Kondo effect to operate, the adatom needs to be surrounded by mobile electrons, that is,

it must be placed in a (semi-)metallic environment. For metallic substrates, it is known that the Kondo effect manifests itself in STS experiments as a narrow resonance near the Fermi level, see Ref. [Mad98] and Chpt. 4.

If the substrate is a conventional superconductor (SC), such as the Ta(001)-p(3×3)-O surface at temperatures below $T_c = 4.5$ K, the electrons near the Fermi level are bound in Cooper pairs, and are at first not available for electron hopping processes. Adsorbing Fe atoms on such a surface, its magnetic moment now interacts with a SC substrate, and a competition develops between the local destruction of the SC order by scattering of Cooper pairs off the local moment and their break-up on the one hand, and a subsequent Kondo screening of the local moment, which is restored by a re-emergence of the substrate metallicity, on the other. Clearly, the screening of the local moment in turn restores the SC order, and the competition will arrive at a balanced state, characterized by the YSR states, which are seen in STS as narrow resonances inside the SC gap [Cor17; Fra11; Kam18; Kam21; Kam19; Rus69; Shi68; Yu65].

We will not go any further into the topic of YSR states, but would like to mention that in Ref. [Cor17] these states have been observed with Fe atoms on the Ta(001)-p(3×3)-O surface, if they are placed in the centre of the 3×3 plaquette. This corresponds to an unusual top-site adsorption, the mechanism for which cannot be described by common DFT approaches. As will be discussed below and in Sec. 2.6, long-range interactions (possibly of vdW-type) may become important here. Furthermore, at the very same lateral position, two Fe adsorption heights are seen to be realizable, with the smaller one leading to the YSR state, while with the larger one spin excitations occur due to the decoupling of the spin states from the substrate electrons by a large magnetic anisotropy. In principle, this situation is similar as with thin insulating layers on metal substrates (such as oxide, nitride, or halide layers) [Hei04; Hir07]. These two states, between which one can switch by application of voltage pulses, represent a further possibility for data storage. An apparent difficulty for technological usage, though, is the low temperature needed for conventional SCs, and the positional stability of the Fe adatom.

As mentioned above, large-scale arrangements of inhomogeneities, for example, one-dimensional chains or two-dimensional islands, are investigated with the aim of realizing the storage of complex data. Spin chains and islands of magnetic atoms on SCs with large SOC have recently been suggested to realize topological SC, which can host Majorana excitations at the end of the chains or at vortices, respectively, see Refs. [Ali12; Nad13; Pie13] and references in the included publication, and that are suitable for topological quantum computation [Nay08]. Tantalum appears convenient to explore these phenomena, as it has a rather high critical temperature of $T_c = 4.5$ K and is known to have a large SOC parameter [Ben93].

At this point we would like to mention that the SC of the Ta(001)-p(3×3)-O surface plays no role in the publication included, as the project was about identification of experimental STM images, and the description of physical, quantum-chemical, structural, and possible adsorption properties. A description of its conventional SC would be possible within current-DFT [Hig17] (Appx. A.1), or by consideration of the electron-phonon coupling within Eliashberg theory [Umm13]. For the competition between the SC order and the tendency of magnetic adatoms to establish a Kondo singlet with its environment, a proper

resolution of the low-energy features within the AIM is needed. Because the SC gap is generally the smallest scale within a SC, for example, smaller than the width of the Kondo resonance, a numerical resolution is difficult. One may hope that a proper inclusion of the SC parameter in the AIM (Sec. 3.2), effectively coupling the different hybridization channels, and a thorough QMC treatment by employing the TRIQS/CTHYB code (Sec. 3.3) results in the emergence of the YSR states in a realistic many-body calculation. At least in model calculations that has been achieved [Pok18], but multi-orbital calculations are much more demanding. Another possibility to account for the SC gap could be standard quantum-mechanical perturbation theory around the non-SC AIM solution.

The first structural investigation of the Ta(001)-O surface was performed by Titov *et al.* [Tit85] suggesting a few models based on different oxygen arrangements that were shown to appear at various temperatures: at very high temperatures one has the clean Ta(001) surface; then upon cooling down appear successively the p(1×3)-O, the p(1×2)-O, and finally the p(3×3)-O pattern. With the high-resolution STM technique it is possible to gain insight into the structural and chemical details of the surface at low temperatures. The Ta(001)-O surface has already been considered in other recent studies [Bo18; Guo17], where reconstruction patterns different from p(3×3)-O are predicted along with the preference of hollow- over bridge-site adsorption, often exhibited by other systems. We extended the interpretation of the STM images gained experimentally by the necessity to consider different arrangements of oxygen states in the same p(3×3)-O formation, with oxygens at bridge positions, and found mechanisms responsible for the STM contrast reversal which are of purely electronic origin. Finally, we made a couple of predictions based on our systematic DFT analysis. For example, even though vdW interactions were neither relevant to obtain the reconstruction pattern, nor for the interpretation of the STM data, nor for the electronic structure (all that has been checked; Sec. 2.6), the electronic structure directly points to the importance of these long-range interactions for the adsorption of other polarizable atoms and molecules on the surface, see Refs. [Cor17; Kam18]. The recognition of vdW interactions being relevant for a correct description of nanoparticle adsorption, in particular, on the related rutile surfaces, goes along such studies as reported in Refs. [Hec17; Kak18].

The project presented in Sec. 2.4 is from the theory side mainly a DFT characterization of the surface. VdW forces will be taken into account on the DFT level, that is, semi-empirically, afterwards in Sec. 2.6. The reason for going beyond standard DFT is the unusual top-site adsorption of Fe atoms in the centre of the 3×3 plaquette [Cor17]. In standard DFT relaxation, an Fe atom placed there immediately drops down into one of the nearby hollow positions, while within vdW-DFT in the variant of the to-be-discussed Tkatchenko-Scheffler (TS) method (Sec. 2.5) the Fe atom remained at the top position (not in less advanced vdW-DFT approaches, though). However, there was no stability with respect to small perturbations in the lateral coordinates of the top position. Furthermore, upon switching on self-consistent screening of the vdW interactions within the TS method, the interaction parameters become smaller, and the top position was again not stable already without small perturbations. Yet another reason for the necessity to go beyond standard DFT – and beyond vdW-DFT as well – is the two possible adsorption heights at the same lateral position, one of them being very large: 3.9 Å (showing spin excitations) instead

of 2.4 Å (showing YSR signatures) [Cor17]. As DFT tends to overestimate bonding (cf. Sec. 2.5), such unusually large adsorption heights cannot be explained within DFT-based approaches.

The DFT (Sec. 2.4) and vdW-DFT (Sec. 2.6) studies collect preliminary results and provide the basis for a possible subsequent GWA/RPA (Sec. 3.1), or any another study on the Ta(001)-p(3×3)-O surface; the in-depth DFT characterization yields a benchmark for such further studies. The GWA or its RPA (Sec. 3.1) are in particular relevant for a realistic description of fluctuations and their vdW interactions [Har09; Har10; Ols13; Ren12; Sch10; Sho16]. Fluctuations can provide different structural stabilization mechanisms: There are the vdW interactions between charge density fluctuations (i.e., plasmonic interactions [Ger72; Kli09]), which possibly organize the fluctuating constituents into a quantum version of the Kapitza pendulum [Ant18; Cit15; Gil03]. But also spin fluctuations may place a role, and perhaps they are necessary for the description of the different Fe adsorption heights and the corresponding magnetic states. Yet another reason to prospect for other approaches is the experience that DFT in the projector augmented wave (PAW) formalism (cf. Appx. B), and the LDAs in general (cf. Sec. 2.1.2), have their difficulties with such inhomogeneous geometries like top-site adsorbed Fe atoms, as one needs a very large basis set to capture the inhomogeneity with plane waves (PWs), what renders convergence slow and sometimes even absent.

Finally, we would like to put the Ta(001)-p(3×3)-O surface in a wider surface science context (albeit surface science is a vast area and only a small selection of references can be given for each of its topics). There are only a few studies on the O-chemisorbed Ta(001) surface [Bo18; Guo17; Tit85]. As mentioned, the p(3×3)-O superstructure was already proposed in Ref. [Tit85] to explain the patterns seen in low-energy electron diffraction (LEED) and atomic emission spectroscopy (AES) experiments. In Refs. [Bo18; Guo17] the high-coordinated hollow-site adsorption was proposed, and the resulting Ta(001)-O variants were studied from an electronic and quantum-chemical point of view following Ref. [Sun14]; a reference which helped us with the interpretation of our own DFT results on the Ta(001)-p(3×3)-O surface, especially the realization of the oxygens states as containing lone pairs. The STM images we acquired experimentally, though, could be interpreted with bridge-site oxygen adsorption only, like proposed in Ref. [Tit85]. As also mentioned in Sec. 2.4, adsorption at low-coordinated bridge positions was also found relevant for other bcc metals as regards reconstruction (Ref. [Kol01] considers various superstructures on V(001) aligned along bridge positions to identify experimental STM images), catalysis (Ref. [Bra13] finds different local oxygen coordinations help induce Cr growth on Fe(001)-p(1×1)-O), and coadsorption (e.g., CO coadsorption on Rh(111)-p(2×2)-O by activated oxygens in bridge positions [Zha00]). We found coadsorption relevant for the superstructure formation on Ta(001)-p(3×3)-O (Sec. 2.4).

The already well studied Fe(001)-p(1×1)-O system, see Refs. [Hea89; Leg77; Par10], is a prototypical example of an oxidized bcc-metal surface [Ada82; Ho76; Jar85; Ueb98]: The bonding structure was clarified by identifying hybridizations of oxygen and iron orbitals via the LDOS [Hua85]; correlations and the SOC were included beyond first principles by relativistic tight-binding Korringa-Kohn-Rostocker calculations augmented by DMFT [Bor15]; and distance-dependent STM contrast reversals were observed, which shift the

p(1×1) corrugation seen on STM images [Pic10]. This contrast reversal is different in mechanism as in gapped systems like NiO(100), where it occurs by altering the bias sign [Dud97]. The Fe-p(1×1)-O surface has also been studied by angle-resolved photo-emission spectroscopy, which allows for a momentum-resolved consideration of Fe-O bonds and O-O interactions [Pan85]. Oxygen adsorption on Fe(001) occurs at hollow positions, but bridge positions at lower coverages [Oss15], and other superstructures were found on the (110) surface orientation as well [Kim98] (Ref. [Ada82] considers hollow positions on Fe(001), but also on V(001), in contrast to Ref. [Kol01]). The clean Fe(110) surface shows a distance- and tip-orbital-dependent contrast reversal in STM maps [Mán14]; Ref. [Hei98] finds purely electronic origins of the corrugation reversals on clean bcc(110)-metal surfaces, though. Regarding oxygen superstructures, there is an abundance of different formations on bcc metals, as, for example, on V(001) [Kol01] and Nb(100) [An03; Usa77], and on and in Nb(110) with a temperature dependence similar as on Ta(001) [Hel03]. For Nb(110), the bonding structure was also clarified [Kil07], and long-range superstructures at later oxidation stages observed (in particular, a Moiré pattern) [Sür01]. A superstructure with substrate and additional incommensurate adlayer reconstructions were seen on Mo(110) [Grz89]. The small list of examples just given refers to bcc metals; oxygen adsorption on fcc-metal surfaces has been studied more extensively, see, for example, Ref. [Liu14] discussing dissociative oxygen chemisorption on fcc(100) surfaces.

2.4 “An atomically thin oxide layer on the elemental superconductor Ta(001) surface”

Reprinted with permission from

R. Mozara, A. Kamlapure, M. Valentyuk, L. Cornils, A. I. Lichtenstein, J. Wiebe,
and R. Wiesendanger
Phys. Rev. Materials 3, 094801 (2019) [[Moz19](#)]

© 2019 American Physical Society

Experiments were conceived and performed by A. Kamlapure, L. Cornils, and J. Wiebe. [DFT](#) simulations were performed by J.R.S.M., and theoretical interpretations established by M. Valentyuk and J.R.S.M. The manuscript was written by A. Kamlapure, M. Valentyuk, and J.R.S.M. All authors discussed the results and commented on the manuscript.

The reference numbers in this reprinted article are valid within this article only.

Atomically thin oxide layer on the elemental superconductor Ta(001) surface

R. Mozara,^{1,*} A. Kamlapure,^{2,†} M. Valentyuk,^{1,3} L. Cornils,² A. I. Lichtenstein,^{1,3} J. Wiebe,² and R. Wiesendanger²¹*Institute of Theoretical Physics, University of Hamburg, Jungiusstraße 9, D-20355 Hamburg, Germany*²*Institute for Nanostructure and Solid State Physics, University of Hamburg, Jungiusstraße 9, D-20355 Hamburg, Germany*³*Department of Theoretical Physics and Applied Mathematics, Ural Federal University, 19 Mira Street, Yekaterinburg 620002, Russia*

(Received 8 November 2018; revised manuscript received 2 April 2019; published 24 September 2019)

Recently, the oxygen-reconstructed tantalum surface Ta(001)-p(3×3)-O has experienced considerable attention due its use as a potential platform for studying spin chains on superconductors. Experimental studies using scanning tunneling microscopy and spectroscopy found rich atomic and electronic structures already for the clean Ta(001)-O surface, which we combine here with *ab initio* methods. We found a significant reconstruction of the surface into a 2D polymorph oxide with two distinct patterns of 1-nm scale. One of the patterns represents an unusual defect structural state. This state appears only in the simulations with the effective presence of oxygen vacancies, which we also discuss in the context of the oxide formation. A specific combination of structural and electronic properties was established behind the diverse shapes detected in topographic maps. We also observed the energy-dependent partial-charge localization effect under applied bias voltages, which includes a contrast reversal. These effects originate solely in miscellaneous ionic and metallic properties of the electronic system. The charge distribution and polarization properties of this atomically thin oxide layer is shown to vary significantly between normal and defective superstructures, possibly contributing to the rich phenomena related to topological superconductivity recently discussed for Fe adsorbates.

DOI: [10.1103/PhysRevMaterials.3.094801](https://doi.org/10.1103/PhysRevMaterials.3.094801)

The surfaces of elementary superconductors have recently attracted a lot of attention due to their potential in being used as platform for spin chains, which may host Majorana quasiparticles [1–6]. One requirement for the formation of Majorana states is a strong spin-orbit coupling in the magnetic chain on superconductor system which facilitates the formation of noncollinear magnetization states. Therefore, high-*Z* elementary superconductors which have an experimentally easily accessible superconducting transition temperature around 5 K are particularly interesting.

While clean Pb and Re surfaces have been explored [1–5], the preparation of clean Ta, La, and Nb surfaces is more challenging [7–10], particularly due to the tendency to form O reconstructions at the surface. The ordered superstructures seen in STM topographic images are typically induced by extra adsorbates [11–13].

On the other hand, such reconstructions also add to the functionality of the surface, as they tend to decouple the spins of adatoms from the substrate conduction electrons [14,15], which enables to tune the coupling of the adatom spins to the Cooper pairs [16]. Ta(110) and Ta(001) have been studied by scanning tunneling microscopy (STM) [7,16]. However, the way the structure of the O reconstruction of Ta(001) is linked to the STM images found in Ref. [16] remained elusive, particularly, as there occurs a contrast reversal at a bias voltage of 1 eV. On Fe(001)-p(1×1)-O, the STM contrast is distance-dependent [17], the reversal is thus different in mechanism compared to well gapped systems like NiO(100) [18]. The

tip-sample interactions were also shown to be responsible for the small shifts of the contrast in rutiles [12,19].

A first attempt to characterize the geometry of the Ta(001)-O surface was done by Titov *et al.* [8]. The best fit to the LEED and AES studies at low coverages was found with a superimposed (3×3)O network. Other structures for the oxidized Ta surface were studied recently by Guo *et al.* [20] and Bo *et al.* [21] from quantum-chemical point of view [22]. In case of Ta(001), Ref. [20] considers hollow positions only, in contrast to the models proposed by Titov *et al.* Adsorption at low-coordinated bridge positions, however, was found relevant for bcc metals in regards of reconstruction [23], catalysis [24], and CO coadsorption [25].

Here, we present a joint study of Ta(001)-p(3×3)-O by means of experimental [STM, scanning tunneling spectroscopy (STS)] and first-principles [density functional theory (DFT)] techniques. We show the interplay between two types of O bridge positions being the reason for normal and defect structural states related to the 3×3 plaquettes. Charge transfer between surface sites revealed a distinct polarization texture, which, together with the electronic structure, we predict to be relevant for adsorption of other atoms and molecules.

The surface under study was prepared as described in Ref. [26]. To investigate local spectroscopic properties of the sample, *dI/dV* spectra were taken using a W tip via Lock-in technique with stabilization voltage and current V_{stab} and I_{stab} , and with a modulation voltage of V_{mod} ($f = 827$ Hz) added to the sample bias voltage V .

Figure 1 shows STM images measured at the same location at various V . From Fig. 1(b), it can be seen that oxidized Ta(001) forms a well ordered superstructure lattice where a regular network of plaquettes of square and circular shapes

*rmozara@physnet.uni-hamburg.de

†akamlapu@physnet.uni-hamburg.de

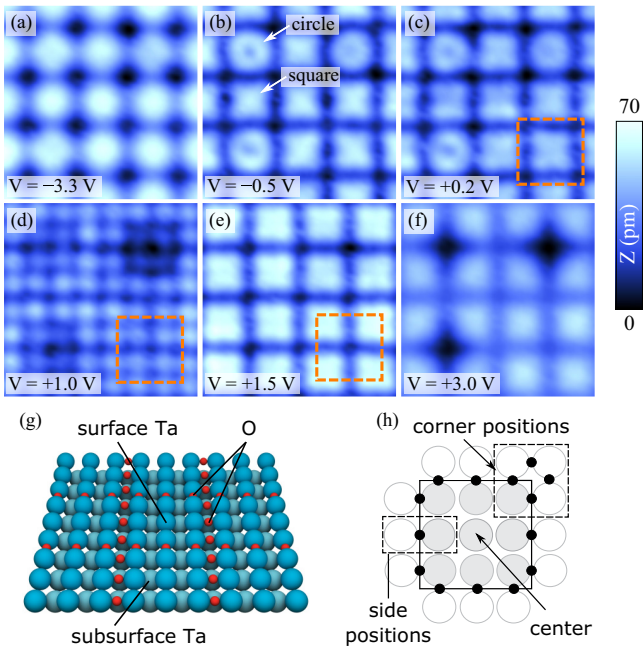


FIG. 1. [(a)–(f)] STM images ($3.8\text{ nm} \times 3.8\text{ nm}$) of the O-reconstructed Ta(001) surface measured at the same location, but at various bias voltages as indicated in each panel ($I = 0.6\text{ nA}$). The dashed square in (c)–(e) represents the same surface area size of $1.34\text{ nm} \times 1.34\text{ nm}$ showing a contrast reversal between $V = 0.2$ and 1.5 V . (g) Schematic perspective view on the surface model indicating the atomic positions as the starting point for the relaxation. (h) Schematic top view indicating the notion of the sites of O and Ta atoms.

separated by continuous depression lines with an apparent depth of $\sim 30\text{ pm}$ at $V = +0.2\text{ V}$ are visible. Square-shaped plaquettes are much more frequent than circular-shaped plaquettes with a relative abundance of about 4:1. The lateral distance of these plaquettes is $1\text{ nm} \sim 3 a_{\text{Ta}}$, with the lattice constant $a_{\text{Ta}} = 3.3\text{ \AA}$ of Ta, which reveals the 3×3 nature of the superstructure formation. The periodicity is consistent with the structure that has been assumed by Titov *et al.* [8] [see Fig. 1(g)]. The identification of the plaquettes is further complicated by a shift of the contrast by half the distance between the depression lines around a bias voltage of 1 V [cf. Figs. 1(c)–1(e)].

To reveal the atomic structure in the experimentally observed 3×3 plaquettes, we performed DFT calculations on the $(3 \times 3)\text{O}$ superstructure on Ta(001) with the VASP package [27]. For this purpose we used spin-polarized DFT functionals, including U on O atoms [28] (see [26]). The starting geometry was chosen as proposed by Titov *et al.* [8]. The result of the relaxation is displayed in Fig. 2(a), and denoted as state I [26]. The length of the 3×3 plaquette is calculated as $3 a_{\text{Ta}} = 9.9\text{ \AA}$, the first interlayer spacing is compressed by 3.4% in comparison to bulk values. The surface exhibits both out-of-plane and in-plane reconstruction with buckling of Ta atoms, and zigzag-ordered (along z axis) rows of O atoms.

As O species can stay mobile on the surface in a wide range of temperatures during chemisorption [11], the type of reconstruction is governed by many factors, including oxygen

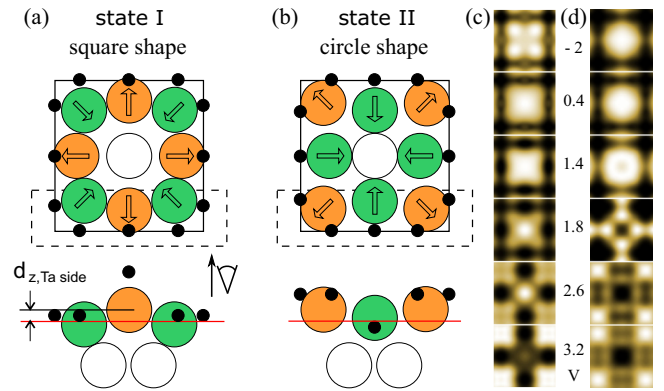


FIG. 2. [(a) and (b)] Schematic top (top) and side (bottom) views of the two DFT calculated structures I and II indicating the Ta (colored circles) and O (black dots) lateral and vertical positions. The red line depicts the average height of the surface Ta atoms. [(c) and (d)] Simulated STM images for states I and II, each at the isosurface value $5 \times 10^{-5} e/\text{\AA}^3$. The numbers give the corresponding voltages at which the images have been calculated. The images have been generated by the code given in Ref. [29].

partial pressure [30], temperature, and competing electronic, electrostatic and elastic interactions [31–33]. Initial simulations with additional oxygen contents uncovered a second energetic minimum for our superstructure [26]. This phase represents a structural isomer to state I, existing at equivalent oxygen coverage [Fig. 2(b)]. We denote it as state II and consider it as a defect superstructure. As we show in Figs. 2(c) and 2(d), and will explain later, states I and II correspond exactly to the cross and circular shapes observed in the STM images. Structural parameters agree perfectly with those proposed by Titov *et al.*

The revealed zigzag-ordered positions along the O rows are due to repulsive interactions between the O atoms, being proposed to be responsible for the ordered patterns at low coverages, in contrast to classic dissociation models [34]. In particular, adjacent O atoms at the corner have overlap of their Wigner-Seitz spheres, especially in state II, where they are elevated. As detailed in Ref. [26] (Table I), after relaxation, the O atoms at the side positions in state I are higher above the surface by 1.19 \AA [Fig. 2(a)], and can be viewed as sp^3 hybridized in a tetrahedral surrounding. Two vacuum-oriented hybrid orbitals host approximately two lone pairs, and are very large in extent (Table II in Ref. [26]). The O atoms at the corner (state I) are located in the surface and form the geometry of the sp hybridization, so we mark them as “ sp ” atoms [26]. In state II, the zigzag-ordered heights are reversed.

To identify the contrast seen in the experimental STM images, we explored the Tersoff-Hamann (TH) model in an analogous way as done by Klijn *et al.* [26,35]. In the rest of the paper, we show results obtained within LDA + U , other functionals are discussed in Ref. [26]. All simulated STM images were evaluated at the charge density isosurface value $5 \times 10^{-5} e/\text{\AA}^3$, corresponding to a tip-to-surface distance of 5.93 \AA at $V = 3.2\text{ V}$, if the tip is above the center of the 3×3 plaquette in state I. Independence of the STM contrast on the tip height was checked in experiments and in simulations.

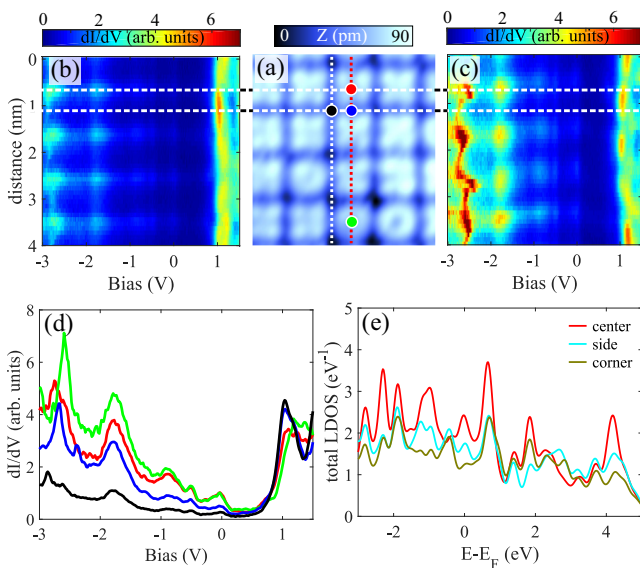


FIG. 3. (a) STM image of a surface area used for spectroscopy ($4.0 \text{ nm} \times 8.0 \text{ nm}$, $V = 300 \text{ mV}$, and $I = 100 \text{ pA}$). [(b) and (c)] 2D representation of dI/dV spectra taken along the white (b) and the red (c) dashed vertical lines marked in (a). (d) Representative dI/dV spectra acquired at four different locations marked by corresponding colored filled circles in (a). $V_{\text{stab}} = 1.5 \text{ V}$, $I_{\text{stab}} = 0.6 \text{ nA}$, and $V_{\text{mod}} = 5 \text{ mV}$. (e) Total DOS of the central, side, and corner Ta in state I.

Exploration of the TH approach on both, states I and II, leads to the simulated topographies in Figs. 2(c) and 2(d), and the corresponding differential conductances in Figs. 1(k) and 1(l) in Ref. [26]. For negative and smaller positive bias up to $\sim 1.4 \text{ eV}$, we observe depressions along the O rows being maximal at the corner positions, and protrusions above the Ta atoms. The latter match perfectly the square (I) and circular (II) shapes seen in STM images around the Fermi energy (Figs. 1(b) and 1(c) and Ref. [26]), and we therefore conclude that, in this bias regime, the depression lines correspond to the O rows.

Oxygen is typically seen in low-bias STM images as depression as discussed in a number of papers [17,22,36–38]. Similar to TiO_2 [12,37,38], the s - d states of the transition metal atom decay much slower into the vacuum above the surface as compared to the O states. This effect overcompensates the stronger exposure of the O atoms to the STM tip expected from their position above the Ta atoms.

For larger positive bias above 1.8 V , both, for states I and II, the simulated STM images show a contrast reversal [Figs. 2(c) and 2(d)]. The cross-shaped depression relocates to the center and side Ta atoms. This appropriately reproduces the contrast reversal observed experimentally around $V = 1 \text{ V}$ [cf. Figs. 1(c)–1(e)]. This energy-dependent effect originates from a redistribution of the electronic density, i.e., less density appears in the vacuum above these Ta atoms at the corresponding bias voltage [26].

Figure 3 shows spatially resolved STS data. Figures 3(b), 3(c) depict 2D color-map representations of STS data acquired along one line on top of the row of O atoms and one line across the Ta plaquettes marked by the white and red dashed lines in Fig. 3(a), respectively. At negative bias the

dI/dV intensity is largest above the Ta plaquettes [Fig. 3(b) and Fig. 3(c), top horizontal dashed line] and reduced above the O rows (bottom horizontal dashed line). This contrast is reversed at positive sample bias around 1 eV , where the dI/dV intensity is shifted towards the O rows and strongest on the corner O atoms [see bottom horizontal dashed line in (b)]. This is further evident from the panel (d) where we plot spectra taken at the four characteristic locations marked by the correspondingly colored circles in panel (a). Here, in the negative bias regime, the dI/dV intensity on the central Ta atoms is larger than that on the side and corner O atoms, while the situation is reversed for positive bias around 1 V .

These experimental STS results are compared to the calculated LDOS within empty spheres arranged along the topographic isosurface at a bias of 3.2 eV (i.e., above the contrast reversal, see Fig. 5 in Ref. [26]). The calculated LDOS shows a dominating weight above the Ta as compared to the O atoms up to about 2 eV . A shift of the vacuum LDOS from the Ta to the O atoms above $\sim 2.5 \text{ eV}$ is in qualitative agreement with the STS results.

In the following, we discuss the origin of these two distinct oxide patterns (I and II) in the context of quantum chemistry. The clean Ta(001) surface represents a sparse structure of atoms, and during annealing, the O atoms diffuse to positions providing the strongest bonds. It was shown for Ta(001) that O atoms do not penetrate into the bulk [39]. As it comes with the LDA + U method, upon adsorption, an individual O atom would prefer the hollow position, as it has lowest energy. The adsorption energy at the twofold bridge position in the sp^3 state (elevated above the surface) is 0.26 eV higher compared to the hollow position, and even 0.50 eV higher in the sp state. This contradiction to the experimentally observed bridge oxygens is resolved by considering a second O atom nearby. The situation is similar to the CO activation, when in the hollow position, the bonding orbitals of an O atom are less chemically active as in bridge positions [25,37]. Indeed, we find that two nearby O atoms at bridge positions (along [100] or [010]), both in the sp^3 state, have the lowest energy, while one O atom at the bridge (sp^3) and one at the closest hollow position is 48 meV higher, and both at the hollow positions are even 60 meV higher in energy.

The effective adsorption energy is higher in state I than in state II (Table I in Ref. [26]), contradicting the total energy assumption. The energy profile of polarizable metallic surfaces demands, at best, a full account of dynamical polarization effects, that is not accessible for such large surfaces. A similar problem is the presence of intrinsic errors in DFT functionals, such as self-interaction, typically resulting in shifts of binding energies [40]. The second source of this energy issue is the instability of neighboring oxygens at the corners: without constraints one oxygen in a pair relaxes to a nearby hollow position. The configurational minimum of this defect superstructure (state II) is thus separated by high barriers from the normal state I in the coordinate phase space, that is in line with the known complex oxygen surface kinetics at higher temperatures [11].

We also provide a charge transfer examination within the surface by means of the Bader Charge Analysis (BCA) [26,41,42] (Fig. 4). A pronounced charge polarization emerges near oxygen sites, with a remarkable difference of

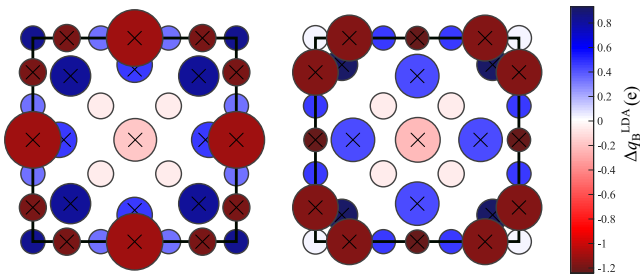


FIG. 4. Schematic colormap of Bader charges within the LDA for state I (left) and state II (right). Displayed are the differences Δq_B measured with respect to the free valencies. Blue and red colors depict charge shortage and excess, respectively. The spheres have been rescaled down by a factor of 2.5 for clearer visibility. Surface atoms are marked by black crosses, to distinguish them from subsurface atoms.

charge volumes at sp and sp^3 locations. We propose that the surface reconstruction is primarily governed by the saturation of two distinct ionic states in the local trimers [12,26,33], with compensation of excessive net charge at defect points near the central Ta.

The BCA result also implies some important considerations for the electronic properties of the surface. As a simple approximation, the pronounced accumulation of negative charge at oxygen locations (Fig. 4) can be regarded as a local electrostatic potential (ESP) [43], additionally shifting the work function near the oxygen rows. Extraordinarily, the central Ta atom is also slightly negatively charged in both structural states. In state II, there are less electronic states at the central Ta atom [26], so it frequently appears as darker spot in STM images. The enhanced polarizability of the surface is also responsible for the gap opening in the STS curves [Fig. 3(d)].

Large volumes of charge spheres at sp^3 locations maps very well to the picture of lone pairs of oxygen [26]. These spheres are very close to the central Ta atom and, taken as lone pairs, are suggested to induce static dipoles at the nearest atoms [22]. Indeed, we see enhanced polarized states on the central Ta atom [Fig. 3(e)]. Due to the smearing of the DOS at the tip positions, and the outward and inward curvatures of protrusions and depressions, respectively, the antibonding dipoles can be observed in the STS curves above E_F on all regions of the surface, while below E_F the peaks are mostly due to the lone pairs [22,26]. The interplay between antibonding electronic states of O and corner Ta atoms with polarized $p-d$ states of the central Ta atom is the source of the observed contrast reversal [26].

The pronounced bonding and antibonding peaks in the central Ta states at approximately -2 , -1 , 0.6 , 2 , and 4 eV [Fig. 3(e)] can mediate the electrostatic interaction with adsorbates possessing a dipole moment [43]. This means also, that induced dipole excitations would lead to vdW forces acting between the central Ta atom and such polarizable atoms and

molecules, similar as shown for the rutiles [44]. In state II, we observe the intensity of polarized peaks almost twice lower (Fig. 5 in Ref. [26]).

In summary, we show that the reconstruction at low oxygen coverages leads to two distinct $p(3 \times 3)$ -O STM patterns on Ta(001). These patterns correspond to the two structural phases, co-existing on the surface at low temperatures. The minor phase (state II) represents a defect superstructure, separated by a large energy barrier from the main phase (state I). Despite the inherited limitations of DFT, these findings suggest that this surface has a nontrivial crystallization kinetics during the formation process. Indeed, we obtained the second phase in simulations through the virtual presence of oxygen vacancies on the surface. Such a vacancy mechanism is justified by the adaptive crystal structure, observed for the thin films and bulk modifications of Ta_2O_5 [45]. It was shown, that such a structure can easily be altered by the presence of defects, that reduce enhanced oxygen vacancy diffusion, with clear anisotropic character [46]. The charge transport in bulk Ta_2O_5 is also predicted to be affected by the appearance of stable polarons in the vicinity of charged vacancies [47]. The building blocks of our 2D tantalum oxide relate to the two distinct local geometries around oxygen, leading to two different characters of oxidation state. Such local trimers are topologically different, thus posing an interesting question of its relevance for the amorphous nature and unique properties of bulk and thin-film oxides. The electronic system splits into groups of saturated ionic states at oxygen locations and polarized metallic states at selected Ta atoms, bringing this surface close to the metal-insulator transition. We explained the observed contrast reversal by taking into account unusually enhanced polarized states of central Ta atom. We also show that calculated static polarization properties of the surface alter in respect to the type of oxygen row in a plaquette. The surface dipoles induced predominantly in state I will have important implications for the adsorption geometry of transition metal adatoms and polarizable molecules. Finally, our results established a microscopic picture of the surface that can be employed to control its unique properties towards the use as a platform to study Majorana physics.

We acknowledge financial support from the Deutsche Forschungsgemeinschaft (DFG) through Project No. SFB668-A3 and A1, and the European Union's Horizon 2020 research and innovation program under Grant Agreement No. 696656 – GrapheneCore1. J.W. acknowledges funding by the Cluster of Excellence ‘Advanced Imaging of Matter’ of the DFG – EXC 2056 – Project No. 390715994. Work of R.W. and A.K. was funded by ERC via the Advanced Grant ASTONISH (No. 338802) and ADMIRE (No. 786020). We thank Carmen Herrmann, Elisaveta Kovbasa, Vladimir Antropov, Sergey Brener, Tomáš Bučko, Malte Harland, Mikhail I. Katsnelson, and Frank Lechermann for helpful discussions.

[1] S. Nadj-Perge, I. K. Drozdov, J. Li, H. Chen, S. Jeon, J. Seo, A. H. MacDonald, B. A. Bernevig, and A. Yazdani, *Science* **346**, 602 (2014).

[2] M. Ruby, F. Pientka, Y. Peng, F. von Oppen, B. W. Heinrich, and K. J. Franke, *Phys. Rev. Lett.* **115**, 197204 (2015).

- [3] M. Ruby, B. W. Heinrich, Y. Peng, F. von Oppen, and K. J. Franke, *Nano Lett.* **17**, 4473 (2017).
- [4] S. Jeon, Y. Xie, J. Li, Z. Wang, B. A. Bernevig, and A. Yazdani, *Science* **358**, 772 (2017).
- [5] H. Kim, A. Palacio-Morales, T. Posske, L. Rózsa, K. Palotás, L. Szunyogh, M. Thorwart, and R. Wiesendanger, *Sci. Adv.* **4**, eaar5251 (2018).
- [6] A. Kamlapure, L. Cornils, J. Wiebe, and R. Wiesendanger, *Nat. Commun.* **9**, 3253 (2018).
- [7] T. Eelbo, V. Zdravkov, and R. Wiesendanger, *Surf. Sci.* **653**, 113 (2016).
- [8] A. V. Titov and H. Jagodzinski, *Surf. Sci.* **152-153**, 409 (1985).
- [9] M. V. Kuznetsov, A. S. Razinkin, and A. L. Ivanovskii, *Phys. Usp.* **53**, 995 (2010).
- [10] A. S. Razinkin and M. V. Kuznetsov, *Phys. Met. Metallogr.* **110**, 531 (2010).
- [11] P. R. Davies and M. W. Roberts, *Atom Resolved Surface Reactions: Nanocatalysis*, RSC Nanoscience & Nanotechnology (RSC, Cambridge, 2008).
- [12] U. Diebold, *Surf. Sci. Rep.* **48**, 53 (2003).
- [13] P. Ferstl, T. Schmitt, M. A. Schneider, L. Hammer, A. Michl, and S. Müller, *Phys. Rev. B* **93**, 235406 (2016).
- [14] A. J. Heinrich, J. A. Gupta, C. P. Lutz, and D. M. Eigler, *Science* **306**, 466 (2004).
- [15] C. F. Hirjibehedin, C.-Y. Lin, A. F. Otte, M. Ternes, C. P. Lutz, B. A. Jones, and A. J. Heinrich, *Science* **317**, 1199 (2007).
- [16] L. Cornils, A. Kamlapure, L. Zhou, S. Pradhan, A. A. Khajetoorians, J. Fransson, J. Wiebe, and R. Wiesendanger, *Phys. Rev. Lett.* **119**, 197002 (2017).
- [17] A. Picone, G. Fratesi, A. Brambilla, P. Sessi, F. Donati, S. Achilli, L. Maini, M. I. Trioni, C. S. Casari, M. Passoni, A. Li Bassi, M. Finazzi, L. Duò, and F. Ciccacci, *Phys. Rev. B* **81**, 115450 (2010).
- [18] S. L. Dudarev, A. I. Liechtenstein, M. R. Castell, G. A. D. Briggs, and A. P. Sutton, *Phys. Rev. B* **56**, 4900 (1997).
- [19] O. Stetsovych, M. Todorović, T. K. Shimizu, C. Moreno, J. W. Ryan, C. P. León, K. Sagisaka, E. Palomares, V. Matolín, D. Fujita, R. Perez, and O. Custance, *Nat. Commun.* **6**, 7265 (2015).
- [20] Y. Guo, M. Bo, Y. Wang, Y. Liu, C. Q. Sun, and Y. Huang, *Appl. Surf. Sci.* **396**, 177 (2017).
- [21] M. Bo, L. Li, Y. Guo, C. Yao, C. Peng, and C. Q. Sun, *Appl. Surf. Sci.* **427**, 1182 (2018).
- [22] C. Q. Sun, *Relaxation of the Chemical Bond: Skin Chemisorption Size Matter ZTP Mechanics H₂O Myths*, Springer Series in Chemical Physics (Springer, Singapore, 2014).
- [23] R. Koller, W. Bergermayer, G. Kresse, E. Hebenstreit, C. Konvicka, M. Schmid, R. Podloucky, and P. Varga, *Surf. Sci.* **480**, 11 (2001).
- [24] A. Brambilla, A. Calloni, A. Picone, M. Finazzi, L. Duò, and F. Ciccacci, *Appl. Surf. Sci.* **267**, 141 (2013).
- [25] C. J. Zhang and P. Hu, *J. Am. Chem. Soc.* **122**, 2134 (2000).
- [26] See Supplemental Material at <http://link.aps.org/supplemental/10.1103/PhysRevMaterials.3.094801> for the details on the surface preparation, DFT calculations and their results, along with the theoretical and computational details behind the physical and quantum-chemical interpretations discussed in the manuscript.
- [27] G. Kresse and J. Furthmüller, *Phys. Rev. B* **54**, 11169 (1996).
- [28] I. A. Nekrasov, M. A. Korotin, and V. I. Anisimov, [arXiv:cond-mat/0009107](https://arxiv.org/abs/cond-mat/0009107).
- [29] <http://vaspnotes.blogspot.de/2013/09/simulated-stm.html>.
- [30] K. Reuter and M. Scheffler, *Phys. Rev. B* **65**, 035406 (2001).
- [31] I. Fernandez-Torrente, S. Monturet, K. J. Franke, J. Fraxedas, N. Lorente, and J. I. Pascual, *Phys. Rev. Lett.* **99**, 176103 (2007).
- [32] J. Goniakowski, C. Noguera, and L. Giordano, *Phys. Rev. Lett.* **98**, 205701 (2007).
- [33] J. Lafemina, *Surf. Sci. Rep.* **16**, 137 (1992).
- [34] J. Winterlin, Scanning tunneling microscopy studies of catalytic reactions, in *Impact of Surface Science on Catalysis*, Advances in Catalysis Vol. 45 (Elsevier, Netherlands, 2000), pp. 131–206.
- [35] J. Klijn, L. Sacharow, C. Meyer, S. Blügel, M. Morgenstern, and R. Wiesendanger, *Phys. Rev. B* **68**, 205327 (2003).
- [36] P. Sautet, *Surf. Sci.* **374**, 406 (1997).
- [37] U. Diebold, J. F. Anderson, K.-O. Ng, and D. Vanderbilt, *Phys. Rev. Lett.* **77**, 1322 (1996).
- [38] T. Woolcot, G. Teobaldi, C. L. Pang, N. S. Beglitis, A. J. Fisher, W. A. Hofer, and G. Thornton, *Phys. Rev. Lett.* **109**, 156105 (2012).
- [39] N. Drandarov and V. Kanev, *Vacuum* **23**, 463 (1973).
- [40] L. Wang, T. Maxisch, and G. Ceder, *Phys. Rev. B* **73**, 195107 (2006).
- [41] <http://theory.cm.utexas.edu/henkelman/code/bader/>.
- [42] T. Bučko, S. Lebègue, J. G. Ángyán, and J. Hafner, *J. Chem. Phys.* **141**, 034114 (2014).
- [43] A. Kakekhani, L. T. Roling, A. Kulkarni, A. A. Latimer, H. Abroshan, J. Schumann, H. AlJama, S. Siahrostami, S. Ismail-Beigi, F. Abild-Pedersen, and J. K. Nørskov, *Inorg. Chem.* **57**, 7222 (2018).
- [44] J. Balajka, U. Aschauer, S. F. L. Mertens, A. Selloni, M. Schmid, and U. Diebold, *J. Phys. Chem. C* **121**, 26424 (2017).
- [45] S.-H. Lee, J. Kim, S.-J. Kim, S. Kim, and G.-S. Park, *Phys. Rev. Lett.* **110**, 235502 (2013).
- [46] H. Jiang and D. A. Stewart, *J. Appl. Phys.* **119**, 134502 (2016).
- [47] J. Lee, W. D. Lu, and E. Kioupakis, *Nanoscale* **9**, 1120 (2017).

SI for “An atomically thin oxide layer on the elemental superconductor Ta(001) surface”

R. Mozara,¹ A. Kamlapure,² M. Valentyuk,^{1,3} L. Cornils,² A. I. Lichtenstein,^{1,3} J. Wiebe,² and R. Wiesendanger²

¹*I. Institute of Theoretical Physics, University of Hamburg, Jungiusstraße 9, D-20355 Hamburg, Germany*

²*Institute for Nanostructure and Solid State Physics, University of Hamburg, Jungiusstraße 9, D-20355 Hamburg, Germany*

³*Department of Theoretical Physics and Applied Mathematics, Ural Federal University, 19 Mira Street, Yekaterinburg, 620002, Russia*

SURFACE PREPARATION

The Ta(001)-p(3×3)-O surface was prepared by first sputter cleaning of a single crystal of Ta(001) using high energy (2 keV) Ar⁺ ions, followed by repeated cycles of annealing at 1250 °C in presence of O atmosphere (1×10⁻⁶ mbar) and flashing up to 2000 °C. The sample was then transferred into the STM, which has a base pressure of 5×10⁻¹¹ mbar, where it was cooled down to the base temperature of $T = 1.1$ K [1].

DFT CALCULATIONS

DFT was done in the framework of the VASP package with the projector augmented-wave (PAW) basis set [2, 3]. To avoid mirror polarizations due to the supercell repetition, the atomic arrangement was chosen mirror symmetric to the central layer within a slab of five 9×9 Ta layers. In this way the supercell contains 12 O and 45 Ta atoms. The Brillouin zone was covered by a 6×6×1 Γ -centred \mathbf{k} -point mesh, and convergence with respect to the number of \mathbf{k} -points was tested. All calculations were performed magnetically, and the surface turned out to be non-magnetic everywhere and in all cases considered. For the exchange-correlation energy two different choices were made with the local-density approximation (LDA) and the generalized gradient approximation (GGA) in the variant of Perdew-Burke-Ernzerhof (PBE) [4]. We included local Coulomb correlation via DFT+ U from the outset by choosing $U = 6$ eV and $J = 0.8$ eV for O atoms, which was found to be relevant for oxidized transition-metal surfaces [5]. Relaxations were performed until forces were below 5×10⁻³ eV/Å. The electronic structure remains essentially unchanged by use of GGA and vdW functionals, what we have checked explicitly. For the calculation of the DOS the number of bands was increased from around 372 (LDA) or 210 (GGA) to around 400 bands, and the energy cutoff from 400 eV to 500 eV, to assure an accurate description of the states above the Fermi energy, and which smoothed the simulated STM maps (see Sec. “Differential conductances and topographs” below). These were generated with a Mathematica code available online [6]. To obtain state II one should add additional four O atoms around the central Ta atom (see Fig. 1(h) of the main manuscript for the notion of the atomic sites), and then relax. Upon removal of these extra atoms and relaxation, the new state II, a structural isomer to state I, appears.

DIFFERENTIAL CONDUCTANCES AND TOPOGRAPHS

For the simulated STM maps, we applied the Tersoff-Hamann model in an analogous way as done by Klijn *et al.* [7], where at sufficiently low voltages the dI/dV signal was related to the LDOS of the surface by

$$\frac{dI(V, x, y)}{dV} \propto e \rho_t(0) \rho_s(eV, x, y) T(eV, V, z). \quad (1)$$

Here, the tip DOS ρ_t is assumed to be constant around and between the Fermi levels of tip and substrate, and $T(E, V, z) = e^{-2\kappa(E, eV)z}$ is the transmission coefficient, with κ the decay rate. The surface is covered by the x - y coordinates, z is the perpendicular distance of the tip, and V the applied bias voltage between tip and surface. The constant-current topography $z(x, y)$ is obtained by considering the tunneling current

$$I(x, y) \propto \int_0^{eV} dE \rho_s(E, x, y) T(E, V, z(x, y)) \quad (2)$$

at a fixed value. The quantity on the r.h.s. is identical to the integrated LDOS of the surface at the position of the tip. Plugging the constant-current topography $z(x, y)$ into Eq. (1), one obtains the dI/dV signal at constant current.

OXYGEN ADSORPTION AND TANTALUM RECONSTRUCTION

Tab. I contains the relevant parameters of the (3×3)O superstructure on Ta(001). The termination of the Ta crystal leads to a compression of the outer surface layers: in the LDA, the first interlayer distance differs from the second interlayer distance by only 0.96 %, but from the bulk value $a_{\text{Ta}}/2$ by 3.35 %. For the clean Ta surface (not shown), the first to second interlayer distance ratio is 16.03 %, which is already near the ratio between the first interlayer distance and the bulk value $a_{\text{Ta}}/2$ of 16.72 % (for comparison, a compression of 10 % ± 3 % was reported in Ref. [8]; and our

GGA calculations yield a first to second interlayer distance ratio of 14.33% for clean Ta(001) (also not shown)). The O adsorption thus reduces the compression of the Ta surface layers considerably.

The collection of surface atoms has been decomposed into trimers (a collection of three atoms) containing one O and its adjacent two Ta atoms, or one O_{side} and two O_{corner} , or one Ta_{side} and two Ta_{corner} . As can be seen from the surface to subsurface interlayer distances d_z , the GGA yields a slightly decompressed surface structure and overall larger bond lengths compared to the LDA. This is a well-known underestimation of the bond-lengths inside L(S)DA [9]. Accordingly, the adsorption energies in the GGA are smaller than in the LDA, but the differences in E_{ads} of the two metastable states are nearly the same for both functionals: 0.36 eV in the LDA and 0.35 eV in the GGA (likewise for the total energies $E_{\text{DFT}}/2$: 2.16 eV in the LDA, 2.13 eV in the GGA).

The strongest variation is the interchange of the O atom heights between state I and II (i.e. d_z of the $O_{\text{corner}}-O_{\text{side}}-O_{\text{corner}}$ trimer, highlighted in blue). While the adsorption height of O_{side} above the surface is large in state I, in state II O_{corner} is elevated (both in gray). Furthermore, the $O_{\text{corner}}-O_{\text{side}}$ distance d is considerably decreased in State II (highlighted in green), leading to a potential overlap of their Wigner-Seitz spheres with radius 1.55 Å. The same applies to the distance between two adjacent O_{corner} in state I. The distance between the O_{corner} in the structure with ideal positions as shown on Figs. 1(g) and (h) of the main manuscript is rather small with 2.33 Å. The reconstruction within the Ta surface layer is illustrated by the angles θ showing substantial deviations from 180°, the vertex of which point in different directions depending on the state (Fig. 2 of the main manuscript). Furthermore, there appears Ta buckling, as can be seen from the corresponding distances d_z , which is also indicated in Figs. 2(a) and (b) of the main manuscript.

| functional + $E_{\text{DFT}}/E_{\text{ads}}$ (eV) | trimer | state I (square-shaped) | | | state II (circle-shaped) | | |
|--|---|-------------------------|--------------------|--------------|--------------------------|---------------------|--------------|
| | | d (Å) | d_z (Å) | θ (°) | d (Å) | d_z (Å) | θ (°) |
| LDA -308.92/-7.43 (I) -311.08/-7.79 (II) | $Ta_{\text{side}} - O_{\text{side}} - Ta_{\text{side}}$ | 1.92 | 1.19 (1.25, 0.06) | 103.73 | 1.96 | -0.11 (-0.09, 0.02) | 186.56 |
| | $Ta_{\text{corner}} - O_{\text{corner}} - Ta_{\text{corner}}$ | 1.97 | 0.08 (0.03, -0.05) | 171.12 | 1.95 | 0.72 (0.77, 0.05) | 106.41 |
| | $Ta_{\text{corner}} - Ta_{\text{side}} - Ta_{\text{corner}}$ | 3.02 | 0.11 (0.06, -0.05) | 162.30 | 3.41 | -0.03 (0.02, 0.05) | 193.39 |
| | $O_{\text{corner}} - O_{\text{side}} - O_{\text{corner}}$ | 3.35 | 1.22 (1.25, 0.03) | 137.28 | 2.62 | -0.86 (-0.09, 0.77) | 218.47 |
| | $Ta_{\text{center}} - Ta_{\text{surface}}$ | | -0.04 | | | -0.26 | |
| | $Ta_{\text{surface}} - Ta_{\text{subsurface}}$ | | 1.60 | | | 1.54 | |
| GGA -282.37/-6.28 (I) -284.49/-6.63 (II) | $Ta_{\text{side}} - O_{\text{side}} - Ta_{\text{side}}$ | 1.95 | 1.22 (1.29, 0.06) | 102.07 | 1.99 | -0.15 (-0.15, 0.00) | 188.79 |
| | $Ta_{\text{corner}} - O_{\text{corner}} - Ta_{\text{corner}}$ | 1.99 | 0.06 (0.00, -0.06) | 171.28 | 1.96 | 0.87 (0.94, 0.07) | 104.42 |
| | $Ta_{\text{corner}} - Ta_{\text{side}} - Ta_{\text{corner}}$ | 3.00 | 0.12 (0.06, -0.06) | 161.19 | 3.43 | -0.07 (0.00, 0.07) | 194.75 |
| | $O_{\text{corner}} - O_{\text{side}} - O_{\text{corner}}$ | 3.36 | 1.29 (1.29, 0.00) | 134.81 | 2.79 | -1.09 (-0.15, 0.94) | 225.95 |
| | $Ta_{\text{center}} - Ta_{\text{surface}}$ | | -0.04 | | | -0.33 | |
| | $Ta_{\text{surface}} - Ta_{\text{subsurface}}$ | | 1.70 | | | 1.65 | |

TABLE I. (3×3)O superstructure on Ta(001): Distances and angles between the surface atoms grouped into trimers, together with distances between the central Ta atom and the Ta surface layer, and the first interlayer (average height of all atoms within a layer). Site notion is defined in Fig. 1(h) of the main manuscript, and the bonding geometry is depicted in Fig. 2. Results are listed for each DFT functional together with total energies $E_{\text{DFT}}/2$ (for half of the slab) and adsorption energies $E_{\text{ads}} = (E_{\text{Ta(001)-O}} - NE_{\text{O}} - E_{\text{Ta(001)}})/N$ with $N = 12$ the number of O atoms in the supercell. The sign for d_z in state I is the reference for the one in state II, and angles above 180° within state II indicate the different direction compared to state I, in which their vertex is pointing (cf. Figs. 2(a) and (b) of the main manuscript). Numbers in round brackets denote distances d_z of second and third trimer atoms to Ta_{surface} .

BADER CHARGES

The Bader charge analysis associates charge and atom in a rigid manner, separating the Bader volume by the minima in the charge density around atoms (see Ref. [10] and references therein). In general, BCA yields larger estimates for the charge transfer than the iterative Hirshfeld algorithm (which we have checked explicitly with vdW functionals), but still showing similar tendencies. Bučko *et al.* suggest an agreement between the iterative Hirshfeld and Born effective charges for ionic crystals [11]. Tab. II, and Fig. 4 of the main manuscript, show a pronounced charge transfer from the Ta surface to the O atoms. O atoms acquire more charge as getting closer to the surface, which is known as high electronegativity of oxygen in chemistry. Accordingly, the O atoms do not reach the complete

O^{-2} state, as well as the Ta surface atoms do not arrive at the complete Ta^+ state either. For both states (I and II) Ta_{corner} donate more charge as they are attached to two O atoms. In respect to the functionals, the charge transfer within the system appears to be balanced between the LDA and the GGA, both assigning only slightly different weights of contribution to the charge transfer from each region. The O atoms obtain slightly more charge in the GGA.

More interestingly, while the Bader charge analysis considers the surface region around Ta_{center} in both states as negatively charged, the $Ta_{\text{center}}^{\text{sub}}$ region is already nearly charge neutral. To some extent, the subsurface Ta layers can be traced back to the almost neutral, but still slightly negative (below $-0.1e$) clean Ta(001) surface and its subsurface, which itself originates from undercoordination due to termination of the crystal. Within the LDA and in state I, $Ta_{\text{corner}}^{\text{sub}}$ donates a considerable amount of its charge to its four adjacent O_{corner} due to the smaller O height in this configuration. In general, we see that the charge distribution around Ta_{center} is very different between state I and state II, that should be of crucial importance for the adsorption of polarizable atoms and molecules on this surface.

The Bader volumes around each atom were assigned to spheres centered at the atomic sites. The Bader radii show a rather diverse behavior, but as with the charge transfer, they show an overall balance between the LDA and the GGA. For most O atoms the Bader radii become smaller in the GGA than in the LDA, although they hold slightly more charge. In contrast to that, for each functional itself and with consideration of the chemical environment dictated by the O atoms, Ta Bader charges and radii behave proportionately to each other. The Bader radius is larger for the Ta atoms, of which their adjacent O atom is lying inside the Ta surface. Finally, the Ta surface atoms always have larger Bader radii than the subsurface atoms, because the surface compression is lifted by O adsorption, and surface atoms have access to the vacuum.

In connection with the adsorption of polarizable atoms and molecules, the Bader spheres of O_{side} and Ta_{center} are nearer to each other in state I than in state II. That contributes to the differences in the Ta_{center} DOS between the two states.

| pattern | ion | Δq_B^{LDA} | Δq_B^{GGA} | R_B^{LDA} | R_B^{GGA} |
|----------------------|-----------------------------------|---------------------------|---------------------------|--------------------|--------------------|
| State I (square) | O_{corner} | -1.21 | -1.23 | 1.74 | 1.73 |
| | O_{side} | -1.12 | -1.13 | 3.58 | 3.53 |
| | Ta_{corner} | +0.80 | +0.79 | 2.57 | 2.57 |
| | Ta_{side} | +0.45 | +0.45 | 2.36 | 2.27 |
| | Ta_{center} | -0.19 | -0.26 | 2.73 | 2.79 |
| | $Ta_{\text{corner}}^{\text{sub}}$ | +0.81 | +0.73 | 1.57 | 1.60 |
| | $Ta_{\text{side}}^{\text{sub}}$ | +0.32 | +0.37 | 1.57 | 1.59 |
| | $Ta_{\text{center}}^{\text{sub}}$ | -0.06 | -0.02 | 1.65 | 1.67 |
| State II (circle) | O_{corner} | -1.18 | -1.18 | 2.90 | 2.92 |
| | O_{side} | -1.24 | -1.26 | 1.50 | 1.49 |
| | Ta_{corner} | +0.91 | +0.99 | 2.03 | 1.91 |
| | Ta_{side} | +0.41 | +0.37 | 2.78 | 2.79 |
| | Ta_{center} | -0.24 | -0.24 | 2.86 | 2.78 |
| | $Ta_{\text{corner}}^{\text{sub}}$ | +0.01 | +0.10 | 1.61 | 1.62 |
| | $Ta_{\text{side}}^{\text{sub}}$ | +0.44 | +0.36 | 1.56 | 1.60 |
| | $Ta_{\text{center}}^{\text{sub}}$ | -0.06 | -0.05 | 1.68 | 1.70 |

TABLE II. Bader charges q_B (e) and radii R_B (\AA) listed for both DFT functionals, where O has free valency $2s^22p^4$, and Ta $5p^65d^46s^1$. Displayed are the differences Δq_B measured w.r.t. the free valencies.

DIFFERENTIAL CONDUCTANCE IMAGES

In Fig. 1, we plot experimental dI/dV images representative for spatial variations of the DOS at a given bias voltage. Here, the area of measurement for the images is the same as in Fig. 1 of the main manuscript. Compared to the STM images, the dI/dV images show numerous fine variations of the features as a function of bias voltage. In particular, there are at least four contrast reversals similar to the one observed in the STM images, i.e. from -1.5 V (d) to -1.1 V (e), from -1.1 V (e) to -0.4 V (f), from -0.4 V (f) to $+0.5$ V (g) and from $+1.2$ V (i) to $+3.8$ V (j). DFT simulation of the conductance leads also to variations of the whole picture, catching contrast reversals in different areas and possible rotation. However, limitations of the TH approach does not allow to discuss it in details. For comparison, we display simulated dI/dV images of the two states in Fig. 1(k),(l). Similar to the experimental dI/dV

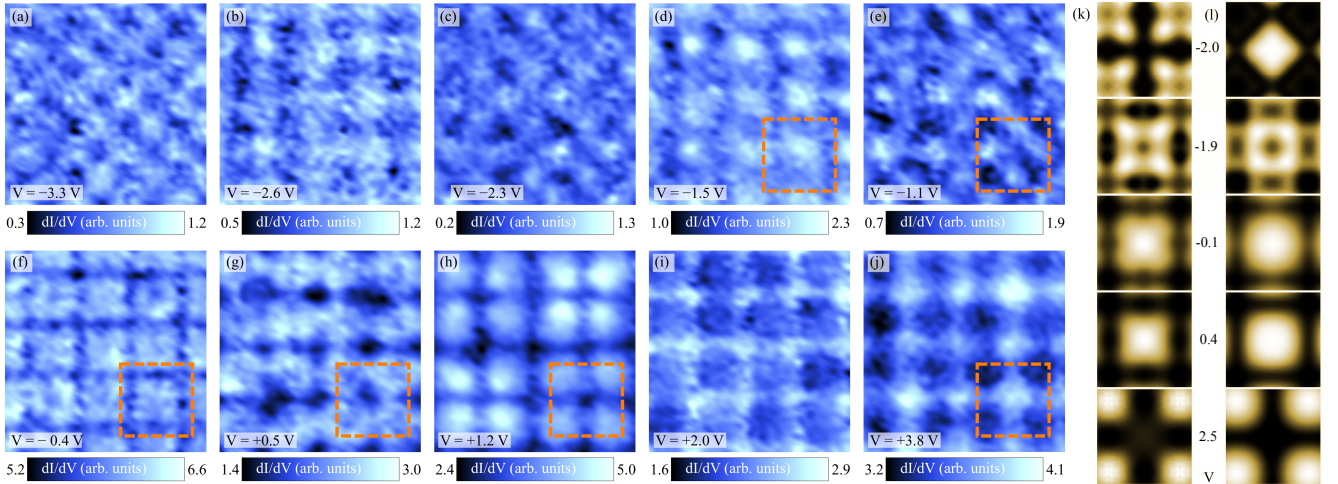


FIG. 1. (a)-(j) dI/dV images ($3.8 \text{ nm} \times 3.8 \text{ nm}$) measured at various bias voltages in the same area as Fig. 1(a)-(f) of the main manuscript ($I_{\text{stab}} = 0.6 \text{ nA}$, $V_{\text{mod}} = 5 \text{ mV}$). Dashed squares marked in some of the panels serve as guides to the eyes showing numerous contrast reversals as a function of bias. (k),(l) Simulated dI/dV images for states I (k) and II (l), each at isosurface value $5 \times 10^{-7} e/\text{\AA}^3$. The integration range around each bias was set to 50 meV (same as Gaussian broadening of the LDOS in Fig. 5). The images have been generated by the code given in Ref. [6].

images, they reveal multiple contrast reversals, of which we show a selection. However, a one-to-one correspondence between the different features is hampered by the limitations of the TH model.

THE Ta_2O MOLECULE AND ORBITAL HYBRIDIZATION

The Ta-O-Ta trimers mentioned in Sec. “Oxygen adsorption and tantalum reconstruction” comprise (hypothetical) Ta_2O molecules. To obtain information on the Ta_2O molecule, simplified DFT calculations were performed after singling out the two trimers $\text{Ta}_{\text{side}}\text{-O}_{\text{side}}\text{-Ta}_{\text{side}}$ and $\text{Ta}_{\text{corner}}\text{-O}_{\text{corner}}\text{-Ta}_{\text{corner}}$. The DFT setup was left unchanged (see Sec. “DFT calculations”). Relaxation starting from all trimers in state I and II yields two different molecular geometries (Tab. III), which were found to be stable upon perturbations w.r.t. their positions.

The first and second molecule listed in Tab. III approximately correspond to the sp^3 - and sp -hybridized configuration, respectively: The bonding angle within the sp^3 state is comparable to the one of the H_2O molecule (104.45°), while in the sp state the trimer with the central O has an almost linear geometry as predicted by the Valence Shell Electron Pair Repulsion (VSEPR) approach [12]. As on the surface, according to the Bader charge analysis the O atoms do not completely reach the O^{-2} state. So the orbitals, which do not participate in bonding, host incomplete lone pairs.

As a molecule itself, the sp -hybridized Ta_2O has a net magnetic moment of $3.54 \mu_{\text{B}}$. Furthermore, it is higher in energy by 3.03 eV compared to the sp^3 -hybridized Ta_2O molecule. As on the surface, the Bader radius of the O atom in the sp^3 state is much larger than in the sp state.

TABLE III. The Ta_2O molecule computed within the LDA: Bond distances d and angles θ , Bader charges Δq_{B} and radii R_{B} , magnetic moments μ , and total energies E_{DFT} .

| trimer | d (\AA) | θ ($^\circ$) | Δq_{B} (e , O) | Δq_{B} (e , Ta) | r_{B} (\AA , O) | r_{B} (\AA , Ta) | μ (μ_{B} , O) | μ (μ_{B} , Ta) | E_{DFT} (eV) |
|--------------------|----------------------|-----------------------|----------------------------------|-----------------------------------|------------------------------------|-------------------------------------|-------------------------------|--------------------------------|-----------------------|
| Ta-O-Ta (sp^3) | 1.91 | 111.63 | -0.99 | +0.50 | 2.34 | 2.22 | 0.00 | 0.00 | -19.77 |
| Ta-O-Ta (sp) | 1.81 | 179.75 | -1.20 | +0.60 | 1.42 | 2.51 | -0.14 | 1.84 | -16.74 |

DENSITY OF STATES AND SURFACE CHEMISTRY

Characterization of the LDOS in state I: Fig. 3 contains the orbital-resolved DOS projected onto the sites of the O and corresponding nearest Ta atoms within state I. We identify the O p states with energies between $-7.4\text{ eV}/-8.3\text{ eV}$ and $-5.2\text{ eV}/-6.2\text{ eV}$ of $O_{\text{side/corner}}$ as bonding states (Ref. [13]), which can be explained by the resonance peaks lying within the same energy range for corresponding peaks in Ta p and d orbitals.

Let us have a closer look on the DOS of O_{side} and O_{corner} which are lying on the vertical O row as shown in Fig. 2. The LDOS of O_{corner} shows a set of non-bonding states between -6.2 eV and -4.8 eV arising from its p_y orbital (Ref. [13] provides a classification of states seen in LDOS of O adsorbates on transition metal surfaces). This can be understood from geometry: The p_y orbital of O_{corner} points to hollows. The p_x orbitals of all O atoms on the vertical O rows are completely filled and contribute only to bonding states with adjacent Ta atoms.

We can apply some quantum chemistry considerations here. According to the Pauling scale of electronegativity, the difference of values between Ta and O in the Ta-O bond reaches 2.0 units, which is close to the border between covalent (< 2) and ionic (> 2) type of bonding. So we expect a charge transfer towards O in this bond. Based on the surface trimer geometry, we also identify sp and sp^3 hybridized O atoms, as in the hypothetical Ta_2O molecules. One should note, that for the sp hybridized O atom embedded into the Ta surface, this localized bonding picture is not relevant, but we use the name, as it carries typical chemical properties. Focusing on O_{side} in state I, one observes s and p states located approximately at the same energy that constitutes the sp^3 hybridization. Then, taking into account the saturation of its hybrid orbitals, two of them are directed towards the adjacent Ta_{side} , and the two remaining point towards the vacuum, along the O row and perpendicular to the other two hybrid orbitals. These host the lone pairs (or non-bonding states), and we argue that these states have important implications for all chemical properties of the system. In the DOS one can see that orbitals of p_y and p_z character are higher in energy, in agreement with the local arrangement. We also identify non-bonding states between -5 eV and up to the Fermi energy, and anti-bonding states above E_F .

Another type of O atom in state I, the sp -hybridized O_{corner} , has a more complex electronic structure. First, the sp state is characterized by a higher electronegativity of the trimer-central atom than the sp^3 state, because it has a larger s -state contribution (see “Bader charge section” in Tab. II). Second, there is the already mentioned non-bonding set of states for the p_y orbital. It is possible, that this orbital is rotated towards the sp^3 orbital of the nearest O_{side} , being aligned inside the O row. Third, there are clear π -bonding and -anti-bonding features on spectra of neighboring Ta atoms.

Characterization of the LDOS in state II: The O-LDOS in Fig. 4 show a reversed tendency in their behavior, which corresponds to the reversed adsorption heights within the O rows. We suggest that the O_{side} p_y and p_z orbitals form a linear combination as $p_y \pm p_z$, with the one lobe pointing to the close-by sp^3 orbitals, and the one pointing into the bulk containing the bonding states. $\text{Ta}_{\text{corner}}$ now shows excitations being more pronounced in the d_{z^2} and $d_{x^2-y^2}$ orbitals as compared to Ta_{side} in state I (also due to polarizations induced by lone pairs; to be discussed below), because the two O_{corner} are now elevated above the surface, and in the analogous state of O_{side} within state I. The Ta_{side} and $\text{Ta}_{\text{corner}}$ p_z orbitals in state II show a reversal in excitation weights compared to state I as well.

Effects of sp and sp^3 hybridization on adsorption geometry: One can understand the adsorption geometry with the help of the proposed sp and sp^3 hybridizations, and the superstructure provided in Tab. I, which is depicted in Figs. 2(a) and (b) of the main manuscript. As we mentioned, the two bonding orbitals of the sp^3 hybridized O_{side} in state I point to the adjacent Ta_{side} , with both DFT functionals having a slightly larger bonding angle than the H_2O molecule (104.45° ; Tab. I). The two remaining lone pairs point diagonally with their orbital lobes to the vacuum along the O row to form the tetrahedral structure.

According to the Bader charge analysis (Sec. “Bader charges” above), the orbital volumes holding the lone pairs are very large, and interact repulsively with O_{corner} , which is then embedded into the Ta surface and forms the geometry of the sp hybridization (the in-plane p_x orbital hybridizes with atoms nearby). The lobe of its non-bonded p_y orbital parallel to the Ta surface occupies the free space along the (vertical) O row and below the lobes of the sp^3 -hybridized orbitals of O_{side} pointing to the vacuum. The geometric situation reverses for State II. As there are more sp^3 -hybridized O atoms than sp -hybridized ones in State II, it has a lower total energy compared to State I (Tab. I). This conclusion can also be drawn from Tab. III, which shows that the Ta_2O molecule in sp^3 -hybridized configuration has lower energy. To sum up, the repulsive character of the formed oxygen lone pairs in the sp^3 state should play an important role during oxygen adsorption and is responsible for the observed surface pattern with zigzag-ordered O structure perpendicular to the surface. Depending on the temperature and pressure, the O coverage and repulsive interactions are balanced, and crossing O rows are admitted until the optimal 3×3 superstructure emerges.

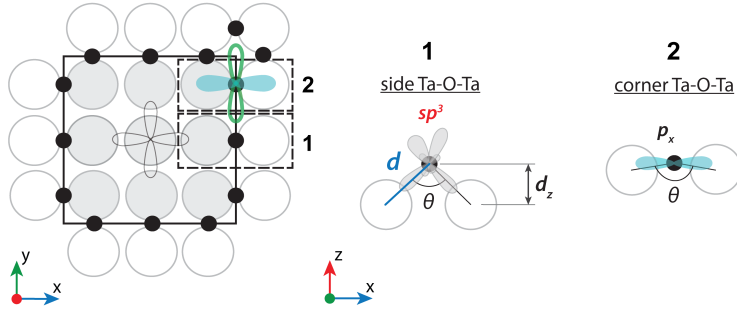


FIG. 2. Idealized surface view with insets showing two configurations of Ta-O-Ta trimers (side views) in state I: side group of atoms (1) and corner group (2). An overlay of orbital sketches shows principal difference in electronic states: in light green the “non-bonding” p_y orbital of the O_{corner} in the vertical row, and in blue its bonding p_x orbital; in (1) we show the proposed sp^3 hybridization state for O_{side} . Color code of orbitals and positions of the atoms under consideration corresponds to Fig. 3. For state II, O elevations are reversed.

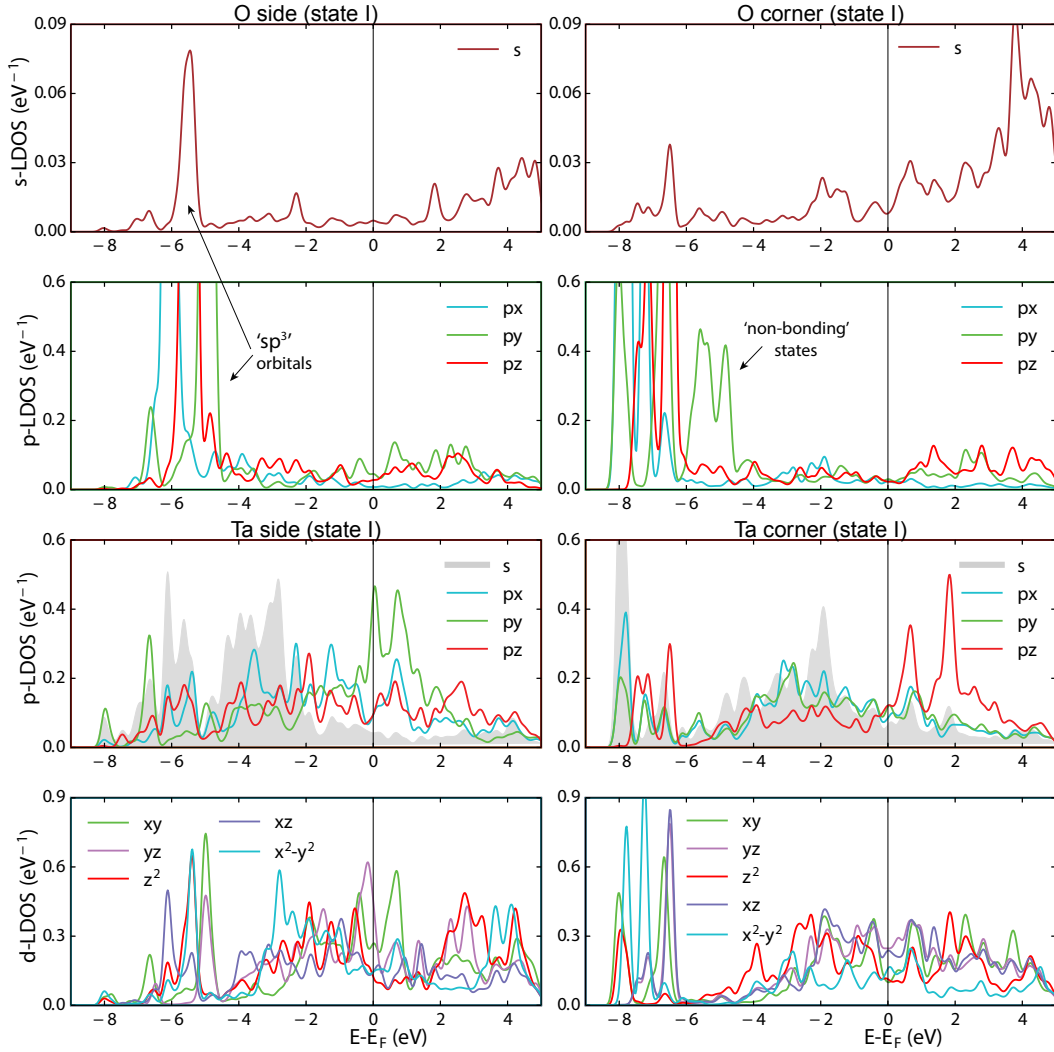


FIG. 3. Orbital-resolved LDOS of Ta(001)-O in state I (LDA). Only the LDOS of atoms sitting on, or next to the vertical rows are shown. See discussion in the text.

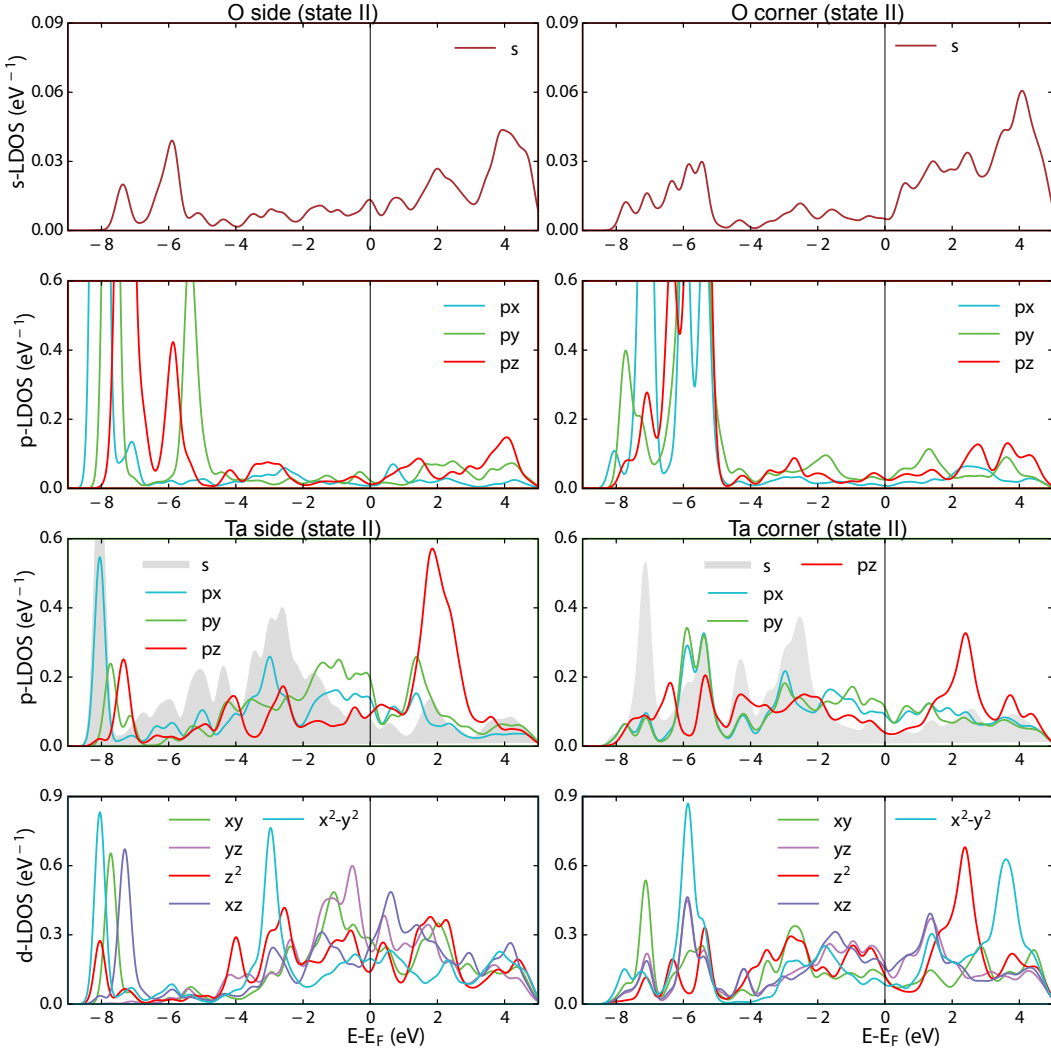


FIG. 4. Orbital-resolved LDOS of Ta(001)-O in state II (LDA). Only the LDOS of atoms sitting on, or next to the vertical rows are shown. See discussion in the text.

Induced polarization effects: In state I, O_{side} has approximately two lone pairs in sp^3 -hybridized orbitals with p_y and p_z contributions. Consequently these can induce dipoles in the Ta_{side} orbitals of the same symmetry (the anti-bonding peaks of p states above E_F), although more pronounced in p_y , which is parallel to the two hybrid orbitals carrying the suggested lone pairs, and being aligned along the O row. The effect of polarization by induced dipoles is more pronounced on the Ta surface and subsurface atoms (latter not shown) in the central region of the 3×3 plaquette and below the O row (not shown; for explanations of lone-pair bonding see Ref. [13]). Excessive peaks above E_F are seen in the Ta_{center} p_z , d_{xy} , $d_{x^2-y^2}$ orbitals (Fig. 5), the latter two pointing to O_{side} and O_{corner} . The p_z peaks are due to π bonding with the p_z orbital of Ta_{corner} , that is consistent with local geometry. Pronounced d_{xy} and $d_{x^2-y^2}$ peaks reflect a non-direct hybridization effect that can be cast to the lone-pair idea: these are the lone-pair induced bonding and anti-bonding dipoles. Indeed, the sp^3 -hybridized states interact with Ta_{side} s - and $d(p)$ -states [14], which in turn induce excessive peaks at xy and x^2-y^2 states of Ta_{center} .

In state II, now the Ta_{side} and Ta_{corner} p_z orbitals participate in π bonding (Fig. 4). Ta_{center} , however, does not show any sharp peaks around and above E_F , and has significantly less intensity of the whole spectrum in comparison to state I (Fig. 5). This can be also attributed to the immersed position of the Ta_{center} in state II. While the long-range effects of the O atoms on the electron structure is less pronounced, the Ta atoms adjacent to the O row show excessive features above and below E_F . Especially in the Ta_{corner} $d_{x^2-y^2}$ orbital we observe bonding and anti-bonding peaks, which we suggest again to reflect dipoles induced by the presence of two adjacent sp^3 -hybridized O_{corner} atoms.

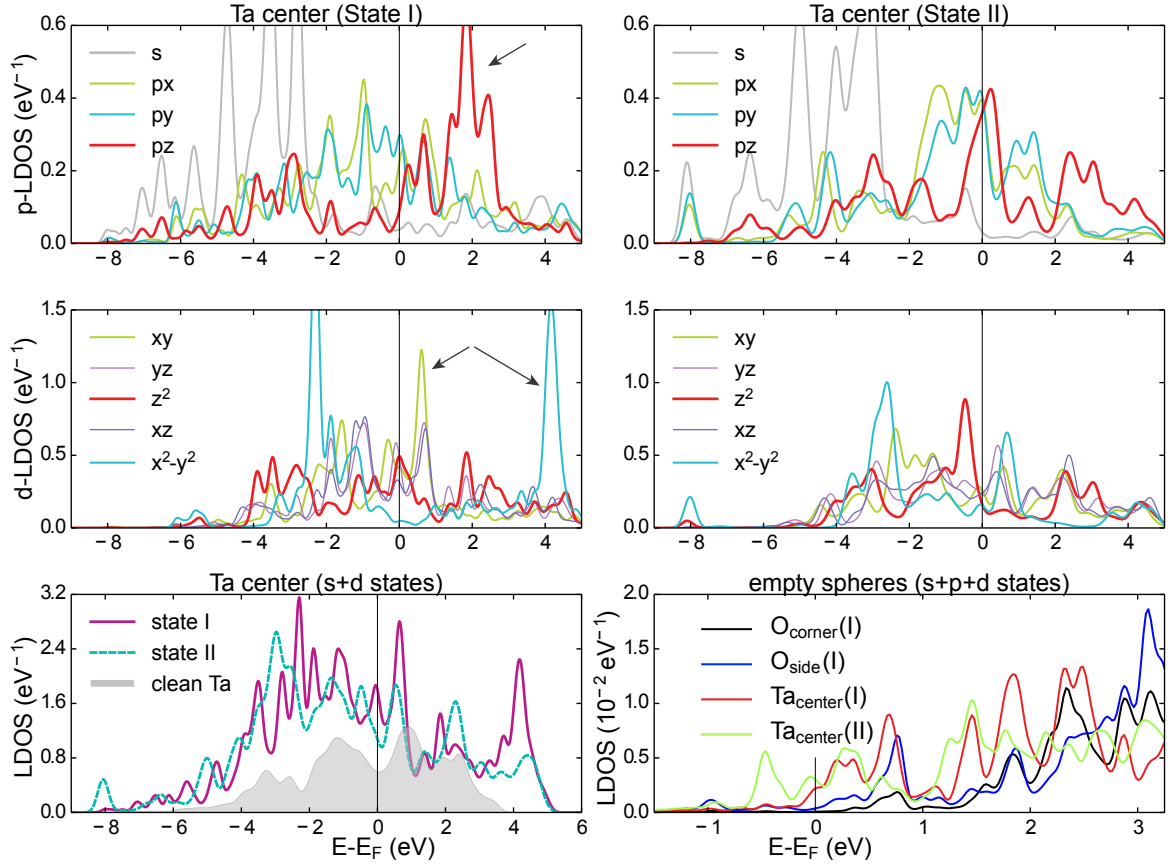


FIG. 5. Orbital-resolved $\text{Ta}_{\text{center}}$ -LDOS of $\text{Ta}(001)\text{-O}$ in states I (top and middle left) and II (top and middle right). Results obtained within the LDA. For state I, arrows indicate anti-bonding π -bond states (p -LDOS) and anti-bonding dipole states (d -LDOS). The comparison of the overall $s + d$ electronic states of the $\text{Ta}_{\text{center}}$ to the clean Ta surface atom is shown in the bottom left spectrum. LDOS projected onto the added s , p , and d orbitals of empty spheres above indicated atomic sites in Fig. 3(a) of the main manuscript, and arranged along the isosurface at 3.2 eV shown in Fig. 2(c) of the main manuscript. The radius of the empty spheres has been chosen as the Wigner-Seitz radius of W. All spectra have been broadened using a Gaussian filter with a FWHM of 50 meV.

Explanation of plaquette shapes and contrast reversal: The alternation of the sp^3 -hybridized O atoms in corner and side positions along the rows leads to the additional broader darkening at its locations on the maps. This effect tunes the square-shaped (sp^3 atom at side positions) and circle-shaped (sp^3 atom at corner positions) protrusions and goes well in line with the lone-pair concept. Also, in state II, the d -orbital weight of $\text{Ta}_{\text{center}}$ at low bias is rather small, and thus the central dark spot in low-bias STM images appears. This is because the O atom Bader spheres are farer away (cf. Fig. 4 in the main manuscript) and lone-pair induced anti-bonding dipole production is low.

Backwards, we define the following rules to identify plaquette shapes. All plaquettes have similar features at small bias: deep minima are at the O_{corner} , plaquette pattern is present in the system everywhere. We distinguish cross shapes (state I) from circle shapes (state II) by additional minima/maxima:

1. The sp^3 -state O site (bent geometry) always shows a minimum (less tunneling probability) and it is delocalized (the minimum spot/area appears broad).
2. The sp -state O site (aligned geometry) also always shows a minimum, but a smaller spot.
3. The Ta regions correspond normally to the protrusions.

Then plaquette attributes goes for the cross shape as:

- Additional broad minima are at O_{side} sites (sp^3),
- maxima are at $\text{Ta}_{\text{corner}}$ and $\text{Ta}_{\text{center}}$ (not strictly).

And for the circle shape as:

- Additional broad minima are at O_{corner} sites,
- maxima are at Ta_{side} ,
- and an additional minimum is at Ta_{center} (central spot).

The contrast reversal means that there are more states above the corner positions at higher biases. There are four Ta_{corner} in contrast to only one Ta_{center} . The antibonding states of O_{corner} contribute additionally. For the measurement with the STM tip are the Ta p_z and d_{z^2} orbitals slightly more relevant, and the charge density from different sites tends to interpenetrate at higher distances above the surfaces, especially as anti-bonding states happen to be more delocalized [15]. Thus, before the contrast reversal, the STM tip measures the orbitals containing anti-bonding dipole states lowering the work function around Ta_{center} . At higher bias the anti-bonding states within orbitals of Ta_{corner} contribute more efficiently [13], also because the potential O-induced gap due to electron-hole production does not prevail anymore.

Summary: In conclusion, we performed a detailed investigation of the experimentally observed electronic properties of the Ta(001)-O surface by means of DFT. Thus, we were able to identify its contrast reversal as seen in the STM images and to predict the adsorption specific properties. One should mention that DFT-GGA in general has a limited access to electrostatic effects on a surface and overall plays towards its metallic character (see, for instance, the experimentally observed induced gap (Fig. 3)). The parental bulk material, especially for the local structure containing the sp^3 -hybridized trimer, is tantalum pentoxide Ta_2O_5 [16, 17]. It is an oxide with a high dielectric constant, and with a reported band gap of $\sim 1-4$ eV. DFT-GW simulations improved the gap values for the crystalline form of Ta_2O_5 , although insufficiently [18]. The contribution of Ta s states in the conductance area for intraplanar bonds was suggested to be the reason for the small gap in β - Ta_2O_5 and δ - Ta_2O_5 [18].

Also, we found the picture of the localized molecular bonds helpful, namely the one in terms of hybrid orbitals hosting non-bonding electrons (lone pairs), that served as a complementary view. Unexpectedly, we could explain some properties of the surface with repulsive and long-range character of the lone-pairs interaction that coincide with DFT results. The possibility for long-range effects is also shown by Ta_2O_5 [16, 17].

The Ta protrusions seen on STM images are due to the dominance of the electronic properties over the structural ones. In particular, we propose lone-pair induced anti-bonding dipole d states, and anti-bonding π -bonded p states should play an important role in the physics of the surface. These states above E_F lower the work function, and thus enhance the tunnel current. At higher bias these lead to the contrast reversal.

We see that polarization properties differ in state I and II of the O-reconstructed Ta(001) surface. The arrangement of sp - and sp^3 -hybridized O atoms along the rows induces excitations in the center of the 3×3 plaquette of state I by means of indirect hybridization, but much less in state II. It is O_{side} in state I, which has the largest Bader radius, and its Bader sphere has the highest proximity to the one of Ta_{center} . The inhomogeneous electrostatic texture (cf. Fig. 4 of the main manuscript) was found to be marked with an unusual formally negative charge on Ta_{center} . The pronounced bonding and anti-bonding peaks in the surface Ta d states at approximately -1 eV, -2 eV, 0.6 eV, 2 eV and 4 eV can mediate the electrostatic interaction with adsorbates possessing a dipole moment [19]. This also means that the induced dipole excitations would lead to vdW forces acting between Ta_{center} and such polarizable atoms and molecules.

-
- [1] L. Cornils, A. Kamlapure, L. Zhou, S. Pradhan, A. A. Khajetoorians, J. Fransson, J. Wiebe, and R. Wiesendanger, Phys. Rev. Lett. **119**, 197002 (2017).
- [2] G. Kresse and J. Furthmüller, Phys. Rev. B **54**, 11169 (1996).
- [3] P. E. Blöchl, Phys. Rev. B **50**, 17953 (1994).
- [4] J. P. Perdew, K. Burke, and M. Ernzerhof, Phys. Rev. Lett. **77**, 3865 (1996).
- [5] I. A. Nekrasov, M. A. Korotin, and V. I. Anisimov, eprint arXiv:cond-mat/0009107 (2000).
- [6] <http://vaspnotes.blogspot.de/2013/09/simulated-stm.html>.
- [7] J. Klijn, L. Sacharow, C. Meyer, S. Blügel, M. Morgenstern, and R. Wiesendanger, Phys. Rev. B **68**, 205327 (2003).
- [8] R. A. Bartynski, D. Heskett, K. Garrison, G. Watson, D. M. Zehner, W. N. Mei, S. Y. Tong, and X. Pan, Journal of Vacuum Science & Technology A **7**, 1931 (1989).
- [9] P. Haas, F. Tran, and P. Blaha, Phys. Rev. B **79**, 085104 (2009).
- [10] <http://theory.cm.utexas.edu/henkelman/code/bader/>.
- [11] T. Bučko, S. Lebègue, J. G. Ángyán, and J. Hafner, The Journal of Chemical Physics **141**, 034114 (2014).

- [12] R. Gillespie, *Molecular Geometry* (Van Nostrand Reinhold Co.,, 1972).
- [13] C. Q. Sun, *Relaxation of the chemical bond: skin chemisorption size matter ZTP mechanics H₂O myths*, Springer Series in Chemical Physics (Springer, Singapore, 2014).
- [14] A. Walsh, D. J. Payne, R. G. Egdell, and G. W. Watson, *Chem. Soc. Rev.* **40**, 4455 (2011).
- [15] F. Jensen, F. Besenbacher, E. Laegsgaard, and I. Stensgaard, *Phys. Rev. B* **42**, 9206 (1990).
- [16] Y. Guo and J. Robertson, *Applied Physics Letters* **104** (2014), 10.1063/1.4869553.
- [17] H. Jiang and D. A. Stewart, *Journal of Applied Physics* **119** (2016).
- [18] J. Lee, W. Lu, and E. Kioupakis, *Applied Physics Letters* **105** (2014).
- [19] A. Kakekhani, L. T. Roling, A. Kulkarni, A. A. Latimer, H. Abroshan, J. Schumann, H. AlJama, S. Siahrostami, S. Ismail-Beigi, F. Abild-Pedersen, and J. K. Nørskov, *Inorganic Chemistry* **57**, 7222 (2018).

2.5 Van der Waals forces in DFT: The Tkatchenko-Scheffler method

Additional to the metallic, covalent, and ionic bonds, non-covalent bonds like the ones induced by the long-range and dispersive **vdW** interactions are often relevant for an accurate description of surfaces and adsorption or arrangement of atoms and molecules thereon, see, for example, Refs. [Hec17; Kak18]. Local fluctuations of the electronic charge density result in temporal dipole moments in distant parts of the system, which happen to be correlated by the long-range Coulomb interaction (i.e., these are plasmon-like interactions [Ger72; Kli09]). This definition makes readily clear that neither **HF** theory (cf. introductory part to this chapter) nor **DFT** with its local approximations contain **vdW** interactions [Stö19; Sto13]; yet these interactions can be included semi-empirically within the **DFT** framework.

In view of the considerations made in Sec. 2.3, of possible future studies on the adsorption of **TMs** on the Ta(001)-p(3×3)-O surface, and of the already obtained experimental results showing Fe adsorbed at the top position in the centre of the 3×3 plaquette [Cor17], it is imperative to include **vdW** interactions within the **DFT** description already for the clean surface. As also mentioned in Sec. 2.3, however, neither the geometric nor the electronic structure of the surface are modified significantly by the semi-empirical consideration of **vdW** interactions within **DFT**, and the numerical Fe adsorption studies already performed within this setup showed no conclusive result for the stability of the top position. The present section introduces **vdW-DFT** on the basis of the calculations reported on in the following Sec. 2.6. A thorough introduction to **vdW** forces in **DFT** can be found in Ref. [Giu05], and especially in the references therein. Reviews on **vdW-DFT** covering ranges of methods (including the one employed in this and the following section) and corresponding results can be found in Refs. [Ber15; Kim16]. An implementation of the **DFT-D2** method (a similar, but more original approach to **vdW-DFT**) together with an explanation of how structural minimization works can be found in Ref. [Buč10]. Benchmarks of the **vdW-DFT** approach employed in this and the following section can be found in Refs. [Cla18; Gou16a; Mar11].

We start with the **TS** method [Tka09], in which an atomically pairwise attractive energy contribution is added to the **DFT-GS** energy (Eq. (2.18)),

$$E_{\text{vdW}} = -\frac{1}{2} \sum_{A,B} \sum_{\mathbf{L}}' f_{\text{damp}}(R_{AB,\mathbf{L}}, R_A, R_B) \frac{C_{6AB}}{R_{AB,\mathbf{L}}^6}. \quad (2.60)$$

The sum runs over pairs of atoms with distance $R_{AB,\mathbf{L}}$ in supercells separated by a lattice translation \mathbf{L} (the prime on the sums indicates $A \neq B$ for $\mathbf{L} = 0$), $R_{A/B}$ and C_{6AB} are their corresponding **vdW** radii (half distance between two atoms, when their Pauli repulsion and London dispersion attraction are balanced) and C_6 coefficients, respectively, and f_{damp} is a damping function which cures the singular behaviour at small distances, where non-**vdW-DFT** is assumed to correctly describe the electronic structure. The C_6 coefficients are given by the Casimir-Polder integral

$$C_{6AB} = \frac{3}{\pi} \int_0^\infty d\omega \alpha_A(i\omega) \alpha_B(i\omega), \quad (2.61)$$

with $\alpha_{A/B}(i\omega)$ the electronic polarizabilities. The zeroth-order Padé approximant is the static polarizability α_A^0 , and the first order is given by $\alpha_A^1(i\omega) = \alpha_A^0/[1 + (\omega/\omega_A)^2]$, with ω_A the characteristic mean excitation frequency (likewise for atom B). Substitution of the first two Padé approximants into Eq. (2.61) gives the London formula $C_{6AB} = \frac{3}{2}[\omega_A\omega_B/(\omega_A + \omega_B)]\alpha_A^0\alpha_B^0$. The physical interpretation of the C_6 coefficients is simple: According to Eq. (2.61), if the polarizabilities of atom A and B are “resonant”, their corresponding vdW interaction becomes strong; within the London approximation the C_{6AB} coefficients are proportional to the static polarizabilities, and increase with larger characteristic mean excitation frequencies. Setting $A = B$, one obtains $\eta_A = \frac{4}{3}C_{6AA}/(\alpha_A^0)^2$, with C_{6AA} the atomic C_6 coefficient, and substitution into the London formula yields

$$C_{6AB} = \frac{2C_{6AA}C_{6BB}}{\frac{\alpha_B^0}{\alpha_A^0}C_{6AA} + \frac{\alpha_A^0}{\alpha_B^0}C_{6BB}}. \quad (2.62)$$

Due to charge transfer, atoms in molecules and solids and on surfaces receive modification of their dispersion coefficients (i.e., R_A , α_A , and C_{6AA}) as compared to the case in vacuum. The coefficients are assumed to be rescaled by the effective volumes the atoms adopt within the system,

$$\begin{aligned} C_{6AA}^{\text{eff}} &= \left(\frac{V_A^{\text{eff}}}{V_A^{\text{free}}}\right)^2 C_{6AA}^{\text{free}}, \\ \alpha_A^{\text{eff}} &= \frac{V_A^{\text{eff}}}{V_A^{\text{free}}} \alpha_A^{\text{free}}. \end{aligned} \quad (2.63)$$

The effective volumes are defined in terms of the DFT electronic density,

$$\frac{V_A^{\text{eff}}}{V_A^{\text{free}}} = \frac{\int d\mathbf{r} r^3 w_A(\mathbf{r}) n^{\text{DFT}}(\mathbf{r})}{\int d\mathbf{r} r^3 n_A^{\text{free}}(\mathbf{r})}, \quad (2.64)$$

with help of the Hirshfeld atomic partitioning weights

$$w_A(\mathbf{r}) = \frac{n_A^{\text{free}}(\mathbf{r})}{\sum_B n_B^{\text{free}}(\mathbf{r})}, \quad (2.65)$$

which are defined in terms of non-interacting atoms, and are also used to determine the Hirshfeld partial charges [Hir77]

$$q_A = -e \int d\mathbf{r} w_A(\mathbf{r}) n^{\text{DFT}}(\mathbf{r}). \quad (2.66)$$

Like the Bader charges shown in Fig. 2.4, the Hirshfeld partial charges computed during the TS method reveal that the O-reconstruction of Ta(001) is accompanied by a considerable charge transfer (Tab. 2.5 and Fig. 2.5). The DOS of the Ta(001)-p(3×3)-O surface (Figs. 2.7, 2.8, and 2.9) show that DFT considers the surface being metallic everywhere, and in conjunction with the STS results (Fig. 2.3), which show rather insulating behaviour

instead, we were able to conclude that the oxygens are chemisorbed on Ta(001) by metallic bonding with prevailing ionic character (Sec. 2.4). The surface reconstruction should thus be quite robust against perturbations induced by an STM tips, electric pulses, or adsorption of other atoms, what could be confirmed experimentally. Chemisorption via metallic bonding was also found in Ref. [Guo17].

2.5.1 The iterative Hirshfeld algorithm

The problem with surfaces containing ionic components is the use of charge-neutral reference systems for the determination of effective volumes (Eqs. (2.64) and (2.65)) [Buč14; Buč13a]. The volume ratios used in Eqs. (2.63), which are related to the vdW radii via [Tka09]

$$R_A^{\text{eff}} = \left(\frac{V_A^{\text{eff}}}{V_A^{\text{free}}} \right)^{1/3} R_A^{\text{free}}, \quad (2.67)$$

are close to unity in the original TS method (Fig. 2.10), in contrast to the charge transfer seen from the Hirshfeld charges (Tab. 2.5). This is counterintuitive because the local effective volumes should somehow scale with the local charge accumulation or depletion (perhaps even inversely proportional); indeed, in many applications the Hirshfeld charges tend to come out as rather small [Buč14; Bul07]. Furthermore, even though there happens to be charge accumulation at oxygen locations (Tab. 2.5), the vdW radii for the adsorbed oxygens decrease only marginally or are unchanged, leading to slightly decreased or unchanged polarizabilities and C_6 coefficients (Tab. 2.6 and Fig. 2.10). And even though the Ta surface layer becomes depleted everywhere, away from the oxygen rows its polarizability is enhanced. Within the TS method alone, this could only be explained by a possible enhancement of metallicity and delocalization, because electronic motion might be freer, and thus larger electronic dipoles could be induced. However, the observations point to the HI algorithm, in which a reference system with fractionally ionic charges is set up, thereby taking care of the charge transfer within the system [Bul07; Van13]. In this algorithm, the Hirshfeld atomic partitioning weights are computed iteratively,

$$w_A^i(\mathbf{r}) = \frac{n_A^{i-1}(\mathbf{r})}{\sum_B n_B^{i-1}(\mathbf{r})}, \quad (2.68)$$

with $w_A^1(\mathbf{r})$ given in Eq. (2.65), and $n_A^i(\mathbf{r})$ determined by the equation

$$\int d\mathbf{r} w_A^i(\mathbf{r}) n^{\text{DFT}}(\mathbf{r}) = \int d\mathbf{r} n_A^i(\mathbf{r}). \quad (2.69)$$

The iteration is performed until convergence in the Hirshfeld charges is obtained, cf. Eq. (2.66). The new effective volumes can then be computed from Eq. (2.64), and subsequently the new polarizabilities and C_6 coefficients from Eq. (2.63).

The problem with the HI algorithm is that anions become unstable due to the inherent delocalization in PW based methods, which try to spread charge excesses over the entire supercell [Van13] (the same problem with pronounced inhomogeneities). Even the method of Watson spheres with compensating positive charges centred at the anions does not yield

sufficient localization to overcome this problem in our case [Buč13a; Wat58]. Thus, we use the method of frozen local orbitals, in which the anions have the same orbitals as the corresponding neutral atom, only their occupancy is changed when the anion is created [Buč18; Gou16b]. This method, however, can still not be applied to the free Ta(001) surface, because during the HI algorithm there happen to arise strong charge concentrations around some atoms in the slab, and the method of Watson spheres again diverges. The Ta(001) surface can thus be considered only without the HI algorithm (that is why the adsorption energies were determined within the TS method alone). In contrast to Sec. 2.4, the energy cut-off for the PW basis set was not increased for the vdW-DFT calculations, because the delocalization problem would become stronger. According to experience, this also served to reduce imbalances in the assignment of HI charges to the atoms.

We would like to mention another route to account for the charge transfer, which is given by the density-dependent dispersion correction, called dDsC-DFT [Ste11a; Ste11b]. In this method the dispersion coefficients depend on the electronic density directly, so that charge transfer as well as local chemical environments are considered.

2.5.2 Self-consistent screening of dispersion coefficients

By going yet one more step, the metallicity of the surface along with its coexisting static polarization texture due to charge transfer can be further addressed within the vdW description. According to the Dobson classification, the additivity of vdW interactions based on Eq. (2.60) is questionable on several levels, because all possible types of non-additivities listed in Ref. [Dob14] apply to our case: First, the squeezing of the atomic spheres is considerable due to charge transfer and bonding. This, however, is captured by the rescalings in Eqs. (2.63) together with the HI algorithm. Second, both, the metallicity and the polarization texture, the latter leading to permanent dipoles acting as additional classical electromagnetic centres, will screen and renormalize the Coulomb interaction in the system, leading to modified dispersion coefficients as well as to other multipolar terms not contained in the vdW-DFT energy (Eq. (2.60)). Third, the energetic degeneracies allowing the electrons to hop through the system may lead to enhanced polarizabilities (due to vanishing energy denominators). Furthermore, as mentioned before, the longer propagation paths and enhanced local electronic flexibility in the metallic regions may lead to larger fluctuating dipoles being induced.

The third point leads to multipolar terms beyond the pairwise approximation for the vdW energy, which cannot be included in its definition within vdW-DFT given in Eq. (2.60). The long-range electrostatic screening in metals, however, can be taken into account by the self-consistent screening (SCS) equations [Buč13b; Tka12],

$$\alpha_A^{\text{TS}+\text{SCS}}(i\omega) = \alpha_A^{\text{TS}}(i\omega) + \alpha_A^{\text{TS}}(i\omega) \sum_{B \neq A} \tau_{AB} \alpha_B^{\text{TS}+\text{SCS}}(i\omega). \quad (2.70)$$

Here, τ_{AB} is the dipole-dipole interaction tensor, and the frequency-dependent polarizabilities $\alpha_A^{\text{TS}}(i\omega)$ are defined in Eq. (2.61). The atomic C_6 coefficients in the TS+SCS method

are again computed from the Casimir-Polder integral

$$C_{6AA}^{\text{TS+SCS}} = \frac{3}{\pi} \int_0^\infty d\omega [\alpha^{\text{TS+SCS}}(i\omega)]^2. \quad (2.71)$$

As detailed in the next section, due to the inhomogeneity of the Ta(001)-p(3×3)-O surface supporting a static polarization texture, strong polarization and depolarization effects occur by taking into account the **SCS**. We would like to note that the **TS+SCS** method was defined for gapped systems, but irrespective of the conceptual problems due to delocalization (**vdW** interactions between nearby and overlapping regions), it has been applied to metallic systems as well (see Ref. [Buč13b] and references therein). According to experience, the imbalances in the assignment of **HI** charges to the atoms are strongly reduced, though.

We would like to mention a possible extension of the **TS+SCS/HI** method by the **many-body dispersion (MBD)** scheme **MBD@_{rs}SCS** (“rs” stands for range-separation) [Amb14; Buč16]. In this approach the general expression for the many-body correlation energy is separated into a short-range contribution, which is treated with common non-**vdW-DFT** functionals, and a long-range contribution (this goes along the definition of plasmons (cf. introductory part to Chpt. 4)). The long-range many-body correlations are accounted for by the **RPA** (Sec. 3.1), which, together with the adiabatic-connection fluctuation-dissipation theorem (ACFDT), provides an expression for the correlation energy in terms of the density-density response function. The latter is again given in terms of the **SCS** polarizabilities in Eq. (2.70). The density-density response function admits a multipole expansion of the correlation energy, in which the dipole part usually identified with **vdW** forces is dominant. In principle, this approach can thus account for the third type of non-additivity as given by the Dobson classification.

2.6 Application of the TS method to the Ta(001)-p(3×3)-O surface

The considerations made in Secs. 2.3 and 2.5, and especially the non-additivities listed in the Dobson classification, call for a thorough **GWA/RPA** treatment of the Ta(001)-p(3×3)-O surface (Sec. 3.1) [Har09; Har10; Ols13; Ren12; Sho16]. This system, however, appears nearly prohibitively complicated for such sophisticated computational approaches, and probably one needs to tune down the structure, that is, to consider perhaps a smaller superstructure (e.g., p(1×3)-O) or just a part thereof, to drop the mirror symmetry of the slab arrangement in the supercell, or to take into account less Ta layers. Before such an endeavour can be made, a **vdW-DFT** characterization and benchmark of the surface seem advisable.

2.6.1 Oxygen adsorption and tantalum reconstruction again

In anticipation of the experimental **STM** images (Fig. 2.1), where two different topographic p(3×3)-O patterns within the superstructure formation can be seen, relaxation of the O-reconstructed surface either has to be performed from two different starting configurations, or one obtains one of the relaxed configurations from the other by an intermediate modification of the surface. Both routes were found to be possible and led to the same result. First, starting from a perfect configuration in which the oxygens are flatly embedded within the Ta surface layer (Fig. 2.1g), a first configuration emerges upon relaxation,

| functional + $E_{\text{DFT}}/E_{\text{ads}}$ (eV) | trimer | state I (square-shaped) | | | state II (circle-shaped) | | |
|--|--|-------------------------|-----------|--------------|--------------------------|-----------|--------------|
| | | d (Å) | d_z (Å) | θ (°) | d (Å) | d_z (Å) | θ (°) |
| GGA+vdW -299.10/-6.25 (I) -301.65/-6.51 (II) | O _{side} - Ta _{side} | 1.95 | 1.22 | 102.48 | 1.97 | -0.08 | 184.63 |
| | O _{corner} - Ta _{corner} | 1.98 | 0.10 | 170.84 | 1.97 | 0.84 | 104.55 |
| | Ta _{side} - Ta _{corner} | 3.01 | 0.08 | 162.15 | 3.42 | -0.08 | 195.95 |
| | O _{side} - O _{corner} | 3.33 | 1.21 | 137.41 | 2.72 | -0.99 | 222.82 |
| | Ta _{centre} - Ta _{surface} | | -0.04 | | | -0.30 | |
| | Ta _{surface} - Ta _{subsurface} | | 1.65 | | | 1.61 | |
| | O _{surface} - Ta _{subsurface} | | 2.11 | | | 2.19 | |
| GGA+vdW(HI) -300.30/ - (I) -302.88/ - (II) | O _{side} - Ta _{side} | 1.95 | 1.22 | 102.56 | 1.96 | -0.11 | 184.82 |
| | O _{corner} - Ta _{corner} | 1.97 | 0.13 | 171.47 | 1.97 | 0.83 | 105.40 |
| | Ta _{side} - Ta _{corner} | 3.02 | 0.12 | 162.63 | 3.41 | -0.07 | 193.61 |
| | O _{side} - O _{corner} | 3.28 | 1.20 | 136.99 | 2.72 | -0.99 | 222.61 |
| | Ta _{centre} - Ta _{subsurface} | | -0.07 | | | -0.32 | |
| | Ta _{surface} - Ta _{subsurface} | | 1.68 | | | 1.61 | |
| | O _{surface} - Ta _{subsurface} | | 2.17 | | | 2.19 | |

Table 2.4: Ta(001)-p(3×3)-O superstructure parameters within vdW-DFT: Distances and angles within the O and Ta surface layers decomposed in trimers, together with distances between the surface layers and the first Ta interlayer (cf. Tab. 2.1). The notion is defined according to Fig. 2.1(g,h), and angles can be understood with help of Fig. 2.2(a,b); see Tab. 2.1 for further explanations. Results are listed for each DFT-vdW functional (TS+SCS method without (upper panel) and with HI algorithm (lower panel), cf. Sec. 2.5) together with the adsorption energies E_{ads} (definition in the text).

which we denoted by state I and termed “square-shaped”, as it leads to square-shaped protrusions in simulated STM topographies (Fig. 2.2c). Having obtained state I, during the adsorption process there will be additional oxygens trying to adsorb on the surface within an already established p(3×3)-O cell in the first configuration. Placing four additional oxygens around the tantalum in the centre of this cell (Ta_{centre}; see Figs. 2.1(g,h) for notion of individual atoms), connecting it with the respective side tantalums (Ta_{side}), and continuing the relaxation, state II, also denoted as “circle-shaped”, emerges and remains stable after removing the four additional oxygens. Placing one additional oxygen above Ta_{centre} does not lead to such a configurational transition, which means that a certain number of oxygens need to intermediately adsorb for the transition to occur. At lower temperatures the p(3×3)-O superstructure is preferred, so the additional oxygens will eventually desorb again [Tit85]. – The other route to obtain state II is by choosing another starting configuration for the relaxation. Shifting the flatly embedded oxygens by 1/4 of the bcc-Ta lattice constant into the surface and allowing the structure to relax leads to state II as well. However, oxygens do not penetrate into the bulk of Ta(001) [Dra73]. Sec. 2.4 contains yet another explanation for the occurrence of state II and for its rarity, the latter being connected with the instability of two neighbouring sp^3 oxygens along the [110] or $[1\bar{1}0]$ (two neighbouring O_{corner} in state II singled out); one of them drops immediately

into a nearby hollow position.

The adsorption energy for the oxygens is given in terms of the total energies by $E_{\text{ads}} = (E_{\text{Ta}(001)\text{-O}} - NE_{\text{O}} - E_{\text{Ta}(001)})/N$ with $N = 12$ the number of oxygens in the supercell. Tab. 2.4 reflects the same tendencies as already detailed in Sec. 2.4 (cf. Tab. 2.1), namely that the adsorption and total energies in state I are always smaller than in state II, irrespective of the energy functional being used. An explanation of these facts was given in Sec. 2.4 as well, and the conclusions made there are not modified by use of **vdW** functionals. The total-energy differences between the two states, I and II, are now increased, while in contrast to that the difference in the adsorption energies E_{ads} are smaller. This can be traced back to the different description of the clean Ta(001) surface and the single O atom within **vdW-DFT**. The total energies in **GGA+vdW** are lower as compared to the **GGA** results (Tab. 2.1) due to the attractive nature of the **vdW** forces, and in the **LDA** the total energies are the lowest. This order reflects the relation **GGA** \rightarrow **GGA+vdW** \rightarrow **LDA** explained in Ref. [Mar11], and is due to the known overbinding in the **LDA** (see also references in Sec. 2.4).

Tab. 2.4 also contains the relevant lattice parameters obtained from relaxation within **vdW-DFT**. Taking into account **vdW** interactions yields the same overall adsorption geometry as with plain **DFT** (cf. Tab. 2.1). As explained in Sec. 2.5, the free Ta(001) does not relax conclusively with the **HI** algorithm, so that adsorption energies could not be computed with the full **TS+SCS/HI** method, but the O-reconstructed Ta(001) accepted the algorithm. The **HI** algorithm takes into account charge transfer within the system, and adapts the **vdW** interaction parameters accordingly (Sec. 2.5).

The $\text{Ta}_{\text{surface}}\text{-Ta}_{\text{subsurface}}$ interlayer distances d_z arrange themselves along the mentioned **GGA** \rightarrow **GGA+vdW** \rightarrow **LDA** relation, so that **GGA+vdW** yields a slightly decompressed surface structure compared to the **LDA**. One is tempted to infer from state I and the $\text{O}_{\text{surface}}\text{-Ta}_{\text{subsurface}}$ distance that the **HI** algorithm tends to decompress the surface as well; however, this is just because of a slightly different positioning of the $\text{O}_{\text{corner}}\text{-Ta}_{\text{corner}}$ and $\text{Ta}_{\text{side}}\text{-Ta}_{\text{corner}}$ trimers (their triangles are slightly more erected); this tendency is only insignificantly exhibited by state II (if at all). The Ta-O bond lengths now lie between the **GGA** and the **LDA**, as with the Ta interlayer distances. The $\text{O}_{\text{side}}\text{-O}_{\text{corner}}$ distances are somewhat reduced in state I, especially with the **HI** algorithm. This latter fact can be explained by the repulsions between the O_{corner} , which become enhanced by stronger charge accumulation on oxygens. In state II the situation is more clear: The enhancement of the O_{corner} repulsion occurs only with the **HI** algorithm; this can be understood by looking at $\text{Ta}_{\text{corner}}^{\text{sub}}$, where now a strong charge accumulation appears in state II, so that the O_{corner} are further repelled. The Ta-O d_z distances are roughly in between the **LDA** and **GGA** for both states; the O-O d_z distances are reduced in state I, but in state II they are organized according to the binding trends of the functionals.

One can conclude that on the whole the **GGA+vdW** parameters interpolate between the ones of the **GGA** and the **LDA** according to the binding strength relation. The **HI** algorithm and the charge transfer mostly affect the oxygen interactions and modify the relative positions. The charge transfer enhances ionicity of all species, and there exists a complex interplay between repulsion and attraction between likewise and different species, respectively, and overall reduced chemical reactivity due to charge saturation.

We would like to note that there exists a third state in **GGA** due to the more flexible bonding structure. One obtains this state by shifting the oxygens by 1/4 of the bcc-Ta lattice constant from the flatly embedded positions into the vacuum ($d_z = 0.83 \text{ \AA}$ between O_{surface} and Ta_{surface}). Then they become elevated (1.14 \AA), but the d_z distance within the $O_{\text{side}}-O_{\text{corner}}$ trimer is only 0.16 \AA . Upon switching on the **vdW** forces within the **TS** method, and allowing the surface to relax again, this adsorption structure disappears and relaxes to state I. Simulated **STM** images of the third p(3×3)-O structure (not shown) do not match any pattern seen in experimental **STM** images. As this third configuration is not seen in experiment, it either cannot exist next to the other configurations, or **GGA** alone is inappropriate, and/or it underlines the necessity of taking into account **vdW** forces, or other additional effects, because it underestimates bonding.

2.6.2 Hirshfeld charges and polarization

| pattern | ion | $\Delta q_{\text{H}}^{(\text{TS})}$ | $\Delta q_{\text{HI}}^{(\text{TS})}$ | $\Delta q_{\text{HI}}^{(\text{TS}+\text{SCS})}$ |
|----------------------|-----------------------------------|-------------------------------------|--------------------------------------|---|
| state I (square) | O_{corner} | -0.309 | -0.407 | -0.443 |
| | O_{side} | -0.359 | -0.426 | -0.464 |
| | Ta_{corner} | 0.282 | 0.582 | 0.528 |
| | Ta_{side} | 0.176 | 0.386 | 0.323 |
| | Ta_{centre} | 0.112 | 0.406 | 0.266 |
| | $Ta_{\text{corner}}^{\text{sub}}$ | 0.283 | 0.472 | 0.386 |
| | $Ta_{\text{side}}^{\text{sub}}$ | 0.028 | 0.161 | 0.012 |
| | $Ta_{\text{centre}}^{\text{sub}}$ | -0.090 | -0.811 | -0.384 |
| state II (circle) | O_{corner} | -0.340 | -0.476 | -0.479 |
| | O_{side} | -0.301 | -0.430 | -0.430 |
| | Ta_{corner} | 0.317 | 0.615 | 0.618 |
| | Ta_{side} | 0.228 | 0.451 | 0.452 |
| | Ta_{centre} | -0.060 | 0.021 | 0.019 |
| | $Ta_{\text{corner}}^{\text{sub}}$ | -0.085 | -0.605 | -0.559 |
| | $Ta_{\text{side}}^{\text{sub}}$ | 0.093 | 0.136 | 0.323 |
| | $Ta_{\text{centre}}^{\text{sub}}$ | -0.108 | -0.552 | -0.530 |

Table 2.5: (Left) Hirshfeld charges (in units of e) computed within the **TS(+SCS)** method in **GGA+vdW** without (Δq_{H}) and with the **HI** algorithm (Δq_{HI}). The results were averaged within the same type of atoms in the supercell (Ta_{corner} , O_{side} , etc.). (Right) Hirshfeld charges as listed on the left for state I (top) and state II (bottom). Results for **TS** method in blue, for **TS/HI** in red, and for **TS+SCS/HI** in green.

The first conclusion from the various Hirshfeld charges (i.e., the differences from neutrality) listed in Tab. 2.5 is the charge transfer from the Ta(001) surface to the O adatoms. The oxygen Hirshfeld charges are smaller than the Bader charges (i.e., their differences from neutrality; Fig. 2.4 and Tab. 2.2), and some ionicities have different trends, but the overall result is the same. The discrepancies might be due to the **Bader charge analysis (BCA)** associating charge and atom in a rigid manner (see Ref. [Hen17] and references therein), while the Hirshfeld weights for each atom cover the whole space [Hir77]. The oxygens acquire the more charge, the more they are distant to the surface (due to regained

localization), while $\text{Ta}_{\text{corner}}$ always donates more charge than Ta_{side} , because the former has two adjacent O_{corner} . Note that the **BCA** tells the opposite story for the oxygens, because the charge of the oxygens located inside the Ta surface layer happens to be strongly compressed around their nuclei, and additionally the delocalized electrons from the Ta surface are associated with them. The Hirshfeld partitioning considers the region around $\text{Ta}_{\text{centre}}$ of state I depleted (in contrast to the **BCA**), while in state II it happens to be nearly charge neutral. In contrast to that, the central subsurface region $\text{Ta}_{\text{centre}}^{\text{sub}}$ is always charged, which leads to strongly enhanced dispersion coefficients (Tab. 2.6 and Fig. 2.10). While the original **TS** method leads here to a modest increase of charge, the **HI** algorithm predicts a strong accumulation, which is again slightly reduced by the **SCS**. To some extent, the allocations at the surface and subsurface layers can be traced back to an (artefact) **CDW** within the Ta(001) surface layers: Removing the oxygens, five layers remain in the supercell, which develop a layer-wise alternating **CDW** with positive Hirshfeld charges in the two outermost surface layers (already in **TS+SCS** without **HI** algorithm, but with values below $0.1e$). In contrast to that, the **BCA** on the free Ta(001) shows a gradual **CDW** with one period only, and assuming maxima at the two outermost layers. This allocation of Bader charges remains with oxygen adsorption, but the **HI** algorithm predicts a rather strong depletion around $\text{Ta}_{\text{centre}}$ in state I, while in case of state II there happens to be approximate charge neutrality, and, carrying more charge, the corresponding C_6 coefficients are very large here (Tab. 2.6 and Fig. 2.10).

The **TS** method predicts a well-balanced charge transfer within the surface layers of state I, only $\text{Ta}_{\text{corner}}^{\text{sub}}$ donates a considerable amount of its charge to its environment. In state II it is $\text{Ta}_{\text{side}}^{\text{sub}}$ which donates, while the others accept. The reason for the ionicities of the subsurface tantalums below the oxygen rows can be traced back to the oxygen ordering: The smaller the oxygen heights, the more they attract electrons from the subsurface, and not only from their adjacent tantalums of the surface layer. For example, in state II, $\text{Ta}_{\text{side}}^{\text{sub}}$ remains positively charged. This tendency is strongly enhanced by use of the **HI** algorithm, and slightly reduced by **SCS**.

Bučko *et al.* observed agreement between the **HI** and the Born effective charges for ionic crystals [Buč14]. As we detect in a similar vein tendencies in charge transfer which are well in line with “chemical intuition”, we may apply their relation to the Ta(001)-p(3×3)-O surface, which happens to exhibit prevailing ionic character against its metallicity. The square of oxygens in the 3×3 cell is supported by the positively charged tantalums of the surface and subsurface layers (except $\text{Ta}_{\text{corner}}^{\text{sub}}$ in state II), and this structure results in a permanent polarization texture of the surface. In state I this texture is more pronounced than in state II for two reasons: First, as it is negatively charged, $\text{Ta}_{\text{centre}}^{\text{sub}}$ might provide a compensation to the polarization, a property which is more pronounced in state II. And second, $\text{Ta}_{\text{corner}}^{\text{sub}}$ is additionally negative here. In principle, such a permanent polarization texture may lead to **vdW** contributions as well, in particular, to the Keesom and to the Debye forces. The Keesom force describes the surface as stabilizing its own polarization texture, especially in state I, where the square of permanent polarization leads to a dipole in the central region around $\text{Ta}_{\text{centre}}$ with reversed orientation. And the Debye force renders the surface experiencing self-interactions by inducing dipole moments locally, again especially in the central region. Both forces, together with the usual London forces included

in **vdW-DFT**, will provide important mechanisms for the understanding of the adsorption of other atoms and molecules on the surface as well as for the surface structure itself.

2.6.3 Dispersion coefficients

The next computational results to be discussed are the dispersion coefficients displaying in detail the actual **vdW** physics of the Ta(001)-p(3×3)-O surface (Tab. 2.6 and Fig. 2.10). All three approaches within the **TS** method led to the same result for the charge order within the surface, while this is not the case for the dispersion coefficients. As mentioned in Sec. 2.5, in the original **TS** method, the dispersion coefficients for the oxygens come out slightly smaller than the free reference values or are unchanged, although they acquire charge, and the region around $\text{Ta}_{\text{centre}}$ shows the reverse tendency. To some extent, the same problem appears within the subsurface layer, and in general, all dispersion coefficients are near their free reference data.

The situation is slightly cured in employing the **HI** algorithm, and now the values for the dispersion coefficients are in line with the charge transfer, the local environments, and the geometry (especially as regards the extended lone pairs on oxygens): the oxygens possess increased values, and the surface tantalums decreased ones. Not shown here are the results of the **BCA** for the effective atomic volumes $\propto R^3$ (Bader volumes/radii), which for the oxygens located within the Ta surface layer in both states, I and II, are roughly the same as in the **TS** and **TS/HI** methods, but for the elevated oxygens come out as one magnitude larger. This property is not reflected in the dispersion coefficients, and, in view of the proportionality between the **vdW** radii and (static) polarizabilities in Fig. 2.10, this either means that the polarizabilities for the elevated oxygens might be much larger than predicted by the **TS** method and its extensions, or that their charge accumulation tends to reduce local dynamics and electronic mobility.

Indeed, in taking into account electrostatic screening effects in metals via **SCS**, all dispersion coefficients for the surface layers are strongly decreased, while the subsurface layer shows a more moderate response. In general, screening appears strongly enhanced at the surface, and reduces the **vdW** interaction considerably. Increase of screening at metal surfaces compared to bulks has already been realized in **cRPA** studies on the Coulomb interaction [Şaş12]. **SCS** reduces the **vdW** radii and polarizabilities of the oxygens stronger than the ones of the tantalums, which might be an effect of combined oxygen ionicity and electronic delocalization (localized charge becomes inert and screened). The C_6 coefficients, however, are not just as strongly reduced, which means that the tails of the polarizability coefficients, and thus the dispersive character of the **vdW** interactions, are important. The $\text{Ta}_{\text{centre}}^{\text{sub}}$ region receives very large C_6 coefficients in both states, I and II, which might thus be a favourable region for polarizable adatoms to adsorb. In state II, the $\text{Ta}_{\text{corner}}^{\text{sub}}$ region might also be favourable for adsorption, but here that might be challenged by the complicated and stronger multipolar environment given by the specific oxygen arrangement, and especially by the strongly reduced dispersion coefficients of the oxygens themselves.

According to Tab. 2.6, all tantalum C_6 coefficients in the **TS+SCS/HI** approach are by one or two magnitudes larger compared to the values for the oxygens. To get a feeling for the adsorbate affinity resulting from these values, let C and α be the C_6 coefficient and polarizability of an atom trying to adsorb on the surface. The C_6 coefficient for the

| pattern | ion | $R_{\text{H}}^{(\text{TS})}$ | $R_{\text{HI}}^{(\text{TS})}$ | $R_{\text{HI}}^{(\text{TS}+\text{SCS})}$ | $C_{6,\text{H}}^{(\text{TS})}$ | $C_{6,\text{HI}}^{(\text{TS})}$ | $C_{6,\text{HI}}^{(\text{TS}+\text{SCS})}$ | $\alpha_{\text{H}}^{(\text{TS})}$ | $\alpha_{\text{HI}}^{(\text{TS})}$ | $\alpha_{\text{HI}}^{(\text{TS}+\text{SCS})}$ |
|-----------|-------------------------------------|------------------------------|-------------------------------|--|--------------------------------|---------------------------------|--|-----------------------------------|------------------------------------|---|
| free | O | 3.194 | | | 15.60 | | | 5.40 | | |
| reference | Ta | 4.157 | | | 1019.92 | | | 82.53 | | |
| state I | O _{corner} | 3.181 | 3.256 | 1.692 | 15.23 | 17.53 | 13.09 | 5.34 | 5.72 | 0.80 |
| (square) | O _{side} | 3.190 | 3.254 | 1.808 | 15.49 | 17.47 | 9.87 | 5.38 | 5.72 | 0.98 |
| | Ta _{corner} | 4.129 | 4.036 | 3.175 | 978.23 | 854.65 | 496.93 | 80.83 | 75.54 | 36.76 |
| | Ta _{side} | 4.167 | 4.110 | 3.318 | 1034.06 | 951.71 | 533.61 | 83.10 | 79.72 | 41.93 |
| | Ta _{centre} | 4.187 | 4.114 | 3.346 | 1064.99 | 957.48 | 527.86 | 84.33 | 79.96 | 43.04 |
| | Ta _{corner} ^{sub} | 4.203 | 4.133 | 3.639 | 1089.01 | 984.32 | 818.03 | 85.28 | 81.08 | 55.37 |
| | Ta _{side} ^{sub} | 4.249 | 4.248 | 3.929 | 1162.53 | 1160.56 | 1164.87 | 88.11 | 88.04 | 69.68 |
| | Ta _{centre} ^{sub} | 4.269 | 4.474 | 4.213 | 1194.90 | 1628.52 | 1706.75 | 89.33 | 103.43 | 85.89 |
| state II | O _{corner} | 3.175 | 3.252 | 1.657 | 15.06 | 17.40 | 10.56 | 5.31 | 5.70 | 0.75 |
| (circle) | O _{side} | 3.189 | 3.260 | 1.675 | 15.46 | 17.66 | 13.63 | 5.38 | 5.75 | 0.78 |
| | Ta _{corner} | 4.135 | 4.031 | 3.113 | 987.87 | 846.98 | 399.52 | 81.22 | 75.21 | 34.67 |
| | Ta _{side} | 4.162 | 4.087 | 3.244 | 1026.93 | 920.54 | 503.20 | 82.81 | 78.46 | 39.20 |
| | Ta _{centre} | 4.256 | 4.248 | 3.696 | 1174.18 | 1160.10 | 1006.64 | 88.55 | 88.02 | 58.01 |
| | Ta _{corner} ^{sub} | 4.259 | 4.485 | 4.261 | 1178.15 | 1607.34 | 1784.03 | 88.70 | 103.61 | 88.87 |
| | Ta _{side} ^{sub} | 4.243 | 4.216 | 3.917 | 1152.25 | 1108.53 | 1147.90 | 87.72 | 86.04 | 69.03 |
| | Ta _{centre} ^{sub} | 4.270 | 4.469 | 4.211 | 1197.49 | 1574.05 | 1761.88 | 89.43 | 102.55 | 85.72 |

Table 2.6: Dispersion coefficients (vdW radii, C_6 coefficients, and static polarizabilities) computed from the **TS(+SCS)** method in **GGA+vdW** without (R_{H} , etc.) and with (R_{HI} , etc) the **HI** algorithm (cf. Sec. 2.5). Free reference values are listed in the first two rows. Units: R (Å), C_6 (eV·Å⁶), α (Å³).

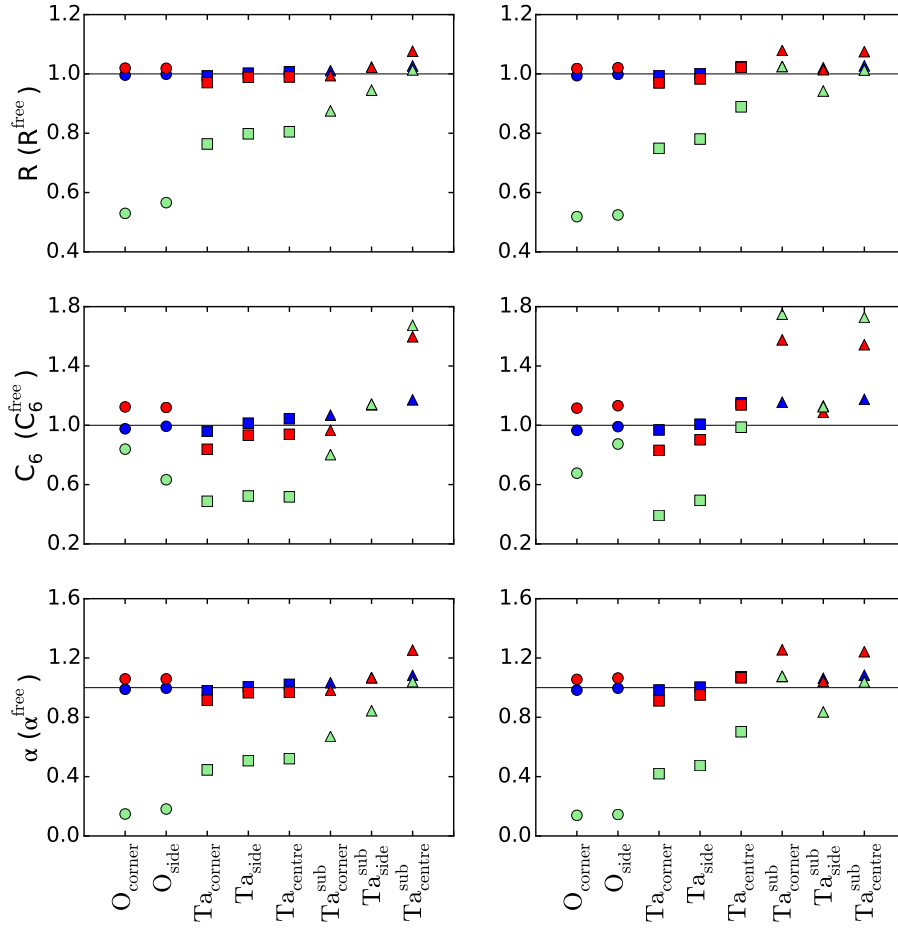


Figure 2.10: Dispersion coefficients: vdW radii, C_6 coefficients, and static polarizabilities in units of their free reference data, see Tab. 2.6. Left column for state I, right column for state II. Results for TS method in blue, for TS/Hi in red, and for TS+SCS/Hi in green.

pair comprising adatom and $\text{Ta}_{\text{centre}}$, or adatom and O_{corner} , respectively, are given by (Eq. (2.61))

$$C_6 \approx \frac{2}{\frac{0.0815}{\alpha} + \frac{\alpha}{43.03C}},$$

$$C_6 \approx \frac{2}{\frac{0.0061}{\alpha} + \frac{\alpha}{0.80C}}. \quad (2.72)$$

The first C_6 coefficient is by more than one magnitude larger than the second. Thus, the vdW energy contributions (Eq. (2.60)) from the $\text{Ta}_{\text{centre}}$ region will more effectively lower the total DFT energy than the oxygen rows, and the adatom is likely to adsorb in the centre of the 3×3 plaquette. As mentioned, however, the complex static dipole/multipole texture of the Ta(001)-p(3×3)-O surface will influence the adsorption quite strongly as well.

Finally, we note once more again, that spin and charge fluctuations are not included in Eq. (2.60), yet they are assumed to be important for the adsorption of atoms and molecules.

CHAPTER 3

QMC solution of the AIM and the Co/graphene system

In Chpt. 2 we saw that **DFT** is a highly sophisticated approach for the determination of the **GS** of real materials and many of its properties. Albeit it appears sometimes limited in its capabilities to explain various physical or chemical properties or structures, mostly related to excitations, long-range order or interactions, or quantum-chemical effects, in the case of the Ta(001)-p(3×3)-O surface it provided at least the basis for an interpretation of the **STM** images and the reconstructions in quantum-chemical terms beyond its own domain of applicability. In particular, it captured the charge transfer only partially and described the surface as rather metallic (albeit the charge redistribution could be seen in the electronic structure and the charge analysis results). In contrast to that, experimentally the charge transfer manifested itself in a wide band gap seen everywhere on the surface, so that quantum-chemical (molecular) interpretations are applicable. **DFT** exhibited certain tendencies of the Ta(001)-p(3×3)-O surface in its results for the electronic structure, such as aligned hybridization peaks or bonding and anti-bonding peaks in the **LDOS**, but an interpretation in terms of lone pairs in sp^3 -hybridized oxygen orbitals or bonding and anti-bonding dipoles, respectively, is beyond the immediate **DFT** description. One of the “predictions” made in Secs. 2.4 and 2.6 - the adsorption site for polarizable atoms and molecules on the Ta(001)-p(3×3)-O surface being in the centre of the 3×3 plaquette defined by the oxygen rows - was already observed before for Fe adatoms [**Cor17**] (albeit the true adsorption site was unclear at that time because the clean surface was not identified). This is rather unintuitive because iron is expected to approach the already adsorbed oxygens in favour for binding to the surface (via polar covalent or ionic Fe-O bond).

Furthermore, the **STM** images in Ref. [**Cor17**] suggest unusual top-site adsorption, directly above the central Ta surface atom of the 3×3 plaquette. In adsorption calculations based on the setup of Sec. 2.5, **vdW-DFT** was at least able to maintain the Fe lateral position after it has been positioned directly above Ta_{centre} (it did not remain geometrically exactly at the top position, though), but it was not found to be stable upon small lateral displacement perturbations. In contrast to that, without **vdW** interactions the Fe adatom directly dropped into one of the nearby hollow positions. Thus, there should be additional interactions present in the system being relevant for the adsorption of atoms and molecules. Even though the application of semi-empirical **vdW-DFT** points to the relevance of such additional interactions, the results were not conclusive.

DFT is a **MF** (static) approach to correlations (cf. introductory part of Chpt. 2 and Subsec. 2.1.4), but many interpretations of the experimental (**STM**, **STS**) and computational (up to semi-empirical **vdW-DFT**) results on the Ta(001)-p(3×3)-O surface indicate the

presence of fluctuations beyond the MF approximation (Secs. 2.4-2.6). In particular, the quantum-chemical concept of lone pairs residing in sp^3 -hybridized orbitals of chemisorbed oxygen and polarizing their substrate environment (Sec. 2.4) cannot be appropriately represented in DFT. As mentioned in Sec. 2.3, it is currently believed that charge and spin fluctuations are necessary to stabilize the Fe adatom in the centre of the 3×3 plaquette. That means, amongst others, that vdW interactions have to be taken into account beyond the semi-empirical approximation. The most relevant charge fluctuations are dipolar excitations, and these happen to be correlated with dipolar excitations on approaching polarizable atoms and molecules. These correlations lead to London dispersion forces, and they result in two distant fluctuating dipoles interacting attractively with each other (Sec. 2.5). But one may assume higher multipoles being relevant as well if one looks at the C_{4v} local symmetry of Ta_{centre} (or its even more complicated symmetry w.r.t. the full oxygen arrangement). Such multipoles might, for example, be accounted for by the $MBD@_{rs}SCS$ approach mentioned in Subsec. 2.5.2, or by the encompassing RPA or GWA introduced below (Sec. 3.1).

The consideration of correlations is essential in condensed matter systems, especially in the ones with pronounced inhomogeneities. As mentioned in Subsec. 2.1.4, the ionic lattice tends to localize the electrons around its heavier elements. While the kinetic energy of the electrons becomes larger (being in turn balanced by an enhancement of the negative potential energy), the kinetic energy of the QPs emerging from the localization is small, and thus they appear in narrow bands near the Fermi surface [Geo04]. The localized electrons, now forced to be near each other, happen to be strongly fluctuating and correlated, so that a strong renormalization of the DFT electronic structure can be expected.

All ingredients for the correlations are contained in the basic second-quantized condensed-matter Hamiltonian given in Eq. 2.1, and instead of trying to account for the two-particle Coulomb interaction part by ever more sophisticated, but probably indeterminable DFT(+U)-XC functionals (Secs. 2.1.2 and 2.1.4), one may try to consider the (time-like) fluctuations by an energy-dependent potential, the so-called self-energy, thereby realizing again a single-particle description, but with taking into account the many body correlation effects [Sza96]. In single-particle quantum mechanics the GF has poles at the EVs of the Hamiltonian. Within the independent-particle description of HF theory, the GF is given by

$$G_0(x, x', E) = \sum_a \frac{\chi_a(x)\chi_a^*(x')}{E - \varepsilon_a}, \quad (3.1)$$

where the sum runs over all occupied and unoccupied states, and ε_a is the energy of the HF orbital $\chi_a(x)$ with x comprising space and spin indices. In the full CI beyond the HF approximation the GF contains all the many body correlation and relaxation effects, while the single-particle picture is retained. This represents a systematic improvement of Koopman's theorem. In particular, the full GF exhibits the exact ionization potentials and electron affinities of the N -particle system. For the excitation spectrum of the N -electron system, however, one needs the two-particle many body GF describing particle-hole pairs within linear-response theory, but these objects will not be considered in the present thesis

(a two-particle GF appears in Eq. (3.20), though).

To acknowledge the GF formalism, one may compare it order-by-order within quantum-mechanical perturbation theory (PT) for the correlation energy [Sza96], that is, within the Møller-Plesset PT, which is given by the Ruelle-Schrödinger PT together with the decomposition of the full Hamiltonian in the form

$$\hat{H} = \hat{H}_0 + \hat{V} = \sum_i \hat{f}(i) + \sum_{i<j} \frac{1}{\hat{r}_{ij}} - \hat{V}_{\text{HF}}, \quad (3.2)$$

where the one-particle terms are given by the single-particle HF terms, $\hat{f}(i) = \hat{h}(i) + \hat{V}_{\text{HF}}(i)$ (cf. Eq. (2.2)), and with $\hat{V}_{\text{HF}} = \sum_i \hat{V}_{\text{HF}}(i)$ subtracted from the two-particle Coulomb interaction (both are included in the two-particle term \hat{V}). In this way the meaning of fluctuations around the MF approximation becomes again readily apparent. As in the DFT+U approach (Subsec. 2.1.4), it is the fluctuations around the HF-MF value which modify the total energy, and the PT will be an expansion in the fluctuations around that MF value. At zeroth order in PT the EV equation is given by

$$\hat{H}_0|\Psi_0\rangle = E_0^{(0)}|\Psi_0\rangle = \left(\sum_a \varepsilon_a\right)|\Psi_0\rangle, \quad (3.3)$$

where $|\Psi_0\rangle$ is the determinantal HF-GS constructed from the HF orbitals $\chi_a(i)$, and ε_a the orbital energies, see Eq. (3.1). The energy to first order is then given by

$$E_0^{(1)} = \langle\Psi_0|\hat{V}|\Psi_0\rangle = -\frac{1}{2}\sum_{ab} (\langle\chi_a\chi_b|\hat{V}|\chi_a\chi_b\rangle - \langle\chi_a\chi_b|\hat{V}|\chi_b\chi_a\rangle), \quad (3.4)$$

and thus the HF energy by $E_0^{(0+1)} = E_0^{(0)} + E_0^{(1)}$. At second order in PT one obtains

$$E_0^{(2)} = \sum_n' \frac{|\langle 0|\hat{V}|n\rangle|^2}{E_0^{(0)} - E_n^{(1)}}, \quad (3.5)$$

where the sum runs over doubly excited states $|n\rangle = |\Psi_{ab}^{rs}\rangle$ only (excluding the GS), which are given by the EV equation $\hat{H}_0|\Psi_{ab}^{rs}\rangle = (E_0^{(0)} - (\varepsilon_a + \varepsilon_b - \varepsilon_r - \varepsilon_s))|\Psi_{ab}^{rs}\rangle$ (electrons in states a and b are excited into states r and s). Rewriting gives

$$E_0^{(2)} = \frac{1}{4}\sum_{abrs}' \frac{|\langle\chi_a\chi_b|\hat{V}|\chi_r\chi_s\rangle - \langle\chi_a\chi_b|\hat{V}|\chi_s\chi_r\rangle|^2}{\varepsilon_a + \varepsilon_b - \varepsilon_r - \varepsilon_s}. \quad (3.6)$$

This is the first relevant correction to the HF energy. One may note at this point, that HF theory does not exhibit any structures which can be related to a diagrammatic representation, while PT does. Furthermore, PT is a simpler way to improve HF theory for larger systems instead of the CI, which is either always limited to small basis sets or small molecules, or in need for some truncations for it to be computable [Sza96].

The exact many body **GF** for an N -particle system is given by [Sza96]

$$(G(E))_{ij} = \sum_m \frac{\langle {}^N\Phi_0 | \hat{a}_i^+ | {}^{N-1}\Phi_m \rangle \langle {}^{N-1}\Phi_m | \hat{a}_j | {}^N\Phi_0 \rangle}{E - ({}^N E_0 - {}^{N-1} E_m)} + \sum_m \frac{\langle {}^N\Phi_0 | \hat{a}_j | {}^{N+1}\Phi_m \rangle \langle {}^{N+1}\Phi_m | \hat{a}_i^+ | {}^N\Phi_0 \rangle}{E - ({}^{N+1} E_m - {}^N E_0)}. \quad (3.7)$$

Here, the sums run over all occupied and unoccupied states of the excited system, and $|{}^N\Phi_0\rangle$ is the exact full **CI-GS-WF** with **HF** spin-orbitals of the N -particle system. The energies are given by ${}^M E_k = \langle {}^M\Phi_k | \hat{H} | {}^M\Phi_k \rangle$, and these are the exact energies of the ground and excited states. The effects of correlations, given by correlated fluctuations around the **MF** approximation, can be seen from the **GF** perturbation expansion which is algebraic in energy, that is, from the Dyson equation

$$G(E) = G_0(E) + G_0(E)\Sigma(E)G(E), \quad (3.8)$$

with $G_0(E)$ given as in Eq. (3.1). The Dyson equation is a matrix equation in spin-orbital space, and it defines the self-energy $\Sigma(E)$ as the quantity containing the correlation effects, which after reordering shows itself as the already mentioned energy-dependent potential: $G^{-1}(E) = G_0^{-1}(E) - \Sigma(E)$. The self-energy can be represented by a perturbation expansion, $\Sigma(E) = \Sigma^{(2)}(E) + \Sigma^{(3)}(E) + \dots$, where the second order is given by

$$\begin{aligned} \Sigma_{ij}^{(2)}(E) &= \frac{1}{2} \sum_{ars} \frac{\langle \chi_r \chi_s | \hat{V} (|\chi_i \chi_a\rangle - |\chi_a \chi_i\rangle) \langle \chi_j \chi_a | \hat{V} (|\chi_r \chi_s\rangle - |\chi_s \chi_r\rangle)}{E + \varepsilon_a - \varepsilon_r - \varepsilon_s} \\ &+ \frac{1}{2} \sum_{abs} \frac{\langle \chi_a \chi_b | \hat{V} (|\chi_i \chi_r\rangle - |\chi_r \chi_i\rangle) \langle \chi_j \chi_r | \hat{V} (|\chi_a \chi_b\rangle - |\chi_b \chi_a\rangle)}{E + \varepsilon_r - \varepsilon_a - \varepsilon_b}, \end{aligned} \quad (3.9)$$

where some terms have been factored out for conciseness. The second-order self-energy may now be compared with Eq. (3.6) for the second-order energy, both having a similar structure. As in the many body **PT** beyond the **HF** approximation, where the **HF** energy becomes improved at second order, the first term in the expansion of the self-energy appears at second order.

Both, the **GF** method and the quantum-mechanical **PT**, may be compared at second order by considering the ionization potential given by the corrected orbital energy [Sza96]

$$\varepsilon'_c = \varepsilon_c + \Sigma_{cc}^{(2)}(\varepsilon_c) = {}^N E_0^{(0+1+2)} - {}^{N-1} \tilde{E}_0^{(0+1+2)}(c), \quad (3.10)$$

where the tilde denotes the fact that the energies are defined with respect to the N -particle system (i.e., the N -particle **HF** Hamiltonian is not used to calculate ${}^{N-1} \tilde{E}_0^{(0+1+2)}(c)$). Thus, the lowest relevant order in the **GF** formalism, that is, the expansion of the self-energy up to second order, is identical to the lowest non-trivial order in **PT**. This can be written

down formally as

$${}^N E_0^{(2)} - {}^{N-1} \tilde{E}_0^{(2)}(c) = \Sigma_{cc}^{(2)}(\varepsilon_c). \quad (3.11)$$

In that way, the ionization potentials are corrected by effects of relaxation of the $(N - 1)$ -particle system upon the removal of a particle from the N -particle system (i.e., it goes beyond the frozen-orbital approximation of HF theory, cf. introductory part of Chpt. 2). The relaxations stabilize the $(N - 1)$ -particle system. Furthermore, the corrected ionization potentials contain the correlations in the $(N - 1)$ -particle system (negative in energy due to relaxing effect), and the ones in the N -particle system (positive in energy), which, together with the relaxations, stabilize the N -particle relative to the $(N - 1)$ -particle system.

Most condensed matter systems containing atoms with open d or f shells turn out to be strongly correlated. The delocalization of electrons due to their kinetic energy competes with their localization due the Coulomb interaction (cf. Sec. 3.2), and in bulk-like systems or repetitive arrangements that interplay is theoretically described by the Hubbard model [Hub63] (which can essentially be obtained from Eq. (2.1) by a tight-binding-like transformation to local orbitals covering all sites [Kar13; Kor08; Kov10; Kun11]). A set of numerical techniques for the solution of the Hubbard model is available; here, and more technically in Subsec. 3.2.1, we shortly discuss the DMFT approach, see Ref. [Geo96] and references therein, which treats exactly the *local* electronic correlations. A full description taking into account non-local correlations is still a numerical challenge, and we will not discuss non-local effects in the present thesis (besides the ones from the vdW interactions which have been discussed in Chpt. 2, cf. 2.5), except mentioning here again the dual-fermion and dual-boson approaches [Rub12; Rub09], which aim at the solution of the Hubbard model beyond the local approximation.

As explained in the introduction (Chpt. 1), and in the introductory part of Chpt. 2, the present thesis aims at a description of real materials and their (local) correlations. Usually, the theoretical description of electronic and magnetic properties of real materials starts with DFT (Chpt. 2, Sec. 2.1), which provides the electronic structure within an effective single-particle MF picture. DFT also provides the necessary ingredients for a projection procedure from continuous energy band states onto discrete local orbital states placed at the correlated sites of the real material. These sites can subsequently be studied within a full many body description while still taking into account their hybridization with the rest of the system. The projection onto the local orbitals provides realistic *ab-initio* parameters of an AIM (Sec. 3.2), which in turn provides the basis for a self-consistent description of the Hubbard model for bulk-like systems. The AIM alone can be used for a single or a set of correlated adatoms or nanosystems on a substrate surface, or for single impurities immersed in a solid bulk (cf. Chpt. 1).

As the present thesis belongs to the realm of computational condensed matter theory, a small overview of the methods for calculating the relevant many body quantity in correlated materials, the GF together with the self-energy, is indicated [Gul11]. In Sec. 3.3 the hybridization expansion variant of the CTQMC method will be explained in more detail, which is at the heart for the solution of AIMS describing strong correlations [Bea96; Gul08; Gul11; Pro96; Rub05]. CTQMC provides an encompassing method incorporating

all AIM energy scales, that is, it does not have to be confined to particular regions within the parameter space (but it has numerical problems at very high or low temperatures, and the more fundamental sign problem); it can be employed on various and general classes of models, and at present is capable of providing the full solution of five(d)- and even seven(f)-orbital AIMS. Together with the self-consistent DMFT embedding of the AIM into the Hubbard model (cf. Subsec. 3.2.1, and references below), CTQMC is one of the most important theoretical companions to experimental studies in nanoscience.

The price ones often pays for the CTQMC solution, however, is the fixing of the AIM parameters after the projection onto the local orbitals has been performed. Two approaches go beyond that approximation: First, there are the charge-self-consistent DFT+AIM(DMFT) extensions containing feedback loops between the DFT calculation and the AIM solution (Subsec. 3.2.1), so that correlations are incorporated into the AIM parameters [Pou07; Sav04]. Second, the GWA and the cRPA (Sec. 3.1 and Subsec. 3.1.2) yield frequency-dependent Coulomb interactions due to dynamical screening, so that the fixing of the AIM parameters means to limit oneself to the static Coulomb interaction part and neglect retardation. In principle, one can extend the AIM solution to account for this frequency dependence (e.g., in the context of GW+DMFT [Bie03; Hel11; Sun02]), and see that it may have effects on the spectral high-energy satellite structures (plasmonic or other collective excitations) as well as on the low-energy physics [Ary04; Cas12; Han13b; Kau17; Shi17b; Wer12]. – In the following we will restrict ourselves to the AIM with static parameters and its CTQMC solution, as the low-energy physics may assumed to be determined to a large extent by the low-energy (static Coulomb interaction) parameters.

CTQMC works in imaginary-time space (after Euclidean rotation of equilibrium action and path integral measure), and thus needs a subsequent analytical continuation of its solution back to real times where the observables are physical. The analytical continuation of QMC data is an ill-defined problem due to the inherent numerical noise (so that there are infinite many solutions), and sophisticated approaches like stochastic optimization method (SOM) (Sec. 3.4) poses another computational effort following the sometimes rather expensive DFT and CTQMC calculations. Furthermore, next to the CTQMC temperature limitations, there may appear problems in resolving the low-energy physics of various systems, where, however, often the interesting quantum behaviour accompanied by spectral renormalizations occurs. Yet, Chpt. 4 on the multi-orbital Kondo effect shows that the implementations of the CTQMC algorithm within the Toolbox for Research on Interacting Quantum Systems (TRIQS) (cf. Sec. 3.3) and the analytical continuation via the SOM (Sec. 3.4) are rather powerful in resolving the low-energy features (the Kondo resonance) at an inverse temperature as high as $\beta = 200 \text{ eV}^{-1}$. Test calculations even suggest that within the multi-orbital Kondo regime (of realistic systems away from half-filling) one could even go as high in inverse temperature as $\beta = 300\text{--}400 \text{ eV}^{-1}$.

The major competitors to QMC are the numerical renormalization group (NRG) [Cos15; De 05; Han13a; Sta15; Wil75], the density-matrix renormalization group (DMRG) [Hal04; Hal06; Sch05], and the exact diagonalization (ED) [Lu17]. NRG lays a logarithmic discretization of the substrate energy spectrum underneath an iterative diagonalization of the AIM Hamiltonian, thereby realizing the idea of the running coupling constants while successively integrating out the high-energy DOF, see Sec. 4.5. The DMRG is similar,

reduces the effective **DOF** to the ones relevant for the low-energy features, and isolates the states lying there. Both methods work in real-time and real-energy space, are naturally designed as to properly resolve the ground and low-lying states of the system, and work well at very low and even vanishing temperatures, where most experiments are performed and the quantum effects are fully developed and prevail. The shortcomings of these two methods is in their difficulties in going beyond the **AIM** and the Hubbard model, and in their limitations to rather small energy ranges around the Fermi level. Satellite and high-energy structures away from the low-energy regime thus cannot be resolved with these two methods. Furthermore, even though there exist **NRG** and **DMRG** implementations and solutions for multi-orbital **AIMs**, up to now the number of orbitals was always rather limited, for the calculations are very demanding and sometimes need the exploration or imposition of symmetries reducing the generality of the model. For example, at most three-orbital **AIMs** could be solved with the **NRG** so far [Cos15; De 05; Han13a; Sta15], but recent progress has been achieved in extending its domain of applicability to spherically symmetric Kanamori-Coulomb interactions and the **SOC** [Hor17]. – **ED** (or, more precisely, the Lanczos method [Lan50]) also first discretizes the non-interacting substrate **DOF**, and subsequently diagonalizes the resulting Hamiltonian. While that procedure works well for overall rather metallic behaviour, like in the Co/graphene system to be considered in Sec. 3.6, it obviously cannot achieve a proper description of the low-energy physics, as that relies on a precise resolution of the substrate energy spectrum in this region.

CTQMC is a successor to the **QMC** procedure developed by Hirsch and Fye in 1986 [Hir86]. **Hirsch-Fye QMC (HFQMC)** discretizes the imaginary-time interval $[0, \beta)$ in equally spaced portions $\Delta\tau = \beta/M$, performs a Hubbard-Stratonovich transformation of the partition function on each time slice, thereby introducing 2^M auxiliary Ising spin variables, and finally performs a trace over this 2^M -dimensional spin space to evaluate the partition function. In principle this procedure resembles the mathematical definition of the partition function. It is clear that such a procedure becomes excessively heavy for multi-orbital **AIMs**, as each orbital is assigned a time interval, and there may occur equilibration issues during sampling [Gul11]. Furthermore, there are regions in imaginary-time space being actually more relevant for the calculation and the physics than others, but all regions are treated likewise. For example, the region around $\tau = \beta/2$ is important for the low-energy physics, while the borders of the imaginary-time interval exhibit discontinuities with strong decreases of the **GF**. Both issues are met only with a very fine imaginary-time grid, because in **HFQMC** the discretization is homogeneous. **CTQMC** does not rely on such a discretization and automatically considers important regions in imaginary time as well as in other directions of the parameter space (Sec. 3.3).

CTQMC is a diagrammatic perturbation theory with a stochastic sampling of the Feynman diagrams appearing in the expansion of the partition function, and a versatile tool for a realistic substantiation of experimental results [Gul11] (cf. Sec. 4.6, where solving the five-orbital **AIM** for the $\text{CoCu}_n/\text{Cu}(111)$ systems with *ab-initio* parameters from **DFT** produced the substructures of the Kondo feature observed experimentally, Sec. 4.6). The **CTQMC** employed in Secs. 3.6 and 4.6 is organized as a **continuous-time hybridization expansion (CTHYB)**, also called strong-coupling expansion, because the Coulomb interaction is assumed stronger than the hybridization coupling and thus treated

non-perturbatively (albeit **CTQMC** on the whole yields a numerically non-perturbative result). If the Coulomb interaction is weaker than the hybridization, which applies to weakly correlated and rather metallic materials, the weak-coupling expansion in the Coulomb interaction (**CTINT**) is more appropriate. For fermionic lattice models and **cDMFT** an additional auxiliary-field decomposition can be introduced (**CTAUX**). Performing a **Schrieffer-Wolff (SW)** transformation of the **AIM** Hamiltonian, one obtains the Kondo model (cf. Sec. 4.5) with high-energy states folded down onto low-energy states which become thus renormalized. The Kondo model belongs to the more general class of Coqblin-Schrieffer models, in which charge fluctuations are suppressed and degeneracies become important. For these the **CTJ** algorithm can be employed, where the coupling J describes the exchange between the degenerate states and the substrate.

For correlated real materials the strong-coupling expansion **CTHYB** and its use within **DMFT** is most appropriate. Fed with *ab-initio* parameters from a projection of **DFT** energy bands onto the impurity states, local correlations can thereby be considered thoroughly and realistically, see Refs. [Ama08; Ani97b; Dan14; Geo04; Gul11; Hau10; Hel07; Hel08; Kot06; Lec06; Nek13; Pau19; Pav14; Pav11; Pou07; Tom12; Zin16] for a selection. For non-local correlations one may use **CTHYB** within extensions to **DMFT**, such as multi-site **cDMFT** (see Ref. [Gul11] and references therein), or dual-fermion and dual-boson approaches [Rub12; Rub09] (see also discussion and references in Subsec. 2.1.3). For the susceptibility, excited-state properties, or assessment of phase boundaries one may use **CTHYB** to calculate four-point correlation functions (higher-order **GFs**); **QP** dynamics, thermal crossover in heavy-fermion materials, and also non-equilibrium problems can be addressed within **CTHYB** or other versions of **CTQMC**, see Ref. [Gul11] and references therein. The present thesis considers the simple case of local correlations on single impurities, such that no extensions to the **AIM** like **DMFT** or beyond are needed.

In Sec. 3.1 the **GWA** is introduced, which is a **GF** method applied to solids capable to describe excitations and to provide a realistic numerical assessment of the Coulomb interaction matrix in the system in the **cRPA** (Subsec. 3.1.2). First definitions of the **GF** and the spectrum are provided in Subsec. 3.1.1. In Sec. 3.2 the **AIM** is introduced, which fully encompasses the local Coulomb correlations. The connection to real-material data is provided in Subsec. 3.2.1. The **AIM-GF** is computed via a particular variant of the quantum Monte Carlo (QMC) method to be discussed in Sec. 3.3. The **AIM-GF** is computed on the imaginary-time axis, and for the spectrum an analytical continuation to real energies has to be performed; this is realized by the **SOM**, to be explained in Sec. 3.4. The Co/graphene system was subject to the **DC** problem, which is explained in more detail in Appx. C.1. Finally, Sec. 3.5 introduces the Co/graphene system by its embedding into the current state of research, and in Sec. 3.6 follows the publication summarizing the research results acquired for this system.

3.1 The *GW* approximation

We have seen in the introduction that the **GF** method can be used to determine the excited states and their properties (cf. Eq. (3.7)) [Ary98; Aul00; Hed65; Hel11]. The **GF** is embedded in a set of equations, the Hedin equations given below in Eqs. (3.13)-(3.17), which fully encompass the physics of the system under consideration: Electron propagation

and Coulomb (self-)interactions, screening of the Coulomb interactions by polarization of the material, radiative corrections to the interaction vertices; the Hedin equations comprise and associate to each other self-consistently all Feynman diagrams. Chpt. 4 introduces the **QP** concept along the Landau theory for the **FL**, where the **QP** energies are expressed in terms of the bare electronic energies renormalized by the **QP** interactions. The difference between the electronic and **QP** energies can also be expressed within the **QP-EV** equation in terms of the self-energy [Ary98],

$$H_0(\mathbf{r})\Psi_i(\mathbf{r}, \omega) + \int d\mathbf{r}' \Sigma(\mathbf{r}, \mathbf{r}', \omega)\Psi_i(\mathbf{r}', \omega) = E_i(\omega)\Psi_i(\mathbf{r}, \omega), \quad (3.12)$$

where $H_0(\mathbf{r})$ comprises all multiplicative single-particle terms, such as kinetic energy, external, chemical, and Hartree potential. The $\Psi_i(\mathbf{r}, \omega)$ are the **QP-WFs**, and $E_i(\omega)$ their ground- and excited-state energies. The self-energy is non-local and energy-dependent, and for its determination one usually has to invoke some approximation. **DMFT** can be used to fully incorporate the local correlations, for example, all local vertex corrections. This is important as higher-order diagrams are induced by the proximity of strongly interacting localized electrons. (Cf. Refs. [Gre09; Kit06], in which Feynman diagram expansions for the multi-orbital Kondo effect were truncated to achieve the highest-possible degree of sophistication within the computability limits at that times; the present thesis employs the **CTQMC** algorithm without any truncations). For the non-local correlations in more weakly interacting systems one may approximate, or even neglect, the vertex corrections as these become less important for delocalized electrons. The neglect of vertex corrections amounts to the **GWA** discussed in the present section. We shortly state and derive the Hedin equations before going into the physical details.

Hedin obtained the following relations between the non-interacting **GF** G^0 , the interacting **GF** G , the polarizability P , the bare Coulomb interaction V , the screened Coulomb interaction W , and the three-point vertex Λ [Ary98; Hed65; Kut12] (summation over repeated spin and integration over repeated space-time variables implied; $x = (\mathbf{r}, t, \sigma)$):

$$G(x^0, x^1) = G^0(x^0, x^1) + G^0(x^0, x^2)\Sigma(x^2, x^3)G(x^3, x^1) \quad (3.13)$$

$$W(x^0, x^1) = V(x^0, x^1) + V(x^0, x^2)P(x^2, x^3)W(x^3, x^1) \quad (3.14)$$

$$P(x^0, x^1) = G(x^0, x^2)\Lambda(x^2, x^3, x^1)G(x^3, x^0) \quad (3.15)$$

$$\Sigma(x^0, x^1) = -G(x^0, x^2)\Lambda(x^2, x^1, x^3)W(x^3, x^0) \quad (3.16)$$

$$\Lambda(x^0, x^1, x^2) = \delta(x^0, x^2)\delta(x^1, x^2) + \frac{\delta\Sigma(x^0, x^1)}{\delta G(x^3, x^4)}G(x^3, x^5)\Lambda(x^5, x^6, x^2)G(x^6, x^4). \quad (3.17)$$

The structure of this set of equations is valid for all Hamiltonians admitting a decomposition into an interacting and a non-interacting part, in particular, for Eq. (2.1). Eq. (3.13) shows the Dyson equation, that is, the representation of the interacting **GF** G in a power series of irreducible self-energies Σ separated by non-interacting **GFs** G^0 . Eq. (3.14) shows the screened Coulomb interaction line, for which the polarizability P has an analogous role

as the self-energy Σ for the interacting GF G . The polarizability P shown in Eq. (3.15) consists of a bubble diagram, in which the vertex denoted as x^1 is modified by the three-point vertex Λ containing the radiative corrections to that vertex. Inserted into Eq. (3.15) for the screened Coulomb interaction line W , one can see that P gives modification to the bare Coulomb interaction line V by virtual electron-hole excitations, that is, by polarization of the material. The self-energy Σ in Eq. (3.16) is given analogously as the polarizability P , but with some GF lines G replaced by screened Coulomb interaction lines W . One has to take into account that in a vertex always end two GF lines G and one interaction line W . These structures can be assessed from Eq. (3.17) for the three-point vertex Λ . In the GWA the second term on the right-hand side in Eq. (3.17) is neglected, which corresponds to the neglect of radiative corrections for the Coulomb interaction vertex. In this way, the polarizability is only a simple bubble diagram, and the self-energy is given by $\Sigma(x^0, x^1) = -G(x^0, x^1)W(x^1, x^0)$, which gives the approximation its name.

A detailed derivation of these equations may be found in Ref. [Ary98; Aul00], and we follow a very few steps. The starting point is the Hamiltonian given in Eq. (2.1), now in the Heisenberg representation, where the one-particle terms (kinetic energy, external and chemical potentials) are collected in the one-particle Hamiltonian $h_0(x)$. An external scalar potential $\phi(x)$ is added to the Hamiltonian, so that the Dirac representation (or also interaction picture) can be defined by

$$\begin{aligned}\hat{\psi}(x) &= \hat{U}^+(t, 0) \hat{\psi}_D(x) \hat{U}(t, 0) \\ \hat{U}(t, t_0) &= \mathbb{T} \exp \left(-i \int_{t_0}^t d\tau \hat{\phi}(t) \right), \\ \hat{\phi}(\tau, \sigma) &= \int d\mathbf{r} \phi(\mathbf{r}, \tau, \sigma) \hat{\psi}_D^+(\mathbf{r}, \tau, \sigma) \hat{\psi}_D(\mathbf{r}, \tau, \sigma),\end{aligned}\tag{3.18}$$

where \mathbb{T} is the time-ordering operator. Expressing the GF in the Dirac representation, one obtains (with $1 = (\mathbf{r}_1, t_1, \sigma_1)$ etc.)

$$iG(1, 2) = \frac{\langle \Psi_0 | \mathbb{T} [\hat{U}(\infty, -\infty) \hat{\psi}_D(1) \hat{\psi}_D^+(2)] | \Psi_0 \rangle}{\langle \Psi_0 | \hat{U}(\infty, -\infty) | \Psi_0 \rangle},\tag{3.19}$$

where $|\Psi_0\rangle$ is the exact GS of the solid. A functional derivative with respect to the external potential $\phi(x)$ yields

$$\frac{\delta G(1, 2)}{\delta \phi(3)} = G(1, 2)G(3, 3^+) - G_2(1, 2, 3, 3^+).\tag{3.20}$$

The second term on the right-hand side is a two-particle GF, obtained from the GF in Eq. (3.19) by further insertions of field operators. Now, from the Heisenberg equation in the Dirac representation,

$$i \frac{\partial \hat{\psi}_D(x)}{\partial t} = [\hat{\psi}_D(x), \hat{H}(\phi(x) = 0)],\tag{3.21}$$

one obtains the equation of motion for the GF,

$$(i\partial_{t_1} - h_0(1))G(1,2) - \int d3 M(1,3)G(3,2) = \delta(1-2). \quad (3.22)$$

The so-called mass operator here is given by

$$\int d3 M(1,3)G(3,2) = i \int d3 V(1-3)G_2(1,2,3,3^+), \quad (3.23)$$

so it is just given by the two-particle GF also appearing in Eq. (3.20). Replacing $G_2(1,2,3,3^+)$ with help of Eq. (3.20), the $G(1,2)G(3,3^+)$ term yields the one-particle Hartree potential $V_H(1)$, which can thus be moved to the one-particle term $h_0(1)$, so that both can be combined into a new one-particle term $H_0(1)$. Defining

$$-i \int d3 V(1,3) \frac{\delta G(1,2)}{\delta \phi(3)} = \int d3 \Sigma(1,3)G(3,2), \quad (3.24)$$

one obtains

$$(i\partial_{t_1} - H_0(1))G(1,2) - \int d3 \Sigma(1,3)G(3,2) = \delta(1-2), \quad (3.25)$$

which is the Dyson equation in Eq. (3.13).

Now, one defines the total potential $V(1) = V_H(1) + \phi(1)$, and the variation

$$\varepsilon^{-1}(1,2) = \frac{\delta V(1)}{\delta \phi(2)} \quad (3.26)$$

is the dielectric function physically characterized below in Subsec. 3.1.2. The screened Coulomb potential $W(1,2)$ is given in terms of the bare Coulomb potential $V(1-2)$ and the dielectric function as

$$W(1,2) = \int d3 \varepsilon^{-1}(1,3)V(3-2). \quad (3.27)$$

Defining furthermore the three-point vertex function as

$$\Lambda(1,2,3) = -\frac{\delta G^{-1}(1,2)}{\delta V(3)}, \quad (3.28)$$

and multiplying Eq. (3.24) from the right with $G^{-1}(2,4)$ and integrating over 2, one obtains

$$\Sigma(1,2) = i \int d(3,4) G(1,3^+) \Lambda(3,2,4) W(4,1), \quad (3.29)$$

that is, Eq. (3.16) for the self-energy diagram. Using furthermore the Dyson equation in

the form

$$G^{-1}(1,2) = (i\partial_{t_1} - H_0(1))\delta(1-2) - \Sigma(1,2), \quad (3.30)$$

which can be obtained from Eq. (3.25), one easily obtains from the definition of the three-point vertex $\Lambda(1,2,3)$ in Eq. (3.28) the recursive (Dyson-like) relation

$$\Lambda(1,2,3) = \delta(1-2)\delta(2-3) + \int d(4,5,6,7) \frac{\delta\Sigma(1,2)}{\delta G(4,5)} G(4,6)G(7,5)\Lambda(6,7,3), \quad (3.31)$$

that is, the three-point vertex function as defined in Eq. (3.17).

The polarization of the solid is defined as the ratio between the change of the charge density at one site, $\delta\rho(1)$, and the change of the total potential at another site, $\delta V(2)$. The charge density can be written in terms of the GF as $\rho(1) = -iG(1,1^+)$, so that with the definition of the three-point vertex in Eq. (3.28) it follows

$$P(1,2) = -i \frac{\delta G(1,1^+)}{\delta V(2)} = i \int d(3,4) G(1,3)\Lambda(3,4,2)G(4,1^+), \quad (3.32)$$

that is, the definition of the polarization function in Eq. (3.15). Furthermore, with $V(1) = V_H(1) + \phi(1)$, and the Hartree potential given by $V_H(1) = \int d2 V(1-2)\rho(2)$, one derives for the dielectric function

$$\begin{aligned} \varepsilon^{-1}(1,2) &= \frac{\delta V(1)}{\delta\phi(2)} \\ &= \delta(1-2) + \int d3 V(1-3) \frac{\delta\rho(3)}{\delta\phi(2)} \\ &= \delta(1-2) + \int d(3,4) V(1-3)P(3,4) \frac{\delta V(4)}{\delta\phi(2)}. \end{aligned} \quad (3.33)$$

Inserting this result into Eq. (3.27) for the screened Coulomb interaction, one obtains its Dyson-like definition in Eq. (3.14). This completes the derivation of the Hedin equations. We finally note that there exists an alternative and very nice way of deriving the Hedin equations from a Feynman diagram point of view [Hel11].

The GWA is the simplest way of going beyond the HF approximation to account for the (weak) non-local correlations [Ary98]. The correlations between electrons of same spin (Pauli exclusion) are contained in HF theory, while the ones between electrons of opposite spin are not. But these latter repulsive correlations lead to the emergence of a screening hole around the electrons, and the resulting QPs have thus a reduced interaction and Coulomb energy, and the material a smaller band gap. Formally, in the PT sense, the self-energies are the same in both, the HF approximation and the GWA, but the latter contains the dynamical screening effects which renormalize the Coulomb strength (not screened in HF theory) and the band gap (often too large in HF theory). In contrast to that, DFT in its LDAs renders the systems often too metallic, thus yielding too small band gaps and sometimes misses the Hubbard-Mott phase. Furthermore, there exists the self-interaction

problem due to the charge density description; and finally, more importantly for the adsorption physics on surfaces, **DFT** yields a wrong exponential instead of the power-law image potential decay. **DFT** and the **GWA** are fundamentally different approaches, but both their results can be expressed as **GFs**; one observes that in **DFT** the approximation pertains to the **XC** potential, while in the **GWA** one truncates the self-energy. Note that, computationally, one usually uses the **DFT-WFs** and energies as input for the **GWA**, and one may eventually observe their renormalization and improvement [Aul00].

The limitations of the **GWA** are given by the above-mentioned fact, that the **GWA** is better suited for weak and non-local correlations, and for systems with enhanced electronic flexibility due to strong polarizability. Core-level spectra and strong electronic interactions with an eventual breakdown of the **QP** description cannot be described by the **GWA** (and thus also not by the **RPA** (cf. Subsec. 3.1.2)), because vertex corrections are needed for short-range interactions. This makes the **GWA** inappropriate for **TM** oxides and other strongly correlated systems [Hel11], and one needs to turn to other approaches. However, the calculation of the realistic screened Coulomb interaction line (Eq. 3.14) opens up the possibility for its use as input for these other approaches; this will be explained in more detail in Subsec. 3.1.2, and exemplified along the Co/graphene system in Secs. 3.6.

3.1.1 The spectral function

Two of the relevant physical quantities measured experimentally are the **QP** energies (i.e., the excitation spectrum) and lifetimes (we follow the exposition in Ref. [Ary98]). Measuring the spectrum amounts to performing photoemission spectroscopy (PES), where the material is irradiated with photons of energy ω which knock out electrons of kinetic energy $E_{\text{kin}}(\mathbf{k})$. Thereby the excitation energies $E_{\mathbf{k}}(\omega) = \omega - E_{\text{kin}}(\mathbf{k})$ and the spectrum with a hole, that is, the occupied **DOSSs**, are measured (one should note, though, that the **DOSSs** yields the number of available states in the system, while the spectrum yields emission/adsorption probabilities and is normalized). Inverse PES probes the unoccupied **DOSSs** by injection of electrons into the system. In the so-called sudden approximation, where electrons have large kinetic energies, relaxation effects become negligible, and the **GF** can be written as (cf. Eq. (3.19))

$$iG(1,2) = \begin{cases} \langle {}^N\Psi_0 | \hat{\psi}(1)\hat{\psi}^+(2) | {}^N\Psi_0 \rangle & \text{for } t_1 > t_2, \\ \langle {}^N\Psi_0 | \hat{\psi}^+(2)\hat{\psi}(1) | {}^N\Psi_0 \rangle & \text{for } t_1 < t_2, \end{cases} \quad (3.34)$$

where the action of the time-ordering operator has already been carried out, and the matrix elements are computed between the exact N -electron **GS**. The first line describes the propagation of an added electron in the system, while the second line the one a hole. In analogy to Eq. (3.1), the solutions (**WFs** and energies) to the **QP-EV** equation (Eq. (3.12)) can be organized into the **GF**

$$G(\mathbf{r}, \mathbf{r}', \omega) = \sum_i \frac{\Psi_i(\mathbf{r}, \omega) \Psi_i^*(\mathbf{r}', \omega)}{\omega - E_i(\omega)}. \quad (3.35)$$

The **EVs** to the **QP-EV** equation are in general complex, with the real part contributing to the **QP** energies, and the imaginary part describing the **QP** damping. In particular, if the equation $\omega = \text{Re}(E_i(\omega))$ can be solved for some $\omega = \omega_i$, and if $\text{Im}(E_i(\omega_i))$ is small, then one has a peak at ω_i describing a **QP** with lifetime $1/\text{Im}(E_i(\omega_i))$. Both, **QP** peaks and satellites, are reflected by these **GF** poles (though the poles for satellites are sometimes approximate only). The **QP** lifetimes are thus inversely proportional to the width of the **QP** peaks, where the broadening occurs due to the interactions and provides decay channels to the other, plasmonic or collective, excitations.

The spectral function $A(\mathbf{r}, \mathbf{r}', \omega)$ can either be given as the integral kernel of a Hilbert transform (cf. Sec. 3.4),

$$G(\mathbf{r}, \mathbf{r}', \omega) = \int d\omega' \frac{A(\mathbf{r}, \mathbf{r}', \omega')}{\omega - \omega' + \text{sgn}(\omega' - \mu)i\delta}, \quad (3.36)$$

where μ is the chemical potential, or as the imaginary part of the **GF**,

$$\begin{aligned} A(\mathbf{r}, \mathbf{r}', \omega) &= -\frac{1}{\pi} \text{Im}[G(\mathbf{r}, \mathbf{r}', \omega) \text{sgn}(\omega - \mu)] \\ &= \sum_i [p_i^*(\mathbf{r})p_i(\mathbf{r}')\delta(\omega - \mu - {}^{N+1}\bar{E}_i) + h_i(\mathbf{r})h_i^*(\mathbf{r}')\delta(\omega - \mu + {}^{N-1}\bar{E}_i)], \end{aligned} \quad (3.37)$$

with

$$\begin{aligned} p_i(\mathbf{r}) &= \langle {}^{N+1}\Psi_i | \hat{\psi}^+(\mathbf{r}, 0) | {}^N\Psi_0 \rangle, \quad h_i(\mathbf{r}) = \langle {}^{N-1}\Psi_i | \hat{\psi}(\mathbf{r}, 0) | {}^N\Psi_0 \rangle, \\ {}^{N\pm 1}\bar{E}_i &= {}^{N\pm 1}E_i - {}^{N\pm 1}E_0 > 0, \quad \mu = {}^{N+1}E_0 - {}^NE_0 \approx {}^NE_0 - {}^{N-1}E_0. \end{aligned} \quad (3.38)$$

The form of the spectral function can be obtained by insertion of a complete set of states for the systems with $(N \pm 1)$ electrons. In this way the spectral function exhibits directly the electronic excitation energies, with electrons and holes belonging to positive- and negative-energy solutions (w.r.t. the chemical potential μ), respectively. Substituting the spectrum in Eq. (3.36) with the second line of Eq. (3.37) yields the Lehmann representation of the **GF** [Fjæ13].

The **QP** peaks can be separated from the continuum (the other spectral parts also comprising the satellites; cf. introductory part to Chpt. 4). To this end, one notes that the **QP** quantum numbers are the same as the ones of the corresponding non-interacting electrons, and suppressing for now the positional dependence of the **GF**, the spectral function is given by (cf. Eq. (3.58))

$$\begin{aligned} A(\omega) &= \frac{1}{\pi} \text{Tr} [|\text{Im}(G(\omega))|] = \frac{1}{\pi} \sum_i |\text{Im}(G_i(\omega))| \\ &= \frac{1}{\pi} \sum_i \frac{|\text{Im}(\Sigma_i(\omega))|}{[\omega - \varepsilon_i - \text{Re}(\Sigma_i(\omega))]^2 + [\text{Im}(\Sigma_i(\omega))]^2}, \end{aligned} \quad (3.39)$$

where the static part of the self-energy corresponding to the energy **EVs** of the non-

interacting system described by H_0 has been extracted (cf. Eq. (3.12)). Once more again, one can see that the **QP** energies are given by peaks at $E_i = \varepsilon_i + \text{Re}(\Sigma_i(E_i))$, that is, at the renormalized energies (cf. discussion after Eq. (4.2)). In the vicinity of these positions, the spectrum can be approximated by

$$A(\omega) \approx \sum_i \frac{Z_i}{(\omega - E_i)^2 + [\text{Im}(\Sigma_i(E_i))]^2}, \quad (3.40)$$

where the **QP** weight (renormalization factor) is given by

$$Z_i = \left(1 - \frac{\partial \text{Re}(\Sigma_i(\omega))}{\partial \omega} \right)^{-1} \Bigg|_{\omega=E_i}, \quad (3.41)$$

and, again, the **QP** lifetime by $1/\text{Im}(\Sigma_i(E_i))$. In principle, this form applies to all pronounced spectral structures, be they belonging to **QP** peaks or to satellites (such as the Kondo peaks near the Fermi level and the residual spectral weights marking the energy levels of the isolated impurity, respectively, cf. Chpt. 4). In the context of weakly interacting **AIMs** (such as the Co/graphene system, Sec. 3.6), the effects of the hybridization function dominate over the ones of the self-energy, and the bare energy levels of the impurity (given by the static part of the hybridization function) become only slightly renormalized by the self-energy (i.e., their spectral positions are nearly unshifted), with the width of the **QP** peaks rather determined by the hybridization strength.

3.1.2 The constrained random phase approximation

In the following we follow the exposition of Ref. [Ary11]. In the **GWA**, the polarizability is a simple bubble diagram given by the product of two **GFs**, $P(1,2) = G(1,2)G(2,1)$. In equilibrium the **GF** satisfies the relation $G(\mathbf{r}, t, \sigma; \mathbf{r}', t', \sigma') = G(\mathbf{r}, \sigma; \mathbf{r}', \sigma'; t - t')$, and the Fourier transform of the polarizability can thus be given by ($r = (\mathbf{r}, \sigma)$)

$$P(r, r', \omega) = -i \int \frac{d\omega'}{2\pi} G(r, r', \omega + \omega') G(r', r, \omega'). \quad (3.42)$$

The **GF** in Eq. (3.35) contains the **QP-WFs** and energies, which are solutions to the **QP-EV** equation in Eq. (3.12). In a periodic solid, the index i comprises band n and momentum \mathbf{k} indices, and these quantum numbers are the same for electrons before the on-set of interactions and for **QPs** (cf. introductory part to Chpt. 4). In the **RPA** the **GFs** for the polarizability are approximated by the non-interacting **GF**

$$G_0(r, r', \omega) = \sum_i^{\text{occ}} \frac{\varphi_i(r) \varphi_i^*(r')}{\omega - \varepsilon_i - i\delta} + \sum_j^{\text{unocc}} \frac{\varphi_j(r) \varphi_j^*(r')}{\omega - \varepsilon_j + i\delta}, \quad (3.43)$$

where the sum over all states has been decomposed into two parts, distinguishing the occupied from the unoccupied states. The **RPA** amounts to the neglect of some higher-order Feynman diagrams assumed to describe the out-of-phase response of randomly distributed electrons to the total electric potential, which thereby cancel out on the average [Ren12],

and it is always employed in computational implementations of the GWA [Hel11]. Now, performing the frequency integral within the polarizability, one obtains

$$P(r, r', \omega) = \sum_{(i,j)}^{(\text{occ}, \text{unocc})} \left(\frac{b_{ij}(r)b_{ji}^*(r')}{\omega - \Delta_{ij} + i\delta} - \frac{b_{ij}^*(r)b_{ji}(r')}{\omega + \Delta_{ij} - i\delta} \right), \quad (3.44)$$

with the pairs of occupied and unoccupied orbitals given by $b_{ij}(r) = \varphi_i^*(r)\varphi_j(r)$, and the energy differences by $\Delta_{ij} = \varepsilon_j - \varepsilon_i$. Having obtained an approximate form for the polarizability, one may now calculate the screened Coulomb interaction in the system.

However, one often needs the screened Coulomb interaction between electrons on specific sites of the system and in specific orbitals, but without screenings due to the electrons which are already on this site and in these orbitals. For example, in the AIM (Sec. 3.2) or in DFT+ U (Subsec. 2.1.4) one treats the Coulomb interactions between the electrons on one site and in the interacting shell already exactly. Thus, in the space of states within the solid, one separates the states which project onto the correlated orbitals from the ones which project onto the weakly or non-correlated (conduction) orbitals, and excludes the screening of the interaction between electrons in the correlated subspace. This decomposition is expressed for the polarizability by

$$P = P_c + P_r, \quad (3.45)$$

where P_c denotes the polarizations within the correlated orbitals, and P_r the ones within the rest of the system, and the ones between the correlated orbitals and the rest of the system. We assume that the energy bands with contributions from the correlated orbitals are the only ones crossing the Fermi level, while all other bands (the rest) are disentangled and sufficiently separated from the correlated bands. A prominent example is given by SrVO₃, where the three correlated bands crossing the Fermi level are of t_{2g} symmetry and are well separated from the rest. Entangled bands have to be considered differently, but the underlying idea of separating screening channels remains the same (see also Ref. [Şağ11] explaining the computational details and the code, which was employed for the Co/graphene system, Sec. 3.6).

Eq. (3.33) provides a Dyson-like expression for the inverse of the dielectric function. Inversion yields the dielectric function itself, and employing the polarizability decomposition given in Eq. (3.45), one calculates

$$\begin{aligned} \varepsilon(1,2) &= \delta(1-2) - \int d3 V(1-3)[P_c(3,2) + P_r(3,2)] \\ &= \varepsilon_r(1,2) + \int d3 V(1-3)P_c(3,2) \\ &= \int d4 \varepsilon_r(1,4)[\delta(4-2) - W_r(4,3)P_c(3,2)] \\ &= \int d4 \varepsilon_r(1,4)\Xi(4,2). \end{aligned} \quad (3.46)$$

In the last line the function $\Xi(4,2)$ was defined for convenience. Inversion on both sides yields

$$\varepsilon^{-1}(1,2) = \int d4 \Xi^{-1}(1,4) \varepsilon_r^{-1}(4,2) \quad (3.47)$$

with the Dyson-like expression

$$\Xi^{-1}(1,4) = \delta(1-4) + \int d(3,5) W_r(1,3) P_c(3,5) \Xi^{-1}(5,4). \quad (3.48)$$

Insertion into Eq. (3.27) gives

$$W(1,2) = \int d3 \Xi^{-1}(1,3) W_r(3,2), \quad (3.49)$$

which allows the conclusion that $W_r(3,2)$ is the partially screened Coulomb interaction within the correlated subspace, because the expansion of $\Xi^{-1}(1,4)$, which contains the polarizability $P_c(3,5)$, yields the full screening. In equilibrium we thus may denote the partially screened Coulomb interaction as

$$U(r, r', \omega) = W_r(r, r', \omega), \quad (3.50)$$

which acquires a frequency dependence (retardation) due to the dynamical screening events.

For the Co/graphene system (Sec. 3.6) we used the static part of the cRPA Coulomb matrix, and used it as an input for a realistic AIM (Sec. 3.2) which we solved by the CTQMC algorithm (Sec. 3.3) in its TRIQS/CTHYB incarnation [Par15; Set16]. This code is able to take into account all Coulomb matrix elements, in particular the ones beyond the density-density approximation (cf. Ref. [Kar13]). These elements are important for the full rotational invariance in spherically symmetric systems or approximations (compare Eqs. (2.43) and (2.46)), or for the consideration of geometric anisotropies such as in the Co/graphene surface system (see also Refs. [Han13b; Han13c; Şaş12]). Geometric anisotropies in the Coulomb interaction matrix have also been found relevant in bulk systems [Sar18; Zha16; Zha17] (see also discussion Sec. 3.5). As mentioned in Subsec. 2.1.3 and the introductory part to the present chapter, the frequency dependence can be taken into account by a suitably generalized AIM solver [Bie03; Hel11; Sun02].

3.2 The Anderson impurity model

The general Hamiltonian in Eq. (2.1) is given in second quantization and with the field operators defined in position space. A transformation into momentum space of the solid can be performed,

$$\hat{\psi}_\sigma^+(\mathbf{r}) = \sum_{n\mathbf{k}} \phi_{n\mathbf{k}\sigma}(\mathbf{r}) \hat{c}_{n\mathbf{k}\sigma}^+, \quad (3.51)$$

with $\phi_{n\mathbf{k}\sigma}(\mathbf{r})$ the solutions to the **KS** equation in Eq. (2.16), so that within the **DFT** approximation the general Hamiltonian can be given in terms of the energy bands,

$$\hat{H} = \sum_{n\mathbf{k}\sigma} \varepsilon_{n\mathbf{k}} \hat{n}_{n\mathbf{k}\sigma}, \quad \hat{n}_{n\mathbf{k}\sigma} = \hat{c}_{n\mathbf{k}\sigma}^+ \hat{c}_{n\mathbf{k}\sigma}. \quad (3.52)$$

This is the **KS** operator in its momentum space representation with the **EVs** already plugged in, and it pertains to delocalized and weakly correlated electrons for which the **DFT** approximation applies. If the system under consideration involves a strongly correlated site, an impurity, one may augment the **DFT** Hamiltonian in Eq. (3.52) by adding its corresponding atomic Hamiltonian, and a hybridization term between the atomic (discrete) and the energy-band (continuous) states, resulting in the Hamiltonian for the **AIM** [And61]:

$$\begin{aligned} \hat{H} = & \sum_{n\mathbf{k}\sigma} \varepsilon_{n\mathbf{k}} \hat{n}_{n\mathbf{k}\sigma} + \sum_{\alpha\beta\sigma} (\varepsilon_{\alpha\beta} - \mu_{\alpha\beta}^{\text{DC}}) \hat{c}_{\alpha\sigma}^+ \hat{c}_{\beta\sigma} + \frac{1}{2} \sum_{\alpha\beta\gamma\delta\sigma\sigma'} U_{\alpha\beta\gamma\delta} \hat{c}_{\alpha\sigma}^+ \hat{c}_{\beta\sigma'}^+ \hat{c}_{\delta\sigma'} \hat{c}_{\gamma\sigma} \\ & + \sum_{n\mathbf{k}\alpha\sigma} [V_{n\mathbf{k}\alpha} \hat{c}_{n\mathbf{k}\sigma}^+ \hat{c}_{\alpha\sigma} + V_{\alpha n\mathbf{k}}^* \hat{c}_{\alpha\sigma}^+ \hat{c}_{n\mathbf{k}\sigma}]. \end{aligned} \quad (3.53)$$

The second term contains the on-site **crystal field (CF)** matrix $\varepsilon_{\alpha\beta}$ labelled by the local orbitals on the correlated site, from which a **DC** term $\mu_{\alpha\beta}^{\text{DC}}$ in the form of a chemical potential is subtracted. The diagonalization of the **CF** matrix would yield the impurity energy levels (cf. Sec. 4.2). The **DC** term accounts for the correlations already contained in **DFT**, which considered thoroughly by the many body treatment beyond (cf. Subsec. 2.1.4). The third term contains the Coulomb interaction parameters, for example, as obtained via the **cRPA** which takes into account that the effective interaction between the correlated electrons is the bare interaction screened by all the non-correlated electrons (cf. Eq. (3.50)). The hybridization matrix elements (hybridization couplings) are given by $V_{n\mathbf{k}\alpha} = \langle n\mathbf{k} | \hat{V}_{\text{imp}} | \alpha \rangle$, with \hat{V}_{imp} the ionic potential operator of the impurity. – One may note that the **AIM** Hamiltonian acts on a tensor product space composed of the Hilbert space for the isolated impurity and the one for conduction electrons, as the energy bands $\varepsilon_{n\mathbf{k}}$ are the ones without the presence of the impurity, while the atomic part given by **CF**, **DC** term, and Coulomb interaction contains information about the yet uncoupled impurity placed into the conduction electron environment (e.g., the **CF** structure is determined by the symmetries of the environment, Sec. 4.2). Both, impurity and conduction electrons, are finally coupled by the hybridization term. The issue that the energy bands $\varepsilon_{n\mathbf{k}}$ should not know anything about the impurity will be considered shortly in Subsec. 3.2.1.

The **AIM** becomes relevant if the Coulomb interaction energies between the correlated electrons on the impurity sites are larger than their kinetic energies (we closely follow Ref. [Col15]). There are several classes of material systems for which the **AIM** is essential for their description. One of them are the cuprate **SCs** which are doped antiferromagnetic Mott insulators. Away from half-filling (the antiferromagnetic order at half-filling is insulating due to the blocking behaviour of localized electrons), the charge excesses happen to be highly mobile, leading to their **SC** behaviour, see also Appx. A.1. Another class is given by heavy-fermion compounds containing electronic **QPs** with large effective masses, which,

due to Hund's rule coupling, provide local magnetic moments immersed in the metallic environment. For such systems the AIM needs to be supplemented with the DMFT self-consistency providing the connection to the Hubbard model (cf. Subsec. 3.2.1, and Subsec. 2.1.3 and references therein), which is at the basis for the description of strongly correlated bulk materials or films. Yet another (rather general) class of systems is given by adatoms or molecules (i.e., nanosystems) on surfaces. For these, the AIM itself fully describes their physics; these surface systems are the ones to which the exposition in the present thesis applies.

Localized electrons lead to the formation of local magnetic moments, which subsequently interact with the conduction sea of electrons [Col15]. This interaction is at the heart of the correlations in strongly correlated materials. Thus, strong local correlations mostly result out of partially filled and well localized orbitals which happen to be placed in a weakly interacting environment. Orbital localization is on hand if the impurity orbitals show only weak overlap with their environment, which translates to narrow energy bands in momentum space (cf. Ref. [Geo04]); in principle, an impurity energy level exists only if its dispersion is weak. The degree of localization is roughly given by the following filtration:

$$5d < 4d < 3d < 5f < 4f. \quad (3.54)$$

Higher principal numbers n lead to more nodes in the radial part of the WF, and thus these are more extended. This tendency can be overruled by the angular momentum number l , because the nuclear charge connected with it becomes higher. With increasing localization there occurs magnetic moment formation, while decreasing localization may lead to SC. The crossover region contains materials such as cerium- ($[\text{Xe}]4f^15d^16s^2$) and uranium-based ($[\text{Rn}]5f^36d^17s^2$) heavy-fermion materials and iron-based ($[\text{Ar}]3d^64s^2$) SCs [Col15].

As mentioned, the Coulomb repulsion blockades the passage of electrons through strong interaction centres if there are already electrons localized, which leads to Mott-insulating behaviour [Col15; Hur41; Mot49; Mot37; Vle53]. On the other hand, via hybridization the interaction centres arrange around themselves electronic virtual bound-state resonances [Bla59; Fri56; Hur41]. The two concepts were unified by Anderson, who considered the tunnelling between the correlated d or f orbitals and the conduction sea and developed the AIM Hamiltonian given in Eq. (3.53) [And61]. The atomic part in Eq. (3.53) leads to the moment formation due to Hund's rule coupling, and the hybridization part leads to the resonance behaviour. – The cRPA Coulomb matrix for the Co/graphene system turned out rather small (Sec. 3.6), which renders the corresponding AIM giving more prominence to the kinetic part, to delocalization and metallic behaviour. In the $\text{CoCu}_n/\text{Cu}(111)$ systems (Sec. 4.6) the Coulomb interaction energies are assumed larger than the other energy scales. Here, most processes have energies below the charge excitation energies, so that the spin DOF become more relevant, which leads to the prevalence of the Kondo effect (Chpt. 4). However, in the multi-orbital context the orbital DOF are relevant as well, so that the Kondo effect becomes enhanced (cf. Subsec. 4.5.3).

3.2.1 DFT+AIM

The implementation and computational details regarding the transition from the **DFT** description and its quantities (cf. Sec. 2.1) to the **AIM** Hamiltonian can be read in Refs. [Kar13; Kar11b; Kre96] (see also Sec. 3.6, and Appx. B for a few more details). There, the projection of delocalized Bloch bands onto local orbitals, which is used for the projects reported on in the present thesis, is explained in full detail. Here, it is only stated that, once the **DFT** energy bands $\varepsilon_{n\mathbf{k}}$ are determined, a local and non-interacting impurity **GF** is obtained by projecting the Bloch **GF** onto the correlated site and summing over all bands and momenta in the first **BZ**,

$$G_{\alpha\beta}^{(0)}(\omega) = \sum_{n\mathbf{k}} \langle \alpha | n\mathbf{k} \rangle \frac{1}{\omega - \varepsilon_{n\mathbf{k}}} \langle n\mathbf{k} | \beta \rangle = \frac{1}{\omega - \varepsilon_{\alpha\beta} - \Delta_{\alpha\beta}(\omega)}. \quad (3.55)$$

The quantity $\langle n\mathbf{k} | \alpha \rangle$ are the projections from Bloch to local-orbital states, and $\Delta_{\alpha\beta}(\omega)$ is the hybridization function (which can also be derived within the path integral approach by integrating out the non-interacting conduction electron **DOF**, cf. Sec. 3.3 and Ref. [Kar13]). These equations need some explanations: First, the impurity is included in the supercell for the **DFT** calculation, that is, the energy bands here contain information about its presence. The Bloch **WFs** $|n\mathbf{k}\rangle$ are computed within **DFT**, and the local orbitals $|\alpha\rangle$ have to be defined. Usually these are the **DFT-WFs** (the **KS** orbitals) projected onto atomic hydrogen orbitals within a certain radius, or one may use **maximally localized Wannier functions** (**MLWFs**) (see Refs. [Kar13; Kun11] and references therein). Eq. (3.55) is one means to computationally determine the on-site **CF** matrix and the hybridization function. The **CF** can be regarded as the static part of the hybridization, and written as such, the hybridization function itself vanishes at high frequencies, $\Delta_{\alpha\beta}(\omega) \rightarrow 0$ ($\omega \rightarrow \infty$). There are other means to determine these two quantities (cf., e.g., Sec. 4.2 and Refs. [Kar13; Pav12; Shi17a]), as it is *a priori* unclear for an impurity immersed in a conduction sea which radius and occupation it has. The problem is analogous to the definition of partial charges (Subsec. 2.5.1).

To distinguish the energy bands appearing in the first equality of Eq. (3.55) from the ones without the impurity in the supercell, we denote the latter as $\varepsilon_{n\mathbf{k}}^{(0)}$ in the following. One may think of the local impurity **GF** $G_{\alpha\beta}^{(0)}(\omega)$ being represented as a Feynman diagram expansion, in which an electron starting in state $|\alpha\rangle$ hops to the conduction sea via the hybridization coupling $V_{n\mathbf{k}\alpha}$, propagates within the sea by the **GF** $G_{n\mathbf{k}}^{(0)}(\omega) = [\omega - \varepsilon_{n\mathbf{k}}^{(0)}]^{-1}$, and hops back onto the impurity into the state $|\beta\rangle$. Such back-and-forth hoppings occur to any order, and due to the algebraicity of the (equilibrium) **GF** in frequency space the expansion is geometric and can be organized into an analytic form, in which the hybridization function

$$\Delta_{\alpha\beta}(\omega) = \sum_{n\mathbf{k}} \frac{V_{\alpha n\mathbf{k}}^* V_{n\mathbf{k}\beta}}{\omega - \varepsilon_{n\mathbf{k}}^{(0)}}. \quad (3.56)$$

is generated (one obtains the same result via the path integral approach mentioned above, cf. Sec. 3.3). The transition from the **DFT** results to the **AIM** is thus consistent as regards

the difference between the energy bands in presence of the impurity, $\varepsilon_{n\mathbf{k}}$, and the ones in its absence, $\varepsilon_{n\mathbf{k}}^{(0)}$. This issue becomes more important in the calculation of the asymmetry factors for realistic Kondo systems (Sec. 4.4), because it is computationally difficult to disentangle the conduction orbitals from the correlated ones, as the former are to first order the non-correlated orbitals on the impurity itself.

In principle, the full set of equations for the GF formalism of the AIM are the local analogue of the Hedin equations (Eqs. (3.13)-(3.17)); even more as the CTQMC algorithm (Sec. 3.3) is capable to take into account all vertex corrections (the slightly more general notation given in Ref. [Hel11] might be more appropriate, though, because the Coulomb interaction vertex has four indices). Thus, the on-site Coulomb interactions between the correlated electrons eventually augment the local impurity GF $G_{\alpha\beta}^{(0)}(\omega)$ (Eq. (3.55)) by the self-energy $\Sigma_{\alpha\beta}(\omega)$. From the Dyson equation given in Eqs. (3.13) and (3.25), transformed into frequency space, one obtains the interacting impurity GF

$$G_{\alpha\beta}(\omega) = \frac{1}{(G_{\alpha\beta}^{(0)}(\omega))^{-1} - \Sigma_{\alpha\beta}(\omega)} = \frac{1}{\omega - \varepsilon_{\alpha\beta} - \Delta_{\alpha\beta}(\omega) - \Sigma_{\alpha\beta}(\omega)}. \quad (3.57)$$

The local spectral function is then given by (cf. Eq. (3.39))

$$\begin{aligned} \rho(\omega) &= -\frac{1}{\pi} \text{Tr} [\text{Im}(\underline{G}(\omega))] \\ &= -\sum_{\alpha} \frac{\text{Im}(\Delta_{\alpha}(\omega) + \Sigma_{\alpha}(\omega))}{[\omega - \varepsilon_{\alpha} - \text{Re}(\Delta_{\alpha}(\omega) + \Sigma_{\alpha}(\omega))]^2 + [\text{Im}(\Delta_{\alpha}(\omega) + \Sigma_{\alpha}(\omega))]^2}, \end{aligned} \quad (3.58)$$

where the diagonal components have been indexed only once. The form of the spectral function here resembles the one of resonances at positions given by the solution to the equation $\omega - \varepsilon_{\alpha} - \text{Re}(\Delta_{\alpha}(\omega) + \Sigma_{\alpha}(\omega)) = 0$, and of widths $-\text{Im}(\Delta_{\alpha}(\omega) + \Sigma_{\alpha}(\omega))$ (see explanations in Subsec. 3.1.1). As also explained in Sec. 3.1.1, the spectral function already yields a lot of information on the physics of the system under consideration, which can be compared to experimental results. In case of STS experiments (Sec. 2.2) one usually continues processing the AIM spectral function to obtain adatom dI/dV curves (cf. Sec. 4.4), which can be directly compared to experimental STS curves, see Sec. 4.6.

We close this section with a very short outline of the DMFT method for strongly correlated bulk materials, but without giving the theoretical background for its effectiveness (see Ref. [Met89] and the references cited in the introductory part to this chapter). In principle, DMFT relies on the simple mathematical fact that the volume of a sphere in infinite dimensions vanishes. Carrying over to correlated bulk materials represented by the Hubbard model, all correlations in infinite dimensions become local. The assumed approximate locality of the correlations in “low-dimensional” materials (i.e., up to dimension three) means that the corresponding self-energy becomes local as well, so that it loses its momentum dependence. As the self-energy for the AIM is local and momentum-independent, it can be used for the Hubbard model within the DMFT self-consistency, which roughly looks as follows (cf. Ref. [Kar13] for computational details): The iteration starts with the non-interacting impurity GF $G_{\alpha\beta}^{(0)}(i\omega)$ given in Eq. (3.55). Then, by solving the AIM for

the impurity, one augments this **GF** by the self-energy $\Sigma_{\alpha\beta}(i\omega)$ (cf. Eq. 3.57). In principle, the first solution of the **AIM** corresponds to single-shot **DMFT**, that is, to **DMFT** without self-consistency. Then one unfolds the obtained self-energy or interacting impurity **GF** to the Hubbard lattice, that is, into the space of Bloch bands, where the self-energy acquires a momentum dependence via the projectors $|n\mathbf{k}\rangle\langle\alpha|$ (cf. Eq. (3.55)), $\Sigma_{nn'}(i\omega, \mathbf{k})$. The Hubbard **GF** in this approximation looks like $G_{nn'}(i\omega, \mathbf{k}) = [i\omega - \varepsilon_n(\mathbf{k})\delta_{nn'} - \Sigma_{nn'}(i\omega, \mathbf{k})]^{-1}$. From this **GF** one again calculates a new impurity **GF** via downfolding as in Eq. (3.55), which now contains the correlation effects on the **AIM** level. From this **GF** one calculates a new non-interacting **GF** $G_{\alpha\beta}^{(0)}(i\omega)$ from Eq. (3.57) with the self-energy already obtained. Then one solves the **AIM** again and obtains a new self-energy. The iteration is to be performed until convergence, and one finally has a Hubbard **GF** in the Bloch space of the lattice. Thus, the point of self-consistency is characterized by an impurity **GF** upfolded to Bloch space, which contains the correlations as if the Hubbard model were infinite-dimensional.

In the context of real materials, the approach just sketched is termed **DFT+DMFT**. One can further augment the **DMFT** self-consistency by an outer one over the charge density. The charge density containing correlations can be computed from the Bloch-Hubbard **GF** from single-shot **DMFT**, and then used as an input for another single-shot **DFT** calculation (one **DFT** step only), in which one again obtains a new band structure for the next **DMFT** step. The partial convergence on both, **DFT** and **DMFT**, sides at each step is important, for otherwise one cannot achieve charge-self-consistency efficiently; either **DFT** would relax to always the original band structure, or most of the **DMFT** calculations (i.e., iterative solutions of the **AIM**) would be performed without them having much impact on later solutions. Details and references on charge-self-consistency can be found in Ref. [Kar13]. An implementation of **DFT+DMFT** and of full charge-self-consistency exists with the **TRIQS/DFTTools** code [Aic16], which can be combined with the **TRIQS/CTHYB** code for the solution of the **AIM** [Set16] (cf. Sec. 3.3); both codes were established within the **TRIQS** collaboration [Par15]. A particular example of its use may be found in Ref. [Kri18]; other implementations, examples of use, and physical implications can be found in Refs. [Hau14; Hau10; Pou07; Shi09; Shi10].

3.3 The continuous-time quantum Monte Carlo method

We shortly describe the general ideas and routines connected with the **QMC** method [Gul11]. With regard to the Feynman diagram expansion of a partition function, it amounts to a stochastic sampling over all orders, topologies, and vertex positions on the (imaginary-)time axis of such Feynman diagrams. **QMC** automatically detects which regions of the high-dimensional configuration space generated by the expansion are important. Additionally, higher orders are correctly suppressed if the coupling constants appearing in the expansion are small compared to the other energy scales (it is not a necessary condition for convergence, though).

Consider a partition function given by

$$Z = \int_C d\mathbf{x} p(\mathbf{x}), \quad p(\mathbf{x}) = e^{-\beta E(\mathbf{x})}. \quad (3.59)$$

The Boltzmann weight $p(\mathbf{x})$ assigns the configuration \mathbf{x} in the configuration space C a probability for its occurrence. The configuration \mathbf{x} has the energy $E(\mathbf{x})$, and all configurations are assumed to exist at the same temperature β , that is, the system is in equilibrium. Expectation values based on the Boltzmann distribution are given by

$$\langle A \rangle_p = \frac{1}{Z} \int d\mathbf{x} A(\mathbf{x}) p(\mathbf{x}). \quad (3.60)$$

To evaluate the partition function in Eq. (3.59), a Markov process is organized on the basis of transition probabilities $W_{\mathbf{xy}}$ which satisfy the normalization condition $\sum_{\mathbf{y}} W_{\mathbf{xy}} = 1$ [How71]. The Markov process converges exponentially fast to the Boltzmann distribution $p(\mathbf{x})$ if the two conditions on ergodicity and (detailed) balance are met. Ergodicity implies that every configuration can be reached starting from any other configuration in a finite number of steps within the Markov process. Balance means that the Boltzmann distribution is recovered if one transforms the whole distribution by one Markov step, $\int_C d\mathbf{x} p(\mathbf{x}) W_{\mathbf{xy}} = p(\mathbf{y})$. A slightly stricter condition is detailed balance, $W_{\mathbf{xy}}/W_{\mathbf{yx}} = p(\mathbf{y})/p(\mathbf{x})$, a sufficient, but not necessary condition for balance itself. The Markov process together with detailed balance is implemented by the Metropolis-Hastings algorithm by decomposing the transition matrix elements into proposal and acceptance rates, $W_{\mathbf{xy}} = W_{\mathbf{xy}}^{\text{prop}} W_{\mathbf{xy}}^{\text{acc}}$. Here, the acceptance rates are given by $W_{\mathbf{xy}}^{\text{acc}} = [1, R_{\mathbf{xy}}]$, with acceptance ratios $R_{\mathbf{xy}} = p(\mathbf{y}) W_{\mathbf{yx}}^{\text{prop}} / p(\mathbf{x}) W_{\mathbf{xy}}^{\text{prop}}$ [Has70].

To numerically solve the **AIMs** for the Co/graphene (Sec. 3.6) and the CoCu_n/Cu(111) systems (Sec. 4.6), that is, to compute their self-energy, the **CTHYB** variant of the **CTQMC** method established within the **TRIQS** collaboration was put into use [Par15; Set16]. The algorithm is defined with respect to the **AIM** partition function as an imaginary-time path integral

$$Z = \int D[c_\alpha^*, c_\alpha, c_{n\mathbf{k}}^*, c_{n\mathbf{k}}] e^{-S[c_\alpha^*, c_\alpha, c_{n\mathbf{k}}^*, c_{n\mathbf{k}}]},$$

$$S[c_\alpha^*, c_\alpha, c_{n\mathbf{k}}^*, c_{n\mathbf{k}}] = \int_0^\beta d\tau H(c_\alpha^*(\tau), c_\alpha(\tau), c_{n\mathbf{k}}^*(\tau), c_{n\mathbf{k}}(\tau)), \quad (3.61)$$

with the action $S[c_\alpha^*, c_\alpha, c_{n\mathbf{k}}^*, c_{n\mathbf{k}}]$ being a functional in terms of the **AIM** Hamiltonian in Eq. (3.53), and the operators now being Grassmannian variables. Integrating out the conduction-electron **DOF** shown in Eq. (3.61), one arrives at the action

$$S[c_\alpha^*, c_\alpha] = \int_0^\beta d\tau H_{\text{loc}}(c_\alpha^*(\tau), c_\alpha(\tau)) + \sum_{\alpha\beta} \int_0^\beta d(\tau, \tau') c_\alpha^*(\tau) \Delta_{\alpha\beta}(\tau - \tau') c_\beta(\tau'). \quad (3.62)$$

Without **SOC**, the index α denotes the free combination of spin and orbital indices, otherwise the latter would become intertwined. The local Hamiltonian $H_{\text{loc}}(c_\alpha^*(\tau), c_\alpha(\tau))$ is the one of the isolated impurity containing **CF**, **DC** term, and screened Coulomb interaction (the second and third terms in Eq. (3.53)), and the second term in Eq. (3.62) contains the hybridization function as defined in Eqs. (3.55) and (3.56). Expanding the partition

function in the hybridization function gives

$$Z = \sum_{k \in \mathbb{N}_0} \int_0^\beta \prod_{i=1}^k d(\tau_i, \tau'_i) \sum_{\{\alpha_i, \alpha'_i\}} w(k, \{\alpha_i, \alpha'_i, \tau_i, \tau'_i\}) \quad (3.63)$$

with the weights

$$w(k, \{\alpha_i, \alpha'_i, \tau_i, \tau'_i\}) = \text{Tr} \left[\text{Te}^{-\beta H_{\text{loc}}} \prod_{i=1}^k c_{\alpha_i}^*(\tau_i) c_{\alpha'_i}(\tau'_i) \right] \cdot \text{Det}_{1 \leq i \leq k} [\Delta_{\alpha_i \alpha'_i}(\tau_i - \tau'_i)]. \quad (3.64)$$

One should note that the Boltzmann weights shown in Eq. (3.63) comprise the infinitesimals $\prod_{i=1}^k d(\tau_i, \tau'_i)$. The first factor in Eq. (3.64) is the dynamical impurity trace. To eventually calculate the GF $G_{\alpha\alpha'}(\tau, \tau') = -\langle c_\alpha(\tau) c_{\alpha'}^+(\tau') \rangle$, one should just add the two operators $c_\alpha(\tau)$ and $c_{\alpha'}^+(\tau')$ into the dynamical trace. The second factor in Eq. (3.64) contains the determinant of hybridization functions (cf. Eq. (3.62)), and results from a rearrangement within the Boltzmann weights which is possible because the conduction electrons are non-interacting. The determinantal form serves to reduce the fermionic sign problem [Gul11; Loh90; Tro05]. From Eqs. (3.63) and (3.64) one can see that the particular expansion order determines the size of the hybridization matrix, and the expansion order is peaked at its mean value $\langle k \rangle$.

The Markov chain consist of QMC updates, by which the configurations appearing in the partition function expansion in Eq. (3.63) are scanned through and their measured weights accumulated according to their importance. The QMC updates comprise insertions and removals of two or four operators, and shifts of the position of an operator. For all such operations between two configurations there exists a transition probability. The insertion of two operators $c_\alpha^*(\tau)$ and $c_{\alpha'}(\tau')$, resulting in the new configuration $(k+1, \{\alpha_i, \alpha'_i, \alpha, \alpha', \tau_i, \tau'_i, \tau, \tau'\}) = (k+1, \{\tilde{\alpha}_i, \tilde{\alpha}'_i, \tilde{\tau}_i, \tilde{\tau}'_i\})$, is proposed with probability

$$W_{(k, \{\alpha_i, \alpha'_i, \tau_i, \tau'_i\}), (k+1, \{\tilde{\alpha}_i, \tilde{\alpha}'_i, \tilde{\tau}_i, \tilde{\tau}'_i\})}^{\text{prop}} = \frac{d(\tau, \tau')}{\beta^2}, \quad (3.65)$$

and the removal of two operators is proposed with

$$W_{(k+1, \{\tilde{\alpha}_i, \tilde{\alpha}'_i, \tilde{\tau}_i, \tilde{\tau}'_i\}), (k, \{\alpha_i, \alpha'_i, \tau_i, \tau'_i\})}^{\text{prop}} = \frac{1}{(k+1)^2}. \quad (3.66)$$

The CTQMC algorithm does not rely on a discretization of the imaginary-time interval of length β , so one can understand the insertion probability as the one for two possible interaction vertex positions, and the removal probability as corresponding to the $(k+1)^2$ possibilities to choose two operators to remove. The acceptance ratio is then given by

$$R_{(k, \{\alpha_i, \alpha'_i, \tau_i, \tau'_i\}), (k+1, \{\tilde{\alpha}_i, \tilde{\alpha}'_i, \tilde{\tau}_i, \tilde{\tau}'_i\})} = \frac{w(k+1, \{\tilde{\alpha}_i, \tilde{\alpha}'_i, \tilde{\tau}_i, \tilde{\tau}'_i\})}{w(k, \{\alpha_i, \alpha'_i, \tau_i, \tau'_i\})} \frac{\beta^2}{(k+1)^2}. \quad (3.67)$$

The infinitesimals thus cancel out within the Metropolis-Hastings algorithm rendering

the continuity of the imaginary-time interval preservable; this leads to the numerical and simulation improvements mentioned in the introductory part to the present chapter; that is, the **CTQMC** algorithm makes the solution of multi-orbital **AIMs** accessible, and it takes care of specific regions in the configuration space important to be measured properly. If a proposed update is rejected during the process, the old configuration is measured again. Additional to these local **QMC** updates, one often introduces global spin-flip or orbital-flip updates to enhance equilibration and sampling efficiency, and to reduce the probability to be trapped in certain regions of the configuration space. Higher-order configurations such as the insertion or removal of four operators has been shown to be necessary for ergodicity to be ensured [Set16].

The **CTHYB** algorithm as implemented in the **TRIQS/CTHYB** code has received a couple of important improvements and optimizations to efficiently treat multi-orbital systems in the strong coupling regime. In particular, we will shortly describe the automatic partitioning (autopartition) algorithm which divides the local Hilbert space into subspaces, and the implementation of the left-leaning red-black tree [Set16].

Each update needs the calculation of the hybridization determinant and the dynamical impurity trace, both shown in Eq. (3.64). The impurity Hilbert space can be very large, in particular, it is $2^{10} = 1024$ -dimensional in case of d -orbital systems, while in case of f -orbital systems it has already $2^{14} = 16384$ dimensions. The calculation of the dynamical trace given by the first factor in Eq. (3.64) is strongly enhanced by partitioning the local Hilbert space in terms of a diagonal block structure consistent with the symmetries of the system under consideration. The matrix multiplications within the dynamical trace are then to be performed independently within the subspaces only. To give an example, the decomposition of the local Hilbert space of the Co/graphene system (Sec. 3.6) in terms of the charge and spin quantum numbers leads to $(2l + 2)^2 = 36$ diagonal blocks ($l = 2$ for d systems), while the autopartition algorithm determined 132 blocks taking into account the full Coulomb matrix (using cubic harmonics for the local orbital basis).

The second main ingredient for the efficient calculation of the dynamical trace is given by representing it in terms of a tree structure. From each node emerge two edges (branches) each ending in a new node (leave), and each node encode the pairwise product of operator products adjacent in the dynamical trace. The storage of the configurations and pairwise operator products within the trace in a tree reduces the amount of matrix multiplications to be recomputed after each **QMC** update, as always only a small subset of the leaves are changed. The computational time needed for the **AIM** solution is greatly reduced by the tree structure compared to the **HFQMC** time discretization (cf. introductory part to this chapter); an example for a five-orbital system hosting three electrons subject to the Slater-Coulomb interaction showed a reduction in computational time of up to three orders of magnitude [Set16]. The scaling of computational demands for the tree is $\mathcal{O}(\log_2(\beta))$, while that of the determinants is $\mathcal{O}(\beta^3)$ (the average perturbation order $\langle k \rangle$ is approximately proportional to β). Hence, at low temperatures the computation of the hybridization determinants dominates over that of the dynamical trace, while for high temperatures it will be the reverse. As the determinants are easier to compute than the dynamical trace, lower temperatures thus become more accessible due to the tree structure.

3.4 The stochastic optimization method

To obtain physical information from the imaginary-time GF one needs to perform an analytical continuation to real times, where the spectrum becomes accessible via a Fourier and Hilbert transform (cf. Eq. (3.36)). The fermionic spectrum is eventually given by the Fredholm integral equation

$$G(\tau) = - \int d\omega \frac{e^{-\tau\omega}}{e^{-\beta\omega} + 1} A(\omega), \quad (3.68)$$

where τ lies on the imaginary-time axis. Due to the noise in the QMC data, the task belongs to the class of ill-posed problem, and no unique mathematical solution exists, that is, there are infinitely many solutions $A(\omega)$ which yield some imaginary-time GF within the error-bars of $G(\tau)$. The principal approach, then, is to choose some method for the solution of the Fredholm equation, and supply some additional information with specifications for the solution [Gou17; Mis12].

We closely follow the exposition in Ref. [Mis12]. The first of such methods is the least-squares fit, which seeks to minimize the deviation measure $\|\mathcal{K}(A) - G\|^2$. The kernel operator \mathcal{K} maps the spectrum to the right hand side of the Fredholm equation in Eq. (3.68). Usually one transforms the continuous version of the least-squares fitting problem to a matrix equation by discretizing the energy interval on which the spectrum is defined, $\|\underline{K}\mathbf{A} - \mathbf{G}\|^2$, where \mathbf{A} is now a vector with as many components as the number of discrete energy points. The kernel operator becomes a (generally rectangular) matrix admitting a singular value decomposition $\underline{K} = \underline{U}\underline{\Sigma}\underline{V}^+$, with \underline{U} and \underline{V} being unitary matrices, and $\underline{\Sigma}$ a (rectangular) diagonal matrix holding the singular values of \underline{K} . As the outcome of a numerical calculation, the GF $G(\tau)$ is already discrete. Simple inversion of the matrix equation then yields the spectrum \mathbf{A} , but often rendered with the sawtooth noise due to the inversion of the sometimes small singular values within $\underline{\Sigma}$. To reduce this problem, the deviation measure is accompanied by some regularization functional $\lambda\mathcal{F}(A)$ which ought to suppress large oscillations of the solution. For example, within the Tikhonov-Phillips regularization method the discretized functional has the form $\lambda^2\|\underline{\Gamma}\mathbf{A}\|^2$ (e.g., with $\underline{\Gamma} = \underline{1}$).

The approaches to solving the Fredholm equation can be represented within Bayes' theorem [Bay63],

$$P[A|G]P[G] = P[G|A]P[A]. \quad (3.69)$$

$P[A|G]$ yields the probability of A given G , and it is proportional to the likelihood function $P[G|A]$ and the prior knowledge $P[A]$, in terms of which the problem is easier to solve. In the Tikhonov-Phillips regularization method both functions are given by $P[G|A] \propto e^{-\|\underline{K}\mathbf{A} - \mathbf{G}\|^2}$ and $P[A] \propto e^{-\lambda^2\|\underline{\Gamma}\mathbf{A}\|^2}$, and if $\underline{\Gamma}$ is just the identity matrix, the modified singular matrix has inverted singular values $\Sigma_{ii}^{-1} = \sigma_i/(\sigma_i^2 + \lambda^2)$, so that contributions with $\sigma_i \ll \lambda$ are now suppressed. However, some interesting physical problems just contain sharp edges or peaks, such as the Kondo model with its narrow QP peak near the Fermi level (Chpt. 4). One approach more appropriate for sharp peaks is the maximum entropy method (MEM) (also called MaxEnt) which takes as prior knowledge about the spectrum that it is close

to some default model. The **MEM** collects possible particular solutions $\tilde{A}(\omega)$ by the likelihood function $P[G|\tilde{A}] = e^{-\chi^2[\tilde{A}]/2}$ with $\chi^2[\tilde{A}] = \sum_{m=1}^M S^{-1}(\tau_m)(G(\tau_m) - \tilde{G}(\tau_m))^2$ ($G(\tau_m)$ being the imaginary-time **GF** from **QMC**, $\tilde{G}(m)$ the particular solution obtained from $\tilde{A}(\omega)$ via Eq. (3.68), and $S(\tau_m)$ proportional to the noise of the **QMC** data), and by the prior knowledge $P[\tilde{A}] = e^{S[\tilde{A}]/\alpha}$ with entropy $S[\tilde{A}] = -\int d\omega \tilde{A}(\omega) \ln(\tilde{A}(\omega)/D(\omega))$ ($D(\omega)$ being the spectrum of the default model). The solution is finally given by the average $A = \int d\tilde{A} \tilde{A} P[\tilde{A}|G]$. The default model may contain often known information, such as peak shapes. Via the parameter α one can balance the weight on either the regularization strength or the deviation minimization. Clearly, not enough regularization may lead to over-fitting, but too much may render the default model having too much importance. More details and references on MEM can be found in Ref. [Kar13]. As the default model is somewhat reducing the flexibility of the **MEM**, one may employ the **stochastic sampling method (SSM)**, which is just given by the likelihood function $P[\tilde{A}|G] = e^{-\chi^2[\tilde{A}]/T}$, where T is a fictitious temperature which may be changed during the optimization (e.g., to escape local minima one may temporarily increase the temperature). Regularization is assumed to be performed by the implicit error cancellation during the averaging between particular solutions (like with the **MEM**). The interpretation of the likelihood function $P[\tilde{A}|G]$ in terms of Boltzmann weights allows the organization of a **QMC** procedure to sample the particular solutions \tilde{A} . No default model is assumed, no artificial smoothing performed, and only little prior knowledge is needed, for example, positive definiteness and normalization.

A variant or successor of such **SSMs** is given by the even more flexible and powerful **SOM** [Kri19; Mis12; Mis15; Mis00], which has been used for the Co/graphene (Sec. 3.6) and the CoCu_n/Cu(111) systems (Sec. 4.6). It does not even rely on an interpretation of conditional probabilities as Boltzmann weights, or of averages as partition functions. Yet it is organized on the basis of a powerful **QMC**-like procedure for the accumulation of particular solutions and the averaging between them. **SOM**, which is going to be discussed below in more detail, is well adapted to resolve spectral fine structures, such as narrow peaks, while not neglecting the overall structure of the spectrum. The latter dominates in more metallic-behaved systems, such as the Co/graphene system is suggest to be by our results. But the power of the **SOM** lies in the resolution of narrow peaks, such as the Kondo features near the Fermi level. In the analytical continuation of the **QMC** data for CoCu_n/Cu(111) systems it allowed for the resolution of the Kondo peaks within each orbital along with their relative arrangement, so that substructures within the narrow energy range around the Fermi level, which emerge due to the symmetry breaking induced by an additional Cu chain near the Co adatom, could be displayed.

In the projects on the Co/graphene (Sec. 3.6) and the CoCu_n/Cu(111) systems (Sec. 4.6) the analytical continuation of the imaginary-time **GF** to real times was performed using the **TRIQS**-based implementation of Mishchenko's **SOM** [Kri19]. It amounts to an accumulation of L particular solutions \tilde{A} , which satisfy the constraint that the deviation measure

$$\chi[\tilde{A}] = \sum_{m=1}^M \left| \frac{G(\tau_m) - \tilde{G}(\tau_m)}{S(\tau_m)} \right| \quad (3.70)$$

is smaller than some small constant, and to a weighted average between them,

$$A(\omega) = \sum_{j=1}^L \xi_j \tilde{A}_j(\omega), \quad (3.71)$$

for example, with $\xi_j = 1/L$. As in the **MEM** approaches, the function $S(\tau_m)$ can be set proportional to the noise of the **QMC** data if it is known. In the projects reported on, it was set to a constant, so all data points were considered with an equal weight. While the **GF** is still given on a discrete data set, the spectrum itself is allowed to live on a continuous energy range. The particular solutions (also called configurations) are parametrized by K rectangles,

$$\tilde{A}(\omega) = \sum_{i=1}^K \eta_{P_i}(\omega), \quad \eta_{P_i} = h_i(\theta(\omega - (c_i - w_i/2)) - \theta(\omega - (c_i + w_i/2))), \quad (3.72)$$

where the tuple $P_i = (h_i, w_i, c_i)$ holds the height, width, and position of the rectangle, which are subject to the normalization constraint

$$\sum_{i=1}^K h_i w_i = 1. \quad (3.73)$$

The imaginary-time **GF** data points computed from the particular solution in Eq. (3.72) are given by

$$\tilde{G}(\tau_m) = \sum_{i=1}^K h_i \int_{c_i - w_i/2}^{c_i + w_i/2} d\omega K(\tau_m, \omega) \quad (3.74)$$

with the kernel given in Eq. (3.68). While the first implementation of the **SOM** by Mishchenko tabulates these integration data beforehand and recomputes the **GF** after each update [Mis12], the more recent **TRIQS**-based implementation [Kri19] improves on this fact by an “aggressive caching” of the integration data, holding added or changed contributions in a separate cache, from where they can be reloaded if needed.

SOM performs a Markov-chain sampling of particular solutions, which is organized according to the Metropolis-Hastings algorithm [Has70; How71]. It starts from a randomly generated configuration $C = \{P_i | i = 1, \dots, K\}$ of $K < K_{\max}$ rectangles satisfying the normalization constraint Eq. (3.73), and performs F global updates $C_j(f) \rightarrow C_j(f+1)$ on the configurations, each consisting of a given number of elementary updates. There are two classes of elementary updates, the ones which do not change the number of rectangles, and the ones which do. To the first class belong the updates which change the parameters of one rectangle $P_i = (h_i, w_i, c_i)$, or the height (weight) of two rectangles, while the other class contains updates which add, remove, or split one rectangle, or glue together two

rectangles. The elementary updates are accepted with probabilities

$$P_{r,r+1} = \begin{cases} 1 & \text{if } \chi[C(r+1)] \leq \chi[C(r)], \\ (\chi[C(r)]/\chi[C(r+1)])^{1+d} & \text{if } \chi[C(r+1)] > \chi[C(r)], \end{cases} \quad (3.75)$$

and the global update is accepted if $\chi[C(f+1)] < \chi[C(f)]$. Starting with a small number L of particular solutions, the number F of global updates is adjusted at the beginning in such a way, that the resulting fit to the QMC result $G(\tau_m)$ is within its error bars in more than half of these L attempts, otherwise the number F is increased. After that, a large number L of particular solutions is accumulated. To ensure ergodicity, for a certain time the parameter d in Eq. (3.75) is first chosen from the interval $(0,1]$, which allows escaping local minima within the Markovian phase space, and for the rest of the time from the interval $[1, d_{\max}]$, to decrease the deviation measure. For regularization and avoidance of over-fitting, all particular solutions satisfying $\chi[\tilde{A}_j] \leq 2 \min(\chi[\tilde{A}_j])$ are included in the final average in Eq. (3.71), so it has the form

$$A(\omega) = \frac{1}{L_{\text{good}}} \sum_{j=1}^L \theta(2 \min(\chi[\tilde{A}_j]) - \chi[\tilde{A}_j]) \tilde{A}_j(\omega), \quad L_{\text{good}} = \sum_{j=1}^L \theta(2 \min(\chi[\tilde{A}_j]) - \chi[\tilde{A}_j]). \quad (3.76)$$

Spectra obtained via the SOM are presented in Fig. 3.5 and in Sec. 4.6.

3.5 Context of the Co/graphene system

The combination of DFT (Sec. 2.1) with the DMFT (Subsec. 3.2.1) is nowadays a common approach to study strongly correlated materials in an advanced setting. DFT is incapable to properly represent the many-body effects present due to the strong Coulomb interaction between the electrons in such materials, as it describes these on the effective single-electron KS level. The reason for the strength of the electronic correlations roots in the competition between delocalization trends due to hybridization, which are well described in DFT, and strong localization trends due to residing TM or rare-earth elements, attracting and localizing electrons in their valence shells. In strongly correlated systems, localization is at least on the same energy scale as delocalization, such as in Hund's metals [Fan15; Geo13; Kha15], or even much stronger, such as in f -element systems (cf. Sec. 3.2).

In order to include material-specific data in the many body treatment, a preceding DFT calculation has to be performed to obtain the background on which the correlations can be formulated and take place. These correlations are well described by the Hubbard lattice model, to which the DMFT is an approximate, local solution (cf. Subsec: 3.2.1, and references in introductory part to this chapter). DMFT amounts to considering a single correlated site within the lattice as an impurity, which is self-consistently embedded in the bath of conduction electrons, so that the resulting lattice GF contains the local correlations. The DFT+DMFT approach thereby is equivalent to a self-consistent embedding of the AIM, for which the parameters were computed previously with DFT, into the Hubbard model (Subsecs. 3.2.1 and Appx. C.2).

To determine the Coulomb interaction matrix for the many body AIM or Hubbard model, the cRPA can be employed (cf. Subsec. 3.1.2 and references therein). The cRPA is capable of computing the screened Coulomb interaction parameters on all sites within the material under consideration. However, most AIM solvers (commonly called quantum impurity (QI) solvers) and DMFT studies resort to different approximations for the Coulomb interaction matrix, for its determination demands extra simulations (and the AIM solvers need to be extended for being able to take all the Coulomb matrix elements into account). The Slater and the density-density approximations, which assume the full Coulomb interaction spherically symmetric or without spin-flip terms, respectively, have become widely used [Kar13]. The CTHYB impurity solver (Sec. 3.3) employed within the projects reported on in this thesis can take into account the full Coulomb interaction matrix provided by the cRPA method. – There are other few such studies which consider the full Coulomb matrix. Ref. [Zha16] finds that the geometric anisotropies, though comparatively small, compete with the SOC and the isotropic part of the Coulomb interaction, leading to a correct reshaping of the Fermi surface in accordance with experiments. Furthermore, the authors find the self-energy in the low-energy region being quantitatively different from the HF counterpart, which is at the root of the reshaping. The results were found for bulk systems (in particular, Sr_2RuO_4), but they apply to surface systems as well. In our Co/graphene study in Sec. 3.6 we made a similar conclusion for the low-energy self-energy and predicted its possible relevance for the Kondo effect in multi-orbital systems (Chpt. 4). Ref. [Han13b] calculated the full Coulomb matrix in a number of surface systems by means of the cRPA, and found additionally the inter-site Coulomb interactions relevant. In Ref. [Han13c] the authors used these results within the $GW+DMFT$ approach to calculate photoemission spectra in a set of two-dimensional correlated systems, though with a QI solver taking into account the frequency-dependence of the Coulomb interaction and not all of its matrix elements.

However, not all systems of interest need the full DMFT self-consistency. There are the systems comprised by correlated impurities embedded in an (approximately) non-interacting environment, for example, TM or rear-earth elemental adsorbates on metallic or differently behaved surfaces. For such systems there is no self-consistency needed since the impurity GF of the corresponding AIM should not be identified with the GF of a lattice system, that is, one performs only one QMC calculation using the CTHYB solver (which amounts to single-shot DMFT).

An interesting example of such a system is given by a Co adatom on a monolayer graphene surface [Eel13]. On the one hand, here we have the situation of a strongly correlated impurity embedded in a non-correlated environment (i.e., the graphene systems is considered as non-interacting in view of the physics to be described on the Co impurity, because its pseudo-gap is actually a result of the electronic correlations, c.f. Ref. [Weh11]). On the other hand, there are further physical effects caused by the symmetry breaking introduced by the two-dimensional geometry. On top of strong electronic correlations on a single atom resulting in many body effects, there will thus be anisotropies appearing in the system, which call for an efficient and full treatment beyond the spherical approximation. In Sec. 3.6 these anisotropies were taken into account by the cRPA, thereby providing us with an anisotropic full Coulomb interaction matrix for the Co adatom. One may expect

that the anisotropies are somewhat relevant in an environment with a reduced DOS near the Fermi level. But we observed this expectation not being met in the Co/graphene system, probably because graphene becomes doped, that is, its Fermi level is shifted away from the Dirac cone due to the presence of the Co adatom. Another reason, which in part might result from this doping, is the generally enhanced screening of the Coulomb interaction on metallic surfaces [Şaş12].

We now shortly recapitulate the working procedure, referring to the sections which have so far worked out the computational details: To compute the full Coulomb interaction matrix using the **cRPA** method (Subsec. 3.1.2), we employed the Spex-Fleur program [Fri10], a part of the Jülich **FLAPW** code family [Jül]. It is based on the **full-potential linearized augmented plane-wave (FLAPW)** method, and uses **MLWFs**. Since the screening is reduced perpendicularly to the graphene surface, we observe that the Coulomb interaction matrix elements are larger along this direction. In parallel we performed a **DFT-GGA** calculation with **VASP** using the same basis set. By using the **DFT++** method [Kar11b], we extracted the **CF** splitting within the cobalt adatom due to the two-dimensional hexagonal graphene environment, and the hybridization between the two (cf. Subsec. 3.2.1).

Since **DFT** already contains some electronic correlations due to the Coulomb interaction, they must be subtracted from the **CF** in the form of a **DC** correction (cf. Sec. 3.2). **DFT** (without the Coulomb correction within **DFT+U**) does not show any anisotropies in the correlation effects as it treats them on a **MF** level, and thus the **DC** correction, measured with respect to an anisotropic Coulomb matrix, will itself already be anisotropic. To determine the **DC** correction, we employed a Hubbard-I approximation, and adjusted occupancies to those obtained by **DFT** using a numerical optimization scheme (differential evolution; for details refer to Sec. 3.6). This procedure is quite a common route [Kar13], though not as sophisticated as the “exact” **DC** approach presented in Appx. C.1.

Having determined all the parameters of the **AIM** for Co on graphene, we subsequently performed the full simulation using the **TRIQS/CTHYB-QI** solver (Sec. 3.3). From the imaginary-time **GF**, analytic continuation to real frequencies with the **SOM** was performed (3.4), which is able to properly resolve multiplet structures within the spectral density. This point turned out as not crucial neither for the Co/graphene system itself nor for the comparison of results obtained with the **cRPA** and the Slater Coulomb matrices; but if there happened to be sharp **QP** peaks (cf. Chpt. 4), such as the narrow Kondo peak at the Fermi level, this ability would have been relevant.

We now proceed with the embedding of the Co/graphene system into the current state of research. First, the graphene substrate itself has already recently attracted a lot of attention since its experimental realization [Nov04]. But its peculiar electronic properties were already known since the 1940s, see Refs. [Cas09; Gei07] and references therein. Graphene is an atomically thin allotrope of carbon arranged in a two-dimensional hexagonal lattice. This arrangement of carbon leads to electronic excitations around the Fermi level which behave like massless Dirac particles, so that graphene can be described within the framework of fully relativistic **QED**, that is, by a Lorentz-invariant theory. The sp^2 hybridization, with the hybrid orbitals arranged within a trigonal planar structure and taking part in σ -bonding, gives graphene its stability and flexibility, while the p_z orbitals, taking part in π -bonding, exhibit the Dirac cone in the band structure of graphene and are

half-filled. The Dirac cone leads likewise to a linearly vanishing DOSs at the Fermi level, a pseudo-gap, which renders graphene being a semi-metal. Together with the consequently reduced screening of the electronic Coulomb interactions, graphene provides a material realization accompanying the studies of strongly interacting electrons on the hexagonal lattice [Hir18]. The electronic flexibility and strong correlations render the vdW forces being relevant for graphene, especially between neighboring graphene layers (graphite), as the screening in the perpendicular direction is even less effective [Ryd03]. The flexibility of graphene in response to external conditions leads to diverse physics, enhances its potential for functionalization, and may establish a new branch next to the semiconductor industry.

The electronic interactions in graphene are such that, together with the lattice structure, they lead to the pseudo-gap, a transitional behaviour between Mottness (a correlation gap) and band-structure-like semi-metallicity, with linearly dispersed excitations [Kot12]. The Dirac cone is the sign that one has a Dirac liquid if Lorentz invariant QPs in the weak-coupling regime. This has to be contrasted to the usual Galilean invariance for fermions leading to different dispersions, and on which Landau's FL theory relies (cf. introductory part to Chpt. 4). Thus also, the Coulomb interaction is not as in metals, for it remains long-ranged at charge-neutrality because the screening is ineffective. However, a slight shift of the chemical potential away from the Fermi level leads again to an efficient screening, as we also observed for the Co/graphene system (Sec. 3.6). The presence of the Co adatom leads to a chemical doping of the graphene sheet, and as screening at metal surfaces appears rather efficient [Şaş12], we obtained a likewise strongly reduced local Coulomb interaction strength.

Within the GF formalism, a pseudo-gap appears from a singularity of the self-energy at low energies. As explained in the introductory part to the present chapter, the self-energy is an effective (single-particle) energy-dependent potential which replaces the Coulomb interaction in the full Hamiltonian, and it thus encompasses all information about the correlations in the system. In principle, via a fluctuation diagnostics one may identify the root of the correlations leading to the pseudo-gap [Gun15], probably also the one seen in our calculated spectrum at lower Co adatom filling (Fig. 5 in Sec. 3.6). Here, the reduced adatom filling leads to an imprint of the graphene pseudo-gap on the adatom itself. However, even though one can see the pseudo-gap in that case, and also in the hybridization function (Fig. 1 in Sec. 3.6), the BZ \mathbf{k} -dependence necessary for the fluctuation diagnostics is lost in the AIM construction. – This also means that the multi-channel Kondo effect often assumed to exist for graphene (Sec. 3.5), and which relies on two of the high-symmetry BZ points, K and K' , cannot be transparently described within the AIM construction given in Sec. 3.2; for this one needs to adapt the AIM to the form used for quantum dots coupled to several leads. Still, one may assume that all realistic AIMs constructed according to Sec. 3.2 will show the usual multi-orbital Kondo effect with Fermi-liquid behaviour (i.e., without under- or overscreening), because there will always be one hybridization channel for each orbital. The Kondo effect on graphene has been subject to intensive research within the last fifteen years, see the discussion below.

The precise adsorption geometry and electronic configuration of the Co/graphene system was addressed in a number of experimental and quantum-chemical studies. These went beyond the relaxation procedures usually performed within DFT, and took into account

the correlations in a more sophisticated manner. Eelbo *et al.* found the Co atom mostly adsorbed directly above a carbon atom of graphene [Eel13], that is, top-site adsorption. Furthermore, they determined the electronic configuration of $3d^84s^1$, with an out-of-plane easy axis leading to sizable spin and orbital moments. Thus, the Co adatom on graphene was found to be in a magnetic state. Fe was found to be magnetic as well, while Ni was non-magnetic. Shortly before that experimental outcome, two other studies were published; one based on an *ab initio* many body treatment within auxiliary-field QMC (AFQMC) and a subsequent size-correction embedding scheme (which corrects for the finiteness of the graphene flake used for the calculations) [Vir12], and another one based on an active-space self-consistent field (ASSCF) approach with second-order PT [Rud12]. Both considered the hollow site being the most stable one, and found mainly three different electronic configurations assumed by the Co atom while it approaches the surface: high-spin ($S = 3/2$) $3d^74s^2$, high-spin ($S = 1$) $3d^84s^1$, and a low-spin ($S = 1/2$) $3d^94s^0$. Virgus *et al.* mentioned, though, that the true spin state remains unclear, and that it depends on the correlations considered. The study of Rudenko *et al.* describes the same electronic transitions while the Co atom approaches the graphene surface above the hollow site, but also laid down some further insights. Dispersive (vdW) interactions are contained in their computational approach, and the Co atom could be stabilized in the high-spin $3d^74s^2$ electronic state (the one of free Co) at a distance of approximately 1.6 Å above the surface. While approaching the surface, the electron is successively transferred from the 4s to the 3d orbital, finally realizing the low-spin $3d^94s^0$ state. This charge transfer is organized according to the Pauli exclusion principle, as the 4s orbital is more extended than the 3d orbital, the Coulomb repulsion within which additionally being screened. However, because the differences in the adsorption energies between the states came out as rather small, and as the $3d^94s^0$ configuration is more unstable due to the localized charge accumulation, the $3d^74s^2$ state is assumed to be preferred by the Co atom. The $3d^84s^1$ state is then considered as a metastable state between the other two states. In this state, as the adsorption height of approximately 2.2 Å is rather large, the Co atom is assumed to be physisorbed, the mechanism being induced by the weak vdW interactions. In principle, this might be a second example next to the Ta(001)-p(3×3)-O surface considered in Chpt. 2, where unusual large adsorption heights might be realized by vdW interactions, against the actually stronger bonding mechanism induced by hybridization and chemisorption, which lead to smaller adsorption heights. In principle, this goes along to many experimentally observed fast surface diffusions of TM atoms on graphene. Intuitively, it is certainly rather difficult to determine the adsorption properties of TM adatoms on graphene due to its Dirac nature. Most computational schemes rely on some approximations, but the vanishing DOSs near the Fermi level (small chemical doping will certainly be realized by adsorption) and the rather large electronic correlations in graphene need some consideration for the numerical results to be reliable. The ASSCF can be considered as an already sophisticated approach to the situation at hand.

The Coulomb correlations on the Co atom are determined to be reduced upon its approach to the surface, from 5.3 eV to $2.6 \text{ eV} \pm 0.2 \text{ eV}$ [Rud12]. The strength and tendency is in line with our results for the local Coulomb interaction strength of the Co/graphene system as determined within the cRPA. Here, the largest strength 2.2 eV was found in the

direction perpendicular to the graphene surface (in the d_{z^2} orbital), while in the other directions screening was even more effective due to the high electron mobility and large polarizability. Furthermore, we considered the Co atom chemisorbed at lower adsorption height. This outcome is rather counterintuitive, as one might think that screening of the local Coulomb interaction is less efficient on surfaces than in bulks, but indeed the reverse seems to be true on metals, as has already been mentioned [Şaş12]. While on metal surfaces one might think that surface charge accumulation and enhanced polarizability due to longer electron propagation paths in the vacuum above the surface might prevail, only the mobility and polarizability in free-standing monolayer graphene will contribute to this enhanced screening.

The Kondo problem in graphene has been debated extensively shortly after its first experimental realization in 2004 [Nov04]. Only very few experimental realizations of adatoms on graphene are published, with different outcomes for the Kondo effect. De Mattos provided the first experiments on the Co/graphene system and discussed the resonance appearing near the Fermi level in terms of the multi-channel Kondo effect [Mat09]. The honeycomb lattice as a bipartite lattice has two inequivalent carbon atoms in real space, and correspondingly two inequivalent points, K and K' , in the first BZ. At these two points the Dirac cones touch, while the van-Hove singularities are at the other high-symmetry points (Γ and M). The energy profile looks as if it has two inequivalent valleys at the Dirac points separated by high-energy states. These act as two separate electron reservoirs coupling to each orbital of the adatom under consideration, which leads to the two-channel Kondo effect, and finally to overscreening and a non-FL state (if the coupling to both valleys has the same strength; cf. introductory part to Chpt. 4). The sublattice symmetry leads to a conserved quantum number, a pseudospin, and to chirality of the electrons in graphene. The Hamiltonian in graphene couples the pseudospin with the direction of motion, which modifies the scattering mechanisms, leading to an even more exotic, highly entangled Kondo behaviour.

Shortly after de Mattos, Brar *et al.* provided another realization of the Co/graphene system, where they observed dip-like features in the differential conductance [Bra11] (cf. also Chpt. 4). Kondo resonances strongly depend on the impurity filling (Chpt. 4), but these authors found the width of the dip independent of the gate voltage (graphene was back-gated), with which the Co adatom ionization can eventually be controlled. Supported by numerical calculations including phononic vibrations, they concluded that these dips are due to vibrational inelastic electron tunneling, induced by a residual magnetic state on the Co adatom, which leads to large screening clouds seen in STM images, and eventually increases the resistivity at low temperatures. Jobst *et al.* also attributed the increase of the resistivity at low temperatures to electron-electron interactions (EEl) and weak localization, the latter being enhanced due to the two-dimensional geometry of graphene [Dat95; Job13]. The contribution from weak localization can be suppressed by the application of an external magnetic field, though, and the EEl and Kondo contributions analysed. The conclusion for the EEl being responsible for the resonances was then attained by a careful disentanglement analysis of the EEl-mediated resistivity increase and the one induced by the Kondo effect. They furthermore point out that adsorbed magnetic molecules can induce inhomogeneities in the sample, and graphene is particularly likely to

produce ripples [Mey07]. Those ripples are the reason for the enhanced **EEIs** in graphene. Based on their findings Jobst *et al.* state that the interpretation of most experimental results in terms of the Kondo effect are probably questionable. – In a theoretical paper, Saffarzadeh *et al.* attribute the resonances appearing at the Fermi level to spin-dependent scattering subject to gate voltage dependence [Saf12], that is, to the inelastic electron tunneling observed in the experiments by Brar *et al.* [Bra11]. In particular, they point out that Co has the highest **magnetic anisotropy energy (MAE)** among **TM** adsorbates on graphene, leading to the residual magnetic moment. The resonance was obtained within the usual T -matrix formalism (cf. Sec. 4.4).

Based on the Kondo interpretation, de Mattos found a Kondo temperature of 15 K [Mat09], which translates to an inverse Kondo temperature of approximately 773 eV^{-1} . The highest inverse temperature used for the test simulations in our Co/graphene study (Sec. 3.6) was 70 eV^{-1} . So even with the consideration of the full anisotropic Coulomb matrix, and even within the sophisticated **TRIQS/CTHYB-QI** solver it would not have been possible to account for any residual traces of the Kondo effect. Irrespective of the physical complexity of an experimentally realized Co/graphene system, which might suppress the Kondo effect, or render **EEIs** responsible for the experimentally observed spectral features near the Fermi level, the parameters of an associated **AIM** as shown in 3.2 will likely lie within the Kondo regime, though probably with a small Kondo temperature. Our study on the Co/graphene system was not directed towards the resolution of the Kondo resonance near the Fermi level, but to the effects of the Coulomb anisotropies on the overall spectral structure (Sec. 3.6). While experimentally realized Co/graphene systems will probably not show any Kondo behaviour at low temperatures, it is, however, still necessary to understand its origins and properties in ideal situations, either because these situations might be the starting points for other analyses, or to know how to disentangle the processes or interactions possibly responsible for the spectral features at the Fermi level.

While inter-valley scattering in graphene might occur, which could merge the two valleys into just one electron reservoir, Kharitonov and Kotliar assumed this scattering as kind of unitary transformation retaining the two-channel structure, and thus the multi-channel Kondo scenario with overscreening and non-**FL** behaviour [Kha13] (in particular, the valleys may be mixed, but the diagonalized states are of the same structure, and so the channels remain independent; cf. Chpt. 4). One of the first such studies on the mathematical structure of the Kondo effect in graphene was performed by Segupta and Baskaran [Sen08] four years after its first experimental realization by Novoselov *et al.* [Nov04]. During their derivation they note that the Dirac nature of the **QPs** in graphene leads to a coupling of different angular momentum channels in the Kondo Hamiltonian, which distinguishes it from the usual Kondo Hamiltonian in metals. Furthermore, due to the vanishing **DOSs** at the Fermi level, the critical coupling for the onset of the Kondo effect at zero temperature is large, and increases logarithmically with temperature. However, at finite gate voltage the critical coupling tends to vanish at low temperatures, which opens the possibility to tune the Kondo effect by gating. The finite critical coupling is associated with the non-**FL** behaviour. Zhu *et al.* further investigated the site dependence, and took into account the vanishing hybridization in the direction perpendicular to the surface (in the hollow site), because the π orbitals of graphene, to which the adatoms are assumed to couple

via hybridization, transform according to the E_1 and E_2 representations of C_{6v} (near the Dirac point) [Zhu10]. The valley degeneracy was only relevant at top-site adsorption, and there it only affects the Kondo temperature, instead of producing the exotic overscreened Kondo effect appearing at the hollow site. The same site dependence and other Kondo scenarios were also considered by Wehling *et al.*, who stated the occurrence of the SU(4) Kondo effect due to the orbital structure of the Co adatom, which gets broken down to SU(2) if the SOC is taken into account [Weh10]. As the M points in the first BZ contain the van-Hove singularities (the strength of the asymmetric Kondo couplings in part results from high-energy processes to those singularities), orbitals of different symmetry couple differently to these points, which is the reason for the different hybridization strengths, and which also leads to the asymmetric behaviour of the Kondo temperature with respect to the chemical potential or the gate voltage, respectively. Wehling *et al.* stated that intervalley scattering is very strong at the hollow site [Weh10], which was also confirmed by Zhu *et al.* [Zhu10], so that the multi-channel Kondo effect should not prevail here. However, as mentioned above, Kharitonov and Kotliar stated that the multi-channel behaviour would be retained also in case of strong intervalley scattering [Kha13]. Even more, these authors extended the scenario to the four-channel Kondo effect because each sublattice has its own two inequivalent high-symmetry BZ points. – The SOC was also considered in Ref. [Mas14] in an effective single-orbital AIM solved by NRG. The SOC occurs in a combined manner intrinsically due to high atomic numbers of the adsorbed species, and extrinsically due to the spatial symmetry breaking due to the two-dimensionality of the graphene sheet. Also in Ref. [Mas14] the Co adatom happens to have a magnetic moment depending on the adsorption site, and the authors considered the top site only. The Kondo effect was found to strongly depend on the SOC strength not only because of the symmetry breaking, but also because it induces a non-vanishing DOSs at the Fermi level.

A series of studies on Kondo impurities in graphene was performed by Fritz and Vojta *et al.* [Voj15; Voj04; Voj10]. As in other studies, they pointed out the similarity of the Kondo effect in d -wave SCs, which exhibit a vanishing DOSs at the Fermi level, and charge-neutral graphene. Thus, most of their studies were directed to pseudo-gapped systems in general. The phase diagram of the Kondo model was analyzed with NRG under consideration of the power-law behaviour of the DOSs near the Fermi level. In particular, they found a highly mathematical behaviour at particle-hole symmetry, in which there is no Kondo effect at any strength of the Kondo coupling, while any deviation from particle-hole symmetry immediately leads to the screened phase. Such a symmetry breaking, however, is already induced by the next-to-nearest-neighbour hopping, so it is in principle unavoidable. Furthermore, charge and spin fluctuations become strongly coupled at the case of unit slope, as is the case for graphene. The complexity of the phase space of the Kondo model for graphene was pointed out, in particular, its multi-dimensional scaling dependence.

There was one other notable study on the Co/graphene system in terms of a realistic many body calculation within the GGA+OCA approach conducted by Jacob and Kotliar [Jac10], in which Dirac point resonances were observed for the AIM, and which were attributed to the Kondo effect. The one-crossing approximation (OCA) is the lowest-order self-consistent approximation to the full perturbation expansion, and exact up to first order in the hybridization. In this sense the hoppings most relevant for the Kondo effect can be

taken into account, and it is especially powerful as the calculation can be performed at zero temperature. The adsorption height was beforehand determined being similar as in our Co/graphene study (i.e., 1.5 Å in Ref. [Jac10] and 1.53 Å in Sec. 3.6), but the starting occupation of 7.5 was lower, with two holes in the E_1 , and one hole in the E_2 orbitals. These combine to yield the spin- $\frac{3}{2}$ Kondo effect. A strong dependence of the Kondo effect on the chemical potential was found, with the resonance pinned to the Dirac point. – In our GGA+QMC study on the Co/graphene system (Sec. 3.6) we refer to Ref. [Jac10] on several occasions due to two reasons: First, as the definition of an impurity filling is to some extent arbitrary, we used their obtained impurity filling for another set of QMC simulations, and compared the results with the ones obtained with the higher fillings our DFT calculations yielded. The QMC results show a strong dependence of the electronic structure on the impurity filling, which is prominently seen in the orbitals of E_1 symmetry, for these are the ones which are hybridized the most. Second, QMC takes into account all diagrams rather than only the ones to first order in the hybridization. Thus, except for the low-temperature problem inherent in all QMC procedures, QMC is a powerful extension and generalization of the OCA. In case of higher temperatures, such as the ones considered in Sec. 3.6 and in test simulations on the Co/graphene system, rather metallic behaviour is seen, so that taking into account all diagrams is indispensable. But also in the Kondo regime of multi-orbital systems higher-order diagrams should be taken into account, for these might contribute significantly to the Kondo effect (Sec. 4.1).

3.6 “Cobalt adatoms on graphene: Effects of anisotropies on the correlated electronic structure”

Reprinted with permission from

R. Mozara, M. Valentyuk, I. Krivenko, E. Şaşıoğlu, J. Kolorenč,
and A. I. Lichtenstein
Phys. Rev. B 97, 085133 (2018) [[Moz18](#)]

© 2018 American Physical Society

DFT calculations were performed by M. Valentyuk, **cRPA** calculations by E. Şaşıoğlu, **CTQMC** and **SOM** calculations by J.R.S.M. I. Krivenko contributed to the **TRIQS/CTHYB** code, and wrote the **SOM** code. **ED** calculations were performed by J. Kolorenč. All results were gathered and organized by J.R.S.M. The manuscript was written by J. Kolorenč and J.R.S.M. All authors discussed the results and commented on the manuscript.

The reference numbers in this reprinted article are valid within this article only.

Cobalt adatoms on graphene: Effects of anisotropies on the correlated electronic structureR. Mozara,^{1,*} M. Valentyuk,^{1,2} I. Krivenko,^{1,3} E. Şaşıoğlu,^{4,5} J. Kolorenč,⁶ and A. I. Lichtenstein^{1,2}¹*Institute of Theoretical Physics, University of Hamburg, Jungiusstraße 9, 20355 Hamburg, Germany*²*Department of Theoretical Physics and Applied Mathematics, Ural Federal University, 19 Mira Street, Yekaterinburg, 620002, Russia*³*LSA Physics, Randall Lab, University of Michigan, 450 Church Street, Ann Arbor, Michigan 48109-1040, USA*⁴*Peter Grünberg Institute and Institute for Advanced Simulation, Forschungszentrum Jülich and JARA, 52425 Jülich, Germany*⁵*Institute of Physics, Martin Luther University Halle-Wittenberg, Von-Seckendorff-Platz 1, 06120 Halle (Saale), Germany*⁶*Institute of Physics, The Czech Academy of Sciences, Na Slovance 2, 18221 Prague, Czech Republic*

(Received 17 November 2017; published 20 February 2018)

Impurities on surfaces experience a geometric symmetry breaking induced not only by the on-site crystal-field splitting and the orbital-dependent hybridization, but also by different screening of the Coulomb interaction in different directions. We present a many-body study of the Anderson impurity model representing a Co adatom on graphene, taking into account all anisotropies of the effective Coulomb interaction, which we obtained by the constrained random-phase approximation. The most pronounced differences are naturally displayed by the many-body self-energy projected onto the single-particle states. For the solution of the Anderson impurity model and analytical continuation of the Matsubara data, we employed new implementations of the continuous-time hybridization expansion quantum Monte Carlo and the stochastic optimization method, and we verified the results in parallel with the exact diagonalization method.

DOI: [10.1103/PhysRevB.97.085133](https://doi.org/10.1103/PhysRevB.97.085133)**I. INTRODUCTION**

Graphene is a remarkable condensed-matter system with various promising applications. Field-effect electronic devices based on graphene [1] as well as a whole wafer-scale integrated circuit built out of graphene components [2] have been demonstrated. The material itself displays an abundance of exotic properties, many of which have their origin in the peculiar feature of the low-energy electronic excitations: they resemble massless Dirac fermions [3].

Enhanced functionality of materials can be achieved by introducing inhomogeneities, of which impurities are one important kind. The first experimental realization of Co adatoms on graphene was described by Mattos [4], who extensively discussed the adsorption geometry as well as the Kondo effect. Since then, only a few further realizations of magnetic impurities on graphene were reported, with controversial conclusions about the existence of the Kondo effect in graphene [5,6].

Diverse theoretical studies have been performed aiming at characterization of the Kondo effect in pseudogap systems in general, and in graphene in particular, see Refs. [7–16] and references therein. The system of a Co atom adsorbed on a single layer of graphene can be accurately represented by the Anderson impurity model (AIM). Jacob *et al.* considered the Kondo effect of the Co/graphene system by performing one of the first realistic many-body studies utilizing this model in the framework combining the density-functional theory with the one-crossing approximation (DFT+OCA) [16]. Our *ab initio* calculation of the Coulomb matrix yields a weaker repulsion when compared to the Coulomb vertex employed by Jacob

et al. Consequently, we were not able to see the Kondo effect since the charge fluctuations were not sufficiently suppressed.

For an impurity placed on a surface, the two-dimensional constraint leads to a geometric symmetry breaking, which additionally to the crystal-field splitting and the orbital-dependent hybridization, induces a pronounced anisotropy of the Coulomb interaction at the impurity [17]. Since electronic screening in the z direction is weaker, electrons in the Co $d_{3z^2-r^2}$ orbital feel a stronger Coulomb repulsion, whereas in the directions parallel to the graphene surface the screening is stronger. It is most efficient for the most hybridized orbitals of the E_1 symmetry. To take these effects into account, we employed the constrained random-phase approximation (cRPA) to calculate the effective (partially screened) Coulomb interaction matrix [18,19]. Since graphene exhibits a high mobility of its conduction electrons [20], its electronic polarizability is rather large, leading to a strong renormalization of the repulsion strength. The present paper aims at an exploration of the effects of geometric anisotropy in the effective Coulomb matrix while solving the corresponding Anderson impurity model by the continuous-time quantum Monte Carlo (CTQMC) method. The results are cross-checked with the exact diagonalization (ED) technique.

This paper is organized as follows. In Sec. II, we describe the DFT setup. In Sec. III A, we introduce the AIM and how its corresponding Hamiltonian is obtained from DFT by projection onto correlated orbitals. Section III B describes the CTQMC algorithm for the solution of the AIM, and how analytical continuation of the Matsubara data is performed using the stochastic optimization method. Section III C explains how we performed the ED method. Section III D explains how we performed the cRPA to obtain the Coulomb matrix, and Sec. III E the method to obtain the corresponding anisotropic

*rmozara@physnet.uni-hamburg.de

TABLE I. First line: occupations and crystal-field splittings from DFT after projection by the PLO method. The window of energy bands was taken such that the total occupation agrees with the one of Co supplied in the VASP pseudopotential package. Second line: occupations as computed by Jacob *et al.* [16].

| n_{tot} | n_{xy} | n_{yz} | $n_{3z^2-r^2}$ | n_{xz} | $n_{x^2-y^2}$ | ε_F | ε_{xy} | ε_{yz} | $\varepsilon_{3z^2-r^2}$ | ε_{xz} | $\varepsilon_{x^2-y^2}$ |
|------------------|----------|----------|----------------|----------|---------------|-----------------|--------------------|--------------------|--------------------------|--------------------|-------------------------|
| 8.2016 | 0.8093 | 0.7487 | 0.9859 | 0.7485 | 0.8084 | -2.273 | -0.720 | -0.564 | -0.711 | -0.541 | -0.714 |
| 7.02 | 0.6875 | 0.5950 | 0.945 | 0.5950 | 0.6875 | | | | | | |

double counting. Sections IV A–IV C present and discuss the QMC results, and in Sec. IV D, we compare QMC with ED. We conclude the paper in Sec. V.

II. DENSITY-FUNCTIONAL THEORY

DFT simulations have been performed to find the equilibrium geometry of the system, and to extract kinetic-energy and Coulomb parameters for the Anderson impurity model. We considered a supercell with the Co adatom above the single-layered $3 \times 3 \times 1$ graphene sheet.

To determine the equilibrium position of the adatom, we explored two possible configurations over graphene: top and hollow. This part of the work was done in the framework of the VASP package with projector augmented wave (PAW) basis set [21]. The cut-off energy of the basis was chosen as 500 eV and the GGA(PW91) [22] approximation was used for the exchange-correlation energy E_{xc} . The relaxation of the chosen structures was performed on a $12 \times 12 \times 1$ Γ -centered \mathbf{k} -point mesh until forces were smaller than 0.01 eV/Å. The graphene layer was kept fixed and the Co adatom was free to relax in all directions. A vacuum separation of 15.0 Å was chosen.

The hollow position of the Co adatom was found to be energetically more favored in comparison to the adsorption site on the top of the carbon atom, which is in agreement with previous work [8]. Therefore we focused only on the hollow position and all further calculations in this paper refer to this absorption geometry. The structural relaxation yielded a distance of the Co impurity from the graphene sheet of about 1.5 Å, which is in line with previous findings for the used functionals [8,23]. The filling of the Co d orbitals at this equilibrium distance $n_{\text{tot}} = 8.2$ was calculated with the aid of the PLO method by taking into account 18 bands around the Fermi level (see Ref. [27] and Sec. III A below). Table I presents occupations of individual d orbitals.

Quantum-chemical calculations performed by Rudenko *et al.* predicted the electronic configuration $3d^9 4s^0$ with $S = 1/2$ for the cobalt atom placed at 1.5 Å above the graphene sheet [24], whereas the $3d^8 4s^1$ configuration, which corresponds to our DFT solution, was stable at larger distances. At yet larger distances, they found the state of the free atom ($3d^7 4s^2$) to be the lowest-energy solution. Virgus *et al.* also observed the transition from $3d^7 4s^2$ over $3d^8 4s^1$ to $3d^9 4s^0$ when the Co impurity approaches the surface [25]. They obtained an equilibrium distance of the Co impurity in case of a $3d^8 4s^1$ configuration, which is comparable to our setting. The x-ray absorption spectra measured experimentally by Eelbo *et al.* also indicate that the Co adatom is in the $3d^8 4s^1$ electronic configuration [26]. Jacob *et al.*, on the other hand, found the filling of the Co d orbitals to be 7.5 in their DFT calculations,

and the subsequent treatment of the electronic correlations within OCA pushed the filling to a lower value near 7.0 [16]. The distance of Co from the graphene surface that they obtained is comparable to ours, and we consider their filling additionally to our $n_{\text{tot}} = 8.2$ in the many-body calculations below.

III. ANDERSON IMPURITY MODEL: SETUP AND SOLUTION

A. From first-principles DFT to a model Hamiltonian

The Co adatom on graphene resembles the case of a magnetic impurity coupled to a noninteracting bath for which the Anderson impurity model can be employed. To obtain *ab initio* parameters for this AIM, we projected the DFT band structure obtained in Sec. II onto Wannier orbitals localized at the Co adatom. To this end, we used the PLO method [27]. Labeling the Bloch states $|\mathbf{k}, n\rangle$ by the momentum \mathbf{k} and the band index n , with \mathbf{k} being from the first Brillouin zone, and the Bloch transformed Wannier orbitals with quantum numbers $\alpha = (\mathbf{r}, l, m)$ by $L_{\alpha\mathbf{k}}$ (\mathbf{r} is the position of the impurity within the unit cell, and the Bloch transform is the Fourier transform over the Bravais lattice), the projectors are given by $\mathcal{P}_{\alpha n}(\mathbf{k}) = \langle L_{\alpha\mathbf{k}} | \mathbf{k}, n \rangle$. The local Green's function of the Co adatom is thereby obtained from the Bloch Green's function $G_n^B(\mathbf{k}, i\omega) = [i\omega - \varepsilon_n(\mathbf{k})]^{-1}$, with $\varepsilon_n(\mathbf{k})$ the band dispersion relative to the chemical potential, as

$$G_{\alpha\beta}(i\omega) = \sum_{\mathbf{k}n} \mathcal{P}_{\alpha n}(\mathbf{k}) G_n^B(\mathbf{k}, i\omega) \mathcal{P}_{\beta n}^+(\mathbf{k}) = [i\omega - \varepsilon - \Delta(i\omega)]_{\alpha\beta}^{-1}, \quad (1)$$

with the on-site crystal-field matrix $\varepsilon_{\alpha\beta}$ and the hybridization function $\Delta_{\alpha\beta}(i\omega)$.

The multiorbital single-impurity Anderson model can be decomposed into three parts:

$$H = H_{\text{Co}} + H_g + H_{\text{hyb}}. \quad (2)$$

The first part is the local Hamiltonian for the Co d states:

$$H_{\text{Co}} = \sum_{\alpha\beta\sigma} (\varepsilon_{\alpha\beta} - \mu_{\alpha}^{\text{DC}} \delta_{\alpha\beta}) c_{\alpha\sigma}^+ c_{\beta\sigma} + \frac{1}{2} \sum_{\alpha\beta\gamma\delta\sigma\sigma'} U_{\alpha\beta\gamma\delta} c_{\alpha\sigma}^+ c_{\beta\sigma'}^+ c_{\delta\sigma'} c_{\gamma\sigma}. \quad (3)$$

The first term is the crystal-field matrix, which is diagonal, i.e., $\varepsilon_{\alpha\beta} = \varepsilon_{\alpha} \delta_{\alpha\beta}$. The greek indices $\alpha, \beta, \gamma, \delta$ label the orbitals, which transform according to the irreducible representations of the C_{6v} point group: $E_2 = \{xy, x^2 - y^2\}$, $E_1 = \{xz, yz\}$, and $A_1 = \{3z^2 - r^2\}$. The spin degrees of freedom are denoted as σ, σ' . The second term in Eq. (3) is the effective on-site Coulomb interaction we obtained by the cRPA method

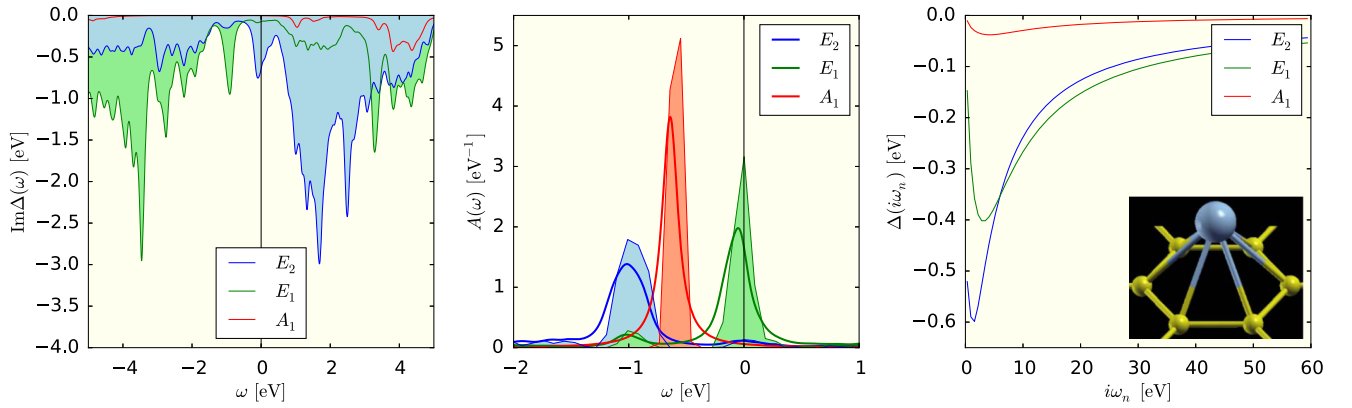


FIG. 1. (Left) Representation-resolved imaginary part of the real-frequency hybridization function $\Delta(\omega)$ for the d orbitals of the Co adatom obtained with the PLO method. (Middle) DFT (filled) and projected (unfilled) DOS $A(\omega)$. (Right) Matsubara hybridization function $\Delta(i\omega_n)$ at $\beta = 20 \text{ eV}^{-1}$. Only the first 60 frequencies are displayed. The inset contains a picture of the geometry.

(Sec. III D). A double-counting (DC) correction μ_α^{DC} has to be subtracted to remove the Coulomb effects present in the DFT band structure.

The second part in Eq. (2) describes the spin-degenerate band structure of graphene,

$$H_g = \sum_{\mathbf{k}n\sigma} \varepsilon_{\mathbf{k}n} f_{\mathbf{k}n\sigma}^+ f_{\mathbf{k}n\sigma}, \quad (4)$$

where n is the band index. The on-site crystal-field matrix $\varepsilon_{\alpha\beta}$ and the energy bands $\varepsilon_{\mathbf{k}n}$ are measured with respect to the Fermi energy of graphene.

The last part in Eq. (2) is the hybridization between the adatom and graphene. It is given by

$$H_{\text{hyb}} = \sum_{\mathbf{k}\alpha\sigma} (V_{\mathbf{k}\alpha} c_{\alpha\sigma}^+ f_{\mathbf{k}\alpha\sigma} + \text{H.c.}). \quad (5)$$

The electron hopping processes to and from the impurity preserve the local symmetry and hence the hopping amplitudes $V_{\mathbf{k}\alpha}$ are diagonal in the basis of the irreducible representations of the point group. The graphene states $f_{\mathbf{k}\alpha\sigma}$ are projections of $f_{\mathbf{k}n\sigma}$ onto this basis. The diagonal hybridization function characterizing the coupling between the adatom and graphene is obtained after integrating out the graphene degrees of freedom. It is defined as

$$\Delta_\alpha(i\omega) = \sum_{\mathbf{k}\alpha} \frac{|V_{\mathbf{k}\alpha}|^2}{i\omega - \varepsilon_{\mathbf{k}\alpha}}. \quad (6)$$

Real-energy and Matsubara representations of the hybridization function and the density of states for all five d orbitals are presented in Fig. 1. Features of the real-energy hybridization for the metallic impurity on graphene repeat findings of Wehling *et al.* [8]: one can see an almost complete suppression of the A_1 orbital whereas E_1 and E_2 form a symmetric slope around the Dirac point that is shifted slightly to the lower energy by an amount of $\mu = 0.2 \text{ eV}$. This might be an effect of the supercell repetition with periodic occurrence of the Co adatom, effectively doping the graphene sheet, whereas a single adatom on an infinite sheet would not produce such a shift of the Fermi level. On the other hand, Mattos reported the same value for the chemical potential together with a low

Kondo temperature [4] (being discussed in other references [8,10,28]).

B. Quantum Monte Carlo method and analytical continuation

The interacting impurity Green's function of the Anderson impurity model is given as

$$G_{\alpha\sigma}(i\omega) = [i\omega - \varepsilon_\alpha + \mu_\alpha^{\text{DC}} - \Delta_\alpha(i\omega) - \Sigma_\alpha(i\omega)]^{-1}. \quad (7)$$

The electronic self-energy $\Sigma(i\omega)$ containing all Coulomb correlation effects was computed employing the hybridization-expansion variant of the continuous-time quantum Monte Carlo (CTHYB QMC) method. The CTHYB solver developed by the TRIQS collaboration [29,30] implements two important optimizations, namely a caching scheme based on a binary-tree data structure [31], and a novel scheme to automatically reduce the local Hamiltonian H_{C_0} to a block-diagonal form (see Sec. 4 of Ref. [30] for details). These optimizations enable solving five-orbital impurity models with the rotationally invariant Coulomb matrix (referred to as Slater from now on) as well as with the cRPA approximation of the interaction matrix in a reasonable time. The ‘‘autopartition’’ algorithm gives a much finer block structure of the local Hamiltonian than one would get from the standard partitioning based on the occupation quantum numbers: \hat{N}_\uparrow and \hat{N}_\downarrow quantum numbers would result in $(2l+2)^2 = 36$ diagonal blocks, while we got 132 blocks in both Slater and cRPA cases (cubic harmonics have been used as the local orbital basis).

Typical computational time taken by one QMC simulation has varied from a few hundreds to a few thousands core hours. Actual values strongly depended on the local occupations as well as on the temperature.

The analytical continuation of the imaginary-time data has been performed using a recently established TRIQS-based implementation of Mishchenko's stochastic optimization method (SOM) [32]. This method amounts to a stochastic solution of the Fredholm integral equation of the first kind,

$$G_\alpha(\tau) = - \int_{-\infty}^{\infty} d\epsilon \frac{e^{-\tau\epsilon}}{1 + e^{-\beta\epsilon}} A_\alpha(\epsilon). \quad (8)$$

For a given thermal Green's function $G_\alpha(\tau)$ measured in a QMC simulation (index α runs over all orbital and spin indices) a number of approximate particular solutions $A_\alpha(\epsilon)$ are constructed. Each particular solution is written as a superposition of N rectangles $\{c_i, w_i, h_i\}$ with the total spectral weight fixed to 1,

$$A_\alpha(\epsilon) = \sum_{i=1}^N h_i \theta(\epsilon - [c_i - w_i/2]) \theta([c_i + w_i/2] - \epsilon),$$

$$1 = \sum_{i=1}^N h_i w_i.$$

A Markovian walk in the space of such superpositions is organized in order to find a minimum of the residue functional corresponding to the Fredholm equation (8). The Markov chain is started from a randomly generated configuration, typically 500–1000 times. Every time it results in another particular solution. Eventually, all particular solutions found by different Markov chains are averaged, so that stochastic noise is approximately canceled. For a more in-depth description of the algorithm we refer to the original paper of Mishchenko *et al.* [33].

C. Exact diagonalization

As an alternative method to QMC, we employ also the exact diagonalization, or more accurately, the Lanczos method. That way, the spectral functions of the impurity model are directly accessible without the need for analytical continuation but at the cost of discretized hybridization function. This discretization amounts to a replacement of the continuous spectrum $\epsilon_{k\alpha}$ with a discrete spectrum $\epsilon_{k\alpha}$ in Eqs. (4) and (5), where k takes values $1, 2, \dots, K$. The parameters $\epsilon_{k\alpha}$ and $V_{k\alpha}$ of such a finite impurity model are determined by minimization of a weighted sum of squares [34,35]

$$d_\alpha = \sum_{n>0} \frac{1}{\omega_n^r} \left| \Delta_\alpha(i\omega_n) - \sum_{k=1}^K \frac{V_{k\alpha}^2}{i\omega_n - \epsilon_{k\alpha}} \right|^2 \quad (9)$$

for each of the Co d orbitals $\alpha = E_1, E_2$, and A_1 . In the formula, Δ_α stands for the diagonal element of the DFT hybridization function, Eq. (1). The result of the fit for $\beta = 1/(k_B T) = 20 \text{ eV}^{-1}$, $K = 4$, and $r = 1/2$ is shown in Fig. 2. The fits represent the DFT hybridization function very accurately, at least by visual inspection. For each α , there are two energies $\epsilon_{k\alpha}$ negative (that is, below the Fermi level) and two energies $\epsilon_{k\alpha}$ positive (above the Fermi level). Since the hybridization in the A_1 orbital is much smaller than in the E_1 and E_2 orbitals, it is neglected in all our ED calculations. For one particular setting of the Coulomb vertex, we have explicitly checked that dropping the A_1 hybridization, indeed, has a very small effect on the quantities of interest.

The fitted impurity model with four bath orbitals attached to each of the Co E_1 and E_2 orbitals is too large to be fully solved by the Lanczos method. To make the solution manageable, we employ a reduced many-body basis inspired by the work of Gunnarsson and Schönhammer [36,37]. A cutoff M is introduced for each N -electron Hilbert space \mathcal{H}_N , and the

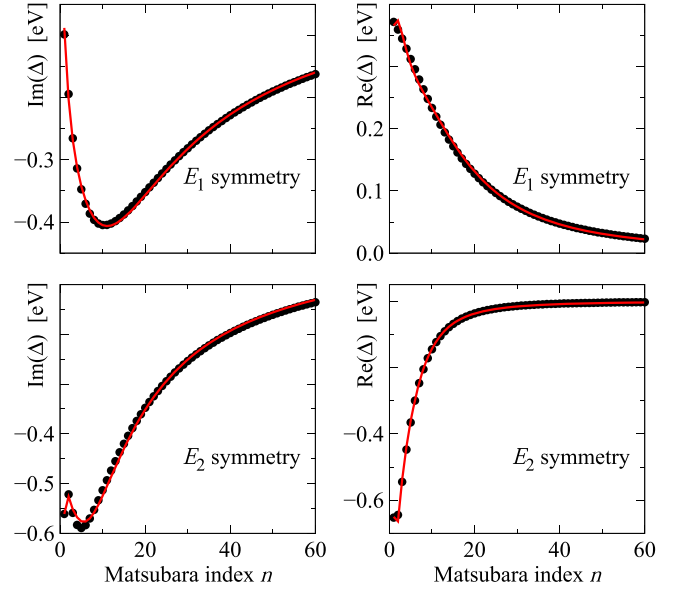


FIG. 2. Fit of the finite impurity model (lines) to the real and imaginary parts of the DFT hybridization function (dots) using Eq. (9). Only the first 60 Matsubara frequencies are plotted but the fit included the lowest 1024 frequencies.

diagonalization is performed only in a subspace,

$$\mathcal{H}_N^{(M)} = \{|d^{N-N_b^<-n+m} b^n \underline{b}^m\rangle, 0 \leq m+n \leq M\}. \quad (10)$$

In this notation, $d^{N-N_b^<-n+m}$ indicates $N - N_b^< - n + m$ electrons in the Co d shell, b^n indicates n electrons in the bath orbitals above the Fermi level, and \underline{b}^m means m holes in the bath orbitals below the Fermi level. The symbol $N_b^<$ denotes the number of bath orbitals located below the Fermi level ($N_b^< = 2 \times 10 = 20$ in the present case). This Hilbert-space reduction can be viewed as an expansion in the hybridization parameters $V_{k\alpha}$ around the atomic limit, that is, around the Hilbert space $\mathcal{H}_N^{(0)} = \{|d^{N-N_b^<} b^0 \underline{b}^0\rangle\}$. We use the cutoff $M = 5$ and we have verified that this setting provides essentially converged spectral densities.

D. Effective Coulomb matrix from the constrained random-phase approximation

The effective, partially screened Coulomb interaction matrix was obtained for the given geometry using the cRPA method [38,39]. The supercell was enlarged to achieve a distance of 28.35 \AA between two adjacent graphene layers. We employed the SPEX code [40], a part of the Jülich full potential linearized augmented-plane-wave (FLEUR) code family [41]. The calculation of the effective interaction in cRPA is based on the separation of a chosen set of target bands and on a consequent consideration of all polarization processes between target and other (screening) bands. In our calculation, we used 19 bands near the Fermi level to project onto the local basis of the five d states of the Co adatom.

The constructed 625 elements of the cRPA Coulomb matrix are shown in Fig. 3. One can contrast this cRPA interaction matrix with the conventional Slater matrix defined by parameters F_0, F_2, F_4 . These parameters have been estimated from the

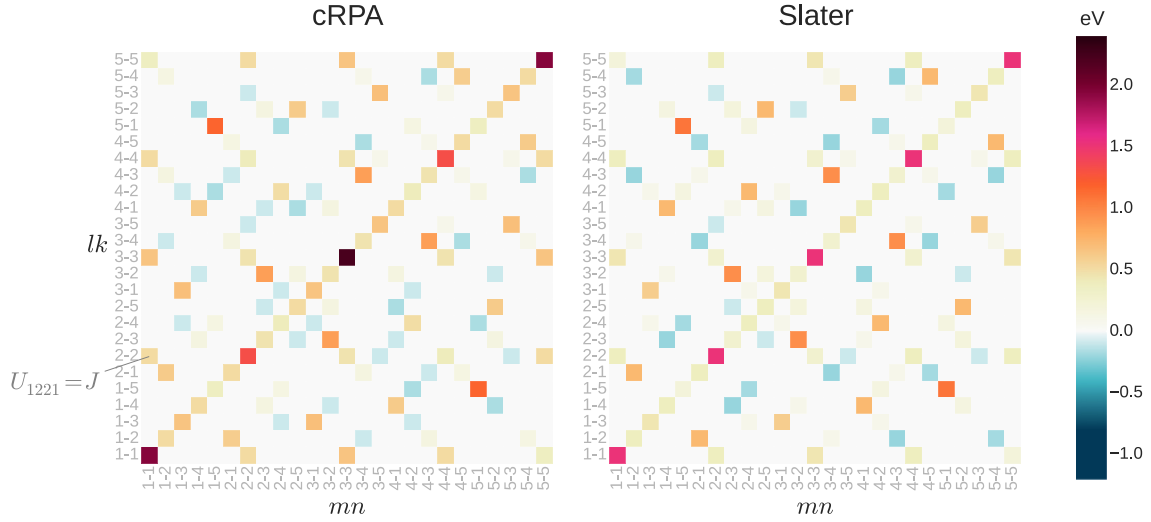


FIG. 3. Coulomb matrix for the d orbitals of the Co adatom obtained with the cRPA method (left) and subsequently rotationally averaged by the Slater approximation (right). The order of the orbitals is given by U_{mlkn} . The outlined element U_{1221} corresponds to the term $U_{1221}c_{1\uparrow}^{\dagger}c_{2\downarrow}^{\dagger}c_{2\downarrow}c_{1\uparrow}$, the index notation 1–5 runs for the orbital ordering (xy , yz , $3z^2 - r^2$, xz , $x^2 - y^2$).

cRPA Coulomb matrix via the effective repulsion and exchange parameters U , U' , J as

$$U = \frac{1}{5} \sum_{m=1}^5 U_{mmmm} = 1.76 \text{ eV},$$

$$U' = \frac{1}{20} \sum_{m \neq m'=1}^5 U_{mm'mm'} = 0.73 \text{ eV},$$

$$J = \frac{1}{20} \sum_{m \neq m'=1}^5 U_{mm'm'm} = 0.52 \text{ eV}, \quad (11)$$

$$F_0 = U/5 + 4U'/5 = 0.93 \text{ eV},$$

$$F_2 = 14J/1.625 = 4.44 \text{ eV},$$

$$F_4 = 0.625F_2 = 2.77 \text{ eV}. \quad (12)$$

First, the cRPA matrix displays a pronounced anisotropy in the density-density terms on the main diagonal of the plot. Interorbital exchange, which is responsible for suppressing parallel alignment on different orbitals, has been found to expose slightly higher amplitude for the cRPA matrix. Second, the intensity of the inter- and intraorbital spin-flip exchange terms (off-diagonal elements) appears to be lower in the cRPA case when compared to the spherically symmetric Slater vertex. Another visible feature is the change of the sign for interorbital spin-flip terms between cRPA and Slater matrices. The Coulomb matrix obtained by the cRPA method is rather small. It is reflected in the Slater parameters extracted from the symmetrized cRPA matrix, Eqs. (11) and (12).

The quantum-chemical considerations made by Rudenko *et al.* may provide a lower bound of the interaction strengths [24]. Our Slater parameters are by a factor of 2 smaller than theirs at comparable adatom-graphene distances. There are possibly three reasons why the cRPA Coulomb matrix turns out so small. First, the Co adatom is closer to the surface, that in turn increases overlaps with the graphene p orbitals, thus

leading to an enhanced screening of the Coulomb interaction. Second, the finite distance between the layers of 28.35 Å, even though very large, might still artificially reduce the interaction matrix, as an extrapolation to the infinite layer distance has not been performed [23,42]. This effect, however, is not expected to contribute by more than 5% at our interlayer distance. And third, a systematic study revealed the screening of the Coulomb interaction at metal and insulator surfaces [43]. In contrast to common expectations, it is found that screening at metal surfaces is much more efficient than in bulk, and as a consequence the Hubbard U is reduced by 30%–40% compared to the bulk values. The situation in the case of the Co/graphene system is very similar where metallic screening is very efficient.

E. Anisotropic double counting

As the two-dimensional geometry of an impurity on a surface breaks rotational invariance, the Coulomb matrix exhibits an anisotropy between its components. The mean-field Coulomb terms incorporated in the DFT band structure have a corresponding anisotropy that has to be taken into account when the DC correction is introduced in Eq. (3). The exact expression for the DC correction is not known. We deduce it from the filling of the Co d orbitals found in DFT, since the DC correction acts similarly to the chemical potential and controls the filling of the impurity states in the impurity model. We considered two cases: the occupations resulting from our PLO projection procedure, and also the smaller occupations computed by Jacob *et al.* [16], all listed in Table I. The anisotropy requires the DC correction to be orbitally dependent, and for its determination we employed the Hubbard-I approximation, which takes into account a large portion of the electronic correlations. We started with the atomic Green's function augmented by the atomic Coulomb self-energy determined by exact diagonalization of H_{Co} with

TABLE II. DC correction (in units of eV) obtained for the anisotropic cRPA (middle columns) and the rotationally invariant Slater Coulomb matrix (last column). For comparison, the respective diagonal cRPA Coulomb matrix elements are (in units of eV) E_2 : 1.95, E_1 : 1.33, A_1 : 2.23.

| $n_{\text{tot}}^{\text{LDA}}$ | $\mu_{E_2}^{\text{DC}}$ | $\mu_{E_1}^{\text{DC}}$ | $\mu_{A_1}^{\text{DC}}$ | μ^{DC} |
|-------------------------------|-------------------------|-------------------------|-------------------------|-------------------|
| 7.02 | 4.39 | 3.65 | 5.25 | 4.87 |
| 8.20 | 4.91 | 4.28 | 6.86 | 5.69 |

$\varepsilon_{\alpha\beta}$ set to zero,

$$G_{\alpha}^{\text{at}}(i\omega) = \frac{1}{i\omega + \mu_{\alpha}^{\text{DC}} - \Sigma_{\alpha}^{\text{at}}(i\omega)}, \quad (13)$$

and then supplied the crystal-field splitting and the hybridization,

$$G_{\alpha}^{\text{HIA}}(i\omega) = \frac{1}{i\omega - \varepsilon_{\alpha} + \mu_{\alpha}^{\text{DC}} - \Sigma_{\alpha}^{\text{at}}(i\omega) - \Delta_{\alpha}(i\omega)}. \quad (14)$$

We included the crystal-field splitting after calculating the atomic self-energy since its effect is small as compared to the Coulomb effects, and the thus obtained DC correction matches superiorly the DFT occupations in the subsequent full QMC simulation. Then, the minimization of the distance

$$\|n_{\text{tot}}^{\text{LDA}} - n_{\text{tot}}^{\text{HIA}}\|^2 = \sum_{\alpha} |n_{\alpha}^{\text{LDA}} - n_{\alpha}^{\text{HIA}}|^2 \quad (15)$$

is performed using the differential evolution procedure [44] as implemented in SCIPY. Differential evolution is a global optimization method, which is able to find the global minimum

of a multivariate and possibly nondifferentiable function in relatively short time.

For the symmetrized Coulomb matrix in the Slater approximation, we calculated the DC correction in the around mean-field (AMF) limit given by the expression

$$\mu^{\text{DC}} = n_{\text{tot}}^{\text{LDA}} \left[U \left(1 - \frac{1}{2N} \right) - J \left(\frac{1}{2} - \frac{1}{2N} \right) \right], \quad (16)$$

where $N = 2l + 1$ with $l = 2$. The choice of the AMF DC correction was motivated by its superior performance in the full QMC test simulations as compared to the fully localized limit (FLL).

The usual way to determine the isotropic DC correction is to identify the U in Eq. (16) with F_0 in Eq. (12) and J with the one in Eq. (11). For our calculations, we determined U and J by spherically averaging the Coulomb matrix twice, which yields U in Eq. (16) to be directly F_0 in Eq. (12), while the Hund's coupling is reduced to $J = 0.37$ eV. The results are summarized in Table II. The magnitude of the anisotropic DC corrections follows the Coulomb strength in the respective directions, as may also be compared with Fig. 3.

IV. DISCUSSION OF QMC RESULTS

QMC has been performed at $\beta = 20$ eV $^{-1}$, using 2.0×10^6 updates and 5.0×10^5 warmup updates on each core, and measuring at each 50th update. The set of possible updates contained double as well as global moves, the latter including global spin-flips and global orbital permutations of vertex

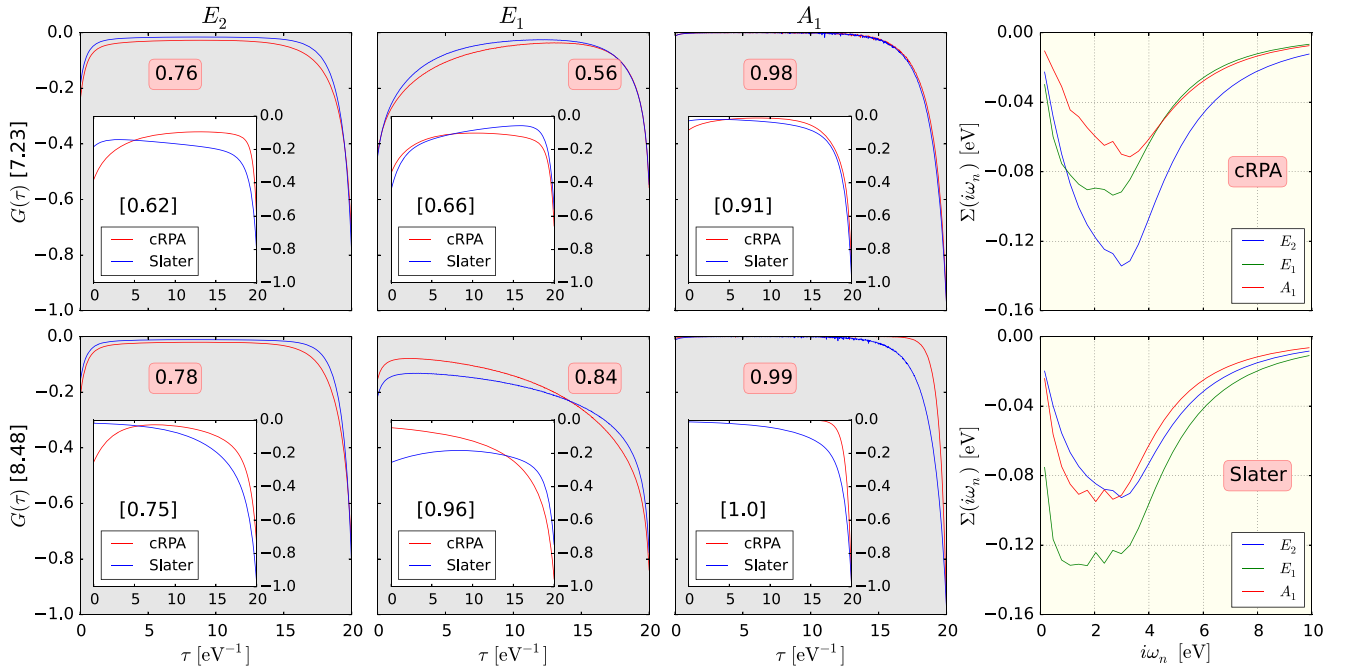


FIG. 4. (First three columns) Comparison between the representation-resolved imaginary-time Green's functions $G(\tau)$ for $5d$ orbitals of the Co impurity calculated with the cRPA and the Slater Coulomb matrix. Total cRPA occupations are given in squared brackets, and orbital ones in round boxes. The upper and lower row contain the full QMC Green's functions at lower and higher filling, respectively, together with the atomic solution in the insets (orbital occupations in brackets). Calculations were performed at $\beta = 20$ eV $^{-1}$. (Last column) Representation-resolved Matsubara self-energy $\Sigma(i\omega_n)$ calculated with the cRPA (upper row) and the Slater Coulomb matrix (lower row), both at higher Co filling. Only the first 10 frequencies are displayed for a better resolution of the low-energy behavior.

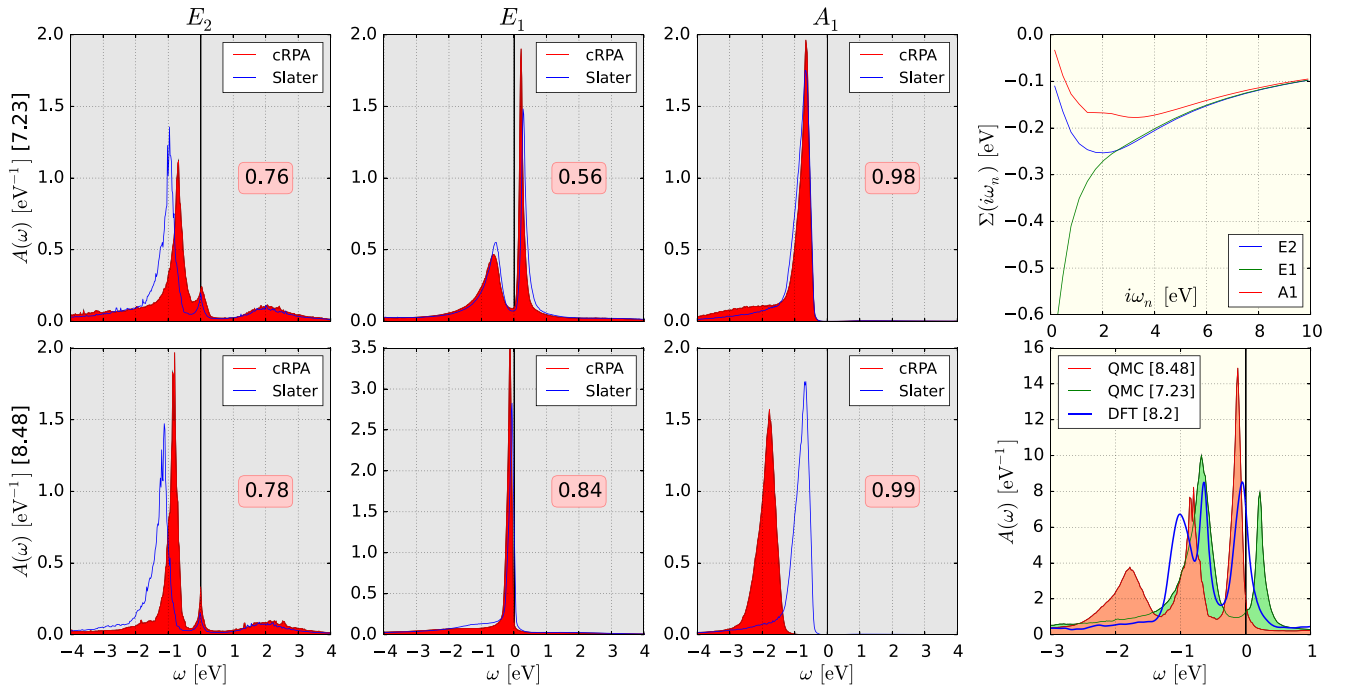


FIG. 5. (First three columns) Comparison between the representation-resolved DOS $A(\omega)$ for the d orbitals of the Co impurity calculated with the cRPA and the Slater Coulomb matrix. The upper and lower rows contain the DOSes at lower and higher Co filling, respectively. Total cRPA occupations are given in squared brackets, and orbital ones in round boxes. The spectra are obtained from the imaginary-time Green's functions in Fig. 4 by analytical continuation with the SOM solver. (Upper right) Representation-resolved Matsubara self-energy $\Sigma(i\omega_n)$ calculated with the cRPA Coulomb matrix at lower Co filling. Tail fitting was performed between the 10th and the 20th Matsubara frequency. (Lower right) Comparison between the QMC (with the cRPA Coulomb matrix) and the DFT total DOSes (total occupations in squared brackets).

indices. The calculations have been performed on 192 cores in parallel and took around 14–15 hours.

A. Physical importance of cRPA

The imaginary-time Green's functions obtained after solving the multiorbital AIM by the methods described in Sec. III B are displayed in Fig. 4. The results obtained with the full cRPA Coulomb matrix are compared to the ones with the Slater matrix. Rotationally averaging the Coulomb matrix by the Slater approximation slightly reduces the overall weight of the interaction strength, and some portions are redistributed, as it is seen in Fig. 3. The most pronounced differences occur for the higher filling considered, $n_{\text{tot}} = 8.2$, especially in the A_1 representation. The hybridization in A_1 is small, thus the effect solely stems from the Coulomb interaction and its reduction in the spherical case. Lowering the Co filling by adjusting the DC correction presents the orbitals with E_1 symmetry as flexible with respect to their occupation, and E_1 crosses the Fermi level. This is a consequence of the orbitals within this representation being the most hybridized as well as having the strongest partial screening of the Coulomb interaction.

From the imaginary-time Green's function, we performed analytical continuation using SOM, and the results are summarized in Fig. 5. In agreement to the Green's functions, the differences for the lower filling are not as pronounced as for the higher one. Corresponding to the difference in the A_1 orbitals at higher Co filling, the peak is shifted towards lower values for the cRPA matrix. Considerable differences,

though not qualitative in nature, can also be seen for the orbitals with E_2 symmetry where the main peak below the Fermi level is slightly shifted. The overall shape of all spectra remains the same, including the shape and position of subpeaks and shoulders. Thus considering anisotropies induced by the breaking of rotational invariance yields spectra that are largely invariant. One may thus conclude that the spectra obtained with the full cRPA Coulomb matrix coincide with the Slater approximation in many important aspects if the DC corrections are chosen such that the impurity filling coincides in both cases.

Notwithstanding the similar shapes of the spectra obtained with the cRPA and the Slater Coulomb matrix, the self-energies show considerable differences at low energies. As Co on graphene at higher Co filling of 8.2 is a usual Fermi-liquid, the self-energies should tend to zero at very low energies. This property is better resolved with the calculations using the cRPA matrix as one may observe in Fig. 4. There is also a change of the order of the self-energy strengths between the orbitals of E_1 and E_2 symmetry, and they intersect in the cRPA case. The interchange at very low energies between the one of E_2 and A_1 symmetry is in agreement with the interchange of the peaks in the corresponding spectra in Fig. 5. The relevance of taking into account anisotropies in the Coulomb matrix by the cRPA lies in the calculation of the self-energies. In particular, eventual estimation of Kondo parameters will rely on a proper determination of the self-energies. Further physical insights into the effects of anisotropy of the self-energy on the electronic configuration will be discussed in Sec. IV C.

TABLE III. Total and representation-resolved Co d -shell occupations, ground state energies ε_{GS} , and expectation values of the local Hamiltonian (H_{Co}) at $\beta = 20 \text{ eV}^{-1}$. The upper part of the table corresponds to the full impurity model, the lower part to the local Hamiltonian H_{Co} alone not coupled to any bath.

| | n_{tot} | n_{E_2} | n_{E_1} | n_{A_1} | $\varepsilon_{\text{GS}}[\text{eV}]$ | $\langle H_{\text{Co}} \rangle [\text{eV}]$ |
|-------------------------|------------------|-----------|-----------|-----------|--------------------------------------|---|
| Impurity problem | | | | | | |
| cRPA vertex (QMC) | 7.23 | 0.75 | 0.56 | 0.98 | – | –22.30 |
| | 8.48 | 0.78 | 0.85 | 0.99 | – | –29.09 |
| cRPA vertex (ED) | 7.26 | 0.76 | 0.55 | 1.00 | –63.10 | –22.32 |
| | 8.57 | 0.79 | 0.86 | 1.00 | –69.66 | –29.11 |
| Slater vertex (QMC) | 7.40 | 0.81 | 0.55 | 0.99 | – | –25.09 |
| | 8.45 | 0.84 | 0.78 | 0.99 | – | –31.18 |
| Atomic problem | | | | | | |
| cRPA vertex (ED) | 6.94 | 0.62 | 0.66 | 0.91 | –23.10 | –23.07 |
| | 8.80 | 0.75 | 0.95 | 1.00 | –29.71 | –29.69 |
| Slater vertex (ED) | 7.43 | 0.81 | 0.56 | 0.97 | –25.09 | –25.05 |
| | 8.87 | 0.92 | 0.75 | 0.98 | –31.74 | –31.71 |

B. Electronic structure

Having a look at the occupations resulting from the QMC calculation with the cRPA Coulomb matrix in Table III, one observes the orbitals in the A_1 representation being nearly fully occupied, and the spectral weight is thus almost exclusively below the Fermi level as may be seen in Fig. 5. Furthermore, the calculations leave the occupation stable within the orbitals of E_2 symmetry, it is exactly 3.0 for the lower Co filling and 3.12 for the higher one. The additional electron at higher Co filling appears in the E_1 representation, as it may also be seen in the corresponding pDOS. The relevant single-particle peak changes its position from slightly above the Fermi level for lower Co filling to slightly below for higher filling, and it merges together with the other main spectral weight from below with a pronounced amplification of its height, while its width remains the same.

From the pDOS, it is seen that the E_2 representation has a small peak at the Fermi level. This peak can also be seen in the pDOS obtained in ED, see Fig. 6, and it corresponds to a bath state which happens to be very near the Fermi level. Furthermore, the self-energy in the E_1 representation shows a singularity upon approaching the low-energy region. This is due to the reduced filling of this representation and the re-emergence of the graphene pseudogap as an imprint on the pDOS of the Co impurity. At last, from the tDOS one observes that QMC with the cRPA Coulomb matrix yields the same overall electronic structure at higher filling like in case of the DFT-DOS projected on the impurity, that is, a three-peak structure, which is slightly stretched to higher energies due to the Coulomb effects. Note, however, the reordering of the peaks; in DFT, the lowest one belongs to E_2 while due to the large DC the lowest one in QMC is A_1 . All these features together lead to the conclusion that, with the cRPA Coulomb matrix, QMC yields the electronic structure of the Co/graphene system very similar to DFT. In essence, this is a consequence of the strong screening predicted by cRPA.

C. Electronic configuration

The TRIQS CTHYB solver provides us with the reduced density matrix ρ_{Imp} of the Co adatom accumulated during the QMC simulation, and we are thus able to compute the grand canonical expectation value

$$\langle H_{\text{Co}} \rangle = \text{Tr}_{\text{Co}}[\rho_{\text{Imp}} H_{\text{Co}}]. \quad (17)$$

The results are included in Table III.

We diagonalized the local Hamiltonian H_{Co} in Eq. (3), and obtained the ground state and excited states of the atomic problem containing the CF splitting. From Table III, one may see the atomic energy expectation values being near the ground-state energy of the local Hamiltonian. This means that the Boltzmann weights of the excited states are small, even at $\beta = 20 \text{ eV}^{-1}$. As the QMC process describes the propagation of the local state from one eigenstate of the local Hamiltonian to another upon a hybridization event, physically relevant details of the impurity system are already reflected by the low-energy eigenstates. In particular, neglecting the small difference between the energy levels within one representation, the ground eigenstate of the local Hamiltonian corresponding to the higher filling has an SU(4) symmetry in the cRPA case, with one hole in the E_2 representation, while in the Slater case the hole is in the E_1 representation. In both cases, the ground state has nine electrons, and the orbital occupations change differently in taking into account the excited states, on the atomic as well as on the impurity level. Enforcing a lower impurity filling, the picture changes considerably: the cRPA case has ground eigenstate filling of seven with a spin-quartet being distributed over all orbitals, while in the Slater case it has a spin-triplet mostly in the E_1 representation with eight electrons in total. These different situations would definitely be reflected in eventual Kondo properties of the Co/graphene system, and apply to any system with pronounced geometric symmetry breaking where anisotropies in the Coulomb interaction occur. In contrast to this atomic picture, reflecting temperature-dependent features of the isolated impurity, the hybridization events lead to highly excited local states during the QMC process, thereby mixing the local states with bath states and leading to metallic behavior far away from the Kondo scenario. As our cRPA Coulomb matrix is small compared to the strength of the hybridization, this situation applies to our case. The local states are then dissolved into broad peaks as may be seen in the QMC DOS projected onto the single-particle states of the Co impurity, see Fig. 5.

To further characterize the effects of anisotropy on the electronic structure of the Co d orbitals, we computed the total and orbital-resolved charge and spin fluctuations $\Delta \mathcal{O} = \langle \mathcal{O}^2 \rangle - \langle \mathcal{O} \rangle^2$, with \mathcal{O} being the corresponding operator for the total or orbital occupancy or spin. The results are presented in Table IV together with the orbital-resolved effective masses given by

$$m_\alpha^* = 1 - \text{Im} \Sigma'_\alpha(i\omega_n) \Big|_{\omega_n=0} - \text{Re} \Delta'_\alpha(0), \quad (18)$$

which are related to the inverse of the quasiparticle weights Z_α at the Fermi level. In both the cRPA and the Slater cases, the total charge fluctuation is on the order of one electron, and for both considered fillings the cRPA case exhibits stronger fluctuations than the Slater case. The effective mass anisotropy

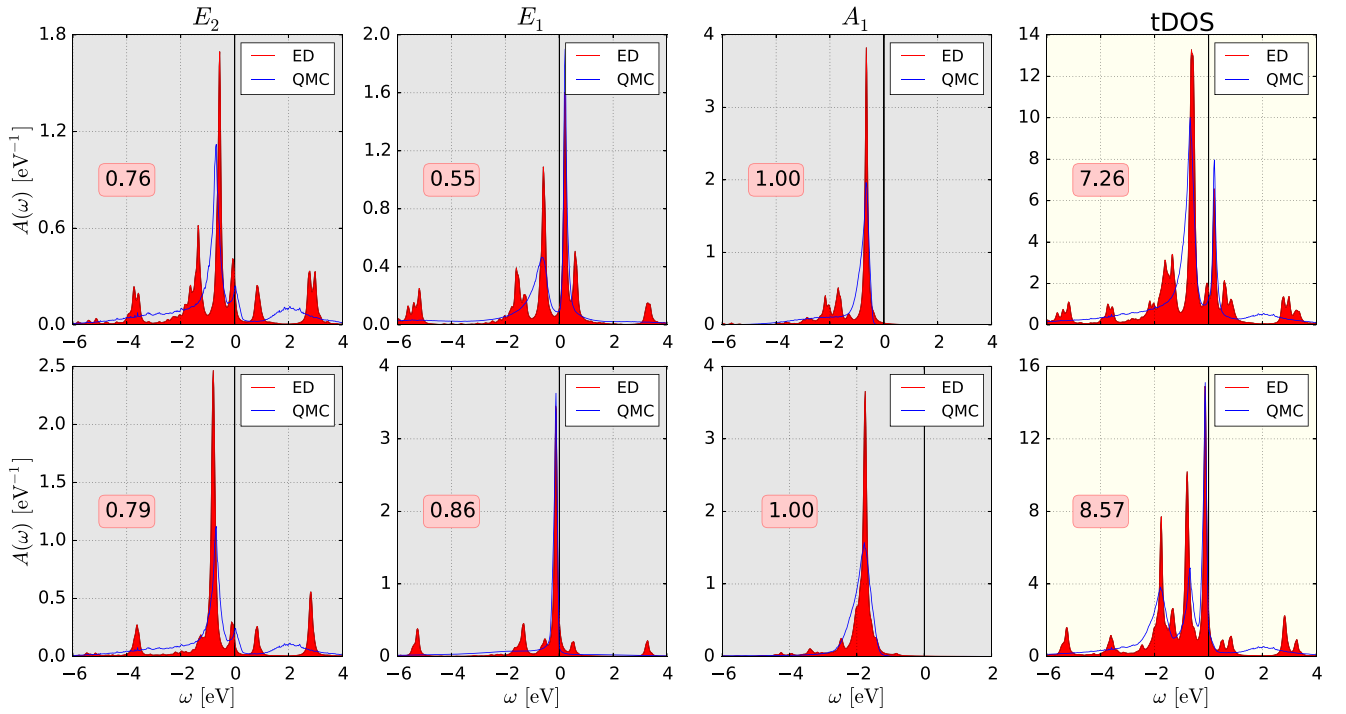


FIG. 6. (First three columns) Comparison between the representation-resolved DOS $A(\omega)$ for the d orbitals of the Co impurity calculated with QMC and ED using the cRPA Coulomb matrix. Orbital and total occupations obtained in ED are given in round boxes. The upper and lower rows contain the DOSes at smaller and larger fillings, respectively. The calculations were performed at $\beta = 20 \text{ eV}^{-1}$. (Last column) Corresponding total DOSes $A(\omega)$ calculated at lower (upper row) and higher Co filling (lower row).

is solely due to the anisotropy of the self-energy. The hybridization term in Eq. (18) is essentially negligible. It can be clearly seen that changing the total impurity occupation away from the DFT value enhances the mass renormalization, especially in the orbitals of the E_1 symmetry where the non-Fermi-liquid behavior prohibits the use of Eq. (18) altogether. Generally, the effective mass scales with the Coulomb strength, and from Fig. 3, it is clear that the reduction in Coulomb strength in the E_2 orbitals upon the spherical average leads to a reduced effective mass. Although not pronounced, the reverse tendency applies to the orbitals of the E_1 symmetry.

D. Comparison of CTHYB with ED

The calculations employing the cRPA approximation to the Coulomb vertex were repeated with the finite-temperature exact-diagonalization method outlined in Sec. III C. The computed d -orbital occupations are listed in Table III. They are very close to the corresponding QMC results, the discrepancy in the total filling n_{tot} is smaller than 0.1 and the discrepancy in the

orbital fillings is at most 0.02. The grand canonical expectation value of the local Hamiltonian is computed as

$$\langle H_{\text{Co}} \rangle = \frac{1}{Z} \sum_{\psi} e^{-\beta E_{\psi}} \langle \psi | H_{\text{Co}} | \psi \rangle, \quad (19)$$

where $|\psi\rangle$ and E_{ψ} are eigenfunctions and eigenvalues of the discretized impurity Hamiltonian, Eq. (2). This expression is equivalent to Eq. (17) and the data listed in Table III indeed confirm that.

The spectral densities calculated with CTHYB and ED are compared in Fig. 6. The agreement of the main features near the Fermi level is very good, discrepancies appear at higher energies where the analytical continuation of QMC data tends to overestimate broadening and ED shows artifacts of the bath discretization. The peak at the Fermi level in the E_2 spectrum appears to originate in a sharp feature of the bath density of states, Fig. 1, and not in any many-body Kondo physics.

TABLE IV. Total and representation-resolved orbital charge and spin fluctuations of the Co impurity displayed against its total d -shell occupation. The last three columns show the effective masses computed from the self-energy $\Sigma(i\omega_n)$.

| vertex | n_{tot} | ΔN_{tot} | ΔN_{E_2} | ΔN_{E_1} | ΔN_{A_1} | ΔS_{tot}^2 | ΔS_{tot}^z | $\Delta S_{E_2}^z$ | $\Delta S_{E_1}^z$ | $\Delta S_{A_1}^z$ | $m_{E_2}^*$ | $m_{E_1}^*$ | $m_{A_1}^*$ |
|--------|------------------|-------------------------|------------------|------------------|------------------|---------------------------|---------------------------|--------------------|--------------------|--------------------|-------------|-------------|-------------|
| cRPA | 7.23 | 0.92 | 0.32 | 0.19 | 0.034 | 2.39 | 0.86 | 0.11 | 0.20 | 0.007 | 1.77 | — | 1.21 |
| | 8.48 | 0.97 | 0.31 | 0.24 | 0.015 | 1.09 | 0.37 | 0.09 | 0.07 | 0.003 | 1.21 | 1.20 | 1.07 |
| Slater | 7.40 | 0.83 | 0.29 | 0.18 | 0.026 | 1.95 | 0.76 | 0.08 | 0.20 | 0.006 | 1.38 | — | 1.15 |
| | 8.45 | 0.89 | 0.26 | 0.28 | 0.026 | 1.05 | 0.38 | 0.07 | 0.10 | 0.006 | 1.20 | 1.27 | 1.15 |

V. CONCLUSIONS

We performed a quantum many-body study of the Co/graphene system within the Anderson impurity model. DFT calculations have been performed to determine the ground-state properties and the basis for the projection onto localized orbitals centered at the Co impurity. To capture all geometric anisotropies in the Coulomb interaction, we calculated the effective, partially screened Coulomb matrix via cRPA. Having determined all the ingredients for the AIM, its QMC solution has been found by the TRIQS CTHYB solver, and subsequently analytically continued to the real axis by SOM. Within the QMC approach, effect of the cRPA Coulomb matrix has been compared against its approximate rotationally-invariant form. Additionally, we applied exact diagonalization to a subset of the investigated cases and we found a very good agreement between QMC and ED results. This comparison verifies the performance of the employed analytical continuation method, and in the same time it illustrates that ED can provide accurate results also in strongly hybridized cases far from the atomic limit.

As regards the differences between the cRPA and the Slater approximation, the electronic structure is not changed considerably, however, profound differences can be found in the single-particle self-energies of the correlated Co impurity. This is natural, as the self-energy contains most of the Coulomb correlation effects. The Coulomb interaction matrix obtained via cRPA is comparably small. Further considerations might

thus be possible if it were determined to be larger; the differences between the cRPA and the Slater approximation are enhanced in this case, and the effects of anisotropies might thus compete against the hybridization dressing of the Co impurity, thereby revealing possible differences also in the electronic structure. Furthermore, an investigation of the possible existence and properties of the Kondo effect of Co on graphene incorporating all crystal-field effects and the graphene pseudogap could be pursued.

ACKNOWLEDGMENTS

We acknowledge financial support from the Deutsche Forschungsgemeinschaft (DFG) through Projects No. SFB668-A3 and No. DFG-LI 1413/8-1, from the Czech Science Foundation (GACR) under the Grant No. 15-05872J, and from the European Union's Horizon 2020 research and innovation program under Grant Agreement No. 696656 - GrapheneCore1. Access to computing facilities owned by parties and projects contributing to the National Grid Infrastructure MetaCentrum, provided under the program Cesnet LM2015042, is appreciated. The authors gratefully acknowledge the computing time granted by the John von Neumann Institute for Computing (NIC) and provided on the supercomputer JURECA at Jülich Supercomputing Centre (JSC) [45]. Computations were performed with resources provided by the North-German Supercomputing Alliance (HLRN).

-
- [1] K. Novoselov, A. Geim, S. Morozov, D. Jiang, Y. Zhang, S. Dubonos, I. Grigorieva, and A. Firsov, Electric field effect in atomically thin carbon films, *Science* **306**, 666 (2004).
- [2] Y.-M. Lin, A. Valdes-Garcia, S.-J. Han, D. Farmer, I. Meric, Y. Sun, Y. Wu, C. Dimitrakopoulos, A. Grill, P. Avouris, and K. Jenkins, Wafer-scale graphene integrated circuit, *Science* **332**, 1294 (2011).
- [3] A. H. Castro Neto, F. Guinea, N. M. R. Peres, K. S. Novoselov, and A. K. Geim, The electronic properties of graphene, *Rev. Mod. Phys.* **81**, 109 (2009).
- [4] L. S. Mattos, *Correlated Electrons Probed by Scanning Tunneling Microscopy*, PhD. thesis, Stanford University, 2009.
- [5] V. W. Brar, R. Decker, H.-M. Solowan, Y. Wang, L. Maserati, K. T. Chan, H. Lee, Ç. O. Girit, A. Zettl, S. G. Louie, M. L. Cohen, and M. F. Crommie, Gate-controlled ionization and screening of cobalt adatoms on a graphene surface, *Nat. Phys.* **7**, 43 (2011).
- [6] J. Jobst, F. Kisslinger, and H. B. Weber, Detection of the Kondo effect in the resistivity of graphene: Artifacts and strategies, *Phys. Rev. B* **88**, 155412 (2013).
- [7] K. Sengupta and G. Baskaran, Tuning Kondo physics in graphene with gate voltage, *Phys. Rev. B* **77**, 045417 (2008).
- [8] T. O. Wehling, A. V. Balatsky, M. I. Katsnelson, A. I. Lichtenstein, and A. Rosch, Orbitaly controlled Kondo effect of Co adatoms on graphene, *Phys. Rev. B* **81**, 115427 (2010).
- [9] A. Saffarzadeh and G. Kirczenow, Scanning tunneling spectroscopy and Dirac point resonances due to a single Co adatom on gated graphene, *Phys. Rev. B* **85**, 245429 (2012).
- [10] L. Fritz and M. Vojta, The physics of Kondo impurities in graphene, *Rep. Prog. Phys.* **76**, 032501 (2013).
- [11] M. Kharitonov and G. Kotliar, Kondo effect in monolayer and bilayer graphene: Physical realizations of the multichannel Kondo models, *Phys. Rev. B* **88**, 201103(R) (2013).
- [12] L. Li, Y.-Y. Ni, Y. Zhong, T.-F. Fang, and H.-G. Luo, The Kondo effect of an adatom in graphene and its scanning tunneling spectroscopy, *New J. Phys.* **15**, 053018 (2013).
- [13] D. Mastrogiuseppe, A. Wong, K. Ingersent, S. E. Ulloa, and N. Sandler, Kondo effect in graphene with Rashba spin-orbit coupling, *Phys. Rev. B* **90**, 035426 (2014).
- [14] M. Vojta, R. Bulla, and P. Wölfle, Critical quasiparticles in single-impurity and lattice Kondo models, *Eur. Phys. J. Spec. Top.* **224**, 1127 (2015).
- [15] A. Allerdt, A. E. Feiguin, and S. Das Sarma, Competition between Kondo effect and RKKY Physics in Graphene Magnetism, *Phys. Rev. B* **95**, 104402 (2017).
- [16] D. Jacob and G. Kotliar, Orbital selective and tunable Kondo effect of magnetic adatoms on graphene: Correlated electronic structure calculations, *Phys. Rev. B* **82**, 085423 (2010).
- [17] P. Hansmann, L. Vaugier, H. Jiang, and S. Biermann, What about U on surfaces? Extended Hubbard models for adatom systems from first principles, *J. Phys. Condens. Matter* **25**, 094005 (2013).
- [18] F. Aryasetiawan, M. Imada, A. Georges, G. Kotliar, S. Biermann, and A. I. Lichtenstein, Frequency-dependent local interactions and low-energy effective models from electronic structure calculations, *Phys. Rev. B* **70**, 195104 (2004).

- [19] E. Şaşıoğlu, C. Friedrich, and S. Blügel, Effective Coulomb interaction in transition metals from constrained random-phase approximation, *Phys. Rev. B* **83**, 121101(R) (2011).
- [20] F. Schedin, A. K. Geim, S. V. Morozov, E. W. Hill, P. Blake, M. I. Katsnelson, and K. S. Novoselov, Detection of individual gas molecules adsorbed on graphene, *Nat. Mater.* **6**, 652 (2007).
- [21] G. Kresse and D. Joubert, From ultrasoft pseudopotentials to the projector augmented-wave method, *Phys. Rev. B* **59**, 1758 (1999).
- [22] J. P. Perdew, J. A. Chevary, S. H. Vosko, K. A. Jackson, M. R. Pederson, D. J. Singh, and C. Fiolhais, Atoms, molecules, solids, and surfaces: Applications of the generalized gradient approximation for exchange and correlation, *Phys. Rev. B* **46**, 6671 (1992).
- [23] T. O. Wehling, E. Şaşıoğlu, C. Friedrich, A. I. Lichtenstein, M. I. Katsnelson, and S. Blügel, Strength of Effective Coulomb Interactions in Graphene and Graphite, *Phys. Rev. Lett.* **106**, 236805 (2011).
- [24] A. N. Rudenko, F. J. Keil, M. I. Katsnelson, and A. I. Lichtenstein, Adsorption of cobalt on graphene: Electron correlation effects from a quantum chemical perspective, *Phys. Rev. B* **86**, 075422 (2012).
- [25] Y. Virgus, W. Purwanto, H. Krakauer, and S. Zhang, Ab initio many-body study of cobalt adatoms adsorbed on graphene, *Phys. Rev. B* **86**, 241406(R) (2012).
- [26] T. Eelbo, M. Waśniowska, P. Thakur, M. Gyamfi, B. Sachs, T. O. Wehling, S. Forti, U. Starke, C. Tieg, A. I. Lichtenstein, and R. Wiesendanger, Adatoms and Clusters of 3d Transition Metals on Graphene: Electronic and Magnetic Configurations, *Phys. Rev. Lett.* **110**, 136804 (2013).
- [27] M. Karolak, T. O. Wehling, F. Lechermann, and A. I. Lichtenstein, General DFT++ method implemented with projector augmented waves: Electronic structure of SrVO₃ and the Mott transition in Ca_{2-x}Sr_xRuO₄, *J. Phys. Condens. Matter* **23**, 085601 (2011).
- [28] H. Kusunose and K. Miyake, Competition between Hund-Rule Coupling and Kondo Effect, *J. Phys. Soc. Jpn.* **66**, 1180 (1997).
- [29] O. Parcollet, M. Ferrero, T. Ayril, H. Hafermann, I. Krivenko, L. Messio, and P. Seth, TRIQS: A Toolbox for Research on Interacting Quantum Systems, *Comp. Phys. Comm.* **196**, 398 (2015).
- [30] P. Seth, I. Krivenko, M. Ferrero, and O. Parcollet, TRIQS/CTHYB: A Continuous-Time Quantum Monte Carlo Hybridization Expansion Solver for Quantum Impurity Problems, *Comp. Phys. Comm.* **200**, 274 (2016).
- [31] E. Gull, *Continuous-Time Quantum Monte Carlo Algorithms for Fermions*, PhD. thesis, ETH Zurich, 2008.
- [32] I. Krivenko, *TRIQS-based Stochastic Optimization Method for Analytic Continuation*, <https://github.com/krivenko/som>.
- [33] A. S. Mishchenko, N. V. Prokof'ev, A. Sakamoto, and B. V. Svistunov, Diagrammatic quantum Monte Carlo study of the Fröhlich polaron, *Phys. Rev. B* **62**, 6317 (2000).
- [34] M. Caffarel and W. Krauth, Exact Diagonalization Approach to Correlated Fermions in Infinite Dimensions: Mott Transition and Superconductivity, *Phys. Rev. Lett.* **72**, 1545 (1994).
- [35] A. Liebsch and H. Ishida, Temperature and bath size in exact diagonalization dynamical mean field theory, *J. Phys. Condens. Matter* **24**, 053201 (2012).
- [36] O. Gunnarsson and K. Schönhammer, Electron spectroscopies for Ce compounds in the impurity model, *Phys. Rev. B* **28**, 4315 (1983).
- [37] J. Kolorenč, A. B. Shick, and A. I. Lichtenstein, Electronic structure and core-level spectra of light actinide dioxides in the dynamical mean-field theory, *Phys. Rev. B* **92**, 085125 (2015).
- [38] T. Miyake and F. Aryasetiawan, Screened Coulomb interaction in the maximally localized Wannier basis, *Phys. Rev. B* **77**, 085122 (2008).
- [39] F. Aryasetiawan, K. Karlsson, O. Jepsen, and U. Schönberger, Calculations of Hubbard U from first-principles, *Phys. Rev. B* **74**, 125106 (2006).
- [40] C. Friedrich, S. Blügel, and A. Schindlmayr, Efficient implementation of the GW approximation within the all-electron FLAPW method, *Phys. Rev. B* **81**, 125102 (2010).
- [41] <http://www.flapw.de>.
- [42] M. Rösner, E. Şaşıoğlu, C. Friedrich, S. Blügel, and T. O. Wehling, Wannier function approach to realistic Coulomb interactions in layered materials and heterostructures, *Phys. Rev. B* **92**, 085102 (2015).
- [43] E. Şaşıoğlu, C. Friedrich, and S. Blügel, Strength of the Effective Coulomb Interaction at Metal and Insulator Surfaces, *Phys. Rev. Lett.* **109**, 146401 (2012).
- [44] R. Storn and K. Price, Differential Evolution - A Simple and Efficient Heuristic for global Optimization over Continuous Spaces, *J. Global Optim.* **11**, 341 (1997).
- [45] Jülich Supercomputing Centre, JURECA: General-purpose supercomputer at Jülich Supercomputing Centre, *Journal of large-scale research facilities*, **2**, A62 (2016).

CHAPTER 4

Multi-orbital Kondo Effect of $\text{CoCu}_n/\text{Cu}(111)$ systems

The Kondo effect, even though known for a long time [Haa34; Hew93; Kon64], has received new interest due to its relevance for the physics of interacting quantum dots and nanosystems coupled to (approximately) non-interacting leads or substrates. The underlying picture of spinful electrons hopping back and forth between the nanosystem and the substrate gets supplemented by the many-body interactions induced by the local Coulomb interaction on the nanosystem. Due to its repulsive nature, there will mostly be only one electron in each orbital, leading to electron localization and the emergence of a local moment via Hund's rules. The hopping due to hybridization, on the other hand, leads to a rapidly changing magnetization on the nanosystem in such a way that the local moment effectively vanishes. This is the famous Kondo screening of the local moment, and for its occurrence there needs to be a right proportioning between the Coulomb and hybridization strengths, but the former needs to be larger than the latter for the local moment to exist.

In the following we closely follow the exposition in Ref. [Col15]. The Kondo effect can be observed experimentally and theoretically from the emergence of a narrow QP peak (also named as Kondo peak) in the STS dI/dV spectrum near or directly at the Fermi level, cf. Secs. 2.2 and 4.4. There are two main theoretical approaches to the Kondo effect, which can be explained along the two-dimensional phase space spanned by the Coulomb interaction and hybridization strengths. One of them is given in terms of the scaling approach, where the Coulomb interaction strength is assumed fixed, and one works on the hybridization by reducing the conduction electron bandwidth, along with renormalizing effective interaction parameters. Thereby, high-energy excitations are successively integrated out, and one obtains an effective low-energy model which exhibits the Kondo peak. The scaling approach is explained in more detail in Sec. 4.5. It has applications in many branches of physics (such as in the renormalization of quantum field theories, see also Appx. A.2, and far-reaching implications, such as the non-renormalizability of quantized gravitational field theories (based on spin-2 tensor-bosonic particles, the gravitons) [Zee03]. Even though the scaling approach is powerful, physically elucidative, and leads to such concepts as universality, it is also rather technical and computationally very demanding, as, for example, in its NRG incarnation (cf. the introductory part to Chpt. 4; in fact, in condensed matter theory renormalization is not about finiteness of physical quantities, for there is the natural cut-off by the lattice itself; it is rather used as a computational tool [Kop10]). In fact, realistic multi-orbital calculations are difficult to perform with NRG (there are to date no results for five(d)-orbital systems), and only possible for effective low-dimensional models (like the spin- $N/2$ Kondo models, $N \leq 3$) together with the imposition of certain symmetries [Sta15].

– Away from well-separated interaction centres and more generally for the extended electron liquid (i.e., bulk-like systems), the separation of low- and high-energy spectral regions dates back to the works of Bohm and Pines [Pin52]. They described the high-energy region by plasmons (collective electronic excitations) containing the effects of the long-ranged Coulomb interactions, which can be separated from the low-energy region by a canonical transformation. The result for the low-energy region is an effective fluid of renormalized electrons, the QPs, containing the effects of the long-ranged Coulomb interaction. In principle, this approach is analogous to the SW transformation (Subsec. 4.5.1), which, applied to the AIM, yields the effective Kondo model.

The other approach is given by Landau's FL theory [Abr59; Bay07; Col15; Lan56; Pin66], which describes the low-energy physics by phenomenological considerations supplemented by microscopic details. Here, the spectral properties of the conduction electrons and the hybridization strengths are held fixed, while the Coulomb interactions are switched on adiabatically. The motivation for such an approach is the robustness of general electron-liquid properties even at strong interactions, such as linear specific heat capacities, temperature-independent paramagnetic susceptibilities, or the existence of a Fermi surface. The latter is obviously relevant for the Kondo effect, and its spectral concentration of QPs within a small energy range around the Fermi level. It was Landau who traced back the robustness of FL behaviour under strongly enhanced interactions to adiabaticity and the Pauli principle (Fermi statistics) [Lan56]. In this way, he introduced the notion of QPs as renormalized electrons, that is, the valid interpretation of the strongly interacting FL as still being composed of independent particles; still indexed by the same quantum numbers, such as momentum, spin, and charge; but weakly interacting only, and featured with effective masses and magnetic moments. And he connected electron liquids with very different spectral properties, for example, the ones before with the ones after the emergence of the narrow QP Kondo peak at the Fermi level.

The stability of the QPs is due to their residing within a small region around the Fermi level, as the phase space for scattering of QPs off the Fermi sea (with subsequent creation of electron-hole pairs carrying away the QP excitation energy) scales quadratically with distance from the Fermi surface and with temperature, $\tau^{-1}(\varepsilon) = \varepsilon^2 + \pi^2 T^2$, and thus an infinite QP lifetime is ensured only in its immediate vicinity. The temperature dependence is due to the Pauli principle, and relates to the temperature dependence of the resistivity of metals [Abr54], $\rho(T) = \rho_0 + AT^2$, which becomes modified in metals containing Kondo impurities, when the temperature is low enough as such that the quantum-mechanical effects prevail over the thermal effects. At zero temperature, a QP above the Fermi level scatters off the Fermi sea while reducing its energy (and thus preserving its existence) by electron-hole pair production; the QP energy difference ω is then absorbed by this electron-hole pair [Sch99]. From Fermi's golden rule and energy conservation follows

$$\frac{1}{\tau(\varepsilon)} = \frac{2\pi}{\hbar} \sum_f |V_{if}|^2 \delta(\varepsilon - \varepsilon_F)$$

$$\approx \frac{1}{2\pi} |V|^2 \int_0^\varepsilon d\omega \rho(0) \int_0^\omega d\varepsilon' \rho(0) \int d\varepsilon'' \rho(0) \delta(\varepsilon - \omega - \varepsilon' + \varepsilon'') = \frac{\pi}{\hbar} |V|^2 \rho^3(0) \varepsilon^2. \quad (4.1)$$

The decay rate must obviously be smaller than the **QP** excitation energy ε , for otherwise the **QP** would not be stable. The existence of **QPs** is accompanied by quasi-holes below the Fermi level. It has to be noted that the **FL** behaviour is only valid up to critical interaction strengths, that is, there will certainly be some range of validity, above which the switching-on of the interactions cannot be performed adiabatically any more, so that a phase transition occurs [Col15].

Most computational investigations in condensed matter theory start from an Hamiltonian, and Landau's **FL** theory is indeed able to provide the most general one for the low-energy excitations in terms of a Taylor expansion to all orders. From the just mentioned stability of **QPs** near the Fermi surface follows the commutation rule $[\hat{H}, \hat{n}_{\mathbf{k}\sigma}] = 0$ for $\mathbf{k} \in \text{FS}$. Thus, there is a dilute **QP** gas around the Fermi surface, in which the **QPs** scatter only forwardly. The occupations $n_{\mathbf{k}\sigma}$ are the ones of excited states which deviate from the equilibrium values $n_{\mathbf{k}\sigma}^{(0)}$ by an amount $\delta n_{\mathbf{k}\sigma}$. The Taylor expansion of the total energy in these deviations yields at zero order the total energy of the equilibrium Fermi sea, at first order the energy contributions of the **QPs** (i.e., their excitation energies), and at second order their two-body interactions,

$$E_{\text{tot}} = E_{\text{tot}}^{(0)} + \sum_{\mathbf{k}\sigma} (\varepsilon_{\mathbf{k}\sigma}^{(0)} - \mu) \delta n_{\mathbf{k}\sigma} + \frac{1}{2} \sum_{\mathbf{k}\sigma \mathbf{k}'\sigma' | \mathbf{q}| < \Lambda} f_{\mathbf{k}\sigma, \mathbf{k}'\sigma'}(q) \delta n_{\mathbf{k}\sigma}(\mathbf{q}) \delta n_{\mathbf{k}'\sigma'}(-\mathbf{q}) + \dots \quad (4.2)$$

The parameter Λ is smaller than the thickness of the **QP** shell around the Fermi surface, and now allows for small momentum transfer between the **QPs**. The energy levels $\varepsilon_{\mathbf{k}\sigma}^{(0)}$ are the ones before the presence of **QPs**, and the first order derivative of the total energy E_{tot} yields the renormalized energy levels $\varepsilon_{\mathbf{k}\sigma} = \varepsilon_{\mathbf{k}\sigma}^{(0)} - \mu + \sum_{\mathbf{k}'\sigma'} f_{\mathbf{k}\sigma, \mathbf{k}'\sigma'} \delta n_{\mathbf{k}'\sigma'}$. The occurrence of the deviations $\delta n_{\mathbf{k}\sigma}$ means that the Fermi sea is polarized, so the interactions are expanded and parametrized in terms of multipole moments of these polarizations. The resulting parameters are called Landau parameters, and they measure the renormalization of the non-interacting **FL** by the interaction effects on the **QP** energies. In the derivation of these renormalized energy levels $\varepsilon_{\mathbf{k}\sigma}$, the rest of the Fermi sea is assumed frozen despite the presence of the **QP** excitations. The same can be assumed to apply for the derivation of the interaction parameters, $f_{\mathbf{k}\sigma, \mathbf{k}'\sigma'} = \delta \varepsilon_{\mathbf{k}\sigma} / \delta n_{\mathbf{k}'\sigma'} |_{n_{\mathbf{k}''\sigma''}}$. But in principle one may allow the Fermi surface to relax upon the presence of **QPs** by considering it as a deformable sphere, now with (as it comes out, collisionless) collective **QP** excitations. The relaxation of the Fermi sea obviously leads to renormalized interactions $\tilde{f}_{\mathbf{k}\sigma, \mathbf{k}'\sigma'} = \delta \varepsilon_{\mathbf{k}\sigma} / \delta n_{\mathbf{k}'\sigma'}$. Indeed, this concept applies to the Coulomb interaction and its screening as well, which has been derived in Sec. 3.1, even though here it has been derived for the neutral **FL** only, with the important qualification that $f_{\mathbf{k}\sigma, \mathbf{k}'\sigma'}(q=0)$ remains finite. This property does not apply for the charged **FL** with **QPs** interacting via the (screened) Coulomb interaction, and we will shortly describe the resolution below. To simplify the rest of the discussion on Landau **FL** theory, the Fermi sea is kept frozen in the following, having in mind, that a subsequent

treatment can account for its relaxation.

The effective mass m^* is defined by the Fermi momentum (or wave vector) k_F ,

$$p_F = m^* \left. \frac{d\varepsilon_{|\mathbf{k}|}^{(0)}}{d|\mathbf{k}|} \right|_{|\mathbf{k}|=k_F}. \quad (4.3)$$

As the Fermi sea is assumed frozen, the Fermi momentum is a constant. In terms of the effective mass m^* , the DOS becomes renormalized as well (the neutral FL is considered),

$$N^*(\varepsilon) = 2 \sum_{\mathbf{k}} \delta(\varepsilon - \varepsilon_{\mathbf{k}}^{(0)}) = 2 \int d|\mathbf{k}| \frac{4\pi|\mathbf{k}|^2}{(2\pi)^3} \delta(\varepsilon - \varepsilon_{|\mathbf{k}|}^{(0)}) = \frac{|\mathbf{k}|^2}{\pi^2} \frac{d|\mathbf{k}|}{d\varepsilon_{\mathbf{k}}^{(0)}} \xrightarrow{\varepsilon \rightarrow \varepsilon_F} \frac{m^* p_F}{\pi^2}. \quad (4.4)$$

The Landau FL interaction parameters shown in Eq. (4.2) can be decomposed into a spin-symmetric and -antisymmetric part, $f_{\mathbf{k}\sigma, \mathbf{k}'\sigma'} = f_{\mathbf{k}\mathbf{k}'}^s + f_{\mathbf{k}\mathbf{k}'}^a \sigma\sigma'$. As mentioned, both parts of the interaction parameters can be expanded in multipole moments of the Fermi sea polarizations, that is, Legendre polynomials with coefficients being the Landau parameters. The expansion is analogous to the one of the Coulomb interaction, see Eqs. (2.47) and (2.48). By application of a chemical potential $\delta\mu$, or an external magnetic field B , the energy levels of the system now contain the change $\delta\varepsilon_{\mathbf{k}\sigma}^{(0)} = -\sigma\mu_S B - \delta\mu$ ($\mu_S = \frac{g}{2}\mu_B$). Together with the interactions, the QP energy levels contain the renormalized changes $\delta\varepsilon_{\mathbf{k}\sigma} = -\sigma\lambda_s\mu_F B - \lambda_c\delta\mu$, where the λ 's are renormalization parameters. As the electron liquid is assumed isotropic, the charge and spin polarizability are renormalized by the $l = 0$ component only,

$$\chi_n = \frac{1}{V} \frac{\partial N}{\partial \mu} = \frac{N^*(0)}{1 + F_0^s}, \quad (4.5)$$

$$\chi_s = \frac{1}{V} \frac{\partial M}{\partial B} = \frac{\mu_S^2 N^*(0)}{1 + F_0^a}. \quad (4.6)$$

The normalized Landau parameter $F_0^s = N^*(0)f_0^s$ usually has a positive sign if the interactions are repulsive, which results in a reduced charge susceptibility. This applies to Kondo systems, in which the charge fluctuations are frozen out. In FLs with strong ferromagnetic interactions the normalized Landau parameter F_0^a is negative, though, and yields an enhanced spin susceptibility. Indeed, the parameter $1/(1 + F_0^a)$ is the normalized Wilson ratio, which measures the ratio between the Pauli paramagnetic susceptibility and the low-temperature specific heat, both being linear in the renormalized DOS at the Fermi level $N^*(0)$. The Wilson ratio is also called the Stoner enhancement factor, and it is obviously positive in ferromagnetic materials. The spin susceptibility diverges in case of $F_0^a \rightarrow -1$, leading to the Stoner instability, a ferromagnetic quantum critical point where the magnetic correlations become infinitely ranged, and to the breakdown of Landau FL theory. Eqs. (4.5) and (4.6) make apparent that the particle-hole excitations near the Fermi surface, and not all electrons, are important for the physics of the system. This explained the experimental findings, which measured smaller values for the susceptibilities than theories predicted before.

In terms of normalized Landau parameters, the effective mass is given by $m^* = m(1 + F_1^s)$, where F_1^s is the positive $l = 1$ (dipole) component of the interactions. That the mass enhancement takes place at dipolar order can be understood by looking at the system of the **QP** moving in one direction, and its surrounding electron fluid flowing in the reverse direction. Now, removing the normalization of the Landau parameter F_1^s , and using $N^*(0) = \frac{m^*}{m}N(0)$, one obtains the expression

$$m^* = \frac{m}{1 - N(0)f_1^s}, \quad (4.7)$$

which may be compared with Eq. (18) in Sec. 3.6, where it has been expressed in terms of **GF** quantities. For strong interactions, the effective mass m^* may become very large, a phenomenon which has first been observed by Mott [Mot68; Mot49], who subsequently characterized the Mott localization based on his findings. Having large effective masses, the fermion will start being localized, and the class of heavy-fermion compounds emerges. One observes for the Co/graphene system that the electrons residing in the different orbitals of the Co adatom have indeed enhanced effective masses, but the enhancement is not that pronounced as such that one may consider the electrons being strongly localized (Tab. IV in Sec. 3.6). Consequently, the Co adatom exhibits rather metallic behaviour, which in turn is connected with the rather weak Coulomb interaction strengths determined by the **cRPA**. In contrast to the situation on graphene, the Co adatom on the Cu(111) surface exhibits a strong mass renormalization due to Kondo charge localization (Sec. 4.6). At last, as described for the Co/graphene system (Sec. 3.6), non-**FL** behaviour may emerge around the Co adatom at lower Co filling due to the peculiarity of the graphene substrate. This can be detected from the self-energy at low frequencies/energies, which exhibits a singularity in the orbitals of E_1 symmetry, meaning that there occurs an enhanced scattering rate and that the **QP** lifetime is too short for the **FL** to emerge.

In charged **FLs** there acts the long-ranged Coulomb interaction. As in real-space, its Fourier transform into momentum space, $V(q) = e^2/\varepsilon_0 q^2$ (ε_0 being the vacuum permittivity), exhibits a singularity at $q \rightarrow 0$. These are the rapid oscillations at small momenta, so that the correlations between electrons passing by slowly become highly effective. It is indeed the long-range behaviour of the Coulomb interaction before screening which results in the singularity, for the Fourier transform of the Coulomb interaction is actually being given as the limit $a \rightarrow 0$ of the Yukawa interaction,

$$\frac{e^{-ar}}{4\pi r} = \int \frac{d\mathbf{q}}{(2\pi)^3} \frac{e^{i\mathbf{q}\mathbf{r}}}{q^2 + a^2}. \quad (4.8)$$

In fact, the Yukawa potential asymptotics on the left-hand side of Eq. (4.8) can be considered as the general real-space screened Coulomb potential behaviour, which is short-ranged. As calculated in the **cRPA** approximation, the polarization of the electron fluid around a **QP** organizes a polarization cloud which screens the **QP** charge, and the screened interaction becomes finite-ranged. Thus, screening is necessary for the Coulomb singularity resolution in momentum space.

Without screening, however, one may split the Coulomb potential into the long-ranged

classical polarization part and a short-ranged fluctuating quantum part, $\phi(\mathbf{r}) = \phi_P(\mathbf{r}) + \phi_Q(\mathbf{r})$ [Col15; Sil58a; Sil58b] (see also the work of Bohm and Pines mentioned above [Pin52]). The electron-hole excitations happen within the immediate vicinity of the QP, and thus belong to the short-ranged quantum part. The renormalized QP energy levels then have the form $\varepsilon_{\mathbf{k}\sigma}(\mathbf{r}) = \varepsilon_{\mathbf{k}\sigma}^{(0)} + e\phi_P(\mathbf{r}) + \sum_{\mathbf{k}'\sigma'} f_{\mathbf{k}\sigma\mathbf{k}'\sigma'} \delta n_{\mathbf{k}'\sigma'}(\mathbf{r})$. Together with the Gauss law, the difference between the bare and renormalized energy levels have the form $\delta\varepsilon_{\mathbf{k}\sigma}(\mathbf{r}) = \sum_{\mathbf{k}'\sigma'} (e^2/\varepsilon_0 q^2 + f_{\mathbf{k}\sigma\mathbf{k}'\sigma'}) \delta n_{\mathbf{k}'\sigma'}(\mathbf{r})$. So the Coulomb singularity contributes to the isotropic spin-symmetric part only, and results in the TF screening of the QP charge. The charge susceptibility for the charged FL now looks like

$$\chi_c(q) = \frac{N^*(0)}{1 + \frac{e^2 N^*(0)}{\varepsilon_0 q^2} + F_0^s} = \frac{\chi_n}{1 + \frac{\kappa^2}{q^2}}, \quad \kappa^2 = \frac{e^2}{\varepsilon_0} \chi_n. \quad (4.9)$$

The TF screening wavelength is defined as $l_{\text{TF}} = \kappa^{-1}$. At short distances below $r \ll l_{\text{TF}}$ (at $q \gg \kappa$) the susceptibility is the one of the neutral FL, while at large distances $r \gg l_{\text{TF}}$ ($q \ll \kappa$) the susceptibility is suppressed. This result is very important for the study of correlations as these happen to be rather local, and, additionally, the strongly correlated electrons behave like a neutral FL. The long-ranged singular part plays only a minor role and remains unrenormalized. With the Fermi sea being further allowed to relax, the QP interactions look like

$$\tilde{F}_{\mathbf{k}\sigma\mathbf{k}'\sigma'} = \frac{1}{(1 + F_0^s)^2} \frac{e^2}{\varepsilon_0 (q^2 + \kappa^2)} + \tilde{F}_{\mathbf{k}\sigma\mathbf{k}'\sigma'}^{\text{neutral}}, \quad (4.10)$$

where the first part is the screened Coulomb correction. The form of the QP interactions also comes out from GWA/cRPA calculations, and was also used as an input for the “exact DC” approach in Ref. [Hau15] (Appx. C.1).

As mentioned, the range of validity of Landau FL theory is given by the adiabaticity of the switching-on procedure for the interactions. If ferromagnetic interactions become too strong, then one obtains the Stoner instability. It is furthermore known that Landau FLs are unstable against SC. The BCS (Bardeen-Cooper-Schrieffer) theory explains the mechanism for the emergence of the SC order by the Cooper pairing of electrons, resulting in QPs obeying bosonic statistics, which are therefore naturally not described by FL theory [Bar90]. Also in high- T_c SCs the resistivity does not show a quadratic, but linear dependence on temperature, so that Landau FL theory is not valid [Sch99]. Such deviations are shared by all non-FLs: susceptibilities and heat capacities with logarithmic dependencies instead of power-law or constant behaviour; scattering rates linear in energy and temperature instead of being quadratic; resistivities with root-like instead of quadratic temperature behaviour. So, near quantum-critical points the concept of QPs break down; but that is already generally the case in one dimension (without the system being near a quantum-critical point) where the Luttinger liquid theory applies instead, which describes the QPs being unstable and immediately decaying into collective modes (spinons and holons, independently carrying away the charge and spin of electrons). The Co/graphene system also may represent a (local) non-FL system for two possible reasons (cf. Sec. 3.6): first, at lower occupation

there is the enhanced scattering rate in the orbitals of E_1 symmetry directly pointing to the graphene carbon atoms; and second, the two-channel Kondo model was suggested to apply due to the two inequivalent graphene **BZ** points providing two independent conduction electron channels for screening the local moment (cf. Sec. 3.5 and references therein, and short explanation below). Next to the high- T_c **SCs** (see Ref. [Sch99] for a review), or, generally, metals close to a quantum-critical point, there are other non-**FLs** like supermassive heavy fermion materials [Col15], or systems exhibiting the fractional quantum Hall effect, with fractionally charged particles described by anyon statistics [Bal90].

But there are also less exotic objects like the phonons and magnons, which cannot be described by Landau **FL** theory (as they are bosonic), or some Kondo systems, like the two-channel or the disordered Kondo models (for an overview of Kondo scenarios see Ref. [Cox98]). The two-channel Kondo model is based on frustration, as the impurity would like to generate a Kondo singlet with one of the conduction electron channels, while the other channel also wants to participate in the Kondo effect (overscreening), so both channels eventually hinder optimal entanglement. A heavy mathematical machinery consisting of conformal field theory (cf. Ref. [Aff95] and references therein) and Bethe ansatz techniques [And80; And84; Tsv85] was necessary for the solution of the two-channel Kondo model, but also a bosonization to obtain a perturbation-theoretic approach is possible [Sch97]. The resulting two-channel Kondo state is characterized by a non-vanishing entropy of $\ln(2)/2$, meaning that it is not a singlet, but an object with $\sqrt{2}$ **DOF**, which can be described by a free Majorana particle. The resistivity in this case has a \sqrt{T} -dependence. – In the disordered Kondo models the temperature dependence results from a continuous distribution of Kondo temperatures along the impurities immersed in the metal [Ber95; Mir97] (a peak-like distribution would yield one Kondo temperature for all). Such a disorder is realized in many alloys, which are able provide a variety of local environments for an impurity, a particular and to some extent well-studied example given by U atoms in the $\text{Cu}_{5-x}\text{Pd}_x$ alloy [Ber95].

The adiabatic switching-on of the interaction can be defined by a unitary transformation acting on the electronic creation and annihilation operators in the interaction representation,

$$a_{\mathbf{k}\sigma}^+ = U c_{\mathbf{k}\sigma}^+ U^\dagger, \quad (4.11)$$

with the time-evolution operator

$$U = \mathbb{T} \exp\left[-i \int_{-\infty}^0 dt V(t)\right], \quad (4.12)$$

and where \mathbb{T} is the time-ordering operator. To obtain the ground and **QP** states in the presence of interactions, one applies the time-evolution operator on them, $|\Psi\rangle = U|\Psi_0\rangle$ and $|\mathbf{p}\sigma\rangle = U|\mathbf{k}\sigma\rangle_0$, respectively. An electron present above the Fermi sea has an overlap with a **QP** in the same state, and this quantity defines the **WF** renormalization factor

$$Z_{\mathbf{k}} = |\langle \mathbf{k}\sigma | c_{\mathbf{k}\sigma}^+ | \Psi \rangle|^2 > 0. \quad (4.13)$$

The renormalization factor may be seen as an order parameter for the FL [Sch97]. Expanding the time-evolution operator and collecting terms in Eq. (4.11), the electronic creation operator in terms of the QP creation operators looks like

$$c_{\mathbf{k}\sigma}^+ = \sqrt{Z_{\mathbf{k}}} a_{\mathbf{k}\sigma}^+ + \sum_{\mathbf{k}_3+\mathbf{k}_4=\mathbf{k}+\mathbf{k}_2} A(\mathbf{k}_4\sigma_4, \mathbf{k}_3\sigma_3, \mathbf{k}_2\sigma_2, \mathbf{k}\sigma) a_{\mathbf{k}_4\sigma_4}^+ a_{\mathbf{k}_3\sigma_3}^+ a_{\mathbf{k}_2\sigma_2} + \dots, \quad (4.14)$$

so the insertion of an electron above the Fermi surface is equivalent to inserting a QP along with exciting a continuum of other states with an odd number of QPs plus quasi-holes, which have the same total quantum numbers as the inserted QP. These excitations are encoded in the spectral function evaluated at the particular quantum numbers of the inserted electron ($M_{\lambda, \mathbf{k}\sigma} = \langle \lambda | c_{\mathbf{k}\sigma}^+ | \Psi \rangle$),

$$\begin{aligned} A(\mathbf{k}, \omega) &= -\frac{1}{\pi} \text{Im}[G(\mathbf{k}, \omega + i\delta)] \\ &= \sum_{\lambda} |M_{\lambda, \mathbf{k}\sigma}|^2 \delta(\varepsilon - \lambda) \\ &= Z_{\mathbf{k}\sigma} \delta(\omega - \varepsilon_{\mathbf{k}\sigma}) + \sum_{\lambda \neq \mathbf{k}\sigma} |M_{\lambda, \mathbf{k}\sigma}|^2 \delta(\omega - \varepsilon_{\lambda}). \end{aligned} \quad (4.15)$$

There is thus a sharp QP peak near the Fermi level (\mathbf{k} is near the Fermi surface), and a continuum elsewhere comprising other excited states with larger broadening and shorter lifetimes. – The spectral function in Eq. (4.15) shows that the BZ will contain a δ -peaked submanifold, but the situation may be carried over to impurity systems as well: Physically, the localization means that the electronic momenta will be strongly dispersed, and mathematically one may perform the projection of the energy bands onto the correlated site as shown in Eq. (3.55). The result is a sum of δ -peaks centred at the Fermi level. In metals there is still a pronounced dispersion of the QP peak, while in Kondo systems it experiences a strong renormalization as there is less tolerance towards the relevant energetic processes to deviate from the Fermi level. The emergence of the peak structure can also be understood from the spectral functions as shown in Eqs. (3.39)-(3.40), and an explicit expression of the renormalization factor in terms of the self-energy is given in Eq. (3.41). Examples for Kondo peaks and renormalization factors can be seen in Fig. 4.3 and Tab. 4.1, respectively.

In equilibrium, and in the picture of discrete particles, there exists a steady transfer of electrons hopping back and forth between the substrate and the adatom. In the dual picture of the continuous charge density, above a certain time scale, the density is constant and, at low temperatures, reflects a highly correlated state. The electronic tunnelling rate defines a temperature scale, the Kondo scale, via $k_{\text{B}}T_{\text{K}} = \hbar/\tau$, where τ is the QP lifetime. Mathematically, below this scale, conventional PT breaks down as the formulas (e.g., for the Curie susceptibility) become non-analytic and exhibit singularities. Physically, the state describing the adatom and the substrate becomes highly entangled. The emergence of the Kondo state is not related to a quantum phase transition, it can rather be described equivalently by the scaling or the adiabatic FL approach, and with a smooth cross-over (e.g.,

to a susceptibility plateau). Sec. 4.5 describes how the Kondo Hamiltonian can be obtained from the more general AIM Hamiltonian by the scaling approach, that is, by integrating out the high-energy DOF. The cross-over region marked by the Kondo scale defines also the region in which the local moment formation described by the AIM Hamiltonian in Eq. (3.53) competes with the quenching of the local magnetic moment via the Kondo effect. Two main strategies were pursued to understand the Kondo effect, and to solve associated Kondo models: One numerically by the NRG defined by Wilson in 1975 [Wil75], and shortly described in the introductory part to Chpt. 3 (see also references therein); and one analytically by Andrei and Wiegmann in 1980 by recognizing the integrability of the Kondo model by the Bethe ansatz [And80]. Another solution was found by Tsvetick and Wiegmann with the ED of the original AIM Hamiltonian [Tsv85]. As mentioned, in Sec. 4.5 the scaling approach is discussed in some detail, which yields an understanding of the emergence of the Kondo state. In the present thesis, though, the general AIM Hamiltonian is solved by the CTQMC machinery discussed in Sec. 3.3, that is, without any Feynman-diagrammatic approximations or prior application of techniques to obtain an effective low-energy model. On the one hand, this means that the microscopic details and the prevalent physics are somewhat hidden within the enormous complexity of the calculation. But on the other hand, one has the complete solution of the AIM and can observe the emergence of the Kondo peak in the spectrum. The prevalent physical effects (i.e., the low-lying impurity states and the transitions between them) can, however, still be extracted and characterized by an ED of the local adatom Hamiltonian. In principle, one can build an effective Kondo Hamiltonian out of that information, and compare its solution against the CTQMC results. An analogous procedure was performed in Sec. 3.6, where the CTQMC results were compared against the ones obtained via the ED, which was eventually possible because the Co/graphene system behaved rather metallic.

There are a few general adatom-substrate geometries in which the Kondo effect operates. With the advent of STM, individual as well as a collection of correlated impurities on and below surfaces possessing different physical properties could be investigated with an unprecedented precision. The Kondo effect could thereby be quantified quite precisely. The high-dimensional orbital complexity of the impurity problem then demands sophisticated numerical approaches, of which their results can be compared against the high-precision experimental data. The bulk materials in which the Kondo effect is important are the already mentioned heavy-fermion compounds, which can be represented by a dense lattice of Kondo impurities, the Kondo lattice model. Low densities of impurities were already investigated in the 30s of the last century [Haa34], and high densities lead to competitions, such as via the RKKY (Ruderman-Kittel-Kasuya-Yosida) effect with a ferromagnetic coupling between neighbouring impurity spins [Rud54]. In general, for all these models the local moments, which emerge out of the localization on the impurity orbitals, transform into composite QPs with very large effective masses. In the simplest model given by the symmetric single-orbital AIM, containing one interacting energy level immersed in a bath of non-interacting conduction electrons with a DOS symmetrically arranged around the Fermi level, the single energy scale marking the middle of the cross-over region is given by the Kondo temperature $T_K = \sqrt{2U\Delta/\pi} \exp(-\pi U/8\Delta)$, where Δ is the width of the Kondo resonance [Col15]. According to the Curie-Weiss law, in a magnetic system a local

moment exists for $T \leq U/\Delta$, that is, at sufficiently low temperatures. Experiments and the numerical or analytical solution of the **AIM**, or the associated Kondo model then show that this local moment is screened below $T \leq T_K$, that is, when the quantum-mechanical electron-hopping processes start to become more important than the thermal effects.

This section we investigate the Kondo effect in realistic multi-orbital systems. To this end, we consider Co adatoms in different coordination environments on the $\text{Cu}(111)$ surface, and describe them within the **DFT+AIM** approach. – In general, the properties of Anderson impurities, on the one hand, are to a large extent fixed by the choice of the adatom, and by the characteristics of the local Coulomb interaction on it. In particular, alongside with the suppression of a two-valued occupancy in an orbital, the electronic densities in different orbitals will interact with each other, or a pair of electrons may interchange their spin. Furthermore, the environment in which the impurity is placed will lift the degeneracies of its energy levels. The properties of the substrate, on the other hand, can be very diverse. These may be geometric in nature, as, for example, in the $\text{CoCu}_n/\text{Cu}(111)$ systems to be considered. Or these may be physical in nature, as it will be the case if the **SOC**, intertwining the spin and orbital **DOF**, is effective. The $\text{Fe}/\text{TaO}(001-3\times 3)$ system belongs to this class of materials (cf. Ref. [Cor17], Sec. 2.3, and the introductory part to Chpt. 3; of course, the choice of the Fe adatom will also determine the properties of the **AIM**, but the role of the substrate is what one would focus on in a corresponding study).

The following sections describe the multi-orbital Kondo effect in general, and subsequently presents a detailed study of the Kondo effect in the $\text{CoCu}_n/\text{Cu}(111)$ systems. Sec. 4.1 contains the general overview of the Kondo effect in multi-orbital systems, and its relation to the single-orbital **AIM**. Sec. 4.2 introduces the **CF** theory, which is needed for an understanding of the symmetry breaking due to different coordination environments. The Kondo scenario can be microscopically characterized by knowing the eigensystems of the Kondo impurity under consideration, for which the **ME** operator approach discussed in Sec. 4.3 is needed. To eventually simulate the differential conductance spectra, Sec. 4.4 develops the dI/dV formulas. After having established all ingredients needed to understand and work with the **CTQMC** solution to the **AIM** in the context of the Kondo effect, Sec. 4.5 is devoted to the emergence of the Kondo Hamiltonian from the scaling approach. In particular, Subsec. 4.5.1 describes the **SW** transformation to integrate out the high-energy impurity **DOF**; Subsec. 4.5.2 the poor man’s scaling approach to subsequently integrate out the high-energy **DOF** of the conduction electrons; and Subsec. 4.5.3 the orbital contributions to the Kondo effect. Sec. 4.6 then presents the study on the multi-orbital Kondo effect of the $\text{CoCu}_n/\text{Cu}(111)$ systems.

4.1 The Kondo effect in multi-orbital systems

The **AIM** and its **CTQMC** solution fully encompass the local correlations in the sense of the **CI** approach (c.f. introductory part to Chpt. 3). In principle, the description of nanosystems with a realistic **AIM** alone is of course still limited, as the solution of the **AIM** might still be connected with an outer charge-self-consistency loop [Pou07; Sav04], or the Coulomb matrix be made energy-dependent to account for retardation effects (Sec. 3.1). However, first, one may hope the renormalization of the **DFT** input for the **AIM** by the correlations (e.g., the back-reaction effects of the correlations on the conduction electron structure)

being not that essential for the spectral features near the Fermi level. And second, within DMFT for realistic systems one has made the experience that the retardations mainly effect energy regions farer away from the Fermi level, rather leading to satellite structures only [Bie03; Hel11; Sum02] (see introductory part to Chpt. 3). Albeit within the scaling approach the high-energy regions are folded onto the low-energy region (Sec. 4.5), one may expect only gross high-energy features being relevant, while smaller satellite structures should play a minor, or even negligible, role.

The single-orbital AIM easily explains the formation of local moments in case of one orbital: within the set of eigensystems the state with one electron is energetically the lowest. The formation of the local moment can also be understood from a MF treatment of the Coulomb interaction [Col15],

$$Un_{\uparrow}n_{\downarrow} \approx U(n_{\uparrow}\langle n_{\downarrow} \rangle + \langle n_{\uparrow} \rangle n_{\downarrow}) - U\langle n_{\uparrow} \rangle \langle n_{\downarrow} \rangle. \quad (4.16)$$

The Hamiltonian EVs are to be computed via a self-consistency condition (including the hybridization), which can be reformulated to obtain MF equations for the orbital occupation and magnetic moment. The latter develops for Coulomb strengths larger than a critical value, $U \geq U_c = \pi\Delta$, where Δ is the hybridization strength (a single orbital impurity is connected to a flat DOS via a constant hybridization coupling V ; cf. Eq. (3.56)). – In the multi-orbital context, the local-moment formation is additionally driven by Hund’s rule coupling aligning the spins in different orbitals.

In the single-orbital AIM, the MF treatment neglects the quantum-mechanical many-body effects which start to prevail at low temperatures, where hopping between the impurity and the bath may lead to a rapidly changing magnetic moment on the impurity, so that the spin is effectively screened. This is the well-known Kondo effect detailed in the introductory part to this chapter (see also references therein). At temperatures well below the critical scale, the resulting AIM state describes a (total-)spin singlet, in which the spins on the impurity and in the bath are optimally entangled.

In the multi-orbital context the situation is more complicated. Within the multi-orbital AIM, each orbital has its own coupling to the substrate, and its own Coulomb repulsion. Without any inter-orbital interactions, the Kondo effect would happen independently for each orbital. With a full or rotationally invariant Coulomb interaction (e.g., from a cRPA calculation or a Slater approximation, respectively; cf. Subsecs. 3.1.2 and 2.1.4), the Hund’s coupling acting between the orbitals tends to align the spins (Hund’s first rule). But already the density-density Coulomb matrix adds further interaction terms, which let the different orbitals interact repulsively with each other. According to the Co/graphene system (Sec. 3.6), geometric and screening anisotropies have only little effect on the Hund’s coupling strength, for its origin is quantum-mechanical exchange (cf. Fig. 3.3). The locking of spins in different orbitals makes the Kondo screening less effective, as spin-flip energies are then larger. Following this result, for the quantum-mechanical hopping processes to result in the Kondo effect, temperature must be very low. This implies a very narrow QP peak, as its width is proportional to the Kondo temperature [Col15]. This already known circumstance was given a more quantitative estimation by Nevidomskyy and Coleman in 2009 in the context of the NRG, explaining the “Kondo resonance narrowing” in multi-

orbital systems if the spins are locked together to higher total-spin quantum numbers [Nev09]. In principle, Hund’s rules also align orbital moments and make their flips within the orbital Kondo effect more difficult (Sec. 4.5.3).

All these interactions next to the Hubbard- U intertwine the impurity orbitals and let them appear as “one big orbital” (cf. Subsec. 4.6.9). In principle, a many-body GF is actually of dimension 2^M , where M is the number of orbitals. To analyse the spectrum of the solution to a multi-orbital AIM, the GF is projected onto the single-particle states given by the orbitals, and furthermore one usually looks at the diagonal terms only, and compares their superposition with the experimental spectrum (other components are usually very small in geometrically symmetric environments). This procedure has been done in the Sec. 4.6, see Fig. 4.5, where the multi-orbital Kondo effect, a highly-correlated many-body state, manifests itself as spectral peaks in the single-particle states. Their emergence and superposition according to Fano theory is described in Sec. 4.4. The position of the Kondo peaks and the Kondo temperature, both in the multi-orbital context, can also be understood within the ME operator approach, see Secs. 4.3 and references therein. Clearly, the impurity physics is completely described by transitions between its eigenstates, only they are mediated by the hybridization to the substrate.

Even though the Kondo effect has been known since the 30s of the last century [Haa34], only in the last few decades has been achieved an in-depth understanding beyond preliminary perturbational results [And80; Hew93; Tsv85]. With the invention of the STM and the STS, see Secs. 2.2 and 4.4, the Kondo resonance became experimentally directly visible (e.g., Fig. 4.1), and its dependence on various physical conditions could be investigated. The theoretical understanding, on the contrary, remained uneasy, though. A first analytical solution was found by Andrei using thermodynamic Bethe ansatz and conformal field theory techniques [And80], able only at zero temperature [Sak06]. At non-vanishing temperatures, analytical solutions seem impossible, and one has to resort to numerical approaches. Due to the enormous computational complexity of the AIM, or the associated effective Kondo problem, these were approximative at the beginning. However, these were also the first numerical results showing the main important features of the multi-orbital Kondo effect. The more sophisticated numerical approaches of today, like the CTQMC version employed in the present thesis (Sec. 3.3), are able to completely solve the AIM without any approximation - except if the AIM itself was set up by an approximation (see, e.g., discussion at beginning of the present section). In the remainder of this section we will have a look on a very few on these early numerical results for the multi-orbital Kondo effect, while the ones obtained with more sophisticated approaches will be shortly discussed in Sec. 4.6.

Analogous to the cases of low-dimensional geometry and topology in mathematics, or low-dimensional FLs discussed in the introductory part to the present chapter, the Kondo effect changes strongly between the cases of one, two, and three orbitals, while at higher number of orbitals one may expect no essentially new physics to enter the game (except the case with an infinite number of orbitals, as demonstrated by the $N \rightarrow \infty$ limit in the so-called $1/N$ expansion of $SU(N)$ Kondo or other statistical models [Hew93]). The single-orbital Kondo effect is a spin Kondo effect, and one can either change the chemical potential, and thus the impurity filling away from half-filling, or apply an external magnetic

field to suppress it (besides, of course, changing the model parameters, and shifting the AIM outside of the Kondo regime). The phase space of the single-orbital AIM with respect to Kondo physics is simple. Introducing a second orbital, one may have a pure spin Kondo effect at half-filling, which often is denoted as an SU(2) Kondo effect, or a combined spin and orbital Kondo effect, denoted as SU(4) (albeit in many-orbital models with finite effective Kondo couplings there will always be orbital contributions at higher diagrammatic orders). Any degenerate DOF, between which can be flipped, are available to be eventually screened. In Ref. [Zhu04] the two-orbital model was solved by the NRG. An asymmetry in the overall spectrum occurred also at half-filling, which means that there happen to be orbital contributions as well (states with one or three electrons are different in energy), but the Kondo peak itself is still directly at the Fermi level. At quarter-filling the asymmetry in the spectrum becomes stronger, while additionally the Kondo peak is pushed above the Fermi level, which helps to reduce the spectral weight below the Fermi level. The magnetic-field dependence was also analysed, and shown to include the reduction and splitting of the Kondo peak, which is clear in view of the spin channels becoming populated differently, and thus the screening mechanism reduced. The orbital Kondo effect in two degenerate orbitals was also found on the clean Cr(001) surface [Kol02]. – Three-orbital calculations with the NRG were not feasible some ten years ago, so that one first tried to employ the non-crossing approximation (NCA) to solve the three-orbital AIM [Kit06; Sak06]. The NCA is a self-consistent PT omitting vertex corrections. Even though these were shown to be important for a proper assessment of the Kondo effect [Gre09] (e.g., orbital contributions at half-filling are not contained in the NCA), one was able to work out nicely the essential changes between the two- and three-orbital AIMS with respect to the Kondo effect. In Ref. [Kit06] the tunnelling conductance was determined for the analysis of the competition between Hund’s rule coupling J_H and the CF $\Delta\varepsilon$. Hund’s coupling J_H is more important in three-orbital than in two-orbital models as the locked spin is larger; the Kondo temperature T_K is correspondingly lower. However, in both models $\Delta\varepsilon$ tends to enhance T_K first, as the effect of J_H is reduced between non-degenerate orbitals, while after some maximal conductivity T_K is reduced again, because the reduced degeneracy provides less screening mechanisms. As the effectivity of J_H is larger in the three-orbital model, the conductivity maximum is at larger $\Delta\varepsilon$. In general, the conductivity maxima are characterized by a change of GS with less symmetry. Lowering $\Delta\varepsilon$ with both models away from half-filling, T_K becomes enhanced until the SU(4) point is reached in which the degeneracies are optimal for the orbital flips. – In another study employing the same numerical approach for the solution of the multi-orbital AIM [Sak06], the dependence on the magnetic field was analysed in the two- and three-orbital models. It was found that the SU(2) and SU(4) Kondo models behave similar in an external magnetic field, but while in case of SU(2) there is a suppression of spin flipping and resulting screening, in case of SU(4) there is just a decrease of T_K . In the two- and three-orbital models one may observe again a maximum in the conductivity upon increasing the external magnetic field. Interestingly, in the two-orbital model at zero temperature the Bethe ansatz reveals no magnetic dependence of the conductivity at all, while in the case of three orbitals it even increases with the magnetic field. The temperature is thus modifying the behaviour at stronger external magnetic fields, resulting in the maximum structure, and revealing

a competition between enhancement and suppression of the Kondo effect. – For a more complete overview of different Kondo scenarios, the reader is referred to Ref. [Cox98].

4.2 Crystal Field Theory

We follow Refs. [Ney03; Pav12]. If an atom is placed above or within a substrate, both, atom (adatom/impurity) and substrate, start to hybridize. Conduction electrons are flexible, and move within the ionic geometry of this system and its corresponding electrostatic potential (the geometry of the system is the result of a balance between ionic and electronic DOF, though, see Chpt. 1). The ionic potential the impurity feels, that is, the CF, is mostly determined by the neighbouring substrate atoms, and the potential lowers the impurity energy levels in their directions. The energy levels are thus organized according to the symmetries of the environment, which define the algebra of a point group. The impurity Coulomb interaction exhibits the same geometric anisotropies as the energy levels, for its screening will likewise be directionally dependent, see Subsec. 3.1.2 and Sec. 3.6.

The splitting of the energy levels due to the CF not only reflects the symmetries of the system, but also the local chemical environment of the adatom [Pav12]. According to Eq. (3.56), the energy levels and CF splitting can be seen as the static part of the hybridization function. Alternatively, from the DFT Hamiltonian in Eq. (2.16), the hopping amplitudes can be computed as (see also Ref. [Pav12])

$$t_{\alpha\sigma,\alpha'\sigma'}^{i,i'} = - \int d\mathbf{r} \psi_{i\alpha\sigma}^*(\mathbf{r}) \left[-\frac{1}{2}\Delta + V_{\text{KS}}(\mathbf{r}) \right] \psi_{i'\alpha'\sigma'}(\mathbf{r}). \quad (4.17)$$

They describe the hopping between different sites i and i' , and the local CF matrix ($i = i'$), which contains the inter-orbital hoppings and, on the diagonal, the impurity energy levels. The WFs contained here are usually atomic hydrogen-like orbitals, but one can also use Wannier orbitals, or the KS orbitals projected onto hydrogen-like orbitals [Kar13; Kun11]. For a many-body treatment beyond DFT in terms of an AIM or Hubbard model, the DFT Hamiltonian in Eq. (2.16) can be expressed in these local orbitals via the hopping elements in Eq. (4.17), and subsequently augmented by the local Coulomb interaction and the DC correction (cf. Sec 3.2). Next to exhibiting the symmetries of the environment, the hopping integrals eventually encode the local bonding and the band structure at the same time.

We assume a small SOC, so that the angular momentum yields good quantum numbers, and concentrate on the Coulomb interaction between the impurity and the neighbouring substrate atoms. In the following we consider only the CF splitting, so that the radial contributions, which are spherically symmetric, are not taken into account. We further assume for simplicity that all neighbouring substrate atoms have the same distance from the impurity. The CF potential is given by (cf. Eqs. (2.47)-(2.49))

$$\begin{aligned} V_{\text{CF}}(\mathbf{r}) &= - \sum_{i=1}^{N_s} \frac{Ze^2}{|\mathbf{R}_i - \mathbf{r}|} \\ &= -Ze^2 \sum_{i=1}^{N_s} \sum_{k=0}^{\infty} \frac{r_{\min}^k}{r_{\max}^{k+1}} \frac{4\pi}{2k+1} \sum_{m=-k}^k Y_{km}(\hat{\mathbf{r}}) Y_{km}^*(\hat{\mathbf{r}}_i), \end{aligned} \quad (4.18)$$

where $r_{\min} = \min(a, r)$ and $r_{\max} = \max(a, r)$ for $|\mathbf{R}_i| = a$ and $|\mathbf{r}| = r$ (the impurity is in the origin), and where $Y_{km}^*(\hat{\mathbf{r}}) = (-1)^m Y_{k, -m}(\hat{\mathbf{r}})$ are the spherical harmonics. For the electrons on the impurity it is $r < a$, and defining

$$q_{km} = \sqrt{\frac{4\pi}{2k+1}} \frac{Ze^2}{a^{k+1}} \sum_{i=1}^{N_s} Y_{km}^*(\hat{\mathbf{r}}_i), \quad (4.19)$$

$$C_m^{(k)}(\hat{\mathbf{r}}) = \sqrt{\frac{4\pi}{2k+1}} Y_{km}(\hat{\mathbf{r}}), \quad (4.20)$$

one can write the sum as

$$V_{\text{CF}}(\mathbf{r}) = - \sum_{k=0}^{\infty} \sum_{m=-k}^k r^k q_{km} C_m^{(k)}(\hat{\mathbf{r}}). \quad (4.21)$$

One can now compute the matrix elements of this potential in the basis given by the local orbitals. Within DFT these are given by the KS orbitals projected onto atomic orbitals within a cut-off radius around the atom, and the quantum numbers are the same as for the hydrogen atom. Thus, one calculates

$$\begin{aligned} \langle n_1 l_1 m_1 s_1 | \hat{V}_{\text{CF}} | n_2 l_2 m_2 s_2 \rangle &= -\delta_{s_1 s_2} \sum_{k=0}^{\infty} \sum_{m=-k}^k q_{km} \int dr r^2 r^k R_{n_1 l_1}(r) R_{n_2 l_2}(r) \\ &\quad \times \int_0^\pi d\theta \sin(\theta) \int_0^{2\pi} d\phi Y_{l_1 m_1}^*(\theta, \phi) C_m^{(k)}(\theta, \phi) Y_{l_2 m_2}(\theta, \phi) \\ &= -\delta_{s_1 s_2} \sum_{k=0}^{\infty} \sum_{m=-k}^k q_{km} \langle n_1 l_1 | r^k | n_2 l_2 \rangle \\ &\quad \times \sqrt{\frac{2l_2+1}{2l_1+1}} C_{l_2 0, k 0}^{l_1 0} C_{l_2 m_2, k m}^{l_1 m_1}. \end{aligned} \quad (4.22)$$

The relevant assumption made here is the same angular dependence of the DFT-WFs and the ones of the hydrogen atom. There furthermore appear the radial parts $R_{n_1 l_1}(r)$ and the Clebsch-Gordon coefficients $C_{l_2 m_2, l_3 m_3}^{l_1 m_1}$. The double sum is restricted to the values $|l_2 - k| \leq l_1 \leq l_2 + k$, $(l_1 + l_2 + k) \bmod 2 = 0$, and $m_2 + m = m_1$. Thus, the values $k > 4$ vanish since it is $l_1 = l_2 = 2$. The product of the Clebsch-Gordon coefficients in Eq. (4.22) together with prefactors and restrictions are also known as Gaunt's coefficients.

While the Gaunt coefficients are somewhat universal, the symmetries of the environment are encoded in the q_{km} 's. In case of Co/Cu(111) (Sec. 4.6), when the Co adatom is placed on an fcc-site, it has three nearest Cu neighbours at angles $\phi = 0, 2\pi/3, 4\pi/3$. The non-vanishing expectation values in Eq. (4.22) relevant for the CF are $\langle R^{(k)} = R^{(k)}(n_1 2, n_2 2) \rangle$, where $R^{(k)}(n_1 l_1, n_2 l_2) = \langle n_1 l_1 | r^k | n_2 l_2 \rangle$

$$\langle n_1 2(\pm 2) s_1 | \hat{V}_{\text{CF}} | n_2 2(\pm 2) s_2 \rangle = -\delta_{s_1 s_2} \frac{Ze^2}{a} \left(3R^{(0)} - \frac{6}{7} \frac{R^{(2)}}{a^2} + \frac{1}{7} \frac{R^{(4)}}{a^4} \right)$$

$$\begin{aligned} \langle n_1 2(\pm 1) s_1 | \hat{V}_{\text{CF}} | n_2 2(\pm 1) s_2 \rangle &= -\delta_{s_1 s_2} \frac{Ze^2}{a} \left(3R^{(0)} + \frac{3}{7} \frac{R^{(2)}}{a^2} - \frac{4}{7} \frac{R^{(4)}}{a^4} \right) \\ \langle n_1 20 s_1 | \hat{V}_{\text{CF}} | n_2 20 s_2 \rangle &= -\delta_{s_1 s_2} \frac{Ze^2}{a} \left(3R^{(0)} + \frac{6}{7} \frac{R^{(2)}}{a^2} + \frac{6}{7} \frac{R^{(4)}}{a^4} \right). \end{aligned} \quad (4.23)$$

The first term yields the same constant shift for all angular momenta, while the second terms contribute dominantly to the **CF** splitting. One can observe that the E_2 directions ($m = \pm 2$) of the C_{3v} symmetry group are shifted upwards by the second term, while the A_1 direction ($m = 0$) is shifted more downwards than the E_1 directions ($m = \pm 1$). These results for the **CF** are in line with the ones obtained computationally via downfolding/localization (Eq. (3.55)), which are listed in Tab. 4.1.

4.3 Many-Electron Operators

As was explained in the introductory part to the present chapter, and will be shown in Subsec. 4.6.8, the Kondo effect can be understood by looking at the hybridization events between the adatom/impurity and the substrate, in which the adatom jumps between its ground eigenstates via virtual transitions to its excited eigenstates. The adatom eigenstates are **ME** states determined by the diagonalization of the local Hamiltonian consisting of the **CF** and the Coulomb matrix. We again assume a negligible **SOC**, so that the spin and orbital moments are valid quantum numbers for the adatom eigenlevels. The one-electron states are characterized by quantum numbers $\gamma = \{nlm\sigma\}$, and the **ME** states by the quantum numbers $\Gamma = \{SLS_zM\}$. For the general discussion here, other quantum numbers, such as Racah's seniority number (degree of unpaired electrons), will not be included in the **ME** state Γ . We follow closely the review by Irkhin and Irkhin [Irk94], which treats the **ME** operator approach in the more general context of bulk systems. This review contains also more general formulas on most relevant quantities in condensed matter theory, for example, for the Coulomb interaction.

The **ME** approach is naturally useful in systems with sufficiently localized electrons, so that band dispersion is weak. **TM** systems often are in the intermediate regime, which is determined by an equal importance of **CF**, hybridization, and Coulomb interaction strength. These systems seem to require by default an exhaustive numerical solution of the **AIM** (for bulk systems within **DMFT**), as no kind of truncated **PT**, or one in a subset of diagrams, seem advisable for a proper description of such systems. This seems to be the case for the Co/graphene system (Sec. 3.6), in which the local Coulomb interaction determined by the **cRPA** was sufficiently screened, so that hybridization was strong enough to excite the adatom into its higher-lying eigenstates, which eventually led to a rather metallic adatom behaviour (possibly with an imprint of graphene's semi-metallicity in a subset of orbitals). The **CTQMC** simulation reflects this property by exhibiting high perturbation expansion orders during tracing out the phase space. In contrast, as the $\text{CoCu}_n/\text{Cu}(111)$ systems are seen to exhibit the Kondo effect experimentally, a local, phenomenological description in terms of its **ME** eigenstates along with a full simulation seem advisable (cf. Sec. 4.6, and references therein for experimental results on the Co/Cu(111) system). The Kondo effect is given by transitions between eigenstates with different total spin and/or total orbital

momentum quantum numbers, and the intermediate excitations visited include mostly the ones with one electron more or one less, instead of eigenstates with a larger total particle number difference to the **GS**.

The **ME-WF** can be expanded in Slater determinants consisting of one-electron **WFs** (which corresponds to the **CI** approach). In case the **SOC** strength is small compared to the **CF**, one can alternatively set up the **ME-WF** by successive *LS*-coupling,

$$\Psi_{\Gamma_n}(x_1, \dots, x_n) = \sum_{\Gamma_{n-1}, \gamma} G_{\Gamma_{n-1}}^{\Gamma_n} C_{\Gamma_{n-1}, \gamma}^{\Gamma_n} \Psi_{\Gamma_{n-1}}(x_1, \dots, x_{n-1}) \psi_{\gamma}(x_n). \quad (4.24)$$

Here, $x_i = (\mathbf{r}_i, s_i)$, and the expansion is performed with the Clebsh-Gordan and the fractional parentage coefficients,

$$C_{\Gamma_{n-1}, \gamma}^{\Gamma_n} = C_{L_{n-1} M_{n-1}, l m}^{L_n M_n} C_{S_{n-1} S_{z, n-1}, \frac{1}{2} \sigma}^{S_n S_{z, n}}, \quad G_{\Gamma_{n-1}}^{\Gamma_n} = G_{S_{n-1} L_{n-1}}^{S_n L_n}. \quad (4.25)$$

If the **SOC** is appreciable, the *jj*-coupling scheme has to be used instead. In accordance with Eqs. (4.24) and (4.25), the **ME** states Γ_n are accompanied by creation and annihilation operators,

$$A_{\Gamma_n}^+ = \frac{1}{\sqrt{n}} \sum_{\Gamma_{n-1}, \gamma} G_{\Gamma_{n-1}}^{\Gamma_n} C_{\Gamma_{n-1}, \gamma}^{\Gamma_n} a_{\gamma}^+ A_{\Gamma_{n-1}}^+, \quad (4.26)$$

so that

$$|\Gamma_n\rangle = A_{\Gamma_n}^+ |0\rangle. \quad (4.27)$$

These satisfy the commutation relations

$$[A_{\Gamma}, A_{\Gamma'}^+] = \delta_{\Gamma\Gamma'} + 2 \sum_{\gamma_1, \gamma_2, \gamma_3} C_{\gamma_1 \gamma_3}^{\Gamma} C_{\gamma_2 \gamma_3}^{\Gamma'} a_{\gamma_2}^+ a_{\gamma_1}. \quad (4.28)$$

These operators, however, are not appropriate for systems with variable particle numbers; in particular, $A_{\Gamma_m} A_{\Gamma_n}^+ \neq 0$ if $m < n$. Thus, it is advised to introduce projection factors and define new **ME** operators,

$$\tilde{A}_{\Gamma}^+ = A_{\Gamma}^+ \prod_{\gamma} (1 - n_{\gamma}). \quad (4.29)$$

With these, one has, for example, $\tilde{A}_{\Gamma} \tilde{A}_{\Gamma'}^+ = \delta_{\Gamma\Gamma'} \prod_{\gamma} (1 - n_{\gamma})$. This modification serves enough for the orthogonality of the **ME** operators and the description of the adatom eigenstates (in particular, they do not mediate any more between eigenstates of different total particle number), of which their change in occupation are already described by the hybridization.

One may reformulate the **AIM** Hamiltonian in terms of **ME** operators. To this end, one

defines Hubbard operators $X(\Gamma, \Gamma') = \tilde{A}_\Gamma^+ \tilde{A}_{\Gamma'} = |\Gamma\rangle\langle\Gamma'|$. In terms of these,

$$a_\gamma^\dagger = \sum_n \sqrt{n} \sum_{\Gamma_n \Gamma_{n-1}} G_{\Gamma_{n-1}}^{\Gamma_n} C_{\Gamma_{n-1}, \gamma}^{\Gamma_n} X(\Gamma_n, \Gamma_{n-1}). \quad (4.30)$$

By the very nature of diagonalization, the resulting local Hamiltonian is diagonal in the spin and orbital momentum projections, while it still may mediate between the other quantum number projections (such as the Racah seniority number mentioned above). The hybridization may be expressed likewise in terms of Hubbard operators, see Ref. [Irk94] for a thorough discussion. One may further note at this point that the full power of Clebsh-Gordan coefficients can be used in the context of the AIM Hamiltonian by reformulating both, the local Hamiltonian and the hybridization, as an expansion in density, spin, and orbital momentum operators. This is possible in view of the structure of the Hubbard term given in Eq. (2.46), where the creation and annihilation operators can be organized, together with help of the expansion in Eq. (2.47) and the Clebsh-Gordan coefficients (cf. Eq. (4.21)), into scalar products of irreducible tensor operators, which encode, amongst others, density, spin, and angular momentum operators. Hund's rules then also follow from the treatment of the local part.

The ME operator approach can naturally be used in the context of the multi-orbital Kondo effect. In principle this can be important for the implementation of the CTQMC solution to the AIM or the NRG solution of the corresponding effective Kondo model (cf. Subsec. 4.5.1). Instead of writing here the complicated formulas, which just express the impurity one-electron operators in an expansion of ME Hubbard operators with expansion coefficients given by Clebsh-Gordan couplings (both, in the *LS*- and the *jj*-coupling), and which can be found in Ref. [Irk94], we only discuss the general results, as we do not need more for the understanding of the CTQMC solution. However, a short digression into formulas for the multi-orbital Kondo temperature will be made in the following.

As mentioned, the AIM Hamiltonian can be expressed in terms of ME operators. The most important states for the multi-orbital Kondo effect are the GSs with N electrons, and the excited states with $N - 1$ electrons (the states with $N + 1$ electrons are higher in energy due to Coulomb repulsion). In principle, one can include higher-excited states (which is done by the CTQMC impurity solver), but the formulas then become very demanding, and they are of less relevance for the main contributions to the Kondo effect. The excited states can be integrated out by the SW transformation discussed in Subsec. 4.5.1, and one obtains the effective Kondo model, also called *s-d* exchange model, as it describes the effective direct exchange interaction between the (*d*-)impurity and the conduction (*s*-)electrons in the substrate. After calculating the impurity GFs, one obtains the Kondo temperature as the width of the corresponding Lorentzian-shaped spectrum,

$$T_K \approx D \exp \left[- \left(\frac{(2S+1)(SL+1)}{(2S'+1)(2L'+1)} - 1 \right)^{-1} \frac{1}{2\rho(\varepsilon_F)J_K} \right], \quad (4.31)$$

where D is the conduction electron bandwidth, $\rho(\varepsilon_F)$ the value of the conduction electron DOS at the Fermi level, and $J_K \approx |V|^2/(E_{LS} - E_{L'S'})$ the Kondo coupling strength (cf.

Eq. (4.53)). E_{LS} is the energy of the GSs, and $E_{L'S'}$ the energy of the excited states with one electron less.

Besides that the multi-orbital Kondo temperature T_K given in Eq. (4.31) is shown only up to first order in SW-PT (Subsec. 4.5.1; higher orders can be derived in within renormalization group (RG)-PT), it does neither take into account CF effects as detailed in Sec. 4.2, nor orbital flips as explained in Subsec. 4.5.3, and it considers only the lowest-lying eigenstates. Within these approximations one may observe from Eq. (4.31) that at half-filling T_K is the lowest, while at any occupation away from half-filling it increases because Hund's rules align fewer spins. However, CF effects lower the GS degeneracy, and T_K increases because Hund's rules are less effective between non-degenerate orbitals. Furthermore, orbital contributions enhance T_K as well because they act as additional degeneracies. And at last, according to experience also with the $\text{CoCu}_n/\text{Cu}(111)$ systems (Sec. 4.6), there often happens to exist a bunch of low-lying eigenstates, which neither belong to the GS multiplet, nor are they connected to the GSs by a hybridization event, because they have the same total particle number (they are distinguished by other quantum numbers). These low-lying states contribute with their own Kondo effect. – One may finally note at this point, that the effective Kondo model at half-filling does not take into account the fact that at higher orders in PT orbital contributions may appear, if one starts an orbital flip from an excited state containing a hole or an additional electron. In principle this might enhance T_K as well, albeit to a small extent; but such processes make up one particular difference between the AIM and its effective Kondo model. Especially in the case of TM systems, where Hund's rule couplings are often not much stronger than hybridization strengths, these processes might further decrease the comparability with effective Kondo models (next to other complexities due to the multi-orbital nature).

4.4 Asymmetry factors in multi-orbital systems

In the present section we derive the scanning tunnelling spectra as being used for the $\text{CoCu}_n/\text{Cu}(111)$ systems (Subsec. 4.6.3). To this end, we closely follow the derivation in Ref. [Mad01], and extend the AIM Hamiltonian in Eq. (3.53) by coupling both, adatom and substrate, to the tip above the surface,

$$\begin{aligned} \hat{H}_{\text{tip}} = & \sum_{\sigma} \varepsilon_t \hat{c}_{t\sigma}^+ \hat{c}_{t\sigma} + \sum_{\alpha\sigma} (M_{\alpha t} \hat{c}_{\alpha\sigma}^+ \hat{c}_{t\sigma} + M_{t\alpha}^* \hat{c}_{t\sigma}^+ \hat{c}_{\alpha\sigma}) \\ & + \sum_{nk\sigma} (M_{nkt} \hat{c}_{nk\sigma}^+ \hat{c}_{t\sigma} + M_{tnk}^* \hat{c}_{t\sigma}^+ \hat{c}_{nk\sigma}). \end{aligned} \quad (4.32)$$

The tip is assumed spherical, that is, it has a single s -like orbital, which is labelled by the index t . This assumption is made in many theoretical explanations accompanying STM experiments, and only a few studies go beyond this approximation, cf. Refs. [Mán15; Mán14; Pal12]. The generalization to multi-orbital tips is straightforward, and would imply tracing over all tip states in the following formulas; but it also would imply to simulate the tip electronic structure, which can be very demanding. The current is given by the rate of

change of the tip particle number operator \hat{n}_t ,

$$\begin{aligned}
I &= e \left\langle \frac{\partial \hat{n}_t}{\partial t} \right\rangle = \frac{ie}{\hbar} \left\langle [\hat{H}, \hat{n}_t] \right\rangle \\
&= \frac{ie}{\hbar} \sum_{\alpha\sigma} (M_{\alpha t} \langle \hat{c}_{\alpha\sigma}^+ \hat{c}_{t\sigma} \rangle - M_{t\alpha}^* \langle \hat{c}_{t\sigma}^+ \hat{c}_{\alpha\sigma} \rangle) - \frac{ie}{\hbar} \sum_{n\mathbf{k}\sigma} (M_{n\mathbf{k}t} \langle \hat{c}_{n\mathbf{k}\sigma}^+ \hat{c}_{t\sigma} \rangle - M_{tn\mathbf{k}}^* \langle \hat{c}_{t\sigma}^+ \hat{c}_{n\mathbf{k}\sigma} \rangle) \\
&= \frac{2ie}{\hbar} \int d\varepsilon \rho_{\text{tip}}(\varepsilon) (f(\varepsilon - eV) - f(\varepsilon)) \\
&\quad \times \left[\sum_{\alpha\beta} M_{t\alpha}^* (G_{\alpha\beta}^a(\varepsilon) - G_{\alpha\beta}^r(\varepsilon)) M_{\beta t} \right. \\
&\quad + \sum_{\alpha n\mathbf{k}} M_{t\alpha}^* (G_{\alpha n\mathbf{k}}^a(\varepsilon) - G_{\alpha n\mathbf{k}}^r(\varepsilon)) M_{n\mathbf{k}t} + \sum_{n\mathbf{k}\alpha} M_{tn\mathbf{k}}^* (G_{n\mathbf{k}\alpha}^a(\varepsilon) - G_{n\mathbf{k}\alpha}^r(\varepsilon)) M_{\alpha t} \\
&\quad \left. + \sum_{n\mathbf{k}n'\mathbf{k}'} M_{tn\mathbf{k}}^* (G_{n\mathbf{k}n'\mathbf{k}'}^a(\varepsilon) - G_{n\mathbf{k}n'\mathbf{k}'}^r(\varepsilon)) M_{n'\mathbf{k}'t} \right]. \tag{4.33}
\end{aligned}$$

The last lines rely on a leading-order expansion in M of the expectation values appearing in the second line, that is, on Fermi's golden rule. The difference between advanced and retarded GFs is just the (non-time-ordered) expectation value of respective operators. The conduction electron states within the GFs in the last lines are the ones perturbed by the presence of the adatom, which are given in terms of the unperturbed GFs by

$$\begin{aligned}
G_{\alpha n\mathbf{k}}(\varepsilon) &= G_{\alpha}(\varepsilon) V_{\alpha n\mathbf{k}}^* G_{n\mathbf{k}}^{(0)}(\varepsilon) \\
G_{n\mathbf{k}n'\mathbf{k}'}(\varepsilon) &= \delta_{n\mathbf{k}n'\mathbf{k}'} G_{n\mathbf{k}}^{(0)}(\varepsilon) + \sum_{\alpha\beta} G_{n\mathbf{k}}^{(0)}(\varepsilon) V_{n\mathbf{k}\alpha} G_{\alpha\beta}(\varepsilon) V_{\beta n'\mathbf{k}'}^* G_{n'\mathbf{k}'}^{(0)}(\varepsilon). \tag{4.34}
\end{aligned}$$

Inserting the unperturbed conduction electron GF and reorganizing the expression, one obtains

$$\begin{aligned}
I &= \frac{4e}{\hbar} \int d\varepsilon \rho_{\text{tip}}(\varepsilon) (f(\varepsilon - eV) - f(\varepsilon)) \\
&\quad \times \text{Im} \left[\sum_{n\mathbf{k}} M_{tn\mathbf{k}}^* G_{n\mathbf{k}}^{(0)a}(\varepsilon) M_{n\mathbf{k}t} \right. \\
&\quad \left. + \sum_{\alpha\beta} (M_{t\alpha}^* + \sum_{n\mathbf{k}} M_{tn\mathbf{k}}^* G_{n\mathbf{k}}^{(0)a}(\varepsilon) V_{n\mathbf{k}\alpha}) G_{\alpha\beta}^a(\varepsilon) (M_{\beta t} + \sum_{n\mathbf{k}} V_{\beta n\mathbf{k}}^* G_{n\mathbf{k}}^{(0)a}(\varepsilon) M_{n\mathbf{k}t}) \right]. \tag{4.35}
\end{aligned}$$

Separating the real and imaginary parts from the unperturbed conduction electron GF,

$$\text{Re}(G_{n\mathbf{k}}^{(0)a}(\varepsilon)) = \text{P} \frac{1}{\varepsilon - \varepsilon_{n\mathbf{k}}^{(0)}}, \quad \text{Im}(G_{n\mathbf{k}}^{(0)a}(\varepsilon)) = \pi \delta(\varepsilon - \varepsilon_{n\mathbf{k}}^{(0)}), \tag{4.36}$$

where P denotes the principal value, one defines the parameters

$$A_{\alpha t}(\varepsilon) = M_{\alpha t} + \sum_{n\mathbf{k}} V_{\alpha n\mathbf{k}}^* \operatorname{Re}(G_{n\mathbf{k}}(\varepsilon)) M_{n\mathbf{k}t}, \quad B_{\alpha t}(\varepsilon) = \sum_{n\mathbf{k}} V_{\alpha n\mathbf{k}} \operatorname{Im}(G_{n\mathbf{k}}(\varepsilon)) M_{n\mathbf{k}t}. \quad (4.37)$$

Thus, one simply has

$$I = \frac{4e}{\hbar} \int d\varepsilon \rho_{\text{tip}}(\varepsilon) (f(\varepsilon - eV) - f(\varepsilon)) \times \operatorname{Im} \left[\sum_{n\mathbf{k}} |M_{tn\mathbf{k}}|^2 G_{n\mathbf{k}}^{(0)a}(\varepsilon) + \sum_{\alpha\beta} (A_{t\alpha}^*(\varepsilon) + iB_{t\alpha}^*(\varepsilon)) G_{\alpha\beta}^a(\varepsilon) (A_{\beta t}(\varepsilon) + iB_{\beta t}(\varepsilon)) \right]. \quad (4.38)$$

Due to the non-vanishing imaginary part of the self-energy, the advanced impurity **GF** $G_{\alpha\beta}^a(\varepsilon)$ is the same as given in Eq. (3.57), and we drop its superscript. At this point we assume a diagonal impurity **GF**, thereby reflecting the symmetries of the adatom environment, and thus its orbitals having no overlap, $G_{\alpha\beta}(\varepsilon) = \delta_{\alpha\beta} G_{\alpha}(\varepsilon)$. Writing out the adatom **GF**, using Eq. (4.36), and reorganizing once more again, one obtains

$$I = \frac{4e}{\hbar} \int d\varepsilon \rho_{\text{tip}}(\varepsilon) (f(\varepsilon - eV) - f(\varepsilon)) \times \left[\sum_{n\mathbf{k}} |M_{tn\mathbf{k}}|^2 \operatorname{Im}(G_{n\mathbf{k}}^{(0)}) + \sum_{\alpha} \frac{|B_{t\alpha}(\varepsilon)|^2 |q_{\alpha t}(\varepsilon)|^2 + 2\tilde{\varepsilon}_{\alpha}(\varepsilon) \operatorname{Re}(q_{\alpha t}(\varepsilon)) - 1}{\operatorname{Im}(\tilde{G}_{\alpha}(\varepsilon)) (1 + (\tilde{\varepsilon}_{\alpha}(\varepsilon))^2)} \right] \quad (4.39)$$

with the asymmetry and Fano parameters

$$q_{\alpha t}(\varepsilon) = \frac{A_{\alpha t}(\varepsilon)}{B_{\alpha t}(\varepsilon)}, \quad \tilde{\varepsilon}_{\alpha}(\varepsilon) = \frac{\varepsilon - [\varepsilon_{\alpha} + \operatorname{Re}(\Delta(\varepsilon) + \Sigma(\varepsilon))]}{\operatorname{Im}(\Delta(\varepsilon) + \Sigma(\varepsilon))} \quad (4.40)$$

(cf. Eq. (4.65)). The first term in squared brackets in Eq. (4.39) contains the tunnelling of electrons from the tip to the unperturbed substrate, and can often be assumed as contributing only a constant background to the current. This is for example the case if the substrate is metallic with a slowly varying **DOS**. The second term in squared brackets describes the tunnelling from the tip into the impurity states, including virtual transitions into the substrate (the conduction states), and from the tip into conduction states with virtual transitions into the impurity.

In most, if not all, cases one does not know the explicit \mathbf{k} -dependence of the couplings $V_{n\mathbf{k}\alpha}$ and $M_{n\mathbf{k}\alpha}$, so these are dropped. The remaining \mathbf{k} -summations can then be performed as with the \mathbf{k} -summation of the Bloch **GF** to obtain the localized **GF**, cf. Eq. (3.55). For the B parameter this means the simplification

$$B_{\alpha t}(\varepsilon) = \sum_n V_{\alpha n} \left[\sum_{\mathbf{k}} \operatorname{Im}(G_{n\mathbf{k}}(\varepsilon)) \right] M_{nt}, \quad (4.41)$$

where the expression in squared brackets is proportional to the DOS in the band n . Now, the band states labeled by the band index n can be projected onto local orbitals positioned at the sites through which the conduction electrons propagate. This procedure is discussed in more detail in Ref. [Kar11b], especially the fact that in most cases the number of bands is larger than the number of orbitals (so this projection is not bijective). To leading order, the most important conduction orbitals are the non-correlated orbitals of the impurity itself [Fra15]. This considerably simplifies the determination of the conduction states, because they can be obtained by using regular DFT projectors including both correlated and non-correlated orbitals at the correlated sites. Given the conduction orbitals indexed by ν at the correlated site \mathbf{R} , the states are given by

$$|\nu\mathbf{R}\sigma\rangle = \sum_n T_{\nu n}^* \sum_{\mathbf{k}} e^{i\mathbf{k}\mathbf{R}} |n\mathbf{k}\sigma\rangle. \quad (4.42)$$

For example, one of the hybridization terms in the AIM Hamiltonian in Eq. (3.53) then looks like

$$\sum_{n\mathbf{k}\alpha} V_{n\mathbf{k}\alpha} \hat{c}_{n\mathbf{k}\sigma}^+ \hat{c}_{\alpha\sigma} = \sum_{\nu\mathbf{R}\alpha} V_{\nu\mathbf{R}\alpha} \hat{c}_{\nu\mathbf{R}\sigma}^+ \hat{c}_{\alpha\sigma}. \quad (4.43)$$

Finally, the discussion can be simplified by specifying which correlated orbitals are coupled to which conduction orbitals due to symmetry reasons. This has been done for the $\text{CoCu}_n/\text{Cu}(111)$ systems. In a subset of the systems, however, the correlated Co adatom on the $\text{Cu}(111)$ surface was placed next to symmetry breaking Cu chains supported on the surface. The symmetry breaking induces hybridizations within the conduction and within correlated orbitals, respectively, which were previously defined without the presence of the Cu chain and according to the C_{3v} symmetry of the system. If the correlated orbitals hybridize with each other significantly, one has to consider the off-diagonal elements of the impurity GF matrix $G_{\alpha\beta}(\varepsilon)$ in Eq. (4.39) (as in Eq. (4.38)), which is difficult to compute with CTQMC, though. A diagonalization of the local impurity GF as given in Eq. (3.55) also does not help, because for the CTQMC calculation the Coulomb interaction matrix has to be transformed accordingly, which renders the matrix rather complicated. According to experiences (with the seven(f)-orbital system δ -Pu, which has likewise non-negligible off-diagonal elements and complex hybridizations due to a considerable SOC strength), the autopartition algorithm within TRIQS/CTHYB does not help with this problem (Sec. 3.3). But as the correlated orbitals happen to be rather localized, their hybridization due to symmetry breaking often remains small, so a diagonal approximation can still be employed.

The hybridizations within the conduction orbitals due to symmetry breaking, however, cannot be neglected. In the publication included in the present chapter the situation has been accounted for by adapting the tunnelling ratios $\gamma_\alpha = M_{\alpha t}/M_{nt}$ appearing in the asymmetry factors $q_{\alpha t}(\varepsilon)$ in Eq. (4.40), where M_{nt} has been assumed constant for all conduction orbitals. A more precise approach would be to reconsider which correlated orbitals couple to which conduction orbitals, possibly with the conduction electron GF $G_{\nu\mathbf{R}}(\varepsilon)$ defined in a basis adapted to the geometric environment (a superposition of cubic harmonics, i.e., hybrid orbitals). The form of the equations (e.g., Eq. (4.39)) remains

invariant under basis transformations, though. – In Subsec. 4.6.3 Eq. (4.39) will be further worked on; there also the meanings of the asymmetry and Fano parameters will be clarified along the results for the $\text{CoCu}_n/\text{Cu}(111)$ systems.

4.5 The Kondo Hamiltonian from scaling

As described in the introductory part to the present chapter, there are two complementary approaches to the Kondo model. There is the scaling approach starting from the isolated interacting atom, which is progressively immersed in the sea of conduction electrons. This amounts to equivalently lowering the temperature progressively, so that the local moment forms and finally the **FL** emerges via its screening. And there is the adiabatic approach starting from the non-interacting **FL**, which describes the adiabatic renormalization of its Friedel-Anderson resonance by switching on the interactions, resulting in the well-known Kondo resonance [Col15]. The spectrum is mathematically displayed in Eqs. (3.37) and (3.39), showing the energy positions of the **QP**- and hole-like excitations relative to the Fermi level. In the symmetric single-orbital **AIM**, in the non-interacting limit the Friedel-Anderson resonance is given by a Lorentzian at the Fermi level of width Δ (the hybridization strength), which in the strongly interacting region develops a three-peak structure showing the narrower Kondo resonance associated with the rapid spin-fluctuations of the local moment, and the two symmetrically arranged broad peaks farer away associated with the valence fluctuations (see Fig. 4.3). Still, due to the Friedel sum rule, Langreth found that the spectral value at the Fermi level is an adiabatic invariant, that is, $A_f(\omega = 0) = \sin^2(\delta_f(0))/\pi\Delta$, a formula also valid at infinite interaction strength [Col15] (the scattering phase shift $\delta_f(\omega)$ is the phase of the S-matrix; if $\delta_f(0) = \frac{\pi}{2}$, the Friedel sum rule tells that the occupation of the single-orbital **AIM** is $n_f = 1$, what is the case for an optimal Kondo effect). The resonance narrowing means that the **QP** weight becomes much smaller than the hybridization strength, $Z \ll \Delta$, and most of the spectral weight is pushed away from the Fermi level to the valence peaks. The **QP** weight Z measures the area under the resonance with height $A_f(\omega = 0)$.

What changes within the **GF** upon adiabatically switching on the interactions is the self-energy. In the **FL** theory for an interacting impurity coupled to a substrate, it obeys the general Taylor expansion up to second order

$$\Sigma_f(\omega - i\eta) = \Sigma_f(0) + (1 - Z^{-1})\omega + iA\omega^2. \quad (4.44)$$

The first term on the right-hand side describes a remaining scattering strength at zero energy, and the second term the linear dependence common to **FL** theory (c.f. Figs. 3.4 and 3.5). The last term is due to the Pauli exclusion principle, and describes the quadratic phase-space energy dependence of particle-hole pair production mentioned in the introductory part to the present chapter. There, the **QP** lifetime was stated to be inversely proportional to the square of the energy separation to the Fermi level.

In **STM** experiments, one is mostly interested in the low-energy physics of the nanosystem coupled to the substrate. Small biases are applied, and the electronic structure around the Fermi level can be recorded. High biases can be applied as well, but if the system is electronically flexible and chemically reactive, one cannot be sure that the system

changes its state. The low-energy features measured in **STM** experiments can nowadays be compared one-to-one to numerical solutions to realistic models.

In this section we discuss the emergence of the low-energy Kondo from the **AIM** Hamiltonian via the scaling approach as implemented by the **RG** transformation. The Hamiltonian changes upon integrating out the high-energy **DOF**, the effects of which are included in new effective couplings, which then control the low-energy behaviour of the system. In principle, only certain gross high-energy features are relevant for the low-energy physics; for example, the van-Hove singularities in the graphene **DOS** contribute to the Kondo temperature and its asymmetric voltage dependence [Weh10] (Sec. 3.5). We will not discuss the emergence of universality classes of systems with the same low-energy physics by **RG** transformations [Col15], or the fact that the **AIM** Hamiltonian can itself be derived from an even more general Hamiltonian [Hew93]. Instead, we will introduce the **RG** transformation, and apply it to the **AIM** Hamiltonian. The machinery explained in the following will not be applied computationally to the $\text{CoCu}_n/\text{Cu}(111)$ systems (Sec. 4.6), but serve as a means to understand the Kondo effect; the interpretation of the **CTQMC** results based on the **ME** operator approach (Sec. 4.3) rely on a prior derivation of the Kondo Hamiltonian, as the latter describes the spin and orbital transitions between the adatom eigenstates.

4.5.1 The Schrieffer-Wolff transformation

We again follow the lines of Ref. [Col15]. The **AIM** Hamiltonian (Eq. (3.53)) consists of three parts: The Hamiltonian of the adatom/impurity containing its energy levels and the local interactions, the energies of the non-interacting substrate, and the hybridization between impurity and substrate. In the simplest case, the substrate **DOS** is flat and of finite bandwidth. Transitions between different impurity states are realized via intermediate transitions into conduction electron states, and vice versa. The Hamiltonian can thus be divided into a low- and a high-energy part, \hat{H}_L and \hat{H}_H , and the hybridization \hat{V} (generalization to multi-orbital systems is straightforward, one might think the orbital indices being suppressed):

$$\hat{H}(D) = \begin{pmatrix} \hat{H}_L & \hat{V}^+ \\ \hat{V} & \hat{H}_H \end{pmatrix}. \quad (4.45)$$

The parameter D marks the cut-off between the low- and the high-energy states of both, impurity and conduction electrons. The Hamiltonian in this decomposition is diagonalized by a unitary transformation, $\hat{H} = \hat{U}\hat{H}(D)\hat{U}^+$, and after projection with P onto the upper left part a low-energy Hamiltonian is obtained, $\hat{H}_L = \hat{P}_L\hat{H}\hat{P}_L$. Rescaling, $\hat{H}(D') = b\hat{H}_L$, leads to a renormalized Hamiltonian of the same form as the original Hamiltonian. Eventually one obtains a continuous flow with respect to renormalizing the bandwidth, and the limit is obtained for $b \rightarrow 1$. The **RG** is obviously a semigroup in the mathematical sense as it contains a projection; there is not an element of the group being the inverse of another element of the group.

As the Hamiltonian is supposed to retain its form, its couplings become renormalized,

which is mathematically expressed by the β -function,

$$\frac{\partial g_j}{\partial(\ln(D))} = \beta_j(\{g_i\}). \quad (4.46)$$

The β -function is mostly known from high-energy physics, for example, in relation to the asymptotic freedom in quantum chromodynamics, but its relevance for the low-energy and statistical physics is likewise as high. The logarithm is continuously growing, so one can make immediate characterizations for the running coupling constants: If $\beta < 0$, the coupling is relevant, because it grows if the bandwidth is reduced; for $\beta > 0$ the coupling is irrelevant. Integrating out the high-energy **DOF** means tracing out a path in the phase space from a point in which the system contains the high-energy **DOF** to a point in the low-energy region. Usually, at higher energies the excited states are reached easily, while at lower energies there remain virtual transitions only. There is a cross-over region along the path in phase space in which the Hamiltonian changes its structure, and one finally arrives at some fixed point below the lowest energy scale of the system, where the Hamiltonian remains invariant under further **RG** transformations. The structure of the Hamiltonian and its couplings at the fixed point describe the low-energy physics of the system. In case of the **AIM**, the cross-over region marks the transition from the local-moment to the Kondo regime, where only the spin **DOF** are left, and the interaction is described by spin exchange between the local moment and the conduction electrons.

The diagonalization of the Hamiltonian in Eq. (4.45) is performed by the **SW** transformation [Sch66],

$$\hat{U} \begin{pmatrix} \hat{H}_L & \lambda \hat{V}^+ \\ \lambda \hat{V} & \hat{H}_H \end{pmatrix} \hat{U}^\dagger = \begin{pmatrix} \hat{H}_L & 0 \\ 0 & \hat{H}_H \end{pmatrix}, \quad (4.47)$$

where, as usual, the hybridization strength has been normalized by extracting a coupling λ . As the hybridization induces the virtual transitions into the high-energy states, it acts as a perturbation, and one can divide the Hamiltonian as $\hat{H} = \hat{H}_0 + \lambda \hat{H}_1$, with $\hat{H}_0 = \text{diag}(\hat{H}_L, \hat{H}_H)$, and $\lambda \hat{H}_1$ the off-diagonal parts of Eq. (4.47). The operator \hat{U} has an action operator as its generator, $\hat{U} = e^{\hat{S}}$. This action operator should be anti-Hermitian, and admits an expansion in the coupling λ , $\hat{S} = \lambda \hat{S}_1 + \lambda^2 \hat{S}_2 + \dots$. The Baker-Campbell-Hausdorff formula yields

$$\begin{aligned} e^{\hat{S}}(\hat{H}_0 + \lambda \hat{H}_1)e^{-\hat{S}} &= \hat{H}_0 + \lambda([\hat{S}_1, \hat{H}_0] + \hat{H}_1) \\ &+ \lambda^2 \left(\frac{1}{2}[\hat{S}_1, [\hat{S}_1, \hat{H}_0]] + [\hat{S}_1, \hat{H}_1] + [\hat{S}_2, \hat{H}_0] \right) + \dots \end{aligned} \quad (4.48)$$

For the diagonalization to be realized one has to impose $[\hat{S}_1, \hat{H}_0] = -\hat{H}_1$. Imposing further $\hat{S}_2 = 0$, one obtains

$$\hat{H}_L \approx \hat{H}_L + \lambda^2 \Delta \hat{H}, \quad \Delta \hat{H} = \frac{1}{2} \hat{P}_L [\hat{S}_1, \hat{H}_1] \hat{P}_L. \quad (4.49)$$

The matrix $\Delta\hat{H}$ should be block-diagonal, which can be achieved with the action operator having the form

$$\hat{S}_1 = \begin{pmatrix} 0 & -\hat{s}^+ \\ \hat{s} & 0 \end{pmatrix}. \quad (4.50)$$

Thus, one can write $\hat{V} = -[\hat{S}_1, \hat{H}_0] = -\hat{s}H_L + \hat{H}_H\hat{s}$. Matrix elements of the hybridization operator then have the form $\langle H|\hat{H}_1|L\rangle = V_{HL} = -s_{HL}E_L + E_Hs_{HL}$, so the ones of the action operator are $s_{HL} = V_{HL}/(E_H - E_L)$. For the second-order term of the renormalized Hamiltonian one obtains the representation

$$\Delta\hat{H} = -\frac{1}{2} \sum_{LL'H} |L\rangle \left(\frac{V_{LH}^* V_{HL'}}{E_H - E_L} + \frac{V_{LH}^* V_{HL'}}{E_H - E_{L'}} \right) \langle L'|. \quad (4.51)$$

In an obvious sense this expression can be represented by a Feynman diagram with an incoming and outgoing line, two vertices, and a virtual line connecting the two. In principle, one can go back to the operator notion and write $V_{LH}^* V_{HL'} = \langle L|\hat{V}^+|H\rangle\langle H|\hat{V}|L'\rangle$. Due to the linearity of Hilbert spaces and physical operators, a **ME** low-energy state $|L\rangle$ is mapped onto a unique high-energy state $|H\rangle$ for any of the operators summed in \hat{V} . All **ME** states are mutually orthogonal, so one can simplify $V_{LH}^* V_{HL'} = \langle L|\hat{V}^+\hat{V}|L'\rangle$, while retaining the sum over high-energy states and the energy arguments in the denominators.

One can insert the precise definition of the hybridization operator displayed in Eq. (3.53) into Eq. (4.51). To this end, the impurity creation and annihilation operators should be represented in the space of **ME** states (Sec. 4.3). The lowest eigenstates of the impurity have, say, N electrons (energetic degeneracies are admitted), and the hybridization maps onto states of $N \pm 1$ electrons. With help of the Fierz identity $2\delta_{\sigma\tau}\delta_{\tau'\sigma'} = \delta_{\sigma\sigma'}\delta_{\tau'\tau} + \boldsymbol{\sigma}_{\sigma\sigma'}\boldsymbol{\sigma}_{\tau'\tau}$, the product of hybridization operators can be recast into

$$\begin{aligned} \hat{V}^+\hat{V} = \sum_{\substack{\alpha\alpha',\sigma\sigma' \\ nn',\mathbf{k}\mathbf{k}'}} V_{\alpha n\mathbf{k}}^* V_{n'\mathbf{k}'\alpha'} & \left[\frac{1}{2} \hat{c}_{n'\mathbf{k}'\sigma'}^+ \hat{c}_{n\mathbf{k}\sigma} \hat{c}_{\alpha'\sigma}^+ \hat{c}_{\alpha\sigma} + \frac{1}{2} \hat{c}_{n\mathbf{k}\sigma} \hat{c}_{n'\mathbf{k}'\sigma'}^+ \hat{c}_{\alpha\sigma}^+ \hat{c}_{\alpha'\sigma} \right. \\ & \left. - \hat{c}_{n'\mathbf{k}'\sigma'}^+ \boldsymbol{\sigma}_{\sigma'\sigma} \hat{c}_{n\mathbf{k}\sigma} \sum_{\tau\tau'} \hat{c}_{\alpha\tau}^+ \boldsymbol{\sigma}_{\tau\tau'} \hat{c}_{\alpha'\tau'} \right]. \end{aligned} \quad (4.52)$$

The third term is the effective interaction of the multi-orbital Kondo model describing the singlet formation via the positive Kondo coupling constants

$$\begin{aligned} J_{\alpha n\mathbf{k},\alpha'n'\mathbf{k}'} & = V_{\alpha n\mathbf{k}}^* V_{n'\mathbf{k}'\alpha'} \\ & \times \sum_H \left(\frac{1}{E_H^{N+1} - E_L^N} + \frac{1}{E_H^{N+1} - E_{L'}^N} + \frac{1}{E_H^{N-1} - E_L^N} + \frac{1}{E_H^{N-1} - E_{L'}^N} \right). \end{aligned} \quad (4.53)$$

The indices of these couplings belong to the low-energy states as shown in Eq. (4.51). In the single-orbital **AIM** the first two terms in Eq. (4.52) yield a residual potential scattering

term, which vanishes in the symmetric AIM. In the multi-orbital generalization here, this term describes orbital flips, and it generates the orbital Kondo effect, cf. Subsec. 4.5.3.

4.5.2 Poor man's scaling

The SW transformation to integrate out the high-energy DOF of the impurity states can also be used to reduce the high-energy excitations in the substrate involving the conduction band edges; in the SW procedure, these were reintroduced by the rescaling $\hat{H}(D') = b\hat{H}_L$. The part of the Hamiltonian describing the spin-flip processes in the Kondo effect is given by (cf. Eq. (4.52))

$$\hat{H}_K = \sum_{\substack{\alpha\alpha' \\ |\varepsilon_{n\mathbf{k}}|, |\varepsilon_{n'\mathbf{k}'}| < D}} J_{\alpha n\mathbf{k}, \alpha' n'\mathbf{k}'} \hat{\mathbf{S}}_{n'\mathbf{k}', n\mathbf{k}} \hat{\mathbf{S}}_{\alpha\alpha'}, \quad (4.54)$$

where now D is the bandwidth of the conduction electron states in the substrate, and the impurity states are already of low energy. The aim is now to integrate out the regions with $D' < |\varepsilon_{n\mathbf{k}}| < D$, $D' = D - \delta D$, which are of high energy, thereby reducing the bandwidth, and including high-energy effects by renormalizing the Kondo coupling constants. The hybridization between the low- and high-energy regions is given by

$$\hat{V}_K = \left[\sum_{\substack{\alpha\alpha', |\varepsilon_{n\mathbf{k}}| < D' \\ D' < |\varepsilon_{n'\mathbf{k}'}| < D}} + \sum_{\substack{\alpha\alpha', |\varepsilon_{n'\mathbf{k}'}| < D' \\ D' < |\varepsilon_{n\mathbf{k}}| < D}} \right] J_{\alpha n\mathbf{k}, \alpha' n'\mathbf{k}'} \hat{\mathbf{S}}_{n'\mathbf{k}', n\mathbf{k}} \hat{\mathbf{S}}_{\alpha\alpha'}. \quad (4.55)$$

This part of the Hamiltonian constitutes the off-diagonal elements in Eq. (4.45). One has now first to characterize the low- and high-energy conduction electron states (to first order), between which V_K mediates via the spin operator $\hat{\mathbf{S}}_{n'\mathbf{k}', n\mathbf{k}}$. To the low-energy states belong the GS, additional electrons above, and additional holes below the Fermi level, but both within the range $|\varepsilon_{n\mathbf{k}}| < D'$. To the high-energy states belong electrons within the range $D' < \varepsilon_{n\mathbf{k}} < D$, and holes within $-D < \varepsilon_{n\mathbf{k}} < -D'$.

The calculation of the matrix elements $\langle L|\hat{V}_K|H\rangle$ and $\langle H|\hat{V}_K|L'\rangle$ proceeds similar as before. One has to note that a low-energy electron (hole) state can be excited into a high-energy electron (hole) state only, for otherwise the matrix elements vanishes. The GS does not contribute. The hybridization \hat{V}_K is a tensor product of operators, and it acts correspondingly on the product states consisting of conduction electron and impurity states. For the term involving electrons, that is, $|L\rangle = \hat{c}_{n_1\mathbf{k}_1}^+ |G\rangle$ and $|H\rangle = \hat{c}_{n_2\mathbf{k}_2}^+ |G\rangle$, with $0 < \varepsilon_{n_1\mathbf{k}_1} \ll D'$ (i.e., near the Fermi level) and $D' < \varepsilon_{n_2\mathbf{k}_2} < D$, and $|G\rangle$ the GS, one calculates (working in the space of conduction electron states)

$$\begin{aligned} & \sum_H \frac{\langle L|\hat{V}_K|H\rangle \langle H|\hat{V}_K|L'\rangle}{E_H - E_L} \\ &= \sum_{\substack{\bar{\alpha} \\ D' < \varepsilon_{n'\mathbf{k}'} < D \\ \mu\mu' \in \{x,y,z\}}} \frac{1}{\varepsilon_{n_2\mathbf{k}_2} - \varepsilon_{n_1\mathbf{k}_1}} J_{\bar{\alpha}n\mathbf{k}, \alpha_1 n_1\mathbf{k}_1} J_{\alpha'_1 n'_1\mathbf{k}'_1, \bar{\alpha}n\mathbf{k}} S_{\alpha_1\bar{\alpha}}^\mu S_{\bar{\alpha}\alpha'_1}^{\mu'} (\sigma^\mu \sigma^{\mu'})_{\sigma_1\sigma'_1} \end{aligned}$$

$$\approx \sum_{\substack{\bar{\alpha} \\ \mu\mu' \in \{x,y,z\}}} \frac{\rho(0)|\delta D|}{D} J^2 S_{\alpha_1\bar{\alpha}}^\mu S_{\bar{\alpha}\alpha'_1}^{\mu'} (\sigma^\mu \sigma^{\mu'})_{\sigma_1\sigma'_1}. \quad (4.56)$$

Several approximations were employed to obtain the last line: First, the hybridization couplings $V_{\alpha n\mathbf{k}}$ were assumed momentum-independent. That might or might not be a good approximation, but it is needed for the following differential equation for the Kondo couplings to be derived. In most cases, the hybridization couplings are assumed orbitally independent as well. And second, one approximates $\varepsilon_{n_2\mathbf{k}_2} \approx D$, and $\varepsilon_{n_1\mathbf{k}_1}, \varepsilon_{n'_1\mathbf{k}'_1} \approx 0$. Now, there is the term arising from hole states, $|L\rangle = c_{n_1\mathbf{k}_1}|G\rangle$ and $|H\rangle = c_{n_2\mathbf{k}_2}|G\rangle$, with $-D' \ll \varepsilon_{n_1\mathbf{k}_1} < 0$ and $-D < \varepsilon_{n_2\mathbf{k}_2} < -D'$,

$$\sum_H \frac{\langle L|V_K|H\rangle\langle H|V_K|L'\rangle}{E_H - E_L} \approx - \sum_{\substack{\alpha\bar{\alpha}\alpha' \\ \mu\mu' \in \{x,y,z\}}} \frac{\rho(0)|\delta D|}{D} J^2 S_{\alpha_1\bar{\alpha}}^\mu S_{\bar{\alpha}\alpha'_1}^{\mu'} (\sigma^{\mu'} \sigma^\mu)_{\sigma_1\sigma'_1}. \quad (4.57)$$

The spins of the low-energy electrons (σ_1, σ'_1) were flipped. During calculation of both, Eqs. (4.56) and (4.57), one observes that the Feynman diagram of the first equation is given by a direct scattering of electronic states,

$$\langle H|\hat{V}_K|L'\rangle \propto \langle G|c_{n_2\mathbf{k}_2\sigma_2}c_{n_2\mathbf{k}_2\sigma_2}^+c_{n'_1\mathbf{k}'_1\sigma'_1}c_{n'_1\mathbf{k}'_1\sigma'_1}^+|G\rangle, \quad (4.58)$$

while the second equation describes virtual electron-hole excitations,

$$\langle H|\hat{V}_K|L'\rangle \propto \langle G|c_{n_2\mathbf{k}_2\sigma_2}^+c_{n_1\mathbf{k}_1\sigma_1}c_{n_2\mathbf{k}_2\sigma_2}c_{n'_1\mathbf{k}'_1\sigma'_1}|G\rangle. \quad (4.59)$$

As the latter include fermion exchange, these yield a negative contribution to the resulting Hamiltonian. Adding the results in Eqs. (4.56) and (4.57), one obtains a commutator, for which one computes with the usual spin commutator relations

$$S_{\alpha_1\bar{\alpha}}^\mu S_{\bar{\alpha}\alpha'_1}^{\mu'} ([\sigma^\mu \sigma^{\mu'}])_{\sigma_1\sigma'_1} = 2\mathbf{S}_{\alpha_1\alpha'_1} \cdot \boldsymbol{\sigma}_{\sigma_1\sigma'_1}. \quad (4.60)$$

Thus, the Hamiltonian in Eq. (4.54) with the conduction electrons on the reduced bandwidth exhibits a renormalized Kondo coupling constant, which is given by ($\delta D = -|\delta D|$)

$$J(D - |\delta D|) = J(D) - 2J^2\rho(0)\frac{\delta D}{D} \quad \text{or} \quad \frac{\partial[\rho(0)J]}{\partial[\ln(D)]} = -2[\rho(0)J]^2. \quad (4.61)$$

This is the famous flow equation of **RG** theory up to second order in **PT**, which describes the change of the effective couplings during the renormalization of the conduction electron bandwidth. In particular, the Kondo coupling J increases if the bandwidth is reduced. The generalization of the flow equation to the multi-orbital and momentum-dependent setting is possible and can be read in Ref. [Kog18].

To summarize the renormalization concept, the **SW** transformation reduces the energy scale for both, the impurity and the conduction electrons, while Hamiltonian and bandwidth for the conduction electrons are restored through rescaling. Furthermore, the **AIM** Hamilto-

nian is restructured in the form of the Kondo Hamiltonian plus higher-order terms. These terms start to be negligible if the low-lying impurity eigenstates relevant for the Kondo effect contribute dominantly (i.e., if their couplings in the corresponding perturbative approximation to the full Hamiltonian are larger than the ones of the higher-order terms). Having obtained the Kondo Hamiltonian, one further works on the conduction electrons by reducing their bandwidth with the help of poor man's scaling. Thereby the Kondo couplings are rescaled, and eventually one arrives at the low-energy fixed point.

4.5.3 Orbital Kondo effect

In Eq. (4.52) the first term contains orbital flips, which lead to the orbital Kondo effect. The corresponding Hamiltonian has the form

$$H_{K,\text{orb}} = \sum_{\substack{\alpha\alpha' \\ |\varepsilon_{n\mathbf{k}}|, |\varepsilon_{n'\mathbf{k}'}| < D}} K_{\alpha n\mathbf{k}, \alpha' n'\mathbf{k}'} (c_{n'\mathbf{k}'\sigma'}^+ c_{n\mathbf{k}\sigma} c_{\alpha'\sigma}^+ c_{\alpha\sigma} + c_{n\mathbf{k}\sigma} c_{n'\mathbf{k}'\sigma'}^+ c_{\alpha\sigma}^+ c_{\alpha'\sigma}), \quad (4.62)$$

where the K 's are the orbital Kondo couplings. The hybridization term resulting from this Hamiltonian is of similar form as in Eq. (4.53). Performing the same analysis as before, and adding the contributions from low-energy electron and hole states near the Fermi level as in Eq. (4.56), one obtains

$$\begin{aligned} \Delta H_{n_1\mathbf{k}_1\sigma_1, n_1'\mathbf{k}_1'\sigma_1'} &\propto \frac{\rho(0)|\delta D|}{D} \\ &\times \sum_{\substack{\alpha\alpha', \sigma \\ \bar{\alpha}\bar{\alpha}', \bar{\sigma} \\ n_2\mathbf{k}_2}} (K_{\alpha n_2\mathbf{k}_2, \alpha' n_1'\mathbf{k}_1'} K_{\bar{\alpha} n_1'\mathbf{k}_1', \bar{\alpha}' n_2\mathbf{k}_2} - K_{\alpha n_1\mathbf{k}_1, \alpha' n_2\mathbf{k}_2} K_{\bar{\alpha} n_2\mathbf{k}_2, \bar{\alpha}' n_1'\mathbf{k}_1'}) \\ &\times (c_{\alpha'\sigma}^+ c_{\alpha\sigma} - c_{\alpha\sigma}^+ c_{\alpha'\sigma}) (c_{\bar{\alpha}'\bar{\sigma}}^+ c_{\bar{\alpha}\bar{\sigma}} - c_{\bar{\alpha}\bar{\sigma}}^+ c_{\bar{\alpha}'\bar{\sigma}}) \delta_{\sigma_1\sigma_1'}. \end{aligned} \quad (4.63)$$

One may observe here that dropping the band and momentum dependence of the hybridization couplings would render this term vanishing, and the orbital Kondo coupling would not be renormalized at second order. Writing $c_{\bar{\alpha}'\bar{\sigma}}^+ c_{\bar{\alpha}\bar{\sigma}} = \delta_{\bar{\alpha}'\bar{\alpha}} - c_{\bar{\alpha}\bar{\sigma}}^+ c_{\bar{\alpha}'\bar{\sigma}}$, one can drop terms of higher order than two in the impurity operators, and obtain terms of similar forms as the original orbital Kondo Hamiltonian in Eq. (4.62), albeit somewhat broken up due to the orbital and momentum dependence of the orbital Kondo couplings. For a thorough analysis of the renormalization procedure for anisotropic Kondo couplings one may refer oneself to Ref. [Kog18].

4.6 Kondo effect of Co adatoms at Cu chains

The research group of Prof. A. I. Lichtenstein has collaborated with several experimental groups, in particular with the one of A. Weismann and Prof. R. Berndt at the CAU in Kiel in the context of the SFB 668 (project A3). Recently, this group produced chain-like structures on a clean Cu(111) surface by physically touching it with an STM tip [Spe08] (Fig. 4.1 left). The resulting chains are monatomic in height and width, and are dislocations, which can be modelled by chains of Cu atoms on the surface. Placing one or more Co atoms at different positions along the chain, specific line shapes are seen in the STS curves

recorded afterwards (Fig. 4.1 right). To interpret the experimental results, use of the **DFT+AIM** approach (Subsec. 3.2.1) was made to capture the Kondo behaviour of the Co adatoms by the efficient **CTQMC** procedure as implemented in the **TRIQS/CTHYB** code (Sec. 3.3). The latter is a numerically exact solution of the underlying **AIM**, and the Kondo properties of the system can thereby be assessed properly. The impurity solver is capable to take into account the full Coulomb matrix, and all geometric anisotropies exhibited by the **CF** and the hybridization.

The interaction of an adatom carrying a local magnetic moment with its substrate often happens via the Kondo effect. The associated spectral resonance feature around the Fermi level has been observed for several nanosystems on surfaces, adatoms, small atomic clusters, and organic molecules [DiL12; Kna17; Li98; Mad01; Mad98; Man00; Min12; Née08; Née07; Ott09; Pac17; Piv07; Ter09; Wah04]. Usually the theoretical descriptions accompanying the experimental results rely on single-orbital AIMs or spin- $\frac{1}{2}$ Kondo models, in which a single spin is screened by the conduction electrons of the substrate. These models provide a simplified and well understood scenario, see Refs. [And61; Kon68; Kon64], and are able to qualitatively explain even advanced experimental situations involving the Kondo effect (see, e.g., Refs. [Cor17; Kam21; Kam19]; Sec. 4.1). Important parameters of the experimental data like the Kondo temperature T_K , which determines the energy scale of the effect and is related to the width of the resonance, are extracted by fitting line shapes, for example, Fano [Fan61] and Frota [Fro92; Fro86; Prü11] lines, which are related to these single-orbital models.

Even though the neglect of the adatom orbital structure and the symmetries of its environment appears to be a rather crude approximation, it often leads to useful results at little expense. However, at present experimental evidence accumulates that demonstrate the involvement of multiple orbitals (see also Subsec. 4.6.10). For example, results from adsorbed molecules show that different Kondo signatures can emerge in different orbitals, which reflects the hybridization anisotropies similar as in the $\text{CoCu}_n/\text{Cu}(111)$ systems discussed in this section [Kna17; Pac17]. Moreover, it was reported that Fe-phthalocyanine (FePc) molecules can exhibit $\text{SU}(2)$ and $\text{SU}(4)$ Kondo effects (i.e., the latter comprising orbital contributions), depending on their position, and thus on the respective symmetries of the substrate lattice [Min12]. The superposition of a Kondo resonance with a charge excitation, both in the d_{z^2} orbital, has been proposed for MnPc molecules [Küg15], indicating that several orbitals must be involved for the stability of the Kondo effect (see also Subsec. 4.6.9). The study on the $\text{CoCu}_n/\text{Cu}(111)$ systems presented in the following underlines the need for a full consideration of all correlated orbitals in real Kondo systems.

The present section investigates the Kondo effect of single Co adatoms on $\text{Cu}(111)$ surfaces, and attached to chains of Cu atoms (denoted as $\text{CoCu}_n/\text{Cu}(111)$), by means of the **DFT+AIM** approach as discussed in Chpt. 3, and along the line shapes seen in experimental **STS** data (Fig. 4.1 right). Multi-orbital calculations of the Kondo effect were performed, and quantitatively reproduce the experimental spectra. The hybridization of the Co d orbitals with the Cu chain lifts the orbital degeneracies, which were present on the (111) terrace, and leads to distinct spectral line shapes, which are not consistent with a single-orbital description (Subsec. 4.6.9). More recent **STS** measurements on the $\text{CoCu}_n/\text{Cu}(111)$ systems were able to better resolve the spectral depressions for the Co

adatom at the central part of the chain at approximately ± 10 eV (Fig. 4.1 right), and show that a SOC might be relevant in these systems. The SOC leads to a further symmetry breaking of the spin DOF, and eventually to a magnetic anisotropy, which can be taken into account by an extension of the AIM Hamiltonian. A derivation of the corresponding Hamiltonian for the MAE based on DFT data is provided in Appx. B.

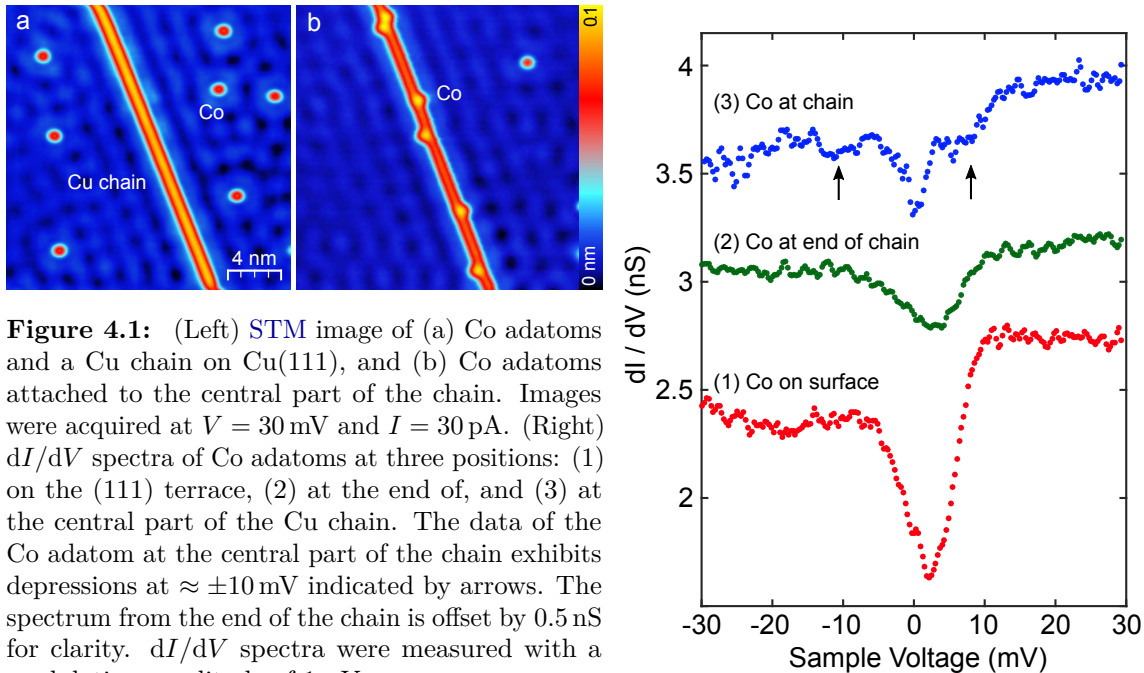


Figure 4.1: (Left) STM image of (a) Co adatoms and a Cu chain on Cu(111), and (b) Co adatoms attached to the central part of the chain. Images were acquired at $V = 30$ mV and $I = 30$ pA. (Right) dI/dV spectra of Co adatoms at three positions: (1) on the (111) terrace, (2) at the end of, and (3) at the central part of the Cu chain. The data of the Co adatom at the central part of the chain exhibits depressions at $\approx \pm 10$ mV indicated by arrows. The spectrum from the end of the chain is offset by 0.5 nS for clarity. dI/dV spectra were measured with a modulation amplitude of 1 mV.

4.6.1 Experimental results

Experiments were conceived and performed by N. Noei and A. Weismann (CAU in Kiel). Fig. 4.1a (left) shows the topography of a chain of monatomic width along with Co adatoms. Using a reduced tunnelling resistance ($V = 30$ mV, $I = 1 \mu\text{A}$) these atoms could be moved with the STM tip to positions aside of the chain (Fig. 4.1b left), or at one of its ends. The dI/dV spectra of the $\text{CoCu}_n/\text{Cu}(111)$ systems exhibit an Abrikosov-Suhl resonance around zero bias [Née11; Née08; Uch08; Wah04] (Fig. 4.1 right).

Three clearly different kinds of spectra (Fig. 4.1 right) could be discriminated as corresponding to three Co adatom positions, namely on the (111) terrace, at the central part of, and at the end of the chain (Fig. 4.1 right). The Abrikosov-Suhl resonance of Co adatoms at the central part of the chain exhibits a remarkably complicated structure, which matches neither a Fano nor a Frota line shape¹. It exhibits an antiresonance at the Fermi level decorated with depressions at approx. ± 10 mV (arrows). The amplitude of the

¹ For comparison with prior work, a Kondo temperature T_K may be extracted using a Frota line shape of the DOS $\rho(E) \propto \text{Re} \sqrt{i\Gamma_F / (E - E_0 + i\Gamma_F)}$, where the Frota parameter Γ_F is related to the Kondo temperature by $k_B T_K = 2.54 \Gamma_F$. For Co adatoms on the (111) terrace, one thus obtains $T_K \approx 52$ K similar to published values [Kno02; Née08; Wah04].

antiresonance is approx. 60 % lower than for Co adatoms on the (111) terrace, and its width is reduced by approx. 30 %. For Co adatoms at the end of the chain a reduction of approx. 55 % in amplitude, and an increase of approx. 10 % in width is observed.

4.6.2 DFT+AIM setup

To analyse the Kondo effect arising from the electronic correlations within the Co d orbitals, DFT (Sec. 2.1) was combined with the multi-orbital AIM (Sec. 3.2) [Dan16; Sur12; Újs00]. For the DFT calculations, the Cu atoms of the chain and the Co adatom were placed on fcc sites above the Cu(111) surface. These calculations were performed with the VASP code [Kre96] using a $6 \times 6 \times 5$ slab for the Cu(111) surface to support the different configurations atop, and with a $9 \times 9 \times 1$ Γ -centred \mathbf{k} -point mesh. A vacuum separation of 12.5 \AA was chosen, and all configurations were relaxed until the forces were below 0.02 eV/\AA . The obtained electronic structure was then projected onto the Co d orbitals to extract parameters for the AIM; the projection of the DFT band structure onto the AIM was done with the method of projected local orbitals (PLO) [Kar11b]. The main weight of the Co d -orbital LDOS from DFT lies within the energy window of $\pm 1.5 \text{ eV}$ (Fig. 4.2), and the bands were selected accordingly. The Coulomb matrix was assessed by the rotationally invariant Slater form with parameters $U = 4.0 \text{ eV}$ and $J = 0.9 \text{ eV}$ (cf. Eq. (2.50)). The thus obtained AIM was solved by the CTQMC procedure as implemented in the TRIQS/CTHYB code [Par15; Set16] (Sec. 3.3). Analytical continuation of the QMC data was done with the SOM [Kri19] (Sec. 3.4). The complete workflow and computational details can be read in Ref. [Kar13], Subsec. 3.2.1, and Sec. 3.6.

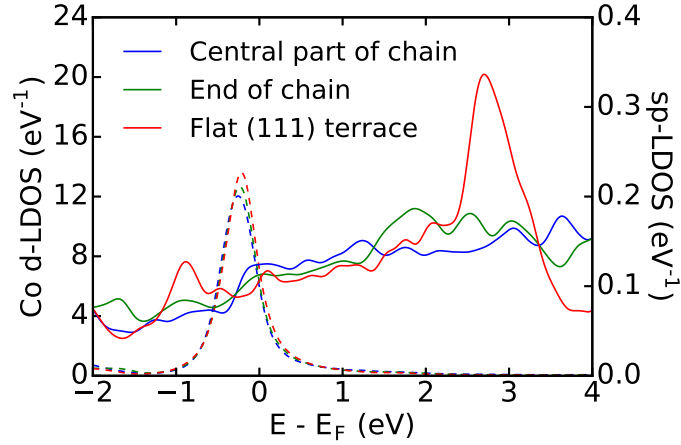


Figure 4.2: Total DFT-LDOS of the Co d orbitals (dashed line; scale on the left), and the conduction s and p orbitals (solid line; scale on the right). The LDOS at the Fermi level increases with higher coordination (cf. Ref. [Née08]).

The CTQMC solution of the AIM yields the GF of the Co d orbitals

$$G_\alpha(\omega) = [\omega + \mu - \varepsilon_\alpha - \Delta_\alpha(\omega) - \Sigma_\alpha(\omega)]^{-1}, \quad (4.64)$$

where α enumerates the Co d orbitals, μ is the chemical potential including the DC

(Subsec. 2.1.4, Appx. C.1), which subtracts the Coulomb correlations already contained in DFT, ε_α are the CF-split orbital energies (Sec. 4.2), and Δ_α are the hybridization functions (Eq. (3.56)). Σ is the self-energy computed by CTQMC (Chpt. 3), and it contains all many-body correlations relevant for the Kondo effect. When the Co atom is adsorbed on a Cu(111) terrace, the GF is approximately diagonal in the symmetry-adapted cubic basis and transforms according to the two irreducible representations of the C_{3v} point group, with one of them decomposing into two two-fold degenerate blocks: the E -irreducible representation $\{E_1(xz, yz), E_2(xy, x^2-y^2)\}$, and $\{A_1(z^2)\}$. With a Cu chain next to the Co adatom, however, the orbital degeneracy of the constituents of E_1 and E_2 is lifted. Orbital-resolved spectral functions are given by $A(\omega) = -\text{Im}[G(\omega + 0^+)/\pi]$ (cf. Eq. (3.39)).

Fig. 4.3 shows the DOS/spectrum obtained by CTQMC at $\beta = 200 \text{ eV}^{-1}$. SOM is particularly suited to resolve the sharp Kondo peak at the Fermi level. The spectrum for the case of a Co adatom on the (111) terrace may be compared with the one obtained in Refs. [Dan16; Sur12]. For the analytical continuation 4001 energy points were used between $\pm 10 \text{ eV}$. From analytical continuation some resonance and (dI/dV) antiresonance peaks had cusps at their highest and lowest point, respectively (see, e.g., the raw curves in Fig. 4.9). These were treated in the small energy range between -0.05 eV and 0.02 eV by substituting each data point by the average of the averages with its two neighbours. Subsequently, the spectra were smoothed on the whole energy range by inserting the geometric mean of two data points between them. If the curve crossed the abscissa between two data points, the arithmetic mean was used instead. Spectra shown in Figs. 4.5 and 4.7 underwent that procedure two times.

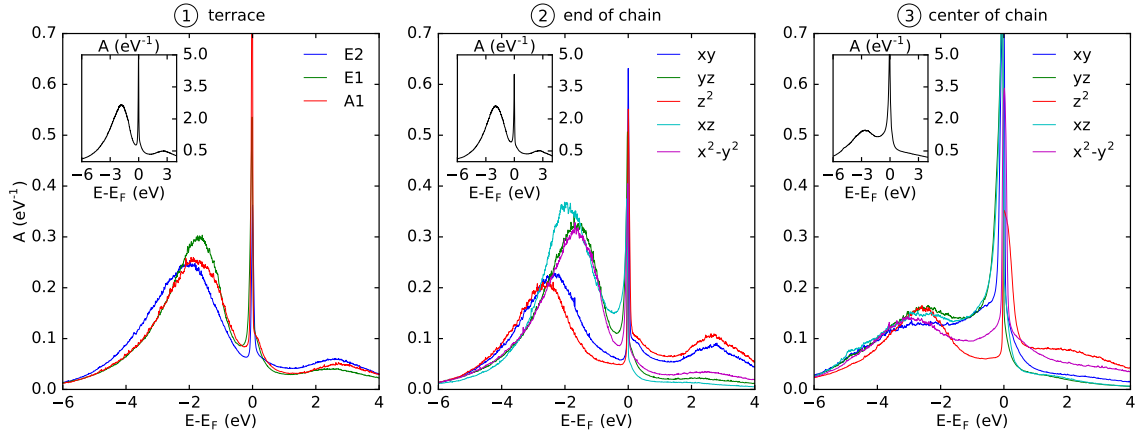


Figure 4.3: Orbital-resolved and total (insets) DOSes A with the Co adatom at the fcc position above the Cu(111) surface without (encircled 1), at the end of (2), and at the side of an fcc-positioned Cu chain (3). Results were obtained by QMC at $\beta = 200 \text{ eV}^{-1}$, and by analytical continuation with SOM (see text for explanations).

4.6.3 Derivation of the differential conductance

To obtain the influence of the orbital Kondo resonances on the conduction DOS of the substrate, the differential conductance was computed from the DFT and the QMC data by

the Fano-like relation [Kno02; Mad01; Prü12] (cf. Eq. (4.39))

$$-\frac{dI}{dV} \propto \frac{|B|^2}{\text{Im } \tilde{\Sigma}} \frac{q^2 - 1 + 2q\varepsilon}{1 + \varepsilon^2} \quad (4.65)$$

for each Co d orbital and at each bias, with $\tilde{\Sigma}(\omega) = -\mu + \varepsilon + \Delta(\omega) + \Sigma(\omega)$. With α enumerating the Co d orbitals, the asymmetry factors are given by (cf. Eqs. (4.40) and (4.41))

$$\begin{aligned} q_\alpha(\omega) &= \frac{\gamma_\alpha + A_\alpha(\omega)}{B_\alpha(\omega)}, \\ A_\alpha(\omega) &= \sum_\beta V_{\alpha\beta} \text{Re } g_\beta(\omega), \\ B_\alpha(\omega) &= \sum_\beta V_{\alpha\beta} \text{Im } g_\beta(\omega). \end{aligned} \quad (4.66)$$

Here, α again denotes the Co d orbitals, and the sums run over the conduction orbitals. V is the hybridization coupling between adatom and substrate, which also enters the Hamiltonian for the AIM (\mathbf{k} -independence has been assumed), and g the GF of the substrate. For symmetry reasons, not all Co d orbitals couple to all conduction orbitals, they rather group into the following three sets [Fra15]:

$$\begin{aligned} (p_x) &\leftrightarrow (d_{xz}, d_{xy}) \\ (p_y) &\leftrightarrow (d_{yz}, d_{x^2-y^2}) \\ (s, p_z) &\leftrightarrow (d_{z^2}). \end{aligned} \quad (4.67)$$

Within these sets, V may be estimated from the approximation $\Delta_\alpha(\omega) = |V_\alpha(\omega)|^2 \sum_\beta g_\beta(\omega)$ as the average of the real and imaginary parts of this equation. The parameters $\gamma_\alpha = M_{t\alpha}/M_{ts}$ measure the ratio between tunnelling from tip to adatom and tip to substrate, and are the only fitting parameters of our theory. The transfer matrix element M_{ts} is assumed to be one constant for all conduction orbitals. Furthermore, the energy parameter ε is given by (cf. Eq. (4.40))

$$\varepsilon_\alpha(\omega) = \frac{\omega - \text{Re } \tilde{\Sigma}_\alpha(\omega)}{\text{Im } \tilde{\Sigma}_\alpha(\omega)} \quad (4.68)$$

Defining the tunnelling matrix elements

$$T_\alpha(\omega) = \gamma_\alpha + A_\alpha(\omega) + iB_\alpha(\omega), \quad (4.69)$$

Eq. (4.65) can be rewritten to obtain,

$$-\frac{dI}{dV}(\omega) \propto \sum_\alpha \text{Im}[T_\alpha^2(\omega)G_\alpha(\omega)], \quad (4.70)$$

and with the phase ϕ of T , Eq. (4.70) can in turn be written as

$$-\frac{dI}{dV}(\omega) \propto \sum_{\alpha} |T_{\alpha}(\omega)|^2 \text{Im}[e^{2i\phi_{\alpha}(\omega)} G_{\alpha}(\omega)]. \quad (4.71)$$

The complex functions T_{α} weigh the contributions of the various orbitals to the current and add a phase ϕ , which leads to the asymmetric line shapes. T_{α} comprises the substrate GF (the corresponding DOS of which is shown in Fig. 4.2), the hybridization strengths (4.4 and Tab. 4.1), and the relative tunnelling matrix elements from the tip to the adatom and the substrate γ_{α} , respectively. The phase ϕ is also referred to as the **line-shape parameter (LSP)** [Prü12]. Even multiples of $\pi/2$ yield a peak (resonance), and odd multiples of $\pi/2$ a dip (antiresonance) in the conduction DOS. In this way, the LSP is in one-to-one correspondence to the tunnelling ratio. In Ref. [Née08] the latter was determined as $\gamma_0 = 0.22$, revealing interference between the competing tunnelling paths. The definition of q in Eq. (4.66) is different in that it contains the hybridization coupling V (cf. also Eq. (4.40)), so that it was rescaled by 20% to $\gamma_0 = 0.264$. To take into account the mixing of the d_{z^2} and $d_{x^2-y^2}$ orbitals (d_{z^2} and d_{xy} orbitals) caused by hybridization at the end (central part) of the chain, their contributions to the tunnelling ratios were adjusted accordingly. This corresponds to two adjustable parameters at the end and the central part of the chain, and none for the Co adatom on the terrace.

The calculated dI/dV curves in Fig. 4.5 exhibit Kondo antiresonances. As the CTQMC simulation has been performed for a temperature of 58 K to obtain convergence, all peaks are broader by an order of magnitude than their experimental counterparts recorded at 5 K, see, for example, Refs. [Nag02; Zha13]. The corresponding orbital-resolved spectral functions are shown in Figs. 4.3. For Co on the flat (111) terrace, the antiresonance is well developed and mainly originates from the Co d_{z^2} orbital. The hybridizations of the d_{xy} and $d_{x^2-y^2}$ orbitals are the weakest among all d orbitals, because these WFs are oriented in the plane parallel to the surface and no adatoms are located nearby. The d_{xz} and d_{yz} orbitals on the other hand show the strongest hybridization to the substrate.

This sequence is reversed when the Co atom is a nearest neighbour of Cu atoms at the

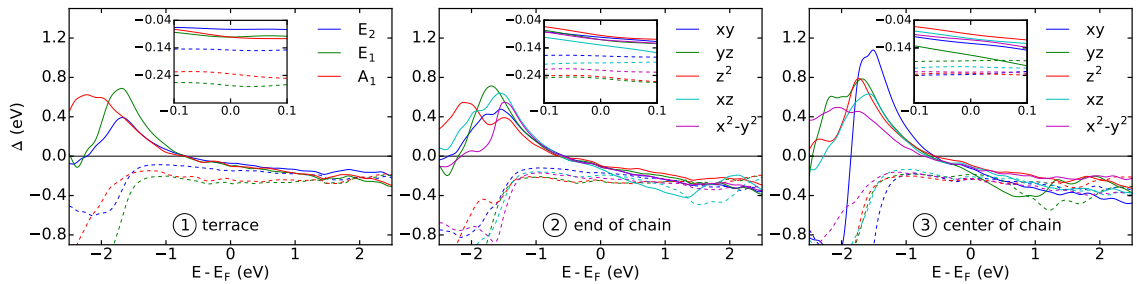


Figure 4.4: Orbital-resolved hybridization function Δ for a Co adatom on the (111) terrace (encircled 1), at the end of a Cu chain (2), and at the central part of a Cu chain (3). The Cu and Cu atoms are located at fcc positions. $\text{Re}(\Delta)$ and $\text{Im}(\Delta)$ are displayed by solid and dashed lines, respectively. Insets show a zoom into the low-energy region.

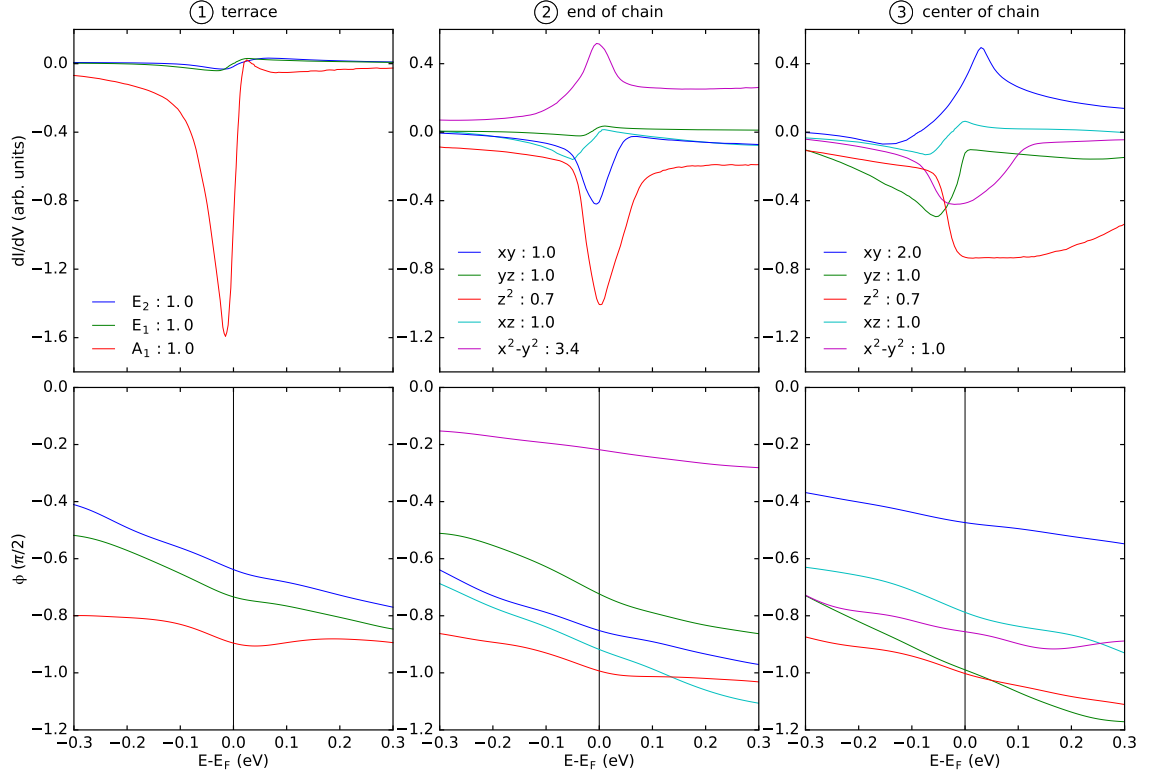


Figure 4.5: (Upper panel) Orbital-resolved differential conductance dI/dV of a Co adatom on the (111) terrace (encircled 1), at the end of (2), and at the central part of a Cu chain (3). The Cu and Cu atoms are located at fcc positions. The tunnelling ratio γ/γ_0 is given in the legend. (Lower panel) Corresponding LSPs.

end or the central part of a Cu chain. When the Co adatom is attached to the end of a Cu chain, the amplitude of the antiresonance is halved, while its width is increased. Moreover, the hybridization of the $d_{x^2-y^2}$ orbital is increased by 48%, because one of its lobes is pointing towards the chain (x direction) Tab. 4.1). Simultaneously, symmetry mismatch between the the d_{xz} orbital and the s orbital of Cu chain atom reduces the hybridization with the conduction band electrons by 30%. With the Co adatom next to the Cu chain, further substructures emerge Figs. 4.1 and 4.5. Subsuming these substructures, which originate from several d orbitals, broadens the overall antiresonance. At the central part of the chain, the d_{yz} orbital hybridization is similarly suppressed (-33%), while the d_{xy} orbital exhibits the strongest hybridization of all d orbitals. The distinct changes of the d orbital spectral functions reflect modified hybridizations that depend on the coordination of the Co atom to its environment. In particular, simulated dI/dV curves for Co at the central part of the chain show depressions corresponding to the experimental ones at approx. ± 10 meV. The orbital-resolved dI/dV spectra reveal that they originate from the broad d_{z^2} and d_{yz} states along with, at positive bias, the strong d_{xy} resonance contribution and, at negative bias, the strong decrease of the d_{z^2} weight.

As has just been explained, the d_{xy} resonance results from enhanced hybridization of this orbital with the substrate (comprising the chain), so the tip increasingly detects the Kondo resonance on this orbital. The same applies for Co at the end of the chain, where the $d_{x^2-y^2}$ resonance contribution is exactly at the Fermi level, and reduces the amplitude of the antiresonance arising from the d_{z^2} and d_{xy} orbitals. The dI/dV data reflect the spectrum of a many-body state comprising single-orbital contributions (Sec. 4.1). Together with the interference between the different tunnelling paths, these add up to yield the complex line shape observed.

The hybridization of the d_{z^2} orbital is virtually identical in all three cases. However, owing to level repulsions in the multi-orbital setting (Fig. 4.6), its energy is successively increased and its occupation decreases from $n = 1.56$ (free surface) over 1.20 (end of chain) to 1.14 (central part of chain). As a result, the Kondo resonance of the d_{z^2} orbital shifts to positive energies. The local environment also strongly affects the occupations of the in-plane orbitals: $(n_{xy}, n_{x^2-y^2}) = (1.330, 1.677)$ at the end, and $(1.588, 1.295)$ at the central part of a chain. Consequently, the sequence of the energies of the d_{xy} and $d_{x^2-y^2}$ Kondo resonances is inverted between the Co positions at the central part and the end of a chain. All these changes reflect intertwined modifications of the Co adatom electronic structure.

The experimental spectra of Co at the central part of a Cu chain have similarities with the line shape observed in Ref. [Jac15], where it has been attributed to spin excitations. However, there are important differences. Most importantly, the central minimum observed in all spectra does not occur directly at zero bias. This observation is particularly important, because it implies an asymmetry of the central part of the spectrum with respect to $V = 0$ mV. If the rising parts at +9 mV and -12 mV in the spectrum of Co at the central part of the chain were due to spin excitations (Fig. 4.1 right), they should be centred around $V = 0$ mV. The rise of the dI/dV spectrum near ± 10 mV is not clear cut, though, because of the scatter of the data. However, given the Kondo effect of Co on Cu(111) terraces, it appears unlikely that Co next to a chain, where its coordination is higher, would develop a local moment. The overall hybridization strength is not much increased with the higher coordination, and remains well below the strength of the Coulomb interaction. As a result, charge fluctuations should not be much enhanced, and the Kondo effect is expected to survive. – However, as mentioned in the introductory part to the present chapter, new data has been acquired in the meantime showing a more symmetric and pronounced distribution around $V = 0$ mV. Considering the derivation of the MAE term in Appx. B, one might think of the symmetry breaking in the CF inducing a SOC on the Co adatom.

4.6.4 Analysis of orbital contributions

The Cu chain breaks the C_{6v} symmetry, and leads to anisotropies within CF, hybridization and Coulomb matrix. The present study focusses on the anisotropies arising in CF and hybridization by assuming a rotationally invariant DC and Coulomb matrix for each configuration. For the Co adatom on the flat (111) terrace and at the end of the Cu chain, the FLL was used to determine the DC ($\mu_{DC} = 26.85$ eV), while next to the chain it was the AMF approach ($\mu_{DC} = 25.92$ eV). The choice of the AMF-DC for the adatom next to the chain is due to enhanced delocalization in this case, which renders the DFT mean-field

picture more suitable. Further details can be found in Subsec. 4.6.7.

The **DFT+AIM** results for the differential conductance (Fig. 4.5) show the Kondo antiresonance emerging in the conduction **DOS** due to local electronic correlations. On the flat (111) terrace, the Kondo antiresonance is well developed, showing a line shape originating from the Co d_{z^2} orbital alone, for which the **LSP** is always near $\pi/2$ (Fig. 4.5). With the Co adatom at the end of the Cu chain, the amplitude of the Kondo antiresonance becomes halved, while its width is slightly enlarged. From the **LSPs** one can infer the reduction of the amplitude from the Co $d_{x^2-y^2}$ orbital. This orbital couples mostly to the p_y conduction orbital due to symmetry reasons [Fra15], and at the same time experiences enhanced hybridization with the Cu chain arranged along the x direction ($-\text{Im}[\Delta(0)]$ for $d_{x^2-y^2}$ now is 48% larger, cf. Figs. 4.4, 4.5, 4.6, and Tab. 4.1). Thus, tunnelling into the Co $d_{x^2-y^2}$ orbital is more effective, because the p_y orbital has remained unchanged, and the $d_{x^2-y^2}$ Kondo peak leads to a resonance contribution in the conduction **DOS**. With the Co adatom next to the Cu chain, it is now the Co d_{xy} orbital which leads to the reduction of the amplitude, because at the same time it mostly couples to the unaffected p_x conduction orbital [Fra15] and to the Cu chain ($-\text{Im}[\Delta(0)]$ now is 59% larger, cf. Figs. 4.4, 4.5, 4.6, and Tab. 4.1). The small peak at 25 meV in the simulated dI/dV curve results from the d_{xy} orbital, as can be seen in Fig. 4.5.

The couplings between the adatom d and conduction s and p orbitals listed in Eq. (4.67) are assumed to be valid for all configurations, that is, with and without the chain. Thus, five γ parameters for configuration have to be determined, and were estimated from geometry considerations. For the Co adatom on the flat (111) terrace, all γ parameters were fixed to the same value γ_0 (Fig. 4.5). At the end of the Cu chain, tunnelling into the adatom $d_{x^2-y^2}$ orbital was increased ($\gamma = 3.4\gamma_0$) and tunnelling into the d_{z^2} orbital was slightly reduced, because its energy level is increased. Next to the chain an enhanced tunnelling into the adatom d_{xy} orbital was considered ($\gamma = 2.0\gamma_0$).

4.6.5 Analysis of orbital Kondo peaks

For the Co adatom on the flat (111) terrace, the Kondo peak is the highest in A_1 , which is perpendicular to the surface, while it is lower in the E_1 , and the lowest in the E_2 directions parallel to the surface. The efficiency of the Kondo singlet pairing depends on various parameters, of which the hybridization is an important one: Optimal screening needs hopping processes to occur, but at the same time relies on a preserved suppression of charge fluctuations. As $\text{Im}[\Delta(0)]$ in E_2 is small, the orbital Kondo temperature T_K is small as well (Figs. 4.4, 4.6, and Tab. 4.1). The latter can be estimated from the formula $T_K = -\pi Z \text{Im}[\Delta(0)]/4$ for each orbital, with $Z = [1 - \Sigma'(0) - \Delta'(0)]^{-1}$ the **QP** weight at the Fermi level (cf. Sec. 3.6; the Matsubara self-energy was used for the derivative) [Dan16; Hew93; Sur12]. As the **QMC** simulations were performed at 58 K, the Kondo peaks are not fully developed and thus appear broad. The true width of the Kondo peak can only be seen deep in the Kondo regime, where five-orbital **QMC** has yet no access to. The result is thus a general temperature broadening of one order of magnitude as compared to experimental Kondo peaks [Nag02; Zha13]. For the Co adatom on the (111) terrace and at the end of the chain, the half-width-at-half-maximum (HWHM) can still be estimated graphically from the total dI/dV curves in Fig. 4.5 as 305 K and 376 K, respectively,

| configuration | orbital | T_K | n/N_{tot} | Z | $-\text{Im}[\Delta(0)]$ | ε |
|-----------------------|---------------|-------|--------------------|--------|-------------------------|---------------|
| Central part of chain | d_{xy} | 165.9 | 1.588 | 0.0843 | 0.236 | -0.184 |
| | d_{yz} | 226.6 | 1.772 | 0.1415 | 0.187 | -0.203 |
| | d_{z^2} | 49.0 | 1.141 | 0.0254 | 0.232 | -0.134 |
| | d_{xz} | 231.9 | 1.743 | 0.1319 | 0.209 | -0.204 |
| | $d_{x^2-y^2}$ | 74.2 | 1.295 | 0.0381 | 0.228 | -0.157 |
| | average/total | 149.5 | 7.539 | | | |
| End of chain | d_{xy} | 35.6 | 1.330 | 0.0256 | 0.169 | -0.160 |
| | d_{yz} | 126.8 | 1.769 | 0.0614 | 0.251 | -0.180 |
| | d_{z^2} | 53.2 | 1.202 | 0.0264 | 0.245 | -0.163 |
| | d_{xz} | 144.9 | 1.870 | 0.0900 | 0.194 | -0.205 |
| | $d_{x^2-y^2}$ | 63.5 | 1.677 | 0.0348 | 0.221 | -0.165 |
| | average/total | 84.8 | 7.848 | | | |
| Flat (111) terrace | d_{xy} | 19.4 | 1.496 | 0.0164 | 0.146 | -0.136 |
| | d_{yz} | 94.5 | 1.622 | 0.0442 | 0.277 | -0.183 |
| | d_{z^2} | 101.4 | 1.567 | 0.0559 | 0.234 | -0.186 |
| | d_{xz} | 97.3 | 1.630 | 0.0451 | 0.277 | -0.184 |
| | $d_{x^2-y^2}$ | 20.1 | 1.532 | 0.0172 | 0.149 | -0.137 |
| | average/total | 66.6 | 7.847 | | | |

Table 4.1: Orbital Kondo temperatures T_K (K) together with their average (last line for each configuration). Furthermore orbital and total occupations n and N_{tot} , orbital QP weights Z , hybridization strengths $-\text{Im}[\Delta(0)]$ (eV), and energies ε (eV). QMC simulations were performed at 58 K.

while for the adatom at the central part of the chain the complicated substructures and their unaligned positions together with the broad appearance of the Kondo peak for the d_{z^2} orbital prevent a graphical estimation of T_K altogether. The estimation via the QP weights, however, always yields an upper bound to the true T_K , but they are already near experimental values. The difference in the order of magnitudes between experimental and theoretical Kondo peak widths corresponds to the difference between the temperatures, at which experiments and simulations were performed, and can further be characterized by the analytical temperature dependence of the Kondo peak given in Refs. [Nag02; Zha13]. The width is proportional to $\sqrt{(\alpha T)^2 + (2T_K)^2}$, where theoretically $\alpha = 2\pi$, and with T_K extracted from the simulations, we arrive at calculated resonance widths of 194 K at the terrace, and 201 K at the end of the chain. Use of the formula in case the Co adatom is aside to the chain gives 236 K.

Other parameters like the orbital energies relative to the chemical potential can change the situation quite strongly as well, as can be inferred from the evolution of the Co d_{z^2} spectrum (Fig. 4.5). The hybridization is not changed, but its energy level is successively increased towards the Fermi level from $\varepsilon = -0.19$ eV in steps of 0.03 eV (Fig. 4.6 and Tab. 4.1). This can be attributed to level repulsions within the multi-orbital setting. Thus, the Kondo temperature T_K decreases, which can be understood by inspection of Fig. 4.1/Tab. 4.1: the QP weight Z also enters into T_K , and it appears to be directly

related to the orbital energies ε . The evolution of T_K listed in Tab. 4.1 in the other orbitals can be attributed to the position of energy levels, and to the hybridization strengths as well, and from Fig. 4.6 one can conclude, that the relevance of the orbital energies is higher. The conclusion can almost certainly be extended, if one compares the configurations with the Co adatom on the (111) terrace and at the end of the chain, while next to the chain the AMF-DC was chosen, which renders the comparison not as direct, but the relation between orbital temperatures T_K and energies ε is still preserved within that configuration.

4.6.6 Estimation of temperature dependence

The relation between the dI/dV line shapes, and their decomposition into orbital contributions (Fig. 4.5), remain valid upon prediction of the different evolutions expected for the orbital Kondo peaks while lowering the simulation temperature. The Kondo temperatures are rather high in the E_1 directions, and the simulation temperature of 58 K is already well inside their Kondo cross-over region, so their evolution will not significantly change the simulated total dI/dV curve. For example, the negative-bias tail of the Co d_{yz} orbital next to the chain will mostly retain its relation to the other peaks, and it corresponds to the depression at -10 meV in the total dI/dV curve. The same retention is expected from all orbitals of Co adatoms on the (111) terrace and at the end of chains. Considering again the adatom next to the chain, T_K is small in d_{z^2} and in $d_{x^2-y^2}$, so at low temperature the corresponding peaks will be narrowed in width and increased in amplitude. The central peak in the total dI/dV curve is mostly due to these orbital contributions, and will be even better resolved. The peak in d_{xy} will develop as well, although not as strongly, because the simulation temperature is already well in its cross-over region. Still, the peak at 5 meV and subsequent depression at 10 meV will remain explicable by the d_{xy} behaviour. Moreover, the asymmetry of the total dI/dV curve can be expected to be seen even more clearly in theory, because the d_{z^2} and $d_{x^2-y^2}$ tails at positive bias will lose their weight more rapidly than the d_{xy} tail.

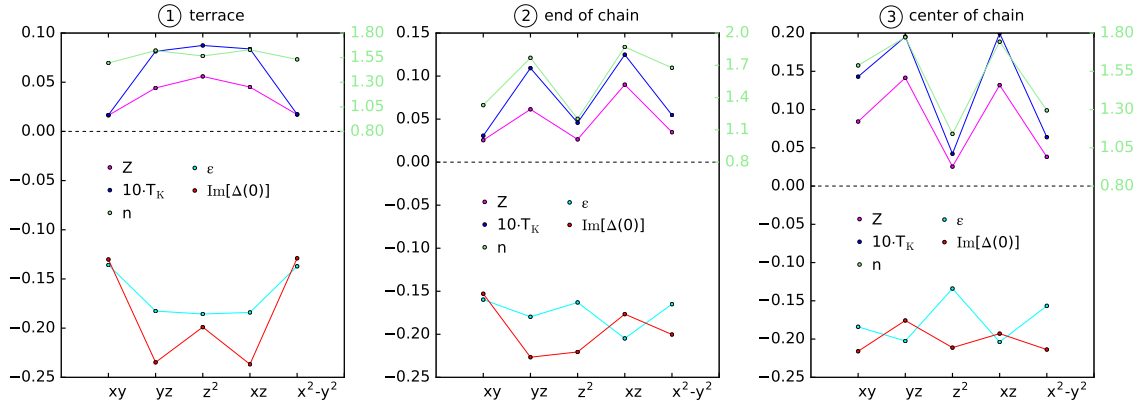


Figure 4.6: Orbital Kondo parameters extracted from QMC with the Co adatom on the (111) terrace (encircled 1), at the end of (2), and next to the Cu chain (3): QP weights Z , Kondo temperatures T_K (K) rescaled by one order of magnitude, and orbital occupations n . DFT input for the AIM: energy levels ε (eV), and hybridization strengths $\text{Im}[\Delta(0)]$ (eV).

4.6.7 Comparison of double countings

The **FLL-DC** often yields better results for the description of the Kondo effect, as it starts from the atomic limit for the estimation of the Coulomb effects in **DFT**, and is thus better suited for strongly correlated systems [Kar13] (Subsec. 2.1.4). However, for the Co adatom next to the chain, although the simulated total dI/dV curve with **FLL-DC** can be adjusted to obtain the experimental line shape, the large γ -parameter for tunnelling into the d_{z^2} orbital, which one needs to assume for the agreement, is difficult to justify. In contrast to that, the **AMF-DC** easily leads to the experimental line shape and its substructures, and both Kondo temperatures extracted from the **QMC** data coincide (145 K from **FLL**, and from **AMF** in Tab. 4.1). For the other configurations, on the contrary, the T_K extracted from the **QMC** results with **AMF-DC** are remote from experimental values: 114 K and 127 K for the adatom on the (111) terrace and at the end of the chain, respectively. The agreement of line shapes and Kondo temperatures between experiment and theory, together with details for the choice of tunnelling parameters, led us to select the **FLL-DC** for the Co adatom on the flat (111) terrace and at the end of the chain, and the **AMF-DC** at the central part of the chain.

4.6.8 Analysis of symmetry breaking

Diagonalization of the local Hamiltonian (cf. Sec. 4.3) of Co on the (111) terrace reveals the presence of an $SU(4)$ Kondo effect as previously reported for phthalocyanine molecules [Fra11; Min12]. This is because both, spin and orbital **DOFs**, are present. The low-lying eigenstates are sixfold degenerate, their filling is 8, and the two holes align their spins via Hund's rules to a total spin of 1. At the chain, the Co orbital degeneracy is lifted and the orbital Kondo effect is partially suppressed. This leads to an approximate $SU(2)$ Kondo effect of the spin **DOF** alone. Still, the symmetry breaking is not as severe as to reduce the Kondo temperature T_K . The main reason is because Hund's rules, which reduce T_K by spin alignment, are less effective within non-degenerate orbitals.

In the multi-orbital context and away from half-filling, symmetries increase the Kondo temperature T_K , because Hund's rule alignment plays a minor role under these conditions (total spins are smaller, and less energy has to be paid to flip the state). Consequently, the orbital Kondo effect needs to be taken into account. On the flat (111) terrace, the diagonalization of the local Hamiltonian reveals the presence of an $SU(4)$ Kondo effect. The **GS** is six-fold degenerate, its filling is $N_{\text{tot}}^{\text{at}} = 8$, and the two holes residing in E_1 and E_2 states align their spins via Hund's rules to yield $S_{\text{tot}}^{\text{at}} = 1$. The orbital contributions to the Kondo effect arise from orbital flips without change of spin. As there are more states with $N_{\text{tot}}^{\text{at}} = 7$ than with $N_{\text{tot}}^{\text{at}} = 9$, and as the excitation energies of the former are lying lower, charge fluctuations yield a filling $N_{\text{tot}} = 7.85$ with all orbitals being approximately at three-quarter filling (Tab. 4.6).

The **CF** depends on the energy window chosen for the projection from the Bloch bands to the correlated orbitals (see Sec. 4.6.2). The d_{z^2} happens to be slightly lower by 2 meV than the orbitals of E_1 symmetry, and thus is filled first. At non-zero temperature the lowest-lying and six-fold degenerate excited states shown in Fig. 4.8 contribute with their own $SU(4)$ Kondo effect. The occupations reveal the orbital contributions to the Kondo effect more clearly than the absolute **GSS** with d_{z^2} filled (not shown), which have a complicated

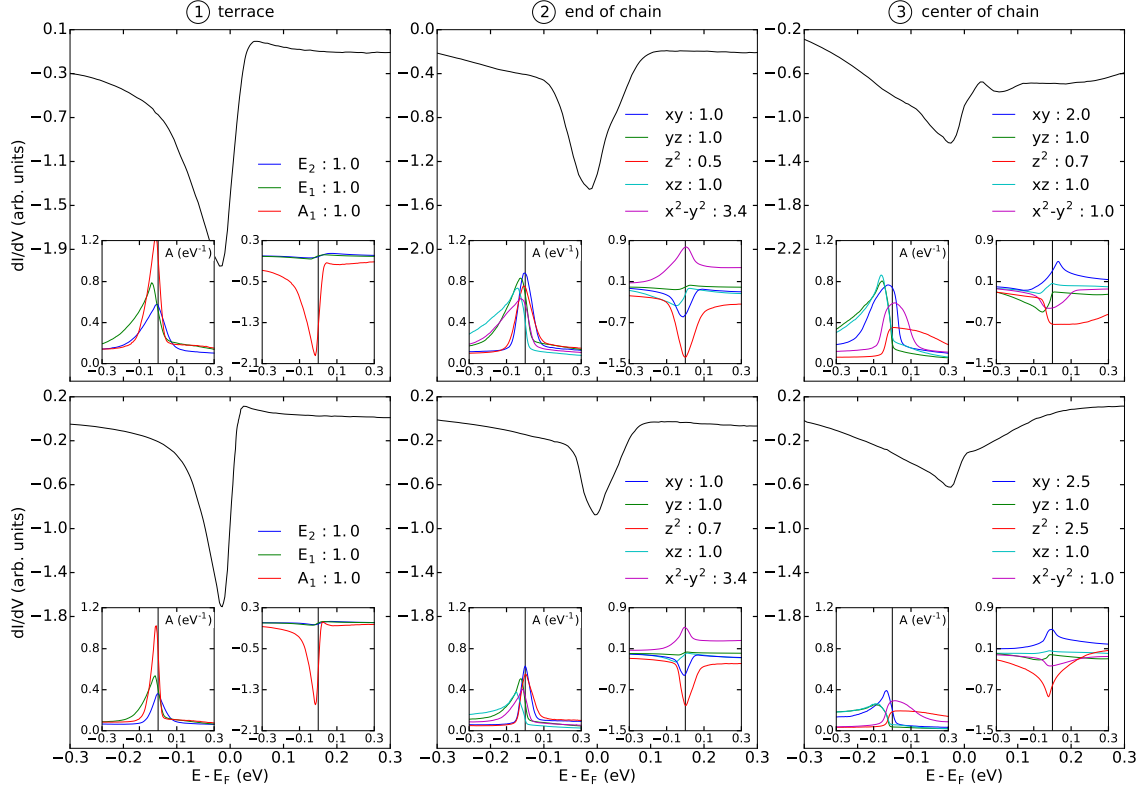


Figure 4.7: Comparison of results obtained with the **AMF-DC** (upper row) and with the **FLL-DC** (lower row): Total and orbital-resolved differential conductance dI/dV and orbital-resolved spectra A (the latter two in insets) with the Co adatom on the (111) terrace (left column, encircled 1), at the end of (middle column, 2), and next to the chain (right column, 3). Best adjustments found for γ/γ_0 are listed in the legends.

distribution of their spin over E_1 and E_2 orbitals. This is similar to the case of a Co adatom next to the chain, whose spin is distributed over all orbitals (shown on the right in Fig. 4.8). The existence of transitions between two degenerate triplets via orbital flips was checked explicitly. Thus, there is a six-fold degenerate **GS**, but also a six-fold degenerate excited state (and even more than that). All these multiplets contribute with their own $\text{SU}(4)$ Kondo effect, and all these Kondo effects add up coherently. In view of that, with the extracted **CF** there occurs a superimposed $\text{SU}(4)$ Kondo effect, albeit temperature might suppress Kondo effects from multiplets other than the **GS** considerably. This situation should be common in multi-orbital systems with unbroken symmetries.

With the Co adatom at the chain, the orbital Kondo effect is partially suppressed depending on the coordination, which results in an approximate $\text{SU}(2)$ Kondo effect. The orbital C_{3v} symmetry is broken (Fig./Tab. 4.1), and the two degenerate triplets are energetically separated, in case of the Co adatom at the end of the chain by 5 meV (**CF** splitting in E_2 ; Fig. 4.8). With the same **FLL-DC**, the Co adatom next to the chain has the same Kondo scenario as at the end, only the **CF** splitting in E_2 is as large as 27 meV. At

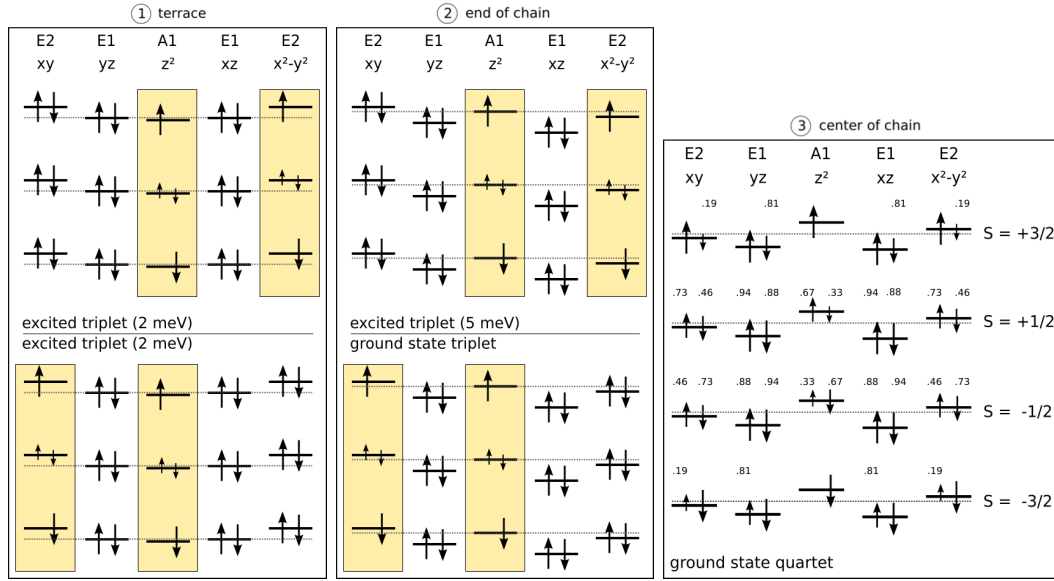


Figure 4.8: Ground and excited state configurations of the Co adatom on the flat (111) terrace (encircled 1), at the end (2), and at the central part of the chain (3). The dashed line is a guide to the eye, which organizes five orbital energy levels into one adatom configuration, and helps to distinguish the positions of the energy levels w.r.t. each other. Boxes in beige highlight the triplets. Large arrows denote occupation of one electron, small arrows without annotated number half an electron, other small and medium-size arrows carry an annotation for the occupation. See text for further explanations.

non-zero temperatures, low-lying eigenstates of the local Hamiltonian contribute with their own Kondo effect as well, but the tendencies in the CF splitting and partial suppression of orbital Kondo contributions remain. As a result they are less relevant at stronger symmetry breaking.

The determination of the Kondo scenario of a realistic adatom is difficult, and depends on the various parameters chosen for the local Hamiltonian, especially on the DC. For all configurations, AMF-DC leads to $S = 3/2$ GSs at filling $N_{\text{tot}}^{\text{at}} = 7$ without the additional orbital degeneracy, like in case of the Co adatom next to the chain (Fig. 4.8). The tendencies in the CF splitting, however, prevail, so that excitations are more difficult the stronger the symmetry breaking. Still, the energy level positions and hybridization strengths overcompensate the reduction of symmetry, and T_K rises at higher coordination.

It should be noted that with the choice of DCs made, the symmetry of the GS formally is higher at the central part of the chain than at its end ($S = 3/2$ quartet vs. $S = 1$ triplet, respectively). This indicates that the contribution of the orbital Kondo effect is strongly suppressed next to the chain, while at its end symmetry breaking and thus the suppression are only partial.

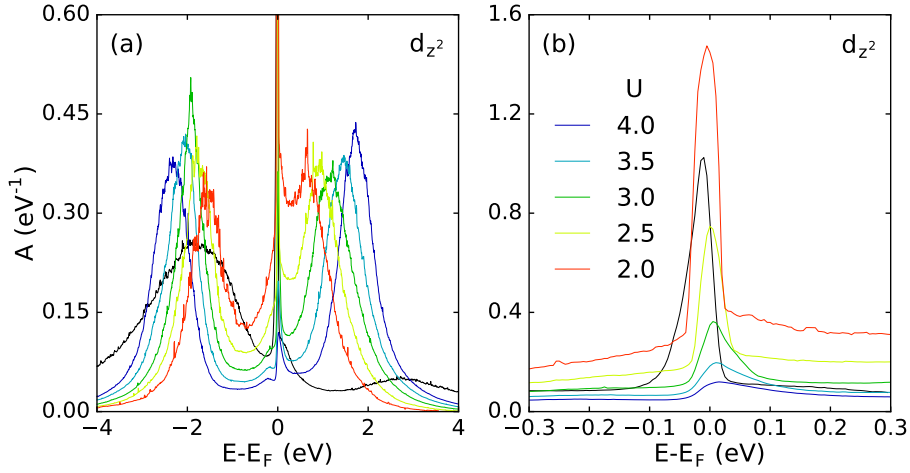


Figure 4.9: Comparison between the d_{z^2} spectral function of Co on the Cu(111) surface from the full five-orbital AIM (black curve) with single-orbital AIM calculations having the same energy level and hybridization function for d_{z^2} , but with the other d orbitals switched off, and the chemical potential adjusted to attain half-filling. In (a) the Hubbard bands are shown, in (b) a zoom into the low-energy region to resolve the Kondo peaks in full amplitude is shown.

4.6.9 Comparison to one-orbital model

Fig. 4.9 compares the spectral function of the Co d_{z^2} orbital on the (111) terrace with single-orbital calculations having the same energy level and hybridization function for d_{z^2} , but with other d orbitals switched off, and the chemical potential adjusted to obtain optimal Kondo behaviour near half-filling. The only adjustable parameter of the single-orbital model is the Coulomb interaction strength U , which has been scanned through a set of values between $U = 4.0 \text{ eV}$, used in the full five-orbital calculations, down to $U = 2.0 \text{ eV}$. Fig. 4.9(a) shows the Hubbard bands approaching the Fermi level upon lowering U . Like in Hubbard models, at lower values for U , metallic behaviour sets in, and the Hubbard bands start to merge. As the hybridization function is asymmetric, the single orbital is slightly above half-filling, so the upper Hubbard band has lower weight and is closer to the Fermi level, but higher in amplitude. This is in contrast to the situation where d_{z^2} is inside the five-orbital environment. Its occupation is much higher, but the behaviour of Hubbard bands is reversed. With a single-orbital model one will thus not obtain the electronic structure for the same orbital in a multi-orbital environment. Local interactions between the orbitals and their respective hybridizations let them appear as one big orbital having space for ten electrons, instead of five orbitals with each having space for two.

Fig. 4.9(b) zooms into the low-energy region to resolve the Kondo peaks in the d_{z^2} orbital. A large U leads to a low T_K , and at simulation temperature above the Kondo scale the resonance is less developed. All calculations were performed at $\beta = 200 \text{ eV}^{-1}$. To achieve reasonable agreement between the d_{z^2} spectrum within the full AIM and of a single-orbital model, one needs to rescale U to physically incorrect values. To obtain a Kondo peak, one furthermore has to fix the occupation near half-filling, for otherwise charge fluctuations increase significantly, and the Kondo effect would disappear. The true shape and stability

of the resonance, however, relies on the orbital occupation and the presence of the other orbitals within the full AIM.

On the (111) terrace, the line shape of the differential conductance dI/dV is largely due to the Co d_{z^2} orbital. This seems to suggest that a single-orbital model of the Kondo effect may be sufficient to analyse experimental data. However, as has been just shown, the line shape of the d_{z^2} orbital itself depends on the local interactions with the other orbitals, but also on the Kondo scenario. The spin in the d_{z^2} orbital couples to other spins in different orbitals via Hund's exchange to yield a large-spin Kondo effect, and the orbital Kondo effect additionally contributes to the line shape. A single-orbital treatment neglects these effects and thus misses the relevance of symmetry and the presence of other orbitals. Within the full description one can discuss CFs, potentially different bonding environments, such as due to a nearby Cu chain, and one obtains a more realistic electronic structure of the Co adatom.

4.6.10 Summary

Distinct line shapes of the Kondo resonance are observed in tunnelling spectra of Co adatoms on the Cu(111) surface in different local environments. The differences are observed because neighbouring atoms of the CU chain lift orbital degeneracies. The results show that a single-orbital description of the Kondo effect of adatoms at surfaces may be oversimplified. The line shapes result from contributions from individual orbitals, and a full five-orbital CTQMC treatment was able to identify all of them. This goes beyond usual NRG model building, which tries to identify the Kondo scenario beforehand by means of DFT data, and is at present not capable to go numerically beyond three orbitals [Cos15; Sta15]. Especially the various features of the dI/dV curve of the Co adatom at the central part of the chain needed full consideration of all five orbitals in the AIM (see Refs. [Fra15; Jac09; Ter09] for analogous statements). Furthermore, the QMC data even provide a means of estimating the Kondo temperature, where fitting with Fano and Frota line shapes to experimental data may not be performable.

The authors of Ref. [Jac09] made analogous studies with TM atoms in Cu nanocontacts, using a DFT+OCA solver (cf. Sec. 3.5), to show that different peaks seen in conductance spectra are due to Kondo resonances in different orbitals. In Ref. [Kar11a] a Co-benzene sandwich molecule between Cu nanocontacts was studied with QMC methods, to further show that the orbital Kondo effect contributes. In Ref. [Fra15] a DFT+OCA study was performed for Co/Cu(111), and it was shown that different Kondo effects superimpose to yield a final multi-orbital Kondo effect. The coupling groups between the adatom and conduction orbitals were used according to this reference (cf. Eq. (4.67); conduction orbitals are the Co s and p orbitals); the authors considered all five orbitals in their calculations, but still fail with the relevant z^2 orbital due to neglect of direct tunnelling into the surface and subsequent interference effects. – The system of a MnPc molecule adsorbed on Pb(111) (MnPc/Pb(111)) shows different orbital Kondo peaks as well [Jac13], and the corresponding authors try to correct the interpretations made in the seminal Ref. [Fra11] on the Kondo effect on SC substrates. Ref. [Küg15] studied the MnPc/Ag(001) system by a combination of STM experiments and DFT+AIM calculations using a CTQMC solver, and found a superposition of Kondo effects and/or orbital states, both residing in different orbitals. In

view of that, already quite a few statements on the importance of multi-orbital Kondo physics to interpret experimental data were made, but none of them performed a full **CTQMC** solution of the **AIM** plus a subsequent evaluation of the differential conductance “as *ab-initio* as possible”; the study presented here closes this gap. Geometric symmetry breaking due to different coordination environments, and its effects on the Kondo physics, has been studied before, see, for example, Refs. [Tsu14; Zha05]; but a direct comparison of one- and five-orbital models as in Subsec. 4.6.9 has been done for the first time.

CHAPTER 5

Summary and Outlook

The present thesis developed an introduction to the **DFT+AIM** approach and reported on its application on real material systems. There were four different threads around which the thesis has been organized. The first thread was defined by **DFT**; the introduction (Chpt. 1) started from **QED** of bound states, and quickly derived from this general perspective on condensed matter systems the approaches in which practical simulations and comparison to experimental results can be performed. The exposition in the subsequent chapters took the converse path, though, and successively developed the theory of non-relativistic **DFT** without the presence of spin (Subsecs. 2.1.1 and 2.1.2), of spin-**DFT** (Subsec. 2.1.3) and **DFT+U** (Subsec. 2.1.4), and eventually of current- and **RDFT** (both in Appx. A), where contact with bound-state **QED** was restored.

The **DFT** approach was applied within a study on the Ta(001)-p(3×3)-O surface which was in parallel under experimental investigation using **STM** and **STS**, and it was able to identify the geometry as well as the electronic and quantum-chemical properties of the surface (Sec. 2.4). Its nature of being a static approach to the inherently dynamical correlations, however, prevents the determination of the adsorption properties of other atoms and molecules, so that a further characterization of the Ta(001)-p(3×3)-O has been performed by application of **DFT** extended as to include **vdW** forces (Secs. 2.5 and 2.6). – The bridge between theory and experiment needed a short account on **STM** theory for weakly correlated surfaces (Sec. 2.2). This theory was later extended to include adatoms hosting strongly interacting electrons (Sec. 4.4), to account for experimental spectra which result from probing the electronic structure of both, adatoms and surfaces, and which thus include local correlations as well as interference effects between the two tunnelling paths.

The second thread was thus the development of the **AIM** and its recognition as an essential ingredient to account for the local electronic correlations present on **TM** or rear-earth adatoms (on surfaces) or impurities (in bulks) Sec. 3.2. While the nature of **DMFT** and the relation to bulk systems is realized by an additional self-consistency condition accompanying the **AIM**, for the systems considered in the present thesis, that is, correlated adatoms on surfaces, the **AIM** itself already provides the basis for their exhaustive many-body treatment.

In principle the **AIM** can also be applied to represent the electronic structure of adatoms hosting weakly correlated electrons, to which the Co/graphene system apparently belongs (Secs. 3.5 and 3.6). In view of that, the **AIM** thus provides a means to describe the electronic structure of adatoms on surfaces in general, for which numerical approaches for its solution have to be devised. The present thesis outlined the combination of **CTQMC** (Sec. 3.3) and

SOM (Sec. 3.4) as the numerical solution to the **AIM**, which includes the evaluation of the imaginary-time **GF** and its analytic continuation to real energies, where the spectral information for comparison to experiment can be found. On the one hand **CTQMC** is a non-perturbative, that is, numerically exact, solution of the **AIM**, and on the other hand **SOM** is capable to calculate very different kinds of spectra from **QMC** data, be they smooth on the whole energy range or peaked at particular energies. Thus, the **CTQMC+SOM** solution was able to provide the spectrum of the rather weakly interacting Co/graphene system (Fig. 3.5) as well as to show the narrow Kondo peak of the $\text{CoCu}_n/\text{Cu}(111)$ systems (Fig. 4.3).

Instead of explaining all too much on the computational and numerical details, except of further explaining the theoretical merge of **DFT** and the **AIM** within the **DFT+AIM** approach for realistic many-body models (Subsec. 3.2.1), the **AIM** was decorated with some of its physical relevances and prospects of its application. In employing the **DFT+AIM** approach to the Co/graphene system we included the Coulomb interaction matrix calculated with help of the **cRPA** (Subsec. 3.1.2) and thereby incorporated the anisotropies which arose from the symmetry breaking due to the surface geometry. The **cRPA** itself is part of the **RPA** and the **GWA**, so further explanations on both these theories was provided - also with respect to the **vdW** interactions which are encompassed by the **RPA**.

After explaining all the theoretical and numerical approaches to correlated electrons on individual interaction centres, in the third thread the thesis ascended to the emergence of the spectral resonance structures which appear if the correlations happen to be strong. In particular, Chpt.4 was dedicated to the multi-orbital Kondo effect, and to its explanation in terms of the complementary pictures of **FL** theory and the scaling approach. The chapter also explained how to determine the Kondo scenario from the **ME** approach (Sec. 4.3), how further symmetry breaking within the **CF** effects the energy levels (Sec. 4.2) and eventually the Kondo scenario (cf. Subsec. 4.6.8), and how to derive the differential conductance (Sec. 4.4 and Subsec. 4.6.3) which can directly be compared to experimentally measured spectra (cf. Figs. 4.1 right and 4.5). The whole theory and computational scheme developed was then applied to the $\text{CoCu}_n/\text{Cu}(111)$ systems (Sec. 4.6).

The relevance of the developed **DFT+AIM** approach became apparent as it properly describes the local correlations of nanosystems on surfaces. Further directions for its extension can be thought of. On the computational side, one can incorporate an outer charge-self-consistency loop to account for the back reaction effects of the local correlations on the **DFT** electronic structure (introductory part to Chpt. 3). This is an extension which works on the **AIM** parameters without changing its form. But of course one can extend the **AIM** Hamiltonian itself, for example, by the **SOC** term (Appx. B) or by the **SC** energy gap (cf. Sec. 2.3). The first extension would be needed to consider the magnetic anisotropy in a system, the second one to describe **YSR** states. But for both these additional terms one would have to think of how to numerically resolve their small energy scales in the **CTQMC+SOM** solution; possibly a quantum-mechanical **PT** seems advisable at first place. However, such extensions are worth the efforts: In case of an additional **CF** splitting possibly inducing a considerable **SOC**, one could realistically simulate the impact of the magnetic anisotropy on the differential conductance and directly compare it to the experimental spectrum. Similarly interesting would be to see the **SC** energy gap and the

YSR states in a realistic many-body calculation, as this amounts to a complete reshaping of the low-energy spectrum.

The realm of surface science is vast and highly complex. Due to the relevance of quantum chemistry in these systems, and the interplay and interpenetration of different physical and quantum-chemical effects, the description of such systems is highly demanding. Furthermore, correlations at all length scales are seen to be important. While DFT is capable to account for weak correlations and metallicity, it cannot properly represent strong correlations and has its difficulties with gapped systems; in particular, quantum-chemical structures can be estimated from the DFT-DOS, but are seen to be rather mimicked by the DFT approach instead of truly represented. Inhomogeneities with strong correlations, such as TM adatoms on surfaces, need the dual picture of the AIM to have their many-body effects be properly accounted for.

The fourth thread was given by the application of DFT and DFT+AIM on the Ta(001)-p(3×3)-O surface (Secs. 2.4 and 2.6), the Co/graphene system (Sec. 3.6), and the CoCu_n/Cu(111) systems (Sec. 4.6). The context of the current state of research and their relevance was explained for each of these systems, and finally the investigations and results themselves were reported on. The DFT approach was applied to the Ta(001)-p(3×3)-O surface and served to identify its physical and quantum-chemical structure; the DFT+AIM approach was developed along, and applied on, the Co/graphene system, and the consideration of the cRPA Coulomb matrix made apparent the relevance of geometric anisotropies on the low-energy physics and possibly the Kondo effect; and the multi-orbital Kondo scenarios and the differential conductances of the CoCu_n/Cu(111) systems were determined.

The Ta(001)-p(3×3)-O surface can be put into the wider context of the Kondo effect on superconducting surfaces. Sec. 2.4 provided a DFT characterization of the substrate, while in Ref. [Cor17] Fe adatoms were investigated in this wider context. The Ta(001)-p(3×3)-O surface provides several possible adsorption sites and different possible arrangements for Fe adatoms, and thus various Kondo effects and their interplay can be observed [Kam18; Kam21; Kam19]. As mentioned, the DFT approach points to aspects of the surface beyond its own actual domain of applicability, albeit within its frame it was able to reveal the underlying quantum-chemistry. A further characterization, possibly within the RPA or GWA is needed (Sec. 3.1), but one has to organize and make possible calculations on such a complicated system. This is especially important in view of the adsorption properties on this surface, which are not fully settled, yet. As regards the Kondo effect of adsorbates from a computational point of view, there remains, as mentioned, the problem of how to resolve the SC gap in QMC calculations.

An analogous statement may apply to the Co/graphene system (Sec. 3.6), for the adatom properties strongly depend on a precise determination of its adsorption and electronic structure because the chemical potential is shifted due to doping. The Kondo effect in pseudo-gapped systems is very sensitive to this fact (Sec. 3.5). As regards the Kondo effect in multi-orbital systems in general, the precise estimation of the DC is important as well (cf. Subsec. 4.6.8), for the Kondo scenario depends on the impurity filling and orbital occupations. Appx. C reported on the exact representation of the DC in terms of the LW functional, but this approach still has to be extended to the geometric anisotropies inherent

to surface systems. – The AIM has the power to naturally describe completely the local physics of adatoms on surfaces, but a precise extraction of the underlying relevant physics is not easy. For example, at the time of writing the thesis it was not known if Co/graphene exhibits the Kondo effect, and other, in part more plausible, interpretations of the few experimental data were given (cf. Sec. 3.5).

Finally, we provided a description of the local electronic correlations present in the $\text{CoCu}_n/\text{Cu}(111)$ systems in terms of the multi-orbital Kondo effect (Sec. 4.6). Further experimental studies revealed that the SOC might be relevant for these systems, and point to the necessity to incorporate further interactions into the AIM. The approach applied in this thesis was *ab initio* to a large extent, but further directions of development are at hand, and were in part realized already. On the one hand, one should include the STM tip and its multi-orbital character in the determination of the differential conductance (cf. Sec. 4.4). On the other hand, there are the tunnelling matrix elements which were determined by physical reasoning, to achieve consistency between theory and experiment (Subsec. 4.6.3). The experimental spectra are often complex enough for not making the consistency a coincidence. Yet, in principle one can compute these tunnelling matrix elements as an overlap of WFs, for example, as in Eq. (2.55). Having realistic tunnelling matrix elements would result in completely *ab initio* differential conductances.

Bibliography

- [Abr54] Abrahams, E.: ‘Electron-Electron Scattering in Alkali Metals’. *Phys. Rev.* (1954), vol. 95(3): p. 839–840 (cit. on p. 114).
- [Abr59] Abrikosov, A. A. and I. M. Khalatnikov: ‘The theory of a fermi liquid (the properties of liquid ^3He at low temperatures)’. *Reports on Progress in Physics* (1959), vol. 22(1): p. 329–367 (cit. on p. 114).
- [Ada82] Adachi, H., M. Tsukada, I. Yasumori, and M. Onchi: ‘Cluster model calculations of oxygen chemisorption on (001) surfaces of bcc V, Cr and Fe’. *Surface Science* (1982), vol. 119(1): p. 10–20 (cit. on pp. 31, 32).
- [Aff95] Affleck, I.: ‘Conformal Field Theory Approach to the Kondo Effect’. *Acta Physica Polonica B* (1995), vol. 26(12): p. 1869–1932 (cit. on p. 119).
- [Aic16] Aichhorn, M., L. Pourovskii, P. Seth, V. Vildosola, M. Zingl, O. E. Peil, X. Deng, J. Mravlje, G. J. Kraberger, C. Martins, M. Ferrero, and O. Parcollet: ‘TRIQS/DFTTools: A TRIQS application for ab initio calculations of correlated materials’. *Computer Physics Communications* (2016), vol. 204: p. 200–208 (cit. on p. 84).
- [Ali12] Alicea, J.: ‘New directions in the pursuit of Majorana fermions in solid state systems’. *Reports on Progress in Physics* (2012), vol. 75(7): p. 076501 (cit. on p. 29).
- [Ama08] Amadon, B., F. Lechermann, A. Georges, F. Jollet, T. O. Wehling, and A. I. Lichtenstein: ‘Plane-wave based electronic structure calculations for correlated materials using dynamical mean-field theory and projected local orbitals’. *Phys. Rev. B* (2008), vol. 77(20): p. 205112 (cit. on pp. 20, 70).
- [Amb14] Ambrosetti, A., A. M. Reilly, R. A. DiStasio, and A. Tkatchenko: ‘Long-range correlation energy calculated from coupled atomic response functions’. *The Journal of Chemical Physics* (2014), vol. 140(18): p. 18A508 (cit. on p. 54).
- [An03] An, B., S. Fukuyama, K. Yokogawa, and M. Yoshimura: ‘Surface structures of clean and oxidized Nb(100) by LEED, AES, and STM’. *Phys. Rev. B* (2003), vol. 68(11): p. 115423 (cit. on p. 32).
- [And61] Anderson, P. W.: ‘Localized Magnetic States in Metals’. *Phys. Rev.* (1961), vol. 124(1): p. 41–53 (cit. on pp. 80, 81, 142).
- [And72] Anderson, P. W.: ‘More Is Different’. *Science* (1972), vol. 177(4047): p. 393–396 (cit. on p. 2).

- [And13] Anderson, P. W.: ‘Twenty-five Years of High-Temperature Superconductivity – A Personal Review’. *Journal of Physics: Conference Series* (2013), vol. 449: p. 012001 (cit. on p. 204).
- [And80] Andrei, N.: ‘Diagonalization of the Kondo Hamiltonian’. *Phys. Rev. Lett.* (1980), vol. 45(5): p. 379–382 (cit. on pp. 119, 121, 124).
- [And84] Andrei, N. and C. Destri: ‘Solution of the Multichannel Kondo Problem’. *Phys. Rev. Lett.* (1984), vol. 52(5): p. 364–367 (cit. on p. 119).
- [Ani97a] Anisimov, V. I., F. Aryasetiawan, and A. I. Lichtenstein: ‘First-principles calculations of the electronic structure and spectra of strongly correlated systems: the LDA+ U method’. *Journal of Physics: Condensed Matter* (1997), vol. 9(4): p. 767–808 (cit. on pp. 20, 21).
- [Ani91a] Anisimov, V. I. and O. Gunnarsson: ‘Density-functional calculation of effective Coulomb interactions in metals’. *Phys. Rev. B* (1991), vol. 43(10): p. 7570–7574 (cit. on pp. 21, 23).
- [Ani97b] Anisimov, V. I., A. I. Poteryaev, M. A. Korotin, A. O. Anokhin, and G. Kotliar: ‘First-principles calculations of the electronic structure and spectra of strongly correlated systems: dynamical mean-field theory’. *Journal of Physics: Condensed Matter* (1997), vol. 9(35): p. 7359 (cit. on pp. 20, 70).
- [Ani91b] Anisimov, V. I., J. Zaanen, and O. K. Andersen: ‘Band theory and Mott insulators: Hubbard U instead of Stoner I ’. *Phys. Rev. B* (1991), vol. 44(3): p. 943–954 (cit. on p. 21).
- [Ant18] Antropov, V. private communication. 2018 (cit. on p. 31).
- [Ary04] Aryasetiawan, F., M. Imada, A. Georges, G. Kotliar, S. Biermann, and A. I. Lichtenstein: ‘Frequency-dependent local interactions and low-energy effective models from electronic structure calculations’. *Phys. Rev. B* (2004), vol. 70(19): p. 195104 (cit. on p. 68).
- [Ary11] Aryasetiawan, F., T. Miyake, and R. Sakuma: ‘The Constrained RPA Method for Calculating the Hubbard U from First-Principles’. *The LDA+DMFT approach to strongly correlated materials*. Ed. by Pavarini, E., E. Koch, A. Lichtenstein, and D. Vollhardt. Vol. 1. Schriften des Forschungszentrums Jülich: Modeling and Simulation. 2011 (cit. on p. 77).
- [Ary98] Aryasetiawan, F. and O. O Gunnarsson: ‘The GW method’. *Reports on Progress in Physics* (1998), vol. 61(3): p. 237–312 (cit. on pp. 70–72, 74, 75).
- [Aul00] Aulbur, Wilfried G., Lars Jönsson, and John W. Wilkins: ‘Quasiparticle Calculations in Solids’. Ed. by Ehrenreich, H. and F. Frans Spaepen. Vol. 54. Solid State Physics. Academic Press, 2000: pp. 1–218 (cit. on pp. 70, 72, 75).
- [Bal90] Balachandran, A. P.: *Hubbard Model and Anyon Superconductivity*. Lecture notes in physics. World Scientific, 1990 (cit. on p. 119).

- [Bam13] Bamidele, J., J. Brndiar, A. Gulans, L. Kantorovich, and I. Štich: ‘Critical Importance of van der Waals Stabilization in Strongly Chemically Bonded Surfaces: Cu(110):O’. *Journal of Chemical Theory and Computation* (2013), vol. 9(12): p. 5578–5584 (cit. on p. 27).
- [Bar90] Bardeen, J.: ‘Superconductivity and other macroscopic quantum phenomena’. *Physics Today* (1990), vol. 43: p. 25–31 (cit. on pp. 118, 203).
- [Bar61] Bardeen, J.: ‘Tunnelling from a Many-Particle Point of View’. *Phys. Rev. Lett.* (1961), vol. 6(2): p. 57–59 (cit. on p. 25).
- [Bar72] Barth, U. von and L. Hedin: ‘A Local Exchange-Correlation Potential for the Spin Polarized Case: I’. *Journal of Physics C: Solid State Physics* (1972), vol. 5(13): p. 1629 (cit. on p. 17).
- [Bas09] Baskaran, G.: ‘Five-fold way to new high T_c superconductors’. *Pramana* (2009), vol. 73(1): p. 61–112 (cit. on p. 204).
- [Bay63] Bayes, T. and R. Price: ‘LII. An essay towards solving a problem in the doctrine of chances. By the late Rev. Mr. Bayes, F. R. S. communicated by Mr. Price, in a letter to John Canton, A. M. F. R. S’. *Philosophical Transactions of the Royal Society of London* (1763), vol. 53: p. 370–418 (cit. on p. 88).
- [Bay61] Baym, G. and L. P. Kadanoff: ‘Conservation Laws and Correlation Functions’. *Phys. Rev.* (1961), vol. 124(2): p. 287–299 (cit. on p. 220).
- [Bay07] Baym, G. and C. Pethick: *Landau Fermi-Liquid Theory*. John Wiley & Sons, Ltd., 2007 (cit. on p. 114).
- [Bea96] Beard, B. B. and U.-J. Wiese: ‘Simulations of Discrete Quantum Systems in Continuous Euclidean Time’. *Phys. Rev. Lett.* (1996), vol. 77(25): p. 5130–5133 (cit. on p. 67).
- [Bec93] Becke, A. D.: ‘A new mixing of Hartree-Fock and local density-functional theories’. *The Journal of Chemical Physics* (1993), vol. 98(2): p. 1372–1377 (cit. on p. 21).
- [Ben93] Bendix, J., M. Brorson, and Claus E. Schaffer: ‘Accurate Empirical Spin-Orbit Coupling Parameters ζ_{nd} for Gaseous nd^q Transition Metal Ions. The Parametrical Multiplet Term Model’. *Inorganic Chemistry* (1993), vol. 32(13): p. 2838–2849 (cit. on p. 29).
- [Ber15] Berland, K., V. R. Cooper, K. Lee, E. Schröder, T. Thonhauser, P. Hyldgaard, and B. I. Lundqvist: ‘van der Waals forces in density functional theory: a review of the vdW-DF method’. *Reports on Progress in Physics* (2015), vol. 78(6): p. 066501 (cit. on p. 50).
- [Ber95] Bernal, O. O., D. E. MacLaughlin, H. G. Lukefahr, and B. Andraka: ‘Copper NMR and Thermodynamics of $\text{UCu}_{5-x}\text{Pd}_x$: Evidence for Kondo Disorder’. *Phys. Rev. Lett.* (1995), vol. 75(10): p. 2023–2026 (cit. on p. 119).

- [Bie03] Biermann, S., F. Aryasetiawan, and A. Georges: ‘First-Principles Approach to the Electronic Structure of Strongly Correlated Systems: Combining the *GW* Approximation and Dynamical Mean-Field Theory’. *Phys. Rev. Lett.* (2003), vol. 90(8): p. 086402 (cit. on pp. 3, 20, 68, 79, 123).
- [Bih06] Bihlmayer, G.: ‘Magnetism in Density Functional Theory’. *Computational Condensed Matter Physics: Lecture Manuscripts of the 37th Spring School of the Institute of Solid State Research in the Forschungszentrum Jülich*. Schriften des Forschungszentrums Jülich: Matter and Material. 2006 (cit. on pp. 17, 19).
- [Bih00] Bihlmayer, G., T. Asada, and S. Blügel: ‘Electronic and magnetic structure of the (001) surfaces of V, Cr, and V/Cr’. *Phys. Rev. B* (2000), vol. 62(18): p. R11937–R11940 (cit. on pp. 19, 204).
- [Bin86] Binnig, G., C. F. Quate, and C. Gerber: ‘Atomic Force Microscope’. *Phys. Rev. Lett.* (1986), vol. 56(9): p. 930–933 (cit. on p. 27).
- [Bin82] Binnig, G., H. Rohrer, C. Gerber, and E. Weibel: ‘Surface Studies by Scanning Tunneling Microscopy’. *Phys. Rev. Lett.* (1982), vol. 49(1): p. 57–61 (cit. on p. 24).
- [Bit06] Bitzek, E., P. Koskinen, F. Gähler, M. Moseler, and P. Gumbsch: ‘Structural Relaxation Made Simple’. *Phys. Rev. Lett.* (2006), vol. 97(17): p. 170201 (cit. on p. 2).
- [Bla59] Blandin, A. and J. Friedel: ‘Propriétés magnétiques des alliages dilués. Interactions magnétiques et antiferromagnétisme dans les alliages du type métal noble-métal de transition’. *J. Phys. Radium* (1959), vol. 20(2-3): p. 160–168 (cit. on p. 81).
- [Ble50] Bleuler, K.: ‘Eine neue Methode zur Behandlung der longitudinalen und skalaren Photonen’. *Helvetica Physica Acta* (1950), vol. 23(5): p. 567–586 (cit. on p. 208).
- [Blö94] Blöchl, P. E.: ‘Projector augmented-wave method’. *Phys. Rev. B* (1994), vol. 50(24): p. 17953–17979 (cit. on p. 215).
- [Blö13] Blöchl, P. E., T. Pruschke, and M. Potthoff: ‘Density-matrix functionals from Green’s functions’. *Phys. Rev. B* (2013), vol. 88(20): p. 205139 (cit. on p. 220).
- [Bo18] Bo, M., L. Li, Y. Guo, C. Yao, C. Peng, and C. Q. Sun: ‘Atomic configuration of hydrogenated and clean tantalum(111) surfaces: Bond relaxation, energy entrapment and electron polarization’. *Applied Surface Science* (2018), vol. 427: p. 1182–1188 (cit. on pp. 30, 31).
- [Bor15] Borek, S., J. Braun, J. Minár, and H. Ebert: ‘*Ab initio* calculation of spin-polarized low-energy electron diffraction pattern for the systems Fe(001) and Fe(001)-*p*(1 × 1)O’. *Phys. Rev. B* (2015), vol. 92(7): p. 075126 (cit. on p. 31).
- [Bra13] Brambilla, A., A. Calloni, A. Picone, M. Finazzi, L. Duò, and F. Ciccacci: ‘X-ray photoemission spectroscopy investigation of the early stages of the oxygen aided Cr growth on Fe(001)’. *Applied Surface Science* (2013), vol. 267: p. 141–145 (cit. on p. 31).

- [Bra11] Brar, V. W., R. Decker, H.-M. Solowan, Y. Wang, L. Maserati, K. T. Chan, H. Lee, Ç. O. Girit, A. Zettl, S. G. Louie, M. L. Cohen, and M. F. Crommie: ‘Gate-controlled ionization and screening of cobalt adatoms on a graphene surface’. *Nature Physics* (2011), vol. 7(1): p. 43–47 (cit. on pp. 96, 97).
- [Buč18] Bučko, T. private communication. 2018 (cit. on p. 53).
- [Buč10] Bučko, T., J. Hafner, S. Lebègue, and J. G. Ángyán: ‘Improved Description of the Structure of Molecular and Layered Crystals: Ab Initio DFT Calculations with van der Waals Corrections’. *The Journal of Physical Chemistry A* (2010), vol. 114(43): p. 11814–11824 (cit. on p. 50).
- [Buč14] Bučko, T., S. Lebègue, J. G. Ángyán, and J. Hafner: ‘Extending the applicability of the Tkatchenko-Scheffler dispersion correction via iterative Hirshfeld partitioning’. *The Journal of Chemical Physics* (2014), vol. 141(3): p. 034114 (cit. on pp. 52, 58).
- [Buč16] Bučko, T., S. Lebègue, T. Gould, and J. G. Ángyán: ‘Many-body dispersion corrections for periodic systems: an efficient reciprocal space implementation’. *Journal of Physics: Condensed Matter* (2016), vol. 28(4): p. 045201 (cit. on p. 54).
- [Buč13a] Bučko, T., S. Lebègue, J. Hafner, and J. G. Ángyán: ‘Improved Density Dependent Correction for the Description of London Dispersion Forces’. *Journal of Chemical Theory and Computation* (2013), vol. 9: p. 4293–4299 (cit. on pp. 52, 53).
- [Buč13b] Bučko, T., S. Lebègue, Jürgen Hafner, and J. G. Ángyán: ‘Tkatchenko-Scheffler van der Waals correction method with and without self-consistent screening applied to solids’. *Phys. Rev. B* (2013), vol. 87(6): p. 064110 (cit. on pp. 53, 54).
- [Bul07] Bultinck, P., C. Van Alsenoy, P. W. Ayers, and R. Carbó-Dorca: ‘Critical analysis and extension of the Hirshfeld atoms in molecules’. *The Journal of Chemical Physics* (2007), vol. 126(14): p. 144111 (cit. on p. 52).
- [Cap01] Capelle, K. and G. Vignale: ‘Nonuniqueness of the Potentials of Spin-Density-Functional Theory’. *Phys. Rev. Lett.* (2001), vol. 86(24): p. 5546–5549 (cit. on p. 210).
- [Cas09] Castro Neto, A. H., F. Guinea, N. M. R. Peres, K. S. Novoselov, and A. K. Geim: ‘The electronic properties of graphene’. *Rev. Mod. Phys.* (2009), vol. 81(1): p. 109–162 (cit. on p. 93).
- [Cas12] Casula, M., A. Rubtsov, and S. Biermann: ‘Dynamical screening effects in correlated materials: Plasmon satellites and spectral weight transfers from a Green’s function ansatz to extended dynamical mean field theory’. *Phys. Rev. B* (2012), vol. 85(3): p. 035115 (cit. on p. 68).
- [Cep80] Ceperley, D. M. and B. J. Alder: ‘Ground State of the Electron Gas by a Stochastic Method’. *Phys. Rev. Lett.* (1980), vol. 45(7): p. 566–569 (cit. on pp. 15, 18).

- [Cha12] Chang, J., E. Blackburn, A. T. Holmes, N. B. Christensen, J. Larsen, J. Mesot, Ruixing Liang, D. A. Bonn, W. N. Hardy, A. Watenphul, M. v. Zimmermann, E. M. Forgan, and S. M. Hayden: ‘Direct observation of competition between superconductivity and charge density wave order in $\text{YBa}_2\text{Cu}_3\text{O}_{6.67}$ ’. *Nature Physics* (2012), vol. 8: p. 871–876 (cit. on p. 203).
- [Che18] Chen, P., W. W. Pai, Y.-H. Chan, V. Madhavan, M. Y. Chou, S.-K. Mo, A.-V. Fedorov, and T.-C. Chiang: ‘Unique Gap Structure and Symmetry of the Charge Density Wave in Single-Layer VSe_2 ’. *Phys. Rev. Lett.* (2018), vol. 121(19): p. 196402 (cit. on p. 204).
- [Cho18] Cho, K., M. Konczykowski, S. Teknowijoyo, M. A. Tanatar, J. Guss, P. B. Gartin, J. M. Wilde, A. Kreyssig, R. J. McQueeney, A. I. Goldman, V. Mishra, P. J. Hirschfeld, and R. Prozorov: ‘Using controlled disorder to probe the interplay between charge order and superconductivity in NbSe_2 ’. *Nature Communications* (2018), vol. 9(1): p. 2796 (cit. on p. 203).
- [Cit15] Citro, R., E. G. Dalla Torre, L. D’Alessio, A. Polkovnikov, M. Babadi, T. Oka, and E. Demler: ‘Dynamical stability of a many-body Kapitza pendulum’. *Annals of Physics* (2015), vol. 360: p. 694–710 (cit. on p. 31).
- [Cla18] Claudot, J., W. J. Kim, A. Dixit, H. Kim, T. Gould, D. Rocca, and S. Lebègue: ‘Benchmarking several van der Waals dispersion approaches for the description of intermolecular interactions’. *The Journal of Chemical Physics* (2018), vol. 148(6): p. 064112 (cit. on p. 50).
- [Coc12] Cococcioni, M.: ‘The LDA+U Approach: A Simple Hubbard Correction for Correlated Ground States’. *Correlated electrons: from models to materials*. Ed. by Pavarini, E., E. Koch, F. Anders, and M. Jarrell. Vol. 2. Schriften des Forschungszentrums Jülich: Modeling and Simulation. 2012 (cit. on pp. 20, 21, 23, 24).
- [Coc05] Cococcioni, M. and S. de Gironcoli: ‘Linear response approach to the calculation of the effective interaction parameters in the LDA + U method’. *Phys. Rev. B* (2005), vol. 71(3): p. 035105 (cit. on pp. 21, 23).
- [Coh08] Cohen, A. J., P. Mori-Sánchez, and W. Yang: ‘Insights into Current Limitations of Density Functional Theory’. *Science* (2008), vol. 321(5890): p. 792–794 (cit. on p. 19).
- [Col15] Coleman, P.: *Introduction to Many-Body Physics*. Cambridge University Press, 2015 (cit. on pp. 80, 81, 113–115, 118, 119, 121, 123, 135, 136).
- [Cor17] Cornils, L., A. Kamlapure, L. Zhou, S. Pradhan, A. A. Khajetoorians, J. Fransson, J. Wiebe, and R. Wiesendanger: ‘Spin-Resolved Spectroscopy of the Yu-Shiba-Rusinov States of Individual Atoms’. *Phys. Rev. Lett.* (2017), vol. 119(19): p. 197002 (cit. on pp. 4, 28–31, 50, 63, 122, 142, 161).

- [Cos15] Costi, T.: ‘Numerical renormalization group and multi-orbital Kondo physics’. *Many-Body Physics: From Kondo to Hubbard*. Ed. by Pavarini, E., E. Koch, and P. Coleman. Vol. 5. Modeling and Simulation. Jülich: Forschungszentrum Jülich GmbH Zentralbibliothek, Verlag, 2015 (cit. on pp. 68, 69, 157).
- [Cox98] Cox, D. L. and A. Zawadowski: ‘Exotic Kondo effects in metals: Magnetic ions in a crystalline electric field and tunnelling centres’. *Advances in Physics* (1998), vol. 47(5): p. 599–942 (cit. on pp. 119, 126).
- [Czy94] Czyżyk, M. T. and G. A. Sawatzky: ‘Local-density functional and on-site correlations: The electronic structure of La_2CuO_4 and LaCuO_3 ’. *Phys. Rev. B* (1994), vol. 49(20): p. 14211–14228 (cit. on p. 21).
- [Dai08] Dai, D., H. Xiang, and M.-H. Whangbo: ‘Effects of spin-orbit coupling on magnetic properties of discrete and extended magnetic systems’. *Journal of Computational Chemistry* (2008), vol. 29(13): p. 2187–2209 (cit. on p. 216).
- [Dai15] Dai, P.: ‘Antiferromagnetic order and spin dynamics in iron-based superconductors’. *Rev. Mod. Phys.* (2015), vol. 87(3): p. 855–896 (cit. on p. 204).
- [Dal14] Dalla Piazza, B., M. Mourigal, N. B. Christensen, G. J. Nilsen, P. Tregenna-Piggott, T. G. Perring, M. Enderle, D. F. McMorrow, D. A. Ivanov, and H. M. Rønnow: ‘Fractional excitations in the square-lattice quantum antiferromagnet’. *Nature Physics* (2014), vol. 11: p. 62–68 (cit. on p. 204).
- [Dan14] Dang, H. T., X. Ai, A. J. Millis, and C. A. Marianetti: ‘Density functional plus dynamical mean-field theory of the metal-insulator transition in early transition-metal oxides’. *Phys. Rev. B* (2014), vol. 90(12): p. 125114 (cit. on pp. 20, 70).
- [Dan16] Dang, H. T., M. dos Santos Dias, A. Liebsch, and S. Lounis: ‘Strong correlation effects in theoretical STM studies of magnetic adatoms’. *Phys. Rev. B* (2016), vol. 93(11): p. 115123 (cit. on pp. 144, 145, 150).
- [Dat95] Datta, S.: *Electronic Transport in Mesoscopic Systems*. Cambridge Studies in Semiconductor Physics and Microelectronic Engineering. Cambridge University Press, 1995 (cit. on p. 96).
- [De 05] De Leo, L. and M. Fabrizio: ‘Surprises in the Phase Diagram of an Anderson Impurity Model for a Single C_{60}^{n-} Molecule’. *Phys. Rev. Lett.* (2005), vol. 94(23): p. 236401 (cit. on pp. 68, 69).
- [DiL12] DiLullo, A., S.-H. Chang, N. Baadji, K. Clark, J.-P. Klöckner, M.-H. Prosenc, S. Sanvito, R. Wiesendanger, G. Hoffmann, and S.-W. Hla: ‘Molecular Kondo Chain’. *Nano Lett.* (2012), vol. 12: p. 3174–3179 (cit. on p. 142).
- [Dir30] Dirac, P. A. M.: ‘Note on Exchange Phenomena in the Thomas Atom’. *Mathematical Proceedings of the Cambridge Philosophical Society* (1930), vol. 26(3): p. 376–385 (cit. on p. 9).
- [Dir26] Dirac, P. A. M.: ‘On the Theory of Quantum Mechanics’. *Proceedings of the Royal Society of London Series A* (1926), vol. 112: p. 661–677 (cit. on p. 7).

- [Dob14] Dobson, J. F.: ‘Beyond pairwise additivity in London dispersion interactions’. *International Journal of Quantum Chemistry* (2014), vol. 114(18): p. 1157–1161 (cit. on p. 53).
- [Dra73] Drandarov, N. and V. Kanev: ‘847. Oxygen adsorption on tantalum and the effects of thermal desorption’. *Vacuum* (1973), vol. 23(12): p. 463 (cit. on p. 55).
- [Dre03] Dreizler, R.: ‘Relativistic Density Functional Theory’. *A Primer in Density Functional Theory. Lecture Notes in Physics*. Ed. by Fiolhais, C., F. Nogueira, and M. Marques. Vol. 620. Berlin, Heidelberg: Springer, 2003: pp. 123–143 (cit. on pp. 210–212).
- [Dud98] Dudarev, S. L., G. A. Botton, S. Y. Savrasov, C. J. Humphreys, and A. P. Sutton: ‘Electron-energy-loss spectra and the structural stability of nickel oxide: An LSDA+U study’. *Phys. Rev. B* (1998), vol. 57(3): p. 1505–1509 (cit. on pp. 21, 24).
- [Dud97] Dudarev, S. L., A. I. Liechtenstein, M. R. Castell, G. A. D. Briggs, and A. P. Sutton: ‘Surface states on NiO (100) and the origin of the contrast reversal in atomically resolved scanning tunneling microscope images’. *Phys. Rev. B* (1997), vol. 56(8): p. 4900–4908 (cit. on p. 32).
- [Duo15] Duong, D. L., M. Burghard, and J. C. Schön: ‘Ab initio computation of the transition temperature of the charge density wave transition in TiSe₂’. *Phys. Rev. B* (2015), vol. 92(24): p. 245131 (cit. on pp. 203, 204).
- [Eel13] Eelbo, T., M. Waśniowska, P. Thakur, M. Gyamfi, B. Sachs, T. O. Wehling, S. Forti, U. Starke, C. Tieg, A. I. Liechtenstein, and R. Wiesendanger: ‘Adatoms and Clusters of 3d Transition Metals on Graphene: Electronic and Magnetic Configurations’. *Phys. Rev. Lett.* (2013), vol. 110(13): p. 136804 (cit. on pp. 92, 95).
- [Eng02] Engel, E.: ‘Chapter 10 - Relativistic Density Functional Theory: Foundations and Basic Formalism’. *Relativistic Electronic Structure Theory*. Ed. by Schwerdtfeger, P. Vol. 11. Theoretical and Computational Chemistry. Elsevier, 2002: pp. 523–621 (cit. on pp. 1, 2, 207, 211).
- [Ess11] Essenberg, F., S. Sharma, J. K. Dewhurst, C. Bersier, F. Cricchio, L. Nordström, and E. K. U. Gross: ‘Magnon spectrum of transition-metal oxides: Calculations including long-range magnetic interactions using the LSDA + U method’. *Phys. Rev. B* (2011), vol. 84(17): p. 174425 (cit. on p. 19).
- [Fan15] Fanfarillo, L. and E. Bascones: ‘Electronic correlations in Hund metals’. *Phys. Rev. B* (2015), vol. 92(7): p. 075136 (cit. on p. 91).
- [Fan61] Fano, U.: ‘Effects of configuration interaction on intensities and phase shifts’. *Phys. Rev.* (1961), vol. 124: p. 1866 (cit. on p. 142).
- [Faw88] Fawcett, E.: ‘Spin-density-wave antiferromagnetism in chromium’. *Rev. Mod. Phys.* (1988), vol. 60(1): p. 209–283 (cit. on pp. 19, 204).

- [Fer27] Fermi, E.: ‘Un Metodo Statistico per la Determinazione di alcune Prioprietà dell’Atomo’. *Rend. Accad. Naz. Lincei.* (1927), vol. 6: p. 602–607 (cit. on p. 9).
- [Fjæ13] Fjærestad, John Ove: ‘Introduction to Green functions and many-body perturbation theory’. 2013 (cit. on p. 76).
- [Fra15] Frank, S. and D. Jacob: ‘Orbital signatures of Fano-Kondo line shapes in STM adatom spectroscopy’. *Phys. Rev. B* (2015), vol. 92(23): p. 235127 (cit. on pp. 134, 146, 150, 157).
- [Fra11] Franke, K. J., G. Schulze, and J. I. Pascual: ‘Competition of Superconducting Phenomena and Kondo Screening at the Nanoscale’. *Science* (2011), vol. 332(6032): p. 940–944 (cit. on pp. 29, 153, 157).
- [Fri56] Friedel, J.: ‘On Some Electrical and Magnetic Properties of Metallic Solid Solutions’. *Canadian Journal of Physics* (1956), vol. 34(12A): p. 1190–1211 (cit. on p. 81).
- [Fri10] Friedrich, C., S. Blügel, and A. Schindlmayr: ‘Efficient implementation of the *GW* approximation within the all-electron FLAPW method’. *Phys. Rev. B* (2010), vol. 81(12): p. 125102 (cit. on p. 93).
- [Frö54] Fröhlich, H.: ‘On the theory of superconductivity: the one-dimensional case’. *Proceedings of the Royal Society of London. Series A. Mathematical and Physical Sciences* (1954), vol. 223(1154): p. 296–305 (cit. on p. 203).
- [Fro92] Frota, H. O.: ‘Shape of the Kondo resonance’. *Phys. Rev. B* (1992), vol. 45: p. 1096 (cit. on p. 142).
- [Fro86] Frota, H. O. and L. N. Oliveira: ‘Photoemission spectroscopy for the spin-degenerate Anderson model’. *Phys. Rev. B* (1986), vol. 33: p. 7871–7874 (cit. on p. 142).
- [Gei07] Geim, A. K. and K. S. Novoselov: ‘The rise of graphene’. *Nature Materials* (2007), vol. 6: p. 183 (cit. on p. 93).
- [Geo04] Georges, A.: ‘Strongly Correlated Electron Materials: Dynamical Mean-Field Theory and Electronic Structure’. *AIP Conference Proceedings* (2004), vol. 715(1): p. 3–74 (cit. on pp. 2, 20, 64, 70, 81).
- [Geo13] Georges, A., L. de’Medici, and J. Mravlje: ‘Strong Correlations from Hund’s Coupling’. *Annual Review of Condensed Matter Physics* (2013), vol. 4(1): p. 137–178 (cit. on p. 91).
- [Geo92] Georges, A. and G. Kotliar: ‘Hubbard model in infinite dimensions’. *Phys. Rev. B* (1992), vol. 45(12): p. 6479–6483 (cit. on pp. 3, 20).
- [Geo96] Georges, A., G. Kotliar, W. Krauth, and M. J. Rozenberg: ‘Dynamical mean-field theory of strongly correlated fermion systems and the limit of infinite dimensions’. *Rev. Mod. Phys.* (1996), vol. 68(1): p. 13–125 (cit. on pp. 3, 20, 67).

- [Ger72] Gerlach, E.: ‘The Role of Surface Plasmons in Van Der Waals Attraction between Solids’. *Journal of Vacuum Science and Technology* (1972), vol. 9(2): p. 747–748 (cit. on pp. 31, 50).
- [Gil03] Gilary, I., N. Moiseyev, S. Rahav, and S. Fishman: ‘Trapping of particles by lasers: the quantum Kapitza pendulum’. *Journal of Physics A: Mathematical and General* (2003), vol. 36(25): p. L409–L415 (cit. on p. 31).
- [Giu05] Giuliani, G. and G. Vignale: *Quantum Theory of the Electron Liquid*. Cambridge University Press, 2005 (cit. on pp. 7–9, 12–14, 16, 50).
- [Giu14] Giustino, F.: *Materials Modelling Using Density Functional Theory: Properties and Predictions*. Oxford University Press, 2014 (cit. on pp. 25, 26).
- [Gou16a] Gould, T. and T. Bučko: ‘C6 Coefficients and Dipole Polarizabilities for All Atoms and Many Ions in Rows 1–6 of the Periodic Table’. *Journal of Chemical Theory and Computation* (2016), vol. 12(8): p. 3603–3613 (cit. on p. 50).
- [Gou16b] Gould, T., S. Lebègue, J. G. Ángyán, and T. Bučko: ‘A Fractionally Ionic Approach to Polarizability and van der Waals Many-Body Dispersion Calculations’. *Journal of Chemical Theory and Computation* (2016), vol. 12(12): p. 5920–5930 (cit. on p. 53).
- [Gou17] Goulko, O., A. S. Mishchenko, L. Pollet, N. Prokof’ev, and B. Svistunov: ‘Numerical analytic continuation: Answers to well-posed questions’. *Phys. Rev. B* (2017), vol. 95(1): p. 014102 (cit. on p. 88).
- [Gra13] Grant, I. S. and W. R. Phillips: *Electromagnetism*. Manchester Physics Series. Wiley, 2013 (cit. on p. 203).
- [Gre00] Greiner, W. and D. A. Bromley: *Relativistic Quantum Mechanics. Wave Equations*. Springer, 2000 (cit. on p. 213).
- [Gre96] Greiner, W. and J. Reinhardt: *Field Quantization*. Springer, 1996 (cit. on pp. 208, 209).
- [Gre09] Grewe, N., T. Jabben, and S. Schmitt: ‘Multi-orbital Anderson models and the Kondo effect: a NCA study enhanced by vertex corrections’. *The European Physical Journal B* (2009), vol. 68(1): p. 23–32 (cit. on pp. 71, 125).
- [Gro01] Grotheer, O., C. Ederer, and M. Fähnle: ‘Fast *ab initio* methods for the calculation of adiabatic spin wave spectra in complex systems’. *Phys. Rev. B* (2001), vol. 63(10): p. 100401 (cit. on p. 19).
- [Grü88] Grüner, G.: ‘The dynamics of charge-density waves’. *Rev. Mod. Phys.* (1988), vol. 60(4): p. 1129–1181 (cit. on p. 203).
- [Grü81] Grüner, G., A. Zawadowski, and P. M. Chaikin: ‘Nonlinear Conductivity and Noise due to Charge-Density-Wave Depinning in NbSe₃’. *Phys. Rev. Lett.* (1981), vol. 46(7): p. 511–515 (cit. on p. 203).
- [Grz89] Grzelakowski, K., I. Lyuksyutov, and E. Bauer: ‘Reconstruction of the (2×2)-O/Mo(110) system’. *Surface Science* (1989), vol. 216(3): p. 472–480 (cit. on p. 32).

- [Gul08] Gull, E.: ‘Continuous-time quantum Monte Carlo algorithms for fermions’. PhD thesis. ETH Zürich, 2008 (cit. on p. 67).
- [Gul11] Gull, E., A. J. Millis, A. I. Lichtenstein, A. N. Rubtsov, M. Troyer, and P. Werner: ‘Continuous-time Monte Carlo methods for quantum impurity models’. *Rev. Mod. Phys.* (2011), vol. 83(2): p. 349–404 (cit. on pp. 20, 67, 69, 70, 84, 86).
- [Gun89] Gunnarsson, O., O. K. Andersen, O. Jepsen, and J. Zaanen: ‘Density-functional calculation of the parameters in the Anderson model: Application to Mn in CdTe’. *Phys. Rev. B* (1989), vol. 39(3): p. 1708–1722 (cit. on pp. 21, 23).
- [Gun15] Gunnarsson, O., T. Schäfer, J. P. F. LeBlanc, E. Gull, J. Merino, G. Sangiovanni, G. Rohringer, and A. Toschi: ‘Fluctuation Diagnostics of the Electron Self-Energy: Origin of the Pseudogap Physics’. *Phys. Rev. Lett.* (2015), vol. 114(23): p. 236402 (cit. on p. 94).
- [Guo17] Guo, Y., M. Bo, Y. Wang, Y. Liu, C. Q. Sun, and Y. Huang: ‘Tantalum surface oxidation: Bond relaxation, energy entrapment, and electron polarization’. *Applied Surface Science* (2017), vol. 396: p. 177–184 (cit. on pp. 30, 31, 52).
- [Gup50] Gupta, S. N.: ‘Theory of Longitudinal Photons in Quantum Electrodynamics’. *Proceedings of the Physical Society. Section A* (1950), vol. 63(7): p. 681 (cit. on p. 208).
- [Haa34] Haas, W. J. de, J. de Boer, and G. J. van den Berg: ‘The electrical resistance of gold, copper and lead at low temperatures’. *Physica* (1934), vol. 1(7): p. 1115–1124 (cit. on pp. 113, 121, 124).
- [Hal04] Hallberg, K.: ‘Density Matrix Renormalization’. *Theoretical Methods for Strongly Correlated Electrons*. Ed. by Sénéchal, D., A.-M. Tremblay, and C. Bourbonnais. New York, NY: Springer New York, 2004: pp. 3–37 (cit. on p. 68).
- [Hal06] Hallberg, K. A.: ‘New trends in density matrix renormalization’. *Advances in Physics* (2006), vol. 55(5-6): p. 477–526 (cit. on p. 68).
- [Han13a] Hanl, M., A. Weichselbaum, T. A. Costi, F. Mallet, L. Saminadayar, C. Bäuerle, and J. von Delft: ‘Iron impurities in gold and silver: Comparison of transport measurements to numerical renormalization group calculations exploiting non-Abelian symmetries’. *Phys. Rev. B* (2013), vol. 88(7): p. 075146 (cit. on pp. 68, 69).
- [Han13b] Hansmann, P., T. Ayrál, L. Vaugier, P. Werner, and S. Biermann: ‘Long-Range Coulomb Interactions in Surface Systems: A First-Principles Description within Self-Consistently Combined *GW* and Dynamical Mean-Field Theory’. *Phys. Rev. Lett.* (2013), vol. 110(16): p. 166401 (cit. on pp. 68, 79, 92).
- [Han13c] Hansmann, P., L. Vaugier, H. Jiang, and S. Biermann: ‘What about U on surfaces? Extended Hubbard models for adatom systems from first principles’. *Journal of Physics: Condensed Matter* (2013), vol. 25(9): p. 094005 (cit. on pp. 79, 92).

- [Har09] Harl, J. and G. Kresse: ‘Accurate Bulk Properties from Approximate Many-Body Techniques’. *Phys. Rev. Lett.* (2009), vol. 103(5): p. 056401 (cit. on pp. 31, 54).
- [Har10] Harl, J., L. Schimka, and G. Kresse: ‘Assessing the quality of the random phase approximation for lattice constants and atomization energies of solids’. *Phys. Rev. B* (2010), vol. 81(11): p. 115126 (cit. on pp. 31, 54).
- [Har16] Harland, M., M. I. Katsnelson, and A. I. Lichtenstein: ‘Plaquette valence bond theory of high-temperature superconductivity’. *Phys. Rev. B* (2016), vol. 94(12): p. 125133 (cit. on p. 20).
- [Has70] Hastings, W. K.: ‘Monte Carlo sampling methods using Markov chains and their applications’. *Biometrika* (1970), vol. 57(1): p. 97–109 (cit. on pp. 85, 90).
- [Hau15] Haule, K.: ‘Exact Double Counting in Combining the Dynamical Mean Field Theory and the Density Functional Theory’. *Phys. Rev. Lett.* (2015), vol. 115(19): p. 196403 (cit. on pp. 118, 219, 220).
- [Hau14] Haule, K., T. Birol, and G. Kotliar: ‘Covalency in transition-metal oxides within all-electron dynamical mean-field theory’. *Phys. Rev. B* (2014), vol. 90(7): p. 075136 (cit. on p. 84).
- [Hau10] Haule, K., C.-H. Yee, and K. Kim: ‘Dynamical mean-field theory within the full-potential methods: Electronic structure of CeIrIn₅, CeCoIn₅, and CeRhIn₅’. *Phys. Rev. B* (2010), vol. 81(19): p. 195107 (cit. on pp. 20, 70, 84).
- [Hea89] Headrick, R. L., P. Konarski, S. M. Yalisove, and W. R. Graham: ‘Medium-energy ion scattering study of the initial stage of oxidation of Fe(001)’. *Phys. Rev. B* (1989), vol. 39(9): p. 5713–5718 (cit. on p. 31).
- [Hec17] Heckel, W., T. Würger, S. Müller, and G. Feldbauer: ‘Van der Waals Interaction Really Matters: Energetics of Benzoic Acid on TiO₂ Rutile Surfaces’. *The Journal of Physical Chemistry C* (2017), vol. 121(32): p. 17207–17214 (cit. on pp. 30, 50).
- [Hed65] Hedin, L.: ‘New Method for Calculating the One-Particle Green’s Function with Application to the Electron-Gas Problem’. *Phys. Rev.* (1965), vol. 139(3A): p. A796–A823 (cit. on pp. 70, 71).
- [Hei13] Heid, R.: ‘Density Functional Perturbation Theory and Electron Phonon Coupling’. *Emergent Phenomena in Correlated Matter*. Ed. by Pavarini, E., E. Koch, and U. Schollwöck. Vol. 3. Modeling and Simulation. Jülich: Forschungszentrum Jülich Zentralbibliothek, Verlag, 2013: 520 p. (Cit. on p. 204).
- [Hei04] Heinrich, A. J., J. A. Gupta, C. P. Lutz, and D. M. Eigler: ‘Single-Atom Spin-Flip Spectroscopy’. *Science* (2004), vol. 306(5695): p. 466–469 (cit. on p. 29).

- [Hei98] Heinze, S., S. Blügel, R. Pascal, M. Bode, and R. Wiesendanger: ‘Prediction of bias-voltage-dependent corrugation reversal for STM images of bcc (110) surfaces: W(110), Ta(110), and Fe(110)’. *Phys. Rev. B* (1998), vol. 58(24): p. 16432–16445 (cit. on p. 32).
- [Hei26] Heisenberg, W.: ‘Mehrkörperproblem und Resonanz in der Quantenmechanik’. *Zeitschrift für Physik* (1926), vol. 38: p. 411–426 (cit. on p. 7).
- [Hel07] Held, K.: ‘Electronic structure calculations using dynamical mean field theory’. *Advances in Physics* (2007), vol. 56(6): p. 829–926 (cit. on pp. 20, 70).
- [Hel08] Held, K., O. K. Andersen, M. Feldbacher, A. Yamasaki, and Y.-F. Yang: ‘Bandstructure meets many-body theory: the LDA+DMFT method’. *Journal of Physics: Condensed Matter* (2008), vol. 20(6): p. 064202 (cit. on pp. 20, 70).
- [Hel11] Held, K., C. Taranto, G. Rohringer, and A. Toschi: ‘Hedin Equations, GW , GW +DMFT, and All That’. *The LDA+DMFT approach to strongly correlated materials*. Ed. by Pavarini, E., E. Koch, A. Lichtenstein, and D. Vollhardt. Vol. 1. Schriften des Forschungszentrums Jülich: Modeling and Simulation. 2011 (cit. on pp. 3, 20, 68, 70, 74, 75, 78, 79, 83, 123).
- [Hel03] Hellwig, O. and H. Zabel: ‘Oxygen ordering in Nb(110) films’. *Physica B: Condensed Matter* (2003), vol. 336(1): p. 90–97 (cit. on p. 32).
- [Hen17] Henkelman group. <http://theory.cm.utexas.edu/henkelman/code/bader/>. 2017 (cit. on p. 57).
- [Hes16] Hess, C.: ‘Introduction to Scanning Tunneling Spectroscopy of Correlated Materials’. *Quantum Materials: Experiments and Theory*. Ed. by Pavarini, E., E. Koch, J. van den Brink, and G. Sawatzky. Vol. 6. Modeling and Simulation. Jülich: Forschungszentrum Jülich, 2016: 420 p. (Cit. on pp. 24, 27).
- [Hew93] Hewson, A. C.: *The Kondo Problem to Heavy Fermions*. Cambridge Studies in Magnetism. Cambridge University Press, 1993 (cit. on pp. 113, 124, 136, 150).
- [Hig17] Higuchi, K., H. Niwa, and M. Higuchi: ‘Current–Density Functional Theory for the Superconductor and Its Exchange–Correlation Energy Functional’. *Journal of the Physical Society of Japan* (2017), vol. 86(10): p. 104705 (cit. on pp. 29, 205).
- [Hir07] Hirjibehedin, C. F., C.-Y. Lin, A.-F. Otte, M. Ternes, C. P. Lutz, B. A. Jones, and A. J. Heinrich: ‘Large Magnetic Anisotropy of a Single Atomic Spin Embedded in a Surface Molecular Network’. *Science* (2007), vol. 317(5842): p. 1199–1203 (cit. on p. 29).
- [Hir86] Hirsch, J. E. and R. M. Fye: ‘Monte Carlo Method for Magnetic Impurities in Metals’. *Phys. Rev. Lett.* (1986), vol. 56(23): p. 2521–2524 (cit. on p. 69).
- [Hir18] Hirschmeier, D., H. Hafermann, and A. I. Lichtenstein: ‘Multiband dual fermion approach to quantum criticality in the Hubbard honeycomb lattice’. *Phys. Rev. B* (2018), vol. 97(11): p. 115150 (cit. on p. 94).

- [Hir77] Hirshfeld, F. L.: ‘Bonded-atom fragments for describing molecular charge densities’. *Theoretica Chimica Acta* (1977), vol. 44: p. 129–138 (cit. on pp. 51, 57).
- [Ho76] Ho, W., S. L. Cunningham, and W. H. Weinberg: ‘Abstract: Chemisorption on a model bcc metal’. *Journal of Vacuum Science and Technology* (1976), vol. 13(1): p. 349–350 (cit. on p. 31).
- [Hob00] Hobbs, D., G. Kresse, and J. Hafner: ‘Fully unconstrained noncollinear magnetism within the projector augmented-wave method’. *Phys. Rev. B* (2000), vol. 62(17): p. 11556–11570 (cit. on p. 216).
- [Hoh64] Hohenberg, P. and W. Kohn: ‘Inhomogeneous Electron Gas’. *Phys. Rev.* (1964), vol. 136(3B): p. B864–B871 (cit. on pp. 2, 9, 11, 15, 16).
- [Hor17] Horvat, A., R. Žitko, and J. Mravlje: ‘Spin-orbit coupling in three-orbital Kanamori impurity model and its relevance for transition-metal oxides’. *Phys. Rev. B* (2017), vol. 96(8): p. 085122 (cit. on p. 69).
- [How71] Howard, R. A.: *Dynamic probabilistic systems*. Dynamic Probabilistic Systems Bd. 2. Wiley, 1971 (cit. on pp. 85, 90).
- [Hua85] Huang, H. and J. Hermanson: ‘Bonding and magnetism of chemisorbed oxygen on Fe(001)’. *Phys. Rev. B* (1985), vol. 32(10): p. 6312–6318 (cit. on p. 31).
- [Hub63] Hubbard, J. and B. H. Flowers: ‘Electron correlations in narrow energy bands’. *Proceedings of the Royal Society of London. Series A. Mathematical and Physical Sciences* (1963), vol. 276(1365): p. 238–257 (cit. on pp. 2, 67).
- [Hur41] Hurwitz, H.: ‘The Theory of Magnetism in Alloys’. PhD thesis. Harvard University, 1941 (cit. on p. 81).
- [Irk94] Irkhin, V. Y. and Y. P. Irkhin: ‘Many-electron operator approach in the solid state theory’. *physica status solidi (b)* (1994), vol. 183(1): p. 9–58 (cit. on pp. 128, 130).
- [Jac09] Jacob, D., K. Haule, and G. Kotliar: ‘Kondo Effect and Conductance of Nanocontacts with Magnetic Impurities’. *Phys. Rev. Lett.* (2009), vol. 103(1): p. 016803 (cit. on p. 157).
- [Jac10] Jacob, D. and G. Kotliar: ‘Orbital selective and tunable Kondo effect of magnetic adatoms on graphene: Correlated electronic structure calculations’. *Phys. Rev. B* (2010), vol. 82(8): p. 085423 (cit. on pp. 98, 99).
- [Jac13] Jacob, D., M. Soriano, and J. J. Palacios: ‘Kondo effect and spin quenching in high-spin molecules on metal substrates’. *Phys. Rev. B* (2013), vol. 88(13): p. 134417 (cit. on p. 157).
- [Jac15] Jacobson, P., T. Herden, M. Muenks, G. Laskin, O. Brovko, V. Stepanyuk, M. Ternes, and K. Kern: ‘Quantum engineering of spin and anisotropy in magnetic molecular junctions’. *Nat. Commun.* (2015), vol. 6: p. 8536 (cit. on p. 149).

- [Jar85] Jardin, J. P., M. C. Desjonqueres, and D. Spanjaard: ‘Adsorption of oxygen and hydrogen on a stepped BCC transition metal surface’. *Journal of Physics C: Solid State Physics* (1985), vol. 18(30): p. 5759 (cit. on p. 31).
- [Jat18] Jat, K. S., V. Nagpal, A. D. Sagar, P. Neha, and S. Patnaik: ‘Coexistence of charge density wave and superconductivity in $\text{Cu}_{0.10}\text{TiSe}_2$ ’. *AIP Conference Proceedings* (2018), vol. 1942(1): p. 130047 (cit. on p. 203).
- [Job13] Jobst, J., F. Kisslinger, and H. B. Weber: ‘Detection of the Kondo effect in the resistivity of graphene: Artifacts and strategies’. *Phys. Rev. B* (2013), vol. 88(15): p. 155412 (cit. on p. 96).
- [Joh08] Johannes, M. D. and I. I. Mazin: ‘Fermi surface nesting and the origin of charge density waves in metals’. *Phys. Rev. B* (2008), vol. 77(16): p. 165135 (cit. on p. 203).
- [Jül] Jülich FLAPW. <http://www.flapw.de> (cit. on p. 93).
- [Kak18] Kakekhani, A., L. T. Røling, A. Kulkarni, A. A. Latimer, H. Abroshan, J. Schumann, H. AlJama, S. Siahrostami, S. Ismail-Beigi, F. Abild-Pedersen, and J. K. Nørskov: ‘Nature of Lone-Pair–Surface Bonds and Their Scaling Relations’. *Inorganic Chemistry* (2018), vol. 57(12): p. 7222–7238 (cit. on pp. 30, 50).
- [Kal16] Kalff, F. E., M. P. Rebergen, E. Fahrenfort, J. Girovsky, R. Toskovic, J. L. Lado, J. Fernández-Rossier, and A. F. Otte: ‘A kilobyte rewritable atomic memory’. *Nature Nanotechnology* (2016), vol. 11: p. 926 EP (cit. on p. 28).
- [Kam18] Kamlapure, A., L. Cornils, J. Wiebe, and R. Wiesendanger: ‘Engineering the spin couplings in atomically crafted spin chains on an elemental superconductor’. *Nature Communications* (2018), vol. 9(1): p. 3253 (cit. on pp. 28–30, 161).
- [Kam21] Kamlapure, A., L. Cornils, R. Žitko, M. Valentyuk, R. Mozara, S. Pradhan, J. Fransson, A. I. Lichtenstein, J. Wiebe, and R. Wiesendanger: ‘Correlation of Yu–Shiba–Rusinov States and Kondo Resonances in Artificial Spin Arrays on an s-Wave Superconductor’. *Nano Letters* (2021), vol.: p. null (cit. on pp. 28, 29, 142, 161).
- [Kam19] Kamlapure, A., L. Cornils, R. Žitko, M. Valentyuk, R. Mozara, S. Pradhan, J. Fransson, A. I. Lichtenstein, J. Wiebe, and R. Wiesendanger: ‘Investigation of the Yu-Shiba-Rusinov states of a multi-impurity Kondo system’. *arXiv:1911.03794*. arXiv e-prints. 2019 (cit. on pp. 28, 29, 142, 161).
- [Kar13] Karolak, M.: ‘Electronic Correlation Effects in Transition Metal Systems: From Bulk Crystals to Nanostructures’. PhD thesis. Hamburg: Fachbereich Physik der Universität Hamburg, 2013 (cit. on pp. 19, 20, 22, 67, 79, 82–84, 89, 92, 93, 126, 144, 153, 219).
- [Kar11a] Karolak, M., D. Jacob, and A. I. Lichtenstein: ‘Orbital Kondo Effect in Cobalt-Benzene Sandwich Molecules’. *Phys. Rev. Lett.* (2011), vol. 107(14): p. 146604 (cit. on p. 157).

- [Kar11b] Karolak, M., T. O. Wehling, F. Lechermann, and A. I. Lichtenstein: ‘General DFT++ method implemented with projector augmented waves: electronic structure of SrVO_3 and the Mott transition in $\text{Ca}_{2-x}\text{Sr}_x\text{RuO}_4$ ’. *Journal of Physics: Condensed Matter* (2011), vol. 23(8): p. 085601 (cit. on pp. 20, 82, 93, 134, 144).
- [Kau17] Kaufmann, J., P. Gunacker, and K. Held: ‘Continuous-time quantum Monte Carlo calculation of multiorbital vertex asymptotics’. *Phys. Rev. B* (2017), vol. 96(3): p. 035114 (cit. on p. 68).
- [Kha15] Khajetoorians, A. A., M. Valentyuk, M. Steinbrecher, T. Schlenk, A. Shick, J. Kolorenc, A. I. Lichtenstein, T. O. Wehling, R. Wiesendanger, and J. Wiebe: ‘Tuning emergent magnetism in a Hund’s impurity’. *Nature Nanotechnology* (2015), vol. 10: p. 958 (cit. on p. 91).
- [Kha13] Kharitonov, M. and G. Kotliar: ‘Kondo effect in monolayer and bilayer graphene: Physical realizations of the multichannel Kondo models’. *Phys. Rev. B* (2013), vol. 88(20): p. 201103 (cit. on pp. 97, 98).
- [Kil07] Kilimis, D. A. and C. E. Lekka: ‘Oxidation of the Nb(110) surface by ab initio calculations’. *Materials Science and Engineering: B* (2007), vol. 144(1): p. 27–31 (cit. on p. 32).
- [Kim98] Kim, H.-J. and E. Vescovo: ‘Spin-resolved photoemission investigation of the $c(2 \times 2)$ and $c(3 \times 1)$ oxygen overlayers on the Fe(110) surface’. *Phys. Rev. B* (1998), vol. 58(20): p. 14047–14050 (cit. on p. 32).
- [Kim16] Kim, M., W. J. Kim, E. K. Lee, S. Lebègue, and H. Kim: ‘Recent development of atom-pairwise van der waals corrections for density functional theory: From molecules to solids’. *International Journal of Quantum Chemistry* (2016), vol. 116(8): p. 598–607 (cit. on p. 50).
- [Kin16] Kinoshita, Y., R. Turanský, J. Brndiar, Y. Naitoh, Y. J. Li, L. Kantorovich, Y. Sugawara, and I. Štich: ‘Promoting Atoms into Delocalized Long-Living Magnetically Modified State Using Atomic Force Microscopy’. *Nano Letters* (2016), vol. 16(12): p. 7490–7494 (cit. on p. 27).
- [Kit06] Kita, T., R. Sakano, T. Ohashi, and S. Suga: ‘Non-Crossing Approximation Study of Multi-Orbital Kondo Effect in Quantum Dot Systems’. *Controllable Quantum States*. 2006: pp. 233–238 (cit. on pp. 71, 125).
- [Kle09] Kleinert, H.: *Path Integrals in Quantum Mechanics, Statistics, Polymer Physics, and Financial Markets*. EBL-Schweitzer. World Scientific, 2009 (cit. on pp. 2, 207, 211).
- [Kli09] Klimov, V. V. and A. Lambrecht: ‘Van der Waals Forces Between Plasmonic Nanoparticles’. *Plasmonics* (2009), vol. 4(1): p. 31–36 (cit. on pp. 31, 50).
- [Kna17] Knaak, T., M. Gruber, C. Lindström, M.-L. Bocquet, J. Heck, and R. Berndt: ‘Ligand-Induced Energy Shift and Localization of Kondo Resonances in Cobalt-Based Complexes on Cu(111)’. *Nano Lett.* (2017), vol. 17: p. 7146 (cit. on p. 142).

- [Kno02] Knorr, N., M. A. Schneider, L. Diekhöner, P. Wahl, and K. Kern: ‘Kondo Effect of Single Co Adatoms on Cu Surfaces’. *Phys. Rev. Lett.* (2002), vol. 88(9): p. 096804 (cit. on pp. 143, 146).
- [Kog18] Kogan, E.: ‘Poor man’s scaling: anisotropic Kondo and Coqblin–Schrieffer models’. *Journal of Physics Communications* (2018), vol. 2(8): p. 085001 (cit. on pp. 140, 141).
- [Koh65] Kohn, W. and L. J. Sham: ‘Self-Consistent Equations Including Exchange and Correlation Effects’. *Phys. Rev.* (1965), vol. 140(4A): p. A1133–A1138 (cit. on pp. 2, 9, 12, 14, 15).
- [Kol02] Kolesnychenko, O. Y., R. de Kort, M. I. Katsnelson, A. I. Lichtenstein, and H. van Kempen: ‘Real-space imaging of an orbital Kondo resonance on the Cr(001) surface’. *Nature* (2002), vol. 415: p. 507–509 (cit. on pp. 19, 27, 125, 204).
- [Kol05] Kolesnychenko, O. Yu., G. M. M. Heijnen, A. K. Zhuravlev, R. de Kort, M. I. Katsnelson, A. I. Lichtenstein, and H. van Kempen: ‘Surface electronic structure of Cr(001): Experiment and theory’. *Phys. Rev. B* (2005), vol. 72(8): p. 085456 (cit. on pp. 19, 27, 204).
- [Kol01] Koller, R., W. Bergermayer, G. Kresse, E. L. D. Hebenstreit, C. Konvicka, M. Schmid, R. Podloucky, and P. Varga: ‘The structure of the oxygen induced (1×5) reconstruction of V(100)’. *Surface Science* (2001), vol. 480(1): p. 11–24 (cit. on pp. 31, 32).
- [Kom17] Komsa, H.-P., R. Senga, K. Suenaga, and A. V. Krasheninnikov: ‘Structural Distortions and Charge Density Waves in Iodine Chains Encapsulated inside Carbon Nanotubes’. *Nano Letters* (2017), vol. 17(6): p. 3694–3700 (cit. on p. 203).
- [Kon68] Kondo, J.: ‘Effect of Ordinary Scattering on Exchange Scattering from Magnetic Impurity in Metals’. *Phys. Rev.* (1968), vol. 169: p. 437 (cit. on p. 142).
- [Kon64] Kondo, J.: ‘Resistance Minimum in Dilute Magnetic Alloys’. *Progress of Theoretical Physics* (1964), vol. 32(1): p. 37–49 (cit. on pp. 113, 142).
- [Koo34] Koopmans, T.: ‘Über die Zuordnung von Wellenfunktionen und Eigenwerten zu den Einzelnen Elektronen Eines Atoms’. *Physica* (1934), vol. 1(1): p. 104–113 (cit. on p. 8).
- [Kop10] Kopietz, P., L. Bartosch, and F. Schütz: *Introduction to the Functional Renormalization Group*. Introduction to the Functional Renormalization Group. Springer, 2010 (cit. on p. 113).
- [Kor08] Korotin, D., A. V. Kozhevnikov, S. L. Skornyakov, I. Leonov, N. Binggeli, V. I. Anisimov, and G. Trimarchi: ‘Construction and solution of a Wannier-functions based Hamiltonian in the pseudopotential plane-wave framework for strongly correlated materials’. *The European Physical Journal B* (2008), vol. 65(1): p. 91 (cit. on pp. 19, 67).

- [Kot06] Kotliar, G., S. Y. Savrasov, K. Haule, V. S. Oudovenko, O. Parcollet, and C. A. Marianetti: ‘Electronic structure calculations with dynamical mean-field theory’. *Rev. Mod. Phys.* (2006), vol. 78(3): p. 865–951 (cit. on pp. 20, 70, 220).
- [Kot12] Kotov, V. N., B. Uchoa, V. M. Pereira, F. Guinea, and A. H. Castro Neto: ‘Electron-Electron Interactions in Graphene: Current Status and Perspectives’. *Rev. Mod. Phys.* (2012), vol. 84(3): p. 1067–1125 (cit. on p. 94).
- [Kov10] Kováčik, R. and C. Ederer: ‘Calculation of model Hamiltonian parameters for LaMnO₃ using maximally localized Wannier functions’. *Phys. Rev. B* (2010), vol. 81(24): p. 245108 (cit. on pp. 19, 67).
- [Koz15] Kozik, E., M. Ferrero, and A. Georges: ‘Nonexistence of the Luttinger-Ward Functional and Misleading Convergence of Skeleton Diagrammatic Series for Hubbard-Like Models’. *Phys. Rev. Lett.* (2015), vol. 114(15): p. 156402 (cit. on p. 219).
- [Kre96] Kresse, G. and J. Furthmüller: ‘Efficient iterative schemes for ab initio total-energy calculations using a plane-wave basis set’. *Phys. Rev. B* (1996), vol. 54(16): p. 11169–11186 (cit. on pp. 20, 82, 144, 216).
- [Kre99] Kresse, G. and D. Joubert: ‘From ultrasoft pseudopotentials to the projector augmented-wave method’. *Phys. Rev. B* (1999), vol. 59(3): p. 1758–1775 (cit. on p. 215).
- [Kri18] Kristanovski, O., A. B. Shick, F. Lechermann, and A. I. Lichtenstein: ‘Role of nonspherical double counting in DFT+DMFT: Total energy and structural optimization of pnictide superconductors’. *Phys. Rev. B* (2018), vol. 97(20): p. 201116 (cit. on p. 84).
- [Kri19] Krivenko, I. and M. Harland: ‘TRIQS/SOM: Implementation of the stochastic optimization method for analytic continuation’. *Computer Physics Communications* (2019), vol. 239: p. 166–183 (cit. on pp. 89, 90, 144).
- [Kub16] Kubota, D., S. Sakai, and M. Imada: ‘Real-space renormalized dynamical mean field theory’. *Phys. Rev. B* (2016), vol. 93(20): p. 205119 (cit. on p. 20).
- [Küg15] Kügel, J., M. Karolak, A. Krönlein, J. Senkpiel, P.-J. Hsu, G. Sangiovanni, and M. Bode: ‘State identification and tunable Kondo effect of MnPc on Ag(001)’. *Phys. Rev. B* (2015), vol. 91: p. 235130 (cit. on pp. 142, 157).
- [Kun11] Kuneš, Jan: ‘Wannier Functions and Construction of Model Hamiltonians’. *The LDA+DMFT approach to strongly correlated materials*. Vol. 1. Schriften des Forschungszentrums Jülich: Modeling and Simulation. 2011 (cit. on pp. 19, 67, 82, 126).
- [Kut12] Kutepov, A., K. Haule, S. Y. Savrasov, and G. Kotliar: ‘Electronic structure of Pu and Am metals by self-consistent relativistic GW method’. *Phys. Rev. B* (2012), vol. 85(15): p. 155129 (cit. on p. 71).

- [Lan50] Lanczos, C.: ‘An iteration method for the solution of the eigenvalue problem of linear differential and integral operators’. *J. Res. Natl. Bur. Stand. B* (1950), vol. 45: p. 255–282 (cit. on p. 69).
- [Lan56] Landau, L. D.: ‘The Theory of a Fermi Liquid’. *J. Exp. Theor. Phys.* (1956), vol. 3(6): p. 1058 (cit. on p. 114).
- [Lan13] Lane, N. J., M. W. Barsoum, and J. M. Rondinelli: ‘Correlation effects and spin-orbit interactions in two-dimensional hexagonal 5d transition metal carbides, $Ta_{n+1}C_n$ ($n = 1,2,3$)’. *EPL (Europhysics Letters)* (2013), vol. 101(5): p. 57004 (cit. on p. 24).
- [Lec06] Lechermann, F., A. Georges, A. Poteryaev, S. Biermann, M. Posternak, A. Yamasaki, and O. K. Andersen: ‘Dynamical mean-field theory using Wannier functions: A flexible route to electronic structure calculations of strongly correlated materials’. *Phys. Rev. B* (2006), vol. 74(12): p. 125120 (cit. on pp. 20, 70).
- [Leg77] Legg, K. O., F. Jona, D. W. Jepsen, and P. M. Marcus: ‘Early stages of oxidation of the Fe001 surface: Atomic structure of the first monolayer’. *Phys. Rev. B* (1977), vol. 16(12): p. 5271–5276 (cit. on p. 31).
- [Leo08] Leonov, I., N. Binggeli, D. Korotin, V. I. Anisimov, N. Stojić, and D. Vollhardt: ‘Structural Relaxation due to Electronic Correlations in the Paramagnetic Insulator $KCuF_3$ ’. *Phys. Rev. Lett.* (2008), vol. 101(9): p. 096405 (cit. on p. 2).
- [Li98] Li, J. T., W.-D. Schneider, R. Berndt, and B. Delley: ‘Kondo scattering observed at a single magnetic impurity’. *Phys. Rev. Lett.* (1998), vol. 80: p. 2893 (cit. on p. 142).
- [Lia18] Lian, C.-S., C. Si, and W. Duan: ‘Unveiling Charge-Density Wave, Superconductivity, and Their Competitive Nature in Two-Dimensional $NbSe_2$ ’. *Nano Letters* (2018), vol. 18(5): p. 2924–2929 (cit. on p. 203).
- [Lic13] Lichtenstein, A. I.: ‘Magnetism: From Stoner to Hubbard’. *Emergent Phenomena in Correlated Matter*. Ed. by Pavarini, E., E. Koch, and U. Schollwöck. Vol. 3. Modeling and Simulation. Jülich: Forschungszentrum Jülich Zentralbibliothek, Verlag, 2013: 520 p. (Cit. on p. 19).
- [Lie95] Liechtenstein, A. I., V. I. Anisimov, and J. Zaanen: ‘Density-functional theory and strong interactions: Orbital ordering in Mott-Hubbard insulators’. *Phys. Rev. B* (1995), vol. 52(8): p. R5467–R5470 (cit. on p. 21).
- [Liu14] Liu, D.-J. and J. W. Evans: ‘Dissociative adsorption of O_2 on unreconstructed metal (100) surfaces: Pathways, energetics, and sticking kinetics’. *Phys. Rev. B* (2014), vol. 89(20): p. 205406 (cit. on p. 32).
- [Loh90] Loh, E. Y., J. E. Gubernatis, R. T. Scalettar, S. R. White, D. J. Scalapino, and R. L. Sugar: ‘Sign problem in the numerical simulation of many-electron systems’. *Phys. Rev. B* (1990), vol. 41(13): p. 9301–9307 (cit. on p. 86).

- [Lu17] Lu, Y. and M. W. Haverkort: ‘Exact diagonalization as an impurity solver in dynamical mean field theory’. *The European Physical Journal Special Topics* (2017), vol. 226(11): p. 2549–2564 (cit. on p. 68).
- [Lüd05] Lüders, M., M. A. L. Marques, N. N. Lathiotakis, A. Floris, G. Profeta, L. Fast, A. Continenza, S. Massidda, and E. K. U. Gross: ‘Ab initio theory of superconductivity. I. Density functional formalism and approximate functionals’. *Phys. Rev. B* (2005), vol. 72(2): p. 024545 (cit. on p. 204).
- [Mad01] Madhavan, V., W. Chen, T. Jamneala, M. F. Crommie, and N. S. Wingreen: ‘Local spectroscopy of a Kondo impurity: Co on Au(111)’. *Phys. Rev. B* (2001), vol. 64(16): p. 165412 (cit. on pp. 131, 142, 146).
- [Mad98] Madhavan, V., W. Chen, T. Jamneala, M. F. Crommie, and N. S. Wingreen: ‘Tunneling into a Single Magnetic Atom: Spectroscopic Evidence of the Kondo Resonance’. *Science* (1998), vol. 280(5363): p. 567–569 (cit. on pp. 29, 142).
- [Mán15] Mándi, G. and K. Palotás: ‘Chen’s derivative rule revisited: Role of tip-orbital interference in STM’. *Phys. Rev. B* (2015), vol. 91(16): p. 165406 (cit. on p. 131).
- [Mán14] Mándi, G. and K. Palotás: ‘STM contrast inversion of the Fe(110) surface’. *Applied Surface Science* (2014), vol. 304: p. 65–72 (cit. on pp. 32, 131).
- [Man11] Mann, A.: ‘High-temperature superconductivity at 25: Still in suspense’. *Nature* (2011), vol. 475: p. 280–282 (cit. on p. 204).
- [Man00] Manoharan, H. C., C. P. Lutz, and D. M. Eigler: ‘Quantum mirages formed by coherent projection of electronic structure’. *Nature* (2000), vol. 403: p. 512 (cit. on p. 142).
- [Mar11] Marom, N., A. Tkatchenko, M. Rossi, V. V. Gobre, O. Hod, M. Scheffler, and L. Kronik: ‘Dispersion Interactions with Density-Functional Theory: Benchmarking Semiempirical and Interatomic Pairwise Corrected Density Functionals’. *Journal of Chemical Theory and Computation* (2011), vol. 7(12): p. 3944–3951 (cit. on pp. 50, 56).
- [Mas14] Mastrogiuseppe, D., A. Wong, K. Ingersent, S. E. Ulloa, and N. Sandler: ‘Kondo effect in graphene with Rashba spin-orbit coupling’. *Phys. Rev. B* (2014), vol. 90(3): p. 035426 (cit. on p. 98).
- [Mat09] Mattos, L. S. de: ‘Correlated electrons probed by scanning tunneling microscopy’. PhD thesis. Stanford: Stanford University, 2009 (cit. on pp. 96, 97).
- [Met89] Metzner, W. and D. Vollhardt: ‘Correlated Lattice Fermions in $d = \infty$ Dimensions’. *Phys. Rev. Lett.* (1989), vol. 62(3): p. 324–327 (cit. on pp. 3, 20, 83).
- [Mey07] Meyer, J. C., A. K. Geim, M. I. Katsnelson, K. S. Novoselov, T. J. Booth, and S. Roth: ‘The structure of suspended graphene sheets’. *Nature* (2007), vol. 446(7131): p. 60–63 (cit. on p. 97).

- [Mil18] Miller, D. C., S. D. Mahanti, and P. M. Duxbury: ‘Charge density wave states in tantalum dichalcogenides’. *Phys. Rev. B* (2018), vol. 97(4): p. 045133 (cit. on p. 204).
- [Min12] Minamitani, E., N. Tsukahara, D. Matsunaka, Y. Kim, N. Takagi, and M. Kawai: ‘Symmetry-Driven Novel Kondo Effect in a Molecule’. *Phys. Rev. Lett.* (2012), vol. 109: p. 086602 (cit. on pp. 142, 153).
- [Mir97] Miranda, E., V. Dobrosavljević, and G. Kotliar: ‘Disorder-Driven Non-Fermi-Liquid Behavior in Kondo Alloys’. *Phys. Rev. Lett.* (1997), vol. 78(2): p. 290–293 (cit. on p. 119).
- [Mis12] Mishchenko, A. S.: ‘Stochastic Optimization Method for Analytic Continuation: when *a priori* Knowledge is Missing’. *Correlated electrons: from models to materials*. Ed. by Pavarini, E., E. Koch, F. Anders, and M. Jarrell. Vol. 2. Schriften des Forschungszentrums Jülich: Modeling and simulation. 2012: getr. Paginierung (cit. on pp. 88–90).
- [Mis15] Mishchenko, A. S., N. Nagaosa, G. De Filippis, A. de Candia, and V. Cataudella: ‘Mobility of Holstein Polaron at Finite Temperature: An Unbiased Approach’. *Phys. Rev. Lett.* (2015), vol. 114(14): p. 146401 (cit. on p. 89).
- [Mis00] Mishchenko, A. S., N. V. Prokof’ev, A. Sakamoto, and B. V. Svistunov: ‘Diagrammatic quantum Monte Carlo study of the Fröhlich polaron’. *Phys. Rev. B* (2000), vol. 62(10): p. 6317–6336 (cit. on p. 89).
- [Mot68] Mott, N. F.: ‘Metal-Insulator Transition’. *Rev. Mod. Phys.* (1968), vol. 40(4): p. 677–683 (cit. on p. 117).
- [Mot49] Mott, N. F.: ‘The Basis of the Electron Theory of Metals, with Special Reference to the Transition Metals’. *Proceedings of the Physical Society. Section A* (1949), vol. 62(7): p. 416–422 (cit. on pp. 20, 81, 117).
- [Mot37] Mott, N. F. and R. Peierls: ‘Discussion of the paper by de Boer and Verwey’. *Proceedings of the Physical Society* (1937), vol. 49(4S): p. 72–73 (cit. on pp. 20, 81).
- [Moz19] Mozara, R., A. Kamlapure, M. Valentyuk, L. Cornils, A. I. Lichtenstein, J. Wiebe, and R. Wiesendanger: ‘Atomically thin oxide layer on the elemental superconductor Ta(001) surface’. *Phys. Rev. Materials* (2019), vol. 3(9): p. 094801 (cit. on p. 33).
- [Moz18] Mozara, R., M. Valentyuk, I. Krivenko, E. Şaşıoğlu, J. Kolorenč, and A. I. Lichtenstein: ‘Cobalt adatoms on graphene: Effects of anisotropies on the correlated electronic structure’. *Phys. Rev. B* (2018), vol. 97(8): p. 085133 (cit. on p. 100).
- [Nad13] Nadj-Perge, S., I. K. Drozdov, B. A. Bernevig, and A. Yazdani: ‘Proposal for realizing Majorana fermions in chains of magnetic atoms on a superconductor’. *Phys. Rev. B* (2013), vol. 88(2): p. 020407 (cit. on p. 29).

- [Nag02] Nagaoka, K., T. Jamneala, M. Grobis, and M. F. Crommie: ‘Temperature Dependence of a Single Kondo Impurity’. *Phys. Rev. Lett.* (2002), vol. 88(7): p. 077205 (cit. on pp. 147, 150, 151).
- [Nay08] Nayak, C., S. H. Simon, A. Stern, M. Freedman, and S. Das Sarma: ‘Non-Abelian anyons and topological quantum computation’. *Rev. Mod. Phys.* (2008), vol. 80(3): p. 1083–1159 (cit. on p. 29).
- [Née11] Néel, N., R. Berndt, J. Kröger, T. O. Wehling, A. I. Lichtenstein, and M. I. Katsnelson: ‘Two-Site Kondo Effect in Atomic Chains’. *Phys. Rev. Lett.* (2011), vol. 107(10): p. 106804 (cit. on p. 143).
- [Née08] Néel, N., J. Kröger, R. Berndt, T. O. Wehling, A. I. Lichtenstein, and M. I. Katsnelson: ‘Controlling the Kondo Effect in CoCu_n Clusters Atom by Atom’. *Phys. Rev. Lett.* (2008), vol. 101(26): p. 266803 (cit. on pp. 142–144, 147).
- [Née07] Néel, N., J. Kröger, L. Limot, K. Palotas, W. A. Hofer, and R. Berndt: ‘Conductance and Kondo Effect in a Controlled Single-Atom Contact’. *Phys. Rev. Lett.* (2007), vol. 98: p. 016801 (cit. on p. 142).
- [Nek00] Nekrasov, I. A., M. A. Korotin, and V. I. Anisimov: ‘Coulomb interaction in oxygen p -shell in LDA+U method and its influence on calculated spectral and magnetic properties of transition metal oxides’. *eprint arXiv:cond-mat/0009107* (2000), vol. (cit. on p. 24).
- [Nek13] Nekrasov, I. A., N. S. Pavlov, and M. V. Sadovskii: ‘Consistent LDA’+DMFT approach to the electronic structure of transition metal oxides: Charge transfer insulators and correlated metals’. *Journal of Experimental and Theoretical Physics* (2013), vol. 116(4): p. 620–634 (cit. on pp. 20, 70).
- [Nev09] Nevidomskyy, A. H. and P. Coleman: ‘Kondo Resonance Narrowing in d - and f -Electron Systems’. *Phys. Rev. Lett.* (2009), vol. 103(14): p. 147205 (cit. on p. 124).
- [Ney03] Ney, O.: ‘Magnetism and dynamics of oxide interfaces (electronic theory)’. PhD thesis. Martin-Luther-Universität Halle-Wittenberg, 2003 (cit. on p. 126).
- [Nom14] Nomura, Y., S. Sakai, and R. Arita: ‘Multiorbital cluster dynamical mean-field theory with an improved continuous-time quantum Monte Carlo algorithm’. *Phys. Rev. B* (2014), vol. 89(19): p. 195146 (cit. on p. 20).
- [Nov04] Novoselov, K. S., A. K. Geim, S. V. Morozov, D. Jiang, Y. Zhang, S. V. Dubonos, I. V. Grigorieva, and A. A. Firsov: ‘Electric Field Effect in Atomically Thin Carbon Films’. *Science* (2004), vol. 306(5696): p. 666–669 (cit. on pp. 93, 96, 97).
- [Ols13] Olsen, T. and K. S. Thygesen: ‘Random phase approximation applied to solids, molecules, and graphene-metal interfaces: From van der Waals to covalent bonding’. *Phys. Rev. B* (2013), vol. 87(7): p. 075111 (cit. on pp. 31, 54).
- [Oss15] Ossowski, T. and A. Kiejna: ‘Oxygen adsorption on Fe(110) surface revisited’. *Surface Science* (2015), vol. 637-638: p. 35–41 (cit. on p. 32).

- [Ott09] Otte, A. F., M. Ternes, S. Loth, C. P. Lutz, C. F. Hirjibehedin, and A. J. Heinrich: ‘Spin Excitations of a Kondo-Screened Atom Coupled to a Second Magnetic Atom’. *Phys. Rev. Lett.* (2009), vol. 103: p. 107203 (cit. on p. 142).
- [Pac17] Pacchioni, G. E., M. Pivetta, L. Gragnaniello, F. Donati, G. Autès, O. V. Yazyev, S. Rusponi, and H. Brune: ‘Two-Orbital Kondo Screening in a Self-Assembled Metal–Organic Complex’. *ACS Nano* (2017), vol. 11: p. 2675 (cit. on p. 142).
- [Pal12] Palotás, K., W. A. Hofer, and L. Szunyogh: ‘Simulation of spin-polarized scanning tunneling spectroscopy on complex magnetic surfaces: Case of a Cr monolayer on Ag(111)’. *Phys. Rev. B* (2012), vol. 85(20): p. 205427 (cit. on pp. 26, 131).
- [Pan85] Panzner, G., D. R. Mueller, and T. N. Rhodin: ‘Angle-resolved photoemission studies of oxygen adsorbed on Fe(100)’. *Phys. Rev. B* (1985), vol. 32(6): p. 3472–3478 (cit. on p. 32).
- [Par15] Parcollet, O., M. Ferrero, T. Ayrál, H. Hafermann, I. Krivenko, L. Messio, and P. Seth: ‘TRIQS: A toolbox for research on interacting quantum systems’. *Computer Physics Communications* (2015), vol. 196: p. 398–415 (cit. on pp. 79, 84, 85, 144).
- [Par10] Parihar, S. S., H. L. Meyerheim, K. Mohseni, S. Ostanin, A. Ernst, N. Jedrecy, R. Felici, and J. Kirschner: ‘Structure of O/Fe(001)-p(1 × 1) studied by surface x-ray diffraction’. *Phys. Rev. B* (2010), vol. 81(7): p. 075428 (cit. on p. 31).
- [Pau19] Paul, A. and T. Birol: ‘Applications of DFT+DMFT in Materials Science’. *Annual Review of Materials Research* (2019), vol. 49(1): p. 31–52 (cit. on pp. 20, 70).
- [Pav12] Pavarini, E.: ‘Crystal-Field Theory, Tight-Binding Method and Jahn-Teller Effect’. *Correlated electrons: from models to materials*. Ed. by Pavarini, E., E. Koch, F. Anders, and M. Jarrell. Vol. 2. Schriften des Forschungszentrums Jülich: Modeling and simulation. 2012 (cit. on pp. 82, 126).
- [Pav14] Pavarini, E.: ‘Electronic Structure Calculations with LDA+DMFT’. *Many-Electron Approaches in Physics, Chemistry and Mathematics: A Multidisciplinary View*. Ed. by Bach, V. and L. Delle Site. Cham: Springer International Publishing, 2014: pp. 321–341 (cit. on pp. 20, 70).
- [Pav11] Pavarini, E., E. Koch, A. Lichtenstein, and D. Vollhardt, eds.: *The LDA+DMFT approach to strongly correlated materials*. Vol. 1. Schriften des Forschungszentrums Jülich: Modeling and Simulation. 2011 (cit. on pp. 20, 70).
- [Pei30] Peierls, R.: ‘Zur Theorie der elektrischen und thermischen Leitfähigkeit von Metallen’. *Annalen der Physik* (1930), vol. 396(2): p. 121–148 (cit. on p. 203).
- [Per96] Perdew, J. P., K. Burke, and M. Ernzerhof: ‘Generalized Gradient Approximation Made Simple’. *Phys. Rev. Lett.* (1996), vol. 77(18): p. 3865–3868 (cit. on p. 17).

- [Per17] Perdew, J. P., W. Yang, K. Burke, Z. Yang, E. K. U. Gross, M. Scheffler, G. E. Scuseria, T. M. Henderson, I. Y. Zhang, A. Ruzsinszky, H. Peng, J. Sun, E. Trushin, and A. Görling: ‘Understanding band gaps of solids in generalized Kohn–Sham theory’. *Proceedings of the National Academy of Sciences* (2017), vol. 114(11): p. 2801–2806 (cit. on p. 20).
- [Per81] Perdew, J. P. and A. Zunger: ‘Self-interaction correction to density-functional approximations for many-electron systems’. *Phys. Rev. B* (1981), vol. 23(10): p. 5048–5079 (cit. on p. 15).
- [Pic10] Picone, A., G. Fratesi, A. Brambilla, P. Sessi, F. Donati, S. Achilli, L. Maini, M. I. Trioni, C. S. Casari, M. Passoni, A. Li Bassi, M. Finazzi, L. Duò, and F. Ciccacci: ‘Atomic corrugation in scanning tunneling microscopy images of the Fe(001)– $p(1 \times 1)$ O surface’. *Phys. Rev. B* (2010), vol. 81(11): p. 115450 (cit. on p. 32).
- [Pie13] Pientka, F., L. I. Glazman, and F. von Oppen: ‘Topological superconducting phase in helical Shiba chains’. *Phys. Rev. B* (2013), vol. 88(15): p. 155420 (cit. on p. 29).
- [Pin52] Pines, D. and D. Bohm: ‘A Collective Description of Electron Interactions: II. Collective vs Individual Particle Aspects of the Interactions’. *Phys. Rev.* (1952), vol. 85(2): p. 338–353 (cit. on pp. 114, 118).
- [Pin66] Pines, D. and P. Nozières: *Theory Of Quantum Liquids: Normal Fermi Liquids*. Advanced Books Classics. Avalon Publishing, 1966 (cit. on p. 114).
- [Piv07] Pivetta, M., M. Ternes, F. Patthey, and W.-D. Schneider: ‘Diatomic Molecular Switches to Enable the Observation of Very-Low-Energy Vibrations’. *Phys. Rev. Lett.* (2007), vol. 99: p. 126104 (cit. on p. 142).
- [Pok18] Pokorný, V. and M. Žonda: ‘Correlation effects in superconducting quantum dot systems’. *Physica B: Condensed Matter* (2018), vol. 536: p. 488–491 (cit. on p. 30).
- [Pot18] Potthoff, M.: ‘Cluster Extensions of Dynamical Mean-Field Theory’. *DMFT: From Infinite Dimensions to Real Materials*. Ed. by Pavarini, E., E. Koch, A. I. Lichtenstein, and D. Vollhardt. Vol. 8. Modeling and Simulation. Jülich: Forschungszentrum Jülich GmbH Zentralbibliothek, Velag, 2018 (cit. on p. 20).
- [Pot06] Potthoff, M.: ‘Non-perturbative construction of the Luttinger-Ward functional’. *Condensed Matter Physics* (2006), vol. 9(3(47)): p. 557–567 (cit. on p. 221).
- [Pou07] Pourovskii, L. V., B. Amadon, S. Biermann, and A. Georges: ‘Self-consistency over the charge density in dynamical mean-field theory: A linear muffin-tin implementation and some physical implications’. *Phys. Rev. B* (2007), vol. 76(23): p. 235101 (cit. on pp. 20, 68, 70, 84, 122).
- [Pro96] Prokof’ev, N. V., B. V. Svistunov, and I. S. Tupitsyn: ‘Exact quantum Monte Carlo process for the statistics of discrete systems’. *Journal of Experimental and Theoretical Physics Letters* (1996), vol. 64(12): p. 911–916 (cit. on p. 67).

- [Prü11] Prüser, H., M. Wenderoth, P. E. Dargel, A. Weismann, R. Peters, T. Pruschke, and R. G. Ulbrich: ‘Long-range Kondo signature of a single magnetic impurity’. *Nat. Phys.* (2011), vol. 7: p. 203 (cit. on p. 142).
- [Prü12] Prüser, H., M. Wenderoth, A. Weismann, and R. G. Ulbrich: ‘Mapping Itinerant Electrons around Kondo Impurities’. *Phys. Rev. Lett.* (2012), vol. 108(16): p. 166604 (cit. on pp. 146, 147).
- [Ras86] Rasolt, M. and D. J. W. Geldart: ‘Exchange and correlation energy in a nonuniform fermion fluid’. *Phys. Rev. B* (1986), vol. 34(2): p. 1325–1328 (cit. on p. 16).
- [Ren12] Ren, X., P. Rinke, C. Joas, and M. Scheffler: ‘Random-phase approximation and its applications in computational chemistry and materials science’. *Journal of Materials Science* (2012), vol. 47(21): p. 7447–7471 (cit. on pp. 31, 54, 77).
- [Ren16] Rentrop, J. F., V. Meden, and S. G. Jakobs: ‘Renormalization group flow of the Luttinger-Ward functional: Conserving approximations and application to the Anderson impurity model’. *Phys. Rev. B* (2016), vol. 93(19): p. 195160 (cit. on p. 219).
- [Rub12] Rubtsov, A. N., M. I. Katsnelson, and A. I. Lichtenstein: ‘Dual boson approach to collective excitations in correlated fermionic systems’. *Annals of Physics* (2012), vol. 327(5): p. 1320–1335 (cit. on pp. 3, 20, 23, 67, 70).
- [Rub09] Rubtsov, A. N., M. I. Katsnelson, A. I. Lichtenstein, and A. Georges: ‘Dual fermion approach to the two-dimensional Hubbard model: Antiferromagnetic fluctuations and Fermi arcs’. *Phys. Rev. B* (2009), vol. 79(4): p. 045133 (cit. on pp. 3, 20, 67, 70).
- [Rub05] Rubtsov, A. N., V. V. Savkin, and A. I. Lichtenstein: ‘Continuous-time quantum Monte Carlo method for fermions’. *Phys. Rev. B* (2005), vol. 72(3): p. 035122 (cit. on p. 67).
- [Rud12] Rudenko, A. N., F. J. Keil, M. I. Katsnelson, and A. I. Lichtenstein: ‘Adsorption of cobalt on graphene: Electron correlation effects from a quantum chemical perspective’. *Phys. Rev. B* (2012), vol. 86(7): p. 075422 (cit. on p. 95).
- [Rud54] Ruderman, M. A. and C. Kittel: ‘Indirect Exchange Coupling of Nuclear Magnetic Moments by Conduction Electrons’. *Phys. Rev.* (1954), vol. 96(1): p. 99–102 (cit. on p. 121).
- [Rus69] Rusinov, A. I.: ‘Superconductivity near a Paramagnetic Impurity’. *Soviet Journal of Experimental and Theoretical Physics Letters* (1969), vol. 9: p. 85 (cit. on p. 29).
- [Ryd03] Rydberg, H., M. Dion, N. Jacobson, E. Schröder, P. Hyldgaard, S. I. Simak, D. C. Langreth, and B. I. Lundqvist: ‘Van der Waals Density Functional for Layered Structures’. *Phys. Rev. Lett.* (2003), vol. 91(12): p. 126402 (cit. on p. 94).

- [Saf12] Saffarzadeh, A. and G. Kirczenow: ‘Scanning tunneling spectroscopy and Dirac point resonances due to a single Co adatom on gated graphene’. *Phys. Rev. B* (2012), vol. 85(24): p. 245429 (cit. on p. 97).
- [Sak06] Sakano, R. and N. Kawakami: ‘Conductance via the multiorbital Kondo effect in single quantum dots’. *Phys. Rev. B* (2006), vol. 73(15): p. 155332 (cit. on pp. 124, 125).
- [Sar18] Sarvestani, E., G. Zhang, E. Gorelov, and E. Pavarini: ‘Effective masses, lifetimes, and optical conductivity in Sr_2RuO_4 and $\text{Sr}_3\text{Ru}_2\text{O}_7$: Interplay of spin-orbit, crystal-field, and Coulomb tetragonal tensor interactions’. *Phys. Rev. B* (2018), vol. 97(8): p. 085141 (cit. on p. 79).
- [Şaş11] Şaşıoğlu, E., C. Friedrich, and S. Blügel: ‘Effective Coulomb interaction in transition metals from constrained random-phase approximation’. *Phys. Rev. B* (2011), vol. 83(12): p. 121101 (cit. on p. 78).
- [Şaş12] Şaşıoğlu, E., C. Friedrich, and S. Blügel: ‘Strength of the Effective Coulomb Interaction at Metal and Insulator Surfaces’. *Phys. Rev. Lett.* (2012), vol. 109(14): p. 146401 (cit. on pp. 59, 79, 93, 94, 96).
- [Sav04] Savrasov, S. Y. and G. Kotliar: ‘Spectral density functionals for electronic structure calculations’. *Phys. Rev. B* (2004), vol. 69(24): p. 245101 (cit. on pp. 68, 122).
- [Sch13] Scherz, U.: *Quantenmechanik: Eine Einführung mit Anwendungen auf Atome, Moleküle und Festkörper*. Teubner Studienbücher Physik. Vieweg+Teubner Verlag, 2013 (cit. on pp. 2, 7, 11, 13–16, 18, 215, 216).
- [Sch10] Schimka, L., J. Harl, A. Stroppa, A. Grüneis, M. Marsman, F. Mittendorfer, and G. Kresse: ‘Accurate surface and adsorption energies from many-body perturbation theory’. *Nature Materials* (2010), vol. 9: p. 741–744 (cit. on p. 31).
- [Sch97] Schofield, A. J.: ‘Bosonization in the two-channel Kondo model’. *Phys. Rev. B* (1997), vol. 55(9): p. 5627–5630 (cit. on pp. 119, 120).
- [Sch99] Schofield, A. J.: ‘Non-Fermi liquids’. *Contemporary Physics* (1999), vol. 40(2): p. 95–115 (cit. on pp. 114, 118, 119).
- [Sch05] Schollwöck, U.: ‘The density-matrix renormalization group’. *Rev. Mod. Phys.* (2005), vol. 77(1): p. 259–315 (cit. on p. 68).
- [Sch66] Schrieffer, J. R. and P. A. Wolff: ‘Relation between the Anderson and Kondo Hamiltonians’. *Phys. Rev.* (1966), vol. 149(2): p. 491–492 (cit. on p. 137).
- [Sch16] Schüler, M., S. Barthel, M. Karolak, A. I. Poteryaev, A. I. Lichtenstein, M. I. Katsnelson, G. Sangiovanni, and T. O. Wehling: ‘Many-body effects on Cr(001) surfaces: An LDA+DMFT study’. *Phys. Rev. B* (2016), vol. 93(19): p. 195115 (cit. on pp. 19, 204).
- [Sei96] Seidl, A., A. Görling, P. Vogl, J. A. Majewski, and M. Levy: ‘Generalized Kohn-Sham schemes and the band-gap problem’. *Phys. Rev. B* (1996), vol. 53(7): p. 3764–3774 (cit. on p. 20).

- [Sen08] Sengupta, K. and G. Baskaran: ‘Tuning Kondo physics in graphene with gate voltage’. *Phys. Rev. B* (2008), vol. 77(4): p. 045417 (cit. on p. 97).
- [Set16] Seth, P., I. Krivenko, M. Ferrero, and O. Parcollet: ‘TRIQS/CTHYB: A continuous-time quantum Monte Carlo hybridisation expansion solver for quantum impurity problems’. *Computer Physics Communications* (2016), vol. 200: p. 274–284 (cit. on pp. 79, 84, 85, 87, 144).
- [Shi68] Shiba, H.: ‘Classical Spins in Superconductors’. *Progress of Theoretical Physics* (1968), vol. 40(3): p. 435 (cit. on p. 29).
- [Shi09] Shick, A. B., J. Kolorenč, A. I. Lichtenstein, and L. Havela: ‘Electronic structure and spectral properties of Am, Cm, and Bk: Charge-density self-consistent LDA+HIA calculations in the FP-LAPW basis’. *Phys. Rev. B* (2009), vol. 80(8): p. 085106 (cit. on p. 84).
- [Shi10] Shick, A. B., J. Kolorenč, A. I. Lichtenstein, and L. Havela: ‘Electronic structure and spectral properties of heavy actinides Pu, Am, Cm and Bk’. *IOP Conference Series: Materials Science and Engineering* (2010), vol. 9: p. 012049 (cit. on p. 84).
- [Shi17a] Shick, A. B., D. S. Shapiro, J. Kolorenč, and A. I. Lichtenstein: ‘Magnetic character of holmium atom adsorbed on platinum surface’. *Scientific Reports* (2017), vol. 7(1): p. 2751 (cit. on p. 82).
- [Shi17b] Shinaoka, H., F. Assaad, N. Blümer, and P. Werner: ‘Quantum Monte Carlo impurity solvers for multi-orbital problems and frequency-dependent interactions’. *The European Physical Journal Special Topics* (2017), vol. 226(11): p. 2499–2523 (cit. on p. 68).
- [Sho16] Shoji, T., R. Kuwahara, S. Ono, and K. Ohno: ‘A self-consistent GW approach to the van der Waals potential for a helium dimer’. *Phys. Chem. Chem. Phys.* (2016), vol. 18(35): p. 24477–24483 (cit. on pp. 31, 54).
- [Sil58a] Silin, V. P.: ‘On the Theory of the Anomalous Skin Effect in Metals’. *J. Exp. Theor. Phys.* (1958), vol. 6(5): p. 1282 (cit. on p. 118).
- [Sil58b] Silin, V. P.: ‘Theory of a degenerate Electron Liquid’. *J. Exp. Theor. Phys.* (1958), vol. 6(2): p. 495 (cit. on p. 118).
- [Sin92] Singh, D. J. and J. Ashkenazi: ‘Magnetism with generalized-gradient-approximation density functionals’. *Phys. Rev. B* (1992), vol. 46(18): p. 11570–11577 (cit. on p. 19).
- [Sla29] Slater, J. C.: ‘The Theory of Complex Spectra’. *Physical Review* (1929), vol. 34: p. 1293–1322 (cit. on p. 7).
- [Sol94] Solovyev, I. V., P. H. Dederichs, and V. I. Anisimov: ‘Corrected atomic limit in the local-density approximation and the electronic structure of d impurities in Rb’. *Phys. Rev. B* (1994), vol. 50(23): p. 16861–16871 (cit. on p. 21).
- [Spa12] Spaldin, N. A.: ‘A beginner’s guide to the modern theory of polarization’. *Journal of Solid State Chemistry* (2012), vol. 195: p. 2–10 (cit. on p. 205).

- [Spe08] Sperl, A., J. Kröger, N. Néel, H. Jensen, R. Berndt, A. Franke, and E. Pehlke: ‘Unoccupied states of individual silver clusters and chains on Ag(111)’. *Phys. Rev. B* (2008), vol. 77: p. 085422 (cit. on p. 141).
- [Sri72] Sri Aurobindo: ‘Electron’. *Collected Works, Sri Aurobindo Birth Centenary Library* (1972), vol. 5: p. 085133 (cit. on p. 1).
- [Sta15] Stadler, K. M., Z. P. Yin, J. von Delft, G. Kotliar, and A. Weichselbaum: ‘Dynamical Mean-Field Theory Plus Numerical Renormalization-Group Study of Spin-Orbital Separation in a Three-Band Hund Metal’. *Phys. Rev. Lett.* (2015), vol. 115(13): p. 136401 (cit. on pp. 68, 69, 113, 157).
- [Ste16a] Steiner, So., S. Khmelevskiy, M. Marsmann, and G. Kresse: ‘Calculation of the magnetic anisotropy with projected-augmented-wave methodology and the case study of disordered $\text{Fe}_{1-x}\text{Co}_x$ alloys’. *Phys. Rev. B* (2016), vol. 93(22): p. 224425 (cit. on p. 216).
- [Ste11a] Steinmann, S. N. and C. Corminboeuf: ‘A generalized-gradient approximation exchange hole model for dispersion coefficients’. *The Journal of Chemical Physics* (2011), vol. 134(4): p. 044117 (cit. on p. 53).
- [Ste11b] Steinmann, S. N. and C. Corminboeuf: ‘Comprehensive Benchmarking of a Density-Dependent Dispersion Correction’. *Journal of Chemical Theory and Computation* (2011), vol. 7(11): p. 3567–3577 (cit. on p. 53).
- [Ste16b] Stepanov, E. A., E. G. C. P. van Loon, A. A. Katanin, A. I. Lichtenstein, M. I. Katsnelson, and A. N. Rubtsov: ‘Self-consistent dual boson approach to single-particle and collective excitations in correlated systems’. *Phys. Rev. B* (2016), vol. 93(4): p. 045107 (cit. on p. 23).
- [Ste14] Sterrer, M. and H.-J. Freund: ‘Properties of Oxide Surfaces’. *Surface and Interface Science*. John Wiley & Sons, Ltd., 2014: pp. 229–278 (cit. on p. 28).
- [Stö19] Stöhr, M., T. van Voorhis, and A. Tkatchenko: ‘Theory and practice of modeling van der Waals interactions in electronic-structure calculations’. *Chem. Soc. Rev.* (2019), vol.: p. 4118–4154 (cit. on p. 50).
- [Sto13] Stone, A. J.: *The theory of intermolecular forces*. Oxford: Oxford University Press, 2013 (cit. on p. 50).
- [Str98] Strange, P.: *Relativistic Quantum Mechanics: With Applications in Condensed Matter and Atomic Physics*. Cambridge University Press, 1998 (cit. on p. 212).
- [Sun14] Sun, C. Q.: *Relaxation of the chemical bond: skin chemisorption size matter ZTP mechanics H₂O myths*. Springer Series in Chemical Physics. Singapore: Springer, 2014 (cit. on p. 31).
- [Sun02] Sun, P. and G. Kotliar: ‘Extended dynamical mean-field theory and GW method’. *Phys. Rev. B* (2002), vol. 66(8): p. 085120 (cit. on pp. 3, 20, 68, 79, 123).
- [Sun05] Sun, Q. and X. C. Xie: ‘Definition of the spin current: The angular spin current and its physical consequences’. *Phys. Rev. B* (2005), vol. 72(24): p. 245305 (cit. on p. 212).

- [Sur12] Surer, B., M. Troyer, P. Werner, T. O. Wehling, A. M. Läuchli, A. Wilhelm, and A. I. Lichtenstein: ‘Multiorbital Kondo physics of Co in Cu hosts’. *Phys. Rev. B* (2012), vol. 85(8): p. 085114 (cit. on pp. 144, 145, 150).
- [Sür01] Sürgers, C., M. Schöck, and H. von Löhneysen: ‘Oxygen-induced surface structure of Nb(110)’. *Surface Science* (2001), vol. 471(1): p. 209–218 (cit. on p. 32).
- [Sza96] Szabo, A. and N. S. Ostlund: *Modern Quantum Chemistry: Introduction to Advanced Electronic Structure Theory*. Dover Publications, Inc., 1996 (cit. on pp. 7, 8, 64–66).
- [Tel62] Teller, E.: ‘On the Stability of Molecules in the Thomas-Fermi Theory’. *Rev. Mod. Phys.* (1962), vol. 34(4): p. 627–631 (cit. on p. 9).
- [Ter09] Ternes, M., A. J. Heinrich, and W. D. Schneider: ‘Spectroscopic manifestations of the Kondo effect on single adatoms’. *J. Phys.: Condens. Matter* (2009), vol. 21: p. 053001 (cit. on pp. 142, 157, 217).
- [Ter85] Tersoff, J. and D. R. Hamann: ‘Theory of the scanning tunneling microscope’. *Phys. Rev. B* (1985), vol. 31(2): p. 805–813 (cit. on pp. 25, 26).
- [Tho27] Thomas, L. H.: ‘The calculation of atomic fields’. *Proceedings of the Cambridge Philosophical Society* (1927), vol. 23: p. 542 (cit. on p. 9).
- [Tho11] Thonhauser, T.: ‘Theory of orbital magnetization in solids’. *International Journal of Modern Physics B* (2011), vol. 25(11): p. 1429–1458 (cit. on p. 204).
- [Tit85] Titov, A. V. and H. Jagodzinski: ‘Structure of O layers on the Ta(100) surface’. *Surface Science* (1985), vol. 152-153: p. 409–418 (cit. on pp. 30, 31, 55).
- [Tit12] Titvinidze, I., A. Schwabe, N. Rother, and M. Potthoff: ‘Dynamical mean-field theory of indirect magnetic exchange’. *Phys. Rev. B* (2012), vol. 86(7): p. 075141 (cit. on p. 20).
- [Tka12] Tkatchenko, A., R. A. DiStasio, R. Car, and M. Scheffler: ‘Accurate and Efficient Method for Many-Body van der Waals Interactions’. *Phys. Rev. Lett.* (2012), vol. 108(23): p. 236402 (cit. on p. 53).
- [Tka09] Tkatchenko, A. and M. Scheffler: ‘Accurate Molecular Van Der Waals Interactions from Ground-State Electron Density and Free-Atom Reference Data’. *Phys. Rev. Lett.* (2009), vol. 102(7): p. 073005 (cit. on pp. 50, 52).
- [Tog15] Togo, A. and I. Tanaka: ‘First principles phonon calculations in materials science’. *Scripta Materialia* (2015), vol. 108: p. 1–5 (cit. on p. 204).
- [Tom12] Tomczak, J. M., M. Casula, T. Miyake, F. Aryasetiawan, and S. Biermann: ‘Combined GW and dynamical mean-field theory: Dynamical screening effects in transition metal oxides’. *EPL (Europhysics Letters)* (2012), vol. 100(6): p. 67001 (cit. on pp. 20, 70).
- [Tro05] Troyer, M. and U.-J. Wiese: ‘Computational Complexity and Fundamental Limitations to Fermionic Quantum Monte Carlo Simulations’. *Phys. Rev. Lett.* (2005), vol. 94(17): p. 170201 (cit. on p. 86).

- [Tsu14] Tsukahara, N., E. Minamitani, Y. Kim, M. Kawai, and N. Takagi: ‘Controlling orbital-selective Kondo effects in a single molecule through coordination chemistry’. *The Journal of Chemical Physics* (2014), vol. 141(5): p. 054702 (cit. on p. 158).
- [Tsv85] Tsvetick, A. M. and P. B. Wiegmann: ‘Exact solution of the multichannel Kondo problem, scaling, and integrability’. *Journal of Statistical Physics* (1985), vol. 38(1): p. 125–147 (cit. on pp. 119, 121, 124).
- [Uch08] Uchihashi, T., J. Zhang, J. Kröger, and R. Berndt: ‘Quantum Modulation of the Kondo Resonance of Co Adatoms on Cu/Co/Cu(100)’. *Phys. Rev. B* (2008), vol. 78: p. 033402 (cit. on p. 143).
- [Ueb98] Uebing, C.: ‘Two-dimensional transition metal compounds with carbon, nitrogen and oxygen on BCC(100) metal and alloy surfaces’. *Progress in Solid State Chemistry* (1998), vol. 26(3): p. 155–240 (cit. on p. 31).
- [Újs00] Újsághy, O., J. Kroha, L. Szunyogh, and A. Zawadowski: ‘Theory of the Fano Resonance in the STM Tunneling Density of States due to a Single Kondo Impurity’. *Phys. Rev. Lett.* (2000), vol. 85(12): p. 2557–2560 (cit. on p. 144).
- [Umm13] Ummerino, G. A. C.: ‘Eliashberg Theory’. *Emergent Phenomena in Correlated Matter*. Ed. by Pavarini, E., E. Koch, and U. Schollwöck. Vol. 3. Modeling and Simulation. Jülich: Forschungszentrum Jülich Zentralbibliothek, Verlag, 2013: 520 p. (Cit. on pp. 29, 205).
- [Usa77] Usami, S., N. Tominaga, and T. Nakajima: ‘AES-LEED study of adsorption of common gases on the (100) planes of W and Nb’. *Vacuum* (1977), vol. 27(1): p. 11–16 (cit. on p. 32).
- [Van90] Vanderbilt, D.: ‘Soft self-consistent pseudopotentials in a generalized eigenvalue formalism’. *Phys. Rev. B* (1990), vol. 41(11): p. 7892–7895 (cit. on p. 215).
- [Van13] Vanpoucke, D. E. P., P. Bultinck, and I. Van Driessche: ‘Extending Hirshfeld-I to bulk and periodic materials’. *Journal of Computational Chemistry* (2013), vol. 34(5): p. 405–417 (cit. on p. 52).
- [Vig06] Vignale, G.: ‘Current Density Functional Theory’. *Time-Dependent Density Functional Theory*. Ed. by Marques, M. A. L., C. A. Ullrich, F. Nogueira, A. Rubio, K. Burke, and E. K. U. Gross. Berlin, Heidelberg: Springer Berlin Heidelberg, 2006: pp. 75–91 (cit. on pp. 205, 207).
- [Vig88] Vignale, G. and M. Rasolt: ‘Current- and spin-density-functional theory for inhomogeneous electronic systems in strong magnetic fields’. *Phys. Rev. B* (1988), vol. 37(18): p. 10685–10696 (cit. on pp. 203–206, 212).
- [Vig87] Vignale, G. and M. Rasolt: ‘Density-functional theory in strong magnetic fields’. *Phys. Rev. Lett.* (1987), vol. 59(20): p. 2360–2363 (cit. on p. 205).
- [Vir12] Virgus, Y., W. Purwanto, H. Krakauer, and S. Zhang: ‘Ab initio many-body study of cobalt adatoms adsorbed on graphene’. *Phys. Rev. B* (2012), vol. 86(24): p. 241406 (cit. on p. 95).

- [Vle53] Vleck, J. H. van: ‘Models of Exchange Coupling in Ferromagnetic Media’. *Rev. Mod. Phys.* (1953), vol. 25(1): p. 220–227 (cit. on p. 81).
- [Voj15] Vojta, M., R. Bulla, and P. Wölfle: ‘Critical quasiparticles in single-impurity and lattice Kondo models’. *The European Physical Journal Special Topics* (2015), vol. 224(6): p. 1127–1146 (cit. on p. 98).
- [Voj04] Vojta, M. and L. Fritz: ‘Upper critical dimension in a quantum impurity model: Critical theory of the asymmetric pseudogap Kondo problem’. *Phys. Rev. B* (2004), vol. 70(9): p. 094502 (cit. on p. 98).
- [Voj10] Vojta, M., L. Fritz, and R. Bulla: ‘Gate-controlled Kondo screening in graphene: Quantum criticality and electron-hole asymmetry’. *EPL (Europhysics Letters)* (2010), vol. 90(2): p. 27006 (cit. on p. 98).
- [Vol12] Vollhardt, D.: ‘Dynamical mean-field theory for correlated electrons’. *Annalen der Physik* (2012), vol. 524(1): p. 1–19 (cit. on pp. 3, 20).
- [Vos80] Vosko, S. H., L. Wilk, and M. Nusair: ‘Accurate spin-dependent electron liquid correlation energies for local spin density calculations: a critical analysis’. *Canadian Journal of Physics* (1980), vol. 58(8): p. 1200–1211 (cit. on p. 18).
- [Wah04] Wahl, P., L. Diekhöner, M. A. Schneider, L. Vitali, G. Wittich, and K. Kern: ‘Kondo Temperature of Magnetic Impurities at Surfaces’. *Phys. Rev. Lett.* (2004), vol. 93: p. 176603 (cit. on pp. 142, 143).
- [Wan91] Wang, Y. and J. P. Perdew: ‘Spin scaling of the electron-gas correlation energy in the high-density limit’. *Phys. Rev. B* (1991), vol. 43(11): p. 8911–8916 (cit. on p. 17).
- [Wat58] Watson, R. E.: ‘Analytic Hartree-Fock Solutions for O⁼’. *Phys. Rev.* (1958), vol. 111(4): p. 1108–1110 (cit. on p. 53).
- [Weh10] Wehling, T. O., A. V. Balatsky, M. I. Katsnelson, A. I. Lichtenstein, and A. Rosch: ‘Orbitally controlled Kondo effect of Co adatoms on graphene’. *Phys. Rev. B* (2010), vol. 81(11): p. 115427 (cit. on pp. 98, 136).
- [Weh11] Wehling, T. O., E. Şaşıoğlu, C. Friedrich, A. I. Lichtenstein, M. I. Katsnelson, and S. Blügel: ‘Strength of Effective Coulomb Interactions in Graphene and Graphite’. *Phys. Rev. Lett.* (2011), vol. 106(23): p. 236805 (cit. on p. 92).
- [Wer12] Werner, P., M. Casula, T. Miyake, F. Aryasetiawan, A. J. Millis, and S. Biermann: ‘Satellites and large doping and temperature dependence of electronic properties in hole-doped BaFe₂As₂’. *Nature Physics* (2012), vol. 8: p. 331–337 (cit. on p. 68).
- [Wie94] Wiesendanger, R.: *Scanning Probe Microscopy and Spectroscopy: Methods and Applications*. Cambridge University Press, 1994 (cit. on p. 25).
- [Wil75] Wilson, K. G.: ‘The renormalization group: Critical phenomena and the Kondo problem’. *Rev. Mod. Phys.* (1975), vol. 47(4): p. 773–840 (cit. on pp. 68, 121).
- [Yu65] Yu, L.: ‘Bound state in superconductors with paramagnetic impurities’. *Acta Physica Sinica* (1965), vol. 21(1), 75: p. 75 (cit. on p. 29).

- [Zee03] Zee, A.: *Quantum Field Theory in a Nutshell*. Nutshell handbook. Princeton, NJ: Princeton Univ. Press, 2003 (cit. on p. 113).
- [Zha00] Zhang, C. J. and P. Hu: ‘Why Must Oxygen Atoms Be Activated from Hollow Sites to Bridge Sites in Catalytic CO Oxidation?’ *Journal of the American Chemical Society* (2000), vol. 122(9): p. 2134–2135 (cit. on p. 31).
- [Zha16] Zhang, G., E. Gorelov, E. Sarvestani, and E. Pavarini: ‘Fermi Surface of Sr_2RuO_4 : Spin-Orbit and Anisotropic Coulomb Interaction Effects’. *Phys. Rev. Lett.* (2016), vol. 116(10): p. 106402 (cit. on pp. 79, 92).
- [Zha17] Zhang, G. and E. Pavarini: ‘Mott transition, spin-orbit effects, and magnetism in Ca_2RuO_4 ’. *Phys. Rev. B* (2017), vol. 95(7): p. 075145 (cit. on p. 79).
- [Zha13] Zhang, Y., S. Kahle, T. Herden, C. Stroh, M. Mayor, U. Schlickum, M. Ternes, P. Wahl, and K. Kern: ‘Temperature and magnetic field dependence of a Kondo system in the weak coupling regime’. *Nature Communications* (2013), vol. 4: p. 2110 (cit. on pp. 147, 150, 151).
- [Zha05] Zhao, A., Q. Li, L. Chen, H. Xiang, W. Wang, S. Pan, B. Wang, X. Xiao, J. Yang, J. G. Hou, and Q. Zhu: ‘Controlling the Kondo Effect of an Adsorbed Magnetic Ion Through Its Chemical Bonding’. *Science* (2005), vol. 309(5740): p. 1542–1544 (cit. on p. 158).
- [Zhu10] Zhu, Z.-G., K.-H. Ding, and J. Berakdar: ‘Single- or multi-flavor Kondo effect in graphene’. *EPL (Europhysics Letters)* (2010), vol. 90(6): p. 67001 (cit. on p. 98).
- [Zhu04] Zhuravlev, A. K., V. Yu. Irkhin, M. I. Katsnelson, and A. I. Lichtenstein: ‘Kondo Resonance for Orbitally Degenerate Systems’. *Phys. Rev. Lett.* (2004), vol. 93(23): p. 236403 (cit. on p. 125).
- [Zin16] Zingl, M., E. Assmann, P. Seth, I. Krivenko, and M. Aichhorn: ‘Importance of effective dimensionality in manganese pnictides’. *Phys. Rev. B* (2016), vol. 94(4): p. 045130 (cit. on p. 70).

Acronyms

AFM atomic force microscopy
AIM Anderson impurity model
AMF around **MF**
ASSCF active-space self-consistent field

BCA Bader charge analysis
BZ Brillouin zone

CC constant-current
cDFT constrained **DFT**
cDMFT cluster **DMFT**
CDW charge density wave
CF crystal field
CI configuration interaction
cRPA constrained **RPA**
CTHYB continuous-time hybridization expansion
CTQMC continuous-time quantum Monte Carlo

DC double counting
DFT density functional theory
DMFT dynamical mean-field theory
DMRG density-matrix renormalization group
DOF degrees of freedom
DOS density of states

ED exact diagonalization
EDMFT extended **DMFT**
EEI electron-electron interaction
EV eigenvalue

FL Fermi liquid
FLAPW full-potential linearized augmented plane-wave
FLL fully localized limit

GEA gradient expansion approximation
GF Green's function
GGA generalized gradient expansion
GS ground state

GWA *GW* approximation

HEG homogeneous electron gas

HF Hartree-Fock

HFQMC Hirsch-Fye **QMC**

HI iterative Hirshfeld

HK Hohenberg-Kohn

IHEG inhomogeneous electron gas

KB Kadanoff-Baym

KS Kohn-Sham

LDA local density approximation

LDOS local **DOS**

LSDA local spin density approximation

LSP line-shape parameter

LW Luttinger-Ward

MAE magnetic anisotropy energy

MBD many-body dispersion

ME many-electron

MEM maximum entropy method

MF mean-field

MLWF maximally localized Wannier function

NCA non-crossing approximation

NRG numerical renormalization group

OCA one-crossing approximation

PAW projector augmented wave

PBE Perdew, Burke, and Ernzerhof

PES potential energy surface

PP pseudopotential

PT perturbation theory

PW plane wave

PW91 Perdew-Wang 91

QED quantum electrodynamics

QI quantum impurity

QMC quantum Monte Carlo

QP quasi-particle

RDFT relativistic **DFT**

RG renormalization group

RKS relativistic **KS**

RPA random phase approximation

SC

SC superconductivity

SC superconductor

SC superconducting

SCS self-consistent screening

SDW spin density wave

SOC spin-orbit coupling

SOM stochastic optimization method

SSM stochastic sampling method

STM scanning tunnelling microscopy

STS scanning tunnelling spectroscopy

SW Schrieffer-Wolff

TDFT time-dependent [DFT](#)

TF Thomas-Fermi

TH Tersoff-Hamann

TM transition metal

TRIQS Toolbox for Research on Interacting Quantum Systems

TS Tkatchenko-Scheffler

UV ultraviolet

VASP Vienna *ab-initio* simulation package

vdW van der Waals

VEV vacuum expectation values

WF wave function

XC exchange-correlation

YSR Yu-Shiba-Rusinov

List of Figures

| | | |
|------|---|-----|
| 2.1 | Experimental STM topographies of the Ta(001)-p(3×3)-O surface at various voltages. Schema of the Ta(001)-p(3×3)-O surface. Notion definition. . . . | 35 |
| 2.2 | Schemata of the p(3×3)-O reconstruction of the Ta(001) surface. Simulated STM topographies of the two superstructures. | 35 |
| 2.3 | Experimental dI/dV image of the Ta(001)-p(3×3)-O surface. 2D representation of dI/dV spectra. Local dI/dV spectra. Total LDOS | 36 |
| 2.4 | Bader charges of the Ta(001)-p(3×3)-O surface. | 37 |
| 2.5 | Experimental dI/dV images of the Ta(001)-p(3×3)-O surface at various voltages. Simulated dI/dV images of the Ta(001)-p(3×3)-O surface at various voltages. | 43 |
| 2.6 | Orbital hybridization structures of oxygens within the Ta(001)-p(3×3)-O surface. | 45 |
| 2.7 | Orbital-resolved LDOS of the Ta(001)-p(3×3)-O surface in state I. | 45 |
| 2.8 | Orbital-resolved LDOS of the Ta(001)-p(3×3)-O surface in state II. | 46 |
| 2.9 | Orbital-resolved and partially summed LDOS of the Ta(001)-p(3×3)-O surface at the central Ta atom. Total LDOS in empty spheres above the surface. | 47 |
| 2.10 | Dispersion coefficients of the Ta(001)-p(3×3)-O surface. | 61 |
| 3.1 | Representation-resolved imaginary part of the real-frequency hybridization function for the Co/graphene system. Representation-resolved partial DOS . Matsubara hybridization function. | 103 |
| 3.2 | Fit of DFT hybridization function of the Co/graphene system for the ED | 104 |
| 3.3 | Coulomb matrix of the Co/graphene system obtained from cRPA . Comparison to its Slater approximation. | 105 |
| 3.4 | Comparison of representation-resolved imaginary-time GFs for the Co/graphene system obtained with the cRPA and with the Slater-Coulomb matrix, both at two Co fillings. Atomic solutions for each included as insets. Comparison of representation-resolved Matsubara self-energy for the Co/graphene system obtained with the cRPA and with the Slater-Coulomb matrix, both at higher Co filling. | 106 |

| | | |
|-----|---|-----|
| 3.5 | Comparison of representation-resolved spectral functions for the Co/graphene system obtained with the cRPA and with the Slater-Coulomb matrix, both at two Co fillings. Representation-resolved Matsubara self-energy for the Co/graphene system obtained with the cRPA Coulomb matrix at higher Co filling. Comparison between the AIM total spectrum (at two Co fillings) and DFT total LDOS | 107 |
| 3.6 | Comparison of representation-resolved spectral functions for the Co/graphene system obtained with QMC and with ED , both obtained with the cRPA Coulomb matrix at two Co fillings. Corresponding total DOS at two fillings. | 109 |
| 4.1 | STM image of Co adatoms and a Cu chain on Cu(111), and Co adatoms attached to the central part of the chain. dI/dV spectra of Co adatoms at three positions: on the (111) terrace, at the end of, and at the central part of a Cu chain. | 143 |
| 4.2 | Total DFT-LDOS of the Co d orbitals, and the conduction s and p orbitals, both of the Co adatom above the Cu(111) surface without, at the end of, and at the side of an fcc-positioned Cu chain. | 144 |
| 4.3 | Orbital-resolved and total DOSes of the Co adatom above the Cu(111) surface without, at the end of, and at the side of an fcc-positioned Cu chain. | 145 |
| 4.4 | Orbital-resolved hybridization functions for a Co adatom on the (111) terrace, at the end of a Cu chain, and at the central part of a Cu chain. | 147 |
| 4.5 | Orbital-resolved differential conductance dI/dV of a Co adatom on the (111) terrace, at the end of, and at the central part of a Cu chain. The Co and Cu atoms are located at fcc positions. Corresponding LSPs | 148 |
| 4.6 | Orbital Kondo parameters with the Co adatom on the (111) terrace, at the end of, and next to the Cu chain: QP weights Z , Kondo temperatures T_K rescaled by one order of magnitude, and orbital occupations n . DFT input for the AIM : energy levels ε , and hybridization strengths $\text{Im}[\Delta(0)]$ | 152 |
| 4.7 | Comparison of results obtained with AMF-DC and with FLL-DC : Total and orbital-resolved differential conductance dI/dV and orbital-resolved spectra A with the Co adatom on the (111) terrace, at the end of, and next to the chain. | 154 |
| 4.8 | Ground and excited state configurations of the Co adatom on the flat (111) terrace, at the end, and at the central part of the chain. | 155 |
| 4.9 | Comparison between the d_{z^2} spectral function of Co on the Cu(111) surface from the full five-orbital AIM with single-orbital AIM calculations having the same energy level and hybridization function for d_{z^2} , but with the other d orbitals switched off, and the chemical potential adjusted to attain half-filling: Hubbard bands, and a zoom into the low-energy region. | 156 |

List of Tables

| | |
|---|-----|
| 2.1 Superstructure parameters and total/adsorption energies of the Ta(001)-p(3×3)-O surface. | 41 |
| 2.2 Bader charge parameters of the Ta(001)-p(3×3)-O surface. | 42 |
| 2.3 Structural and Bader charge parameters of the TaO ₂ molecule. | 43 |
| 2.4 Superstructure parameters and total/adsorption energies of the Ta(001)-p(3×3)-O surface within vdW-DFT. | 55 |
| 2.5 Hirshfeld charge parameters of the Ta(001)-p(3×3)-O surface. | 57 |
| 2.6 Dispersion coefficients of the Ta(001)-p(3×3)-O surface. | 60 |
| 3.1 Local occupations and CF splittings of the Co/graphene system. | 102 |
| 3.2 DC values for the cRPA and the Slater-Coulomb matrix. | 106 |
| 3.3 Total and representation-resolved Co occupations, GS energies, and EVs of the local Hamiltonian for both, the impurity and the atomic, problems. | 108 |
| 3.4 Total and representation-resolved orbital charge and spin fluctuations, and effective masses of the Co/graphene system. | 109 |
| 4.1 Orbital Kondo temperatures T_K , and their averages. Orbital and total occupations n and N_{tot} , orbital QP weights Z , hybridization strengths $-\text{Im}[\Delta(0)]$, and energies ε | 151 |

A Beyond spin-DFT and DFT+ U

A.1 Current in DFT

Even though it has not been used in any of the projects and calculations reported in the present thesis, but as it serves for the completeness of the theoretical background, we will shortly digress into current- and spin-DFT as defined by Vignale and Rasolt [Vig88]. But first we make contact with some physical objects which could be described by current- and spin-DFT, and find their relevance for the Ta(001)-p(3×3)-O surface to be presented in Secs. 2.3, 2.4, and 2.6.

An electronic current might exist if there is an inhomogeneous charge distribution present in the material system [Gra13]. In principle this applies for CDWs in which currents with opposite momenta form standing waves [Frö54]. If the CDW is incommensurate, that is, if its wavelength is not a rational or integer multiple of the lattice constant, it might move itself (together with the lattice distortion). Usually, however, CDWs are pinned to impurities present in the system, and as was shown for the TM trichalcogenide NbSe₃, for incommensurate CDWs to move, often an electric field has to be applied above a certain threshold value which can lead to depinning [Grü81].

CDWs (but not charge transport) can in principle be described by DFT extended as to include phonon vibrations of the lattice, as was shown for the TM dichalcogenide TiSe₂ [Duo15]. Below the Peierls transition temperature the phonon mode of wave vector $2k_F$, which couples electrons at the Fermi surface moving in different directions, becomes macroscopically occupied and freezes out, so that a static regular lattice distortion emerges, eventually leading to the CDW [Bar90; Pei30]. The CDW is accompanied by the appearance of a band gap at the Fermi surface due to the transfer of normal electrons into the CDW, which renders the system insulating. Even though most of the original papers considered the CDW mechanism as a possible explanation of SC, it thus turned out that the underlying electron-phonon coupling leads to a rather different behaviour. Then the question remains whether CDWs cooperate or compete with the SC order, as many systems for which the CDWs are observed also superconducting [Cha12; Cho18; Jat18; Lia18]. The coupling of both phenomena is still under active investigation, and both scenarios seem to be realizable in the same system, depending on the degree of disorder, as shown for NbSe₂ [Cho18]. – A review on CDWs and their dynamics is provided in Ref. [Grü88]; a particular realization of the one-dimensional CDW pertaining to the original Peierls theorem is reported in Ref. [Kom17].

The amplitudes of the lattice distortions and CDWs are usually rather small (corresponding to the small band gap), and they appear only in one-dimensional or layered systems which admit nesting vectors in two-dimensional BZ (see, however, Ref. [Joh08] for counter-arguments to the nesting-vector concept). But CDWs may occur also in larger magnitudes at surfaces due to the bulk termination and local charge accumulation, and they are accompanied by reconstruction of the surface into superstructures. This is also the

case for the Ta(001)-p(3×3)-O surface investigated in Secs. 2.4 and 2.6. Reconstructions of surfaces show an abundance of patterns, sometimes with surface CDWs different in symmetry than the corresponding ones in the bulk [Che18].

Usually, one should perform density functional PT or use some other extended DFT for the inclusion of phonon modes which may eventually lead to CDWs [Duo15; Hei13; Lüd05; Tog15]. In this setup one can also determine the Peierls transition temperature [Duo15]. But CDW behaviour can also be described within usual DFT, as shown for Ta-based TM dichalcogenides [Mil18]. As mentioned in Sec. 2.4 presenting the project results on the Ta(001)-p(3×3)-O surface, DFT yields a rather metallic description of the surface even though experiments show the surface being an insulator. However, the simulations point in many aspects to the insulating behaviour if one looks at the results from the BCA, which reveal a pronounced charge accumulation and immobilization at oxygen locations. The charge order, which is connected to the surface reconstruction, admits an interpretation in terms of a CDW accompanied by insulating behaviour of the surface. One can furthermore see in the DOS of the surface and subsurface layers (latter not shown in Sec. 2.4), along which path within the surface the lone pairs on oxygens induce static dipoles on the Ta surface atom in the centre of the (square-shaped) 3×3 plaquettes of the superstructure formation, even though they are not neighbouring each other. Long-range effects are not contained in DFT due its local approximation, yet it mimics them indirectly via such paths as it still contains within its self-consistency some non-local dependence of the KS orbitals on the electronic density.

The magnetic analogue of CDWs are SDWs, which may also appear in incommensurate order and are at least quasi-one-dimensionally arranged. The prototypical example of a SDW material is chromium below its Néel temperature of 311 K [Bih00; Faw88]. The Cr(001) surface was also discussed in the context of the orbital Kondo effect by employing the DMFT machinery [Kol02; Kol05; Sch16] (see also Chpt. 4, and here Sec. 4.5.3). SDWs are discussed in the context of high- T_c SC, where spin-flip excitations induced by a moving electron can attract another electron resulting in Cooper pairing [Dai15]. Still, as mentioned in Sec. 2.1.3, like magnons these spin-flip excitations are to be distinguished from SDWs, as the latter belong to the itinerant magnetism of the material in its GS. The proposal to describe high- T_c SC with such spin flips is based on the observation that all these superconductors are also SDW materials, and an associated excitation mechanism could be given within the resonating valence bond theory, see Refs. [And13; Bas09; Dal14; Man11] and references therein.

In general, there exists neither spin nor current densities without an external magnetic field due to time-reversal invariance. However, there might be a broken symmetry present in the system, such as spin-symmetry breaking leading to ferromagnetism, or current-symmetry breaking in open-shell atoms (i.e., atoms with an incompletely filled valence shell) leading to current and spin-current densities appearing in the GS [Vig88]. Particular examples are just given by incommensurate CDWs and SDWs. Any form of current leads to itinerant magnetization within the system, be it polarization or magnetization currents due to movement or circulation of electric or magnetic dipole moments, respectively, or free currents. The theory for orbital magnetization in infinitely extended systems was established only recently and is reviewed in Ref. [Tho11], and the theory for electronic

polarization in Ref. [Spa12]. Instead of going into this topic here, we assume to have enough motivation for the definition of a current-DFT, which encompasses all kinds of currents, be they located and circulating, or free and traversing the system (cf. remarks after Eq. (A.39)). Furthermore, the second main motivation for its presentation is to see how causality eventually re-emerges in taking the current density into account. This becomes more important in TDFT where the XC potential is time-dependent and contains retardation effects, which implies yet another non-locality next to the usual one due to non-local correlations already present in time-independent DFT [Vig06]. While the latter can be cured by the local density approximations (with some non-local effects taken into account by the DFT self-consistency), the former signifies that charge and spin densities as basic variables are not sufficient for retardation to be respected, and additionally current and spin-current densities need to be considered instead. However, while in current- and spin-DFT as to be developed in this section the introduction of the currents yields the coupling to *external* electromagnetic potentials along with corresponding magnetism, causality and retardation are actually fully restored only by taking into account the current-current interaction (along with the instantaneous Coulomb interaction) resulting from the electron-photon coupling in QED (Appx. A.2). – We would also like to note at this point that SC pertains to a current in the system, and actually needs a current-DFT description as well [Hig17]. However, SC results from electron-phonon coupling, and is usually addressed within Eliashberg theory [Umm13].

The first formulation of DFT including the current density generated by strong external magnetic fields was given by Vignale and Rasolt in Ref. [Vig87]. The main result was an explicit expression for the part of the XC functional depending on the paramagnetic current density $\mathbf{j}_p(\mathbf{r})$, which will be given Eq. (A.9) for the generalization of current-DFT to include spin. The explicit form follows from gauge invariance and vice versa, and results in the dependence $E_{xc}[n, \mathbf{j}_p] = \bar{E}_{xc}[n, \mathbf{v}]$, where $\mathbf{v}(\mathbf{r}) = \nabla \times \mathbf{j}_p(\mathbf{r})/n(\mathbf{r})$. The proof of gauge invariance and the continuity relation needed a special treatment within the DFT one-particle approximation. Furthermore, one has to use the paramagnetic current density instead of the physical one as the basic variable (cf. Eq. (A.3)), as this is the one which happens to be conjugate to the external vector potential (i.e., it determines the external vector potential in the sense of the generalized HK theorem I). The use of non-gauge-invariant, unphysical quantities is rooted in the non-relativistic approximation, and the decomposition of the Hamiltonian into the part describing the electronic system itself and the one providing the coupling to the external fields. Finally, they found the dependence of the XC potential on $\mathbf{v}(\mathbf{r})$ advantageous, for in this variable a local approximation can be defined, while there is no such approximation for the paramagnetic current density $\mathbf{j}_p(\mathbf{r})$.

The current-DFT for the charge and current density was subsequently extended by Vignale and Rasolt to include the spin and spin-current density [Vig88]. The Hamiltonian in the collinear case (the non-collinear case is analogous) with external electromagnetic potentials is written as

$$\hat{H} = \hat{H}_0 + \sum_{\sigma} \int d\mathbf{r} \left[\hat{n}_{\sigma}(\mathbf{r}) V'_{\text{ext},\sigma}(\mathbf{r}) + \hat{\mathbf{j}}_{p\sigma}(\mathbf{r}) \mathbf{V}_{\sigma}(\mathbf{r}) + \frac{1}{2} \hat{n}_{\sigma}(\mathbf{r}) \mathbf{V}_{\sigma}^2(\mathbf{r}) \right], \quad (\text{A.1})$$

with \hat{H}_0 containing the kinetic energy and Coulomb interactions of the electrons. The external electric and magnetic fields are given by the relations $V_{\text{ext}}(\mathbf{r}) = \frac{1}{2}[V'_{\text{ext},\uparrow}(\mathbf{r}) + V'_{\text{ext},\downarrow}(\mathbf{r})]$ and $\mu_B \hbar B(\mathbf{r}) = \frac{1}{2}[V'_{\text{ext},\uparrow}(\mathbf{r}) - V'_{\text{ext},\downarrow}(\mathbf{r})]$, and they couple to the charge and spin densities, respectively (cf. again remarks after Eq. (A.39)). The external vector potential is subject to the condition $\mathbf{V}_{\uparrow}(\mathbf{r}) = \mathbf{V}_{\downarrow}(\mathbf{r}) = \mathbf{V}(\mathbf{r})$, with $\hat{\mathbf{z}}B(\mathbf{r}) = \nabla \times \mathbf{V}(\mathbf{r})$, and $\hat{\mathbf{z}}$ being the quantization axis. As before, the density components are $\hat{n}_{\sigma}(\mathbf{r}) = \hat{\psi}_{\sigma}^{\dagger}(\mathbf{r})\hat{\psi}_{\sigma}(\mathbf{r})$, and the paramagnetic current density is given by

$$\hat{\mathbf{j}}_{p\sigma}(\mathbf{r}) = -\frac{i}{2} \left[\hat{\psi}_{\sigma}^{\dagger}(\mathbf{r}) \nabla \hat{\psi}_{\sigma}(\mathbf{r}) - \nabla \hat{\psi}_{\sigma}^{\dagger}(\mathbf{r}) \hat{\psi}_{\sigma}(\mathbf{r}) \right]. \quad (\text{A.2})$$

The physical current density comprises the paramagnetic and the diamagnetic current,

$$\hat{\mathbf{j}}_{\sigma}(\mathbf{r}) = \hat{\mathbf{j}}_{p\sigma}(\mathbf{r}) + n_{\sigma}(\mathbf{r}) \mathbf{V}_{\sigma}(\mathbf{r}). \quad (\text{A.3})$$

For the gauge invariance of the Hamiltonian to be ensured, only the paramagnetic current density has to appear in it. Still, it is the physical current density with which the density obeys the continuity relations for charge and spin (as an equation for DFT variables, not operators),

$$\frac{\partial n_{\sigma}(\mathbf{r}, t)}{\partial t} + \nabla \cdot \mathbf{j}_{\sigma}(\mathbf{r}, t) = 0. \quad (\text{A.4})$$

The universal functional $F[n_{\sigma}, \mathbf{j}_{p\sigma}]$ ($\equiv F[n_{\uparrow}, n_{\downarrow}, \mathbf{j}_{p,\uparrow}, \mathbf{j}_{p,\downarrow}]$) is given by the GS expectation value

$$F[n_{\sigma}, \mathbf{j}_{p\sigma}] = \langle \Psi_0[n_{\sigma}, \mathbf{j}_{p\sigma}] | \hat{H}_0 | \Psi_0[n_{\sigma}, \mathbf{j}_{p\sigma}] \rangle, \quad (\text{A.5})$$

and the implementation of the correspondingly generalized HK theorems yields the KS potential

$$V_{\text{KS},\sigma}[n_{\sigma}](\mathbf{r}) = V'_{\text{ext},\sigma}(\mathbf{r}) + V_{\text{H},\sigma}[n_{\sigma}](\mathbf{r}) + V_{\text{xc},\sigma}[n_{\sigma}](\mathbf{r}) \quad (\text{A.6})$$

$$+ \frac{1}{2} \left[\mathbf{V}_{\sigma}^2(\mathbf{r}) - \{ \mathbf{V}_{\sigma}(\mathbf{r}) + \mathbf{V}_{\text{xc},\sigma}[n_{\sigma}, \mathbf{j}_{p\sigma}](\mathbf{r}) \}^2 \right], \quad (\text{A.7})$$

with the XC external vector potential given by

$$\mathbf{V}_{\text{xc},\sigma}[n_{\sigma}, \mathbf{j}_{p\sigma}](\mathbf{r}) = \frac{\delta E_{\text{xc}}[n_{\sigma}, \mathbf{j}_{p\sigma}]}{\delta \mathbf{j}_{p\sigma}(\mathbf{r})}. \quad (\text{A.8})$$

The XC functional in the high-density limit and until second order in the current density (or rather $\mathbf{v}^2(\mathbf{r})$) can be obtained by using results from linear response theory (see Ref. [Vig88] for details), and the result is

$$E_{\text{xc}}[n_{\sigma}, \mathbf{j}_{p\sigma}] = E_{\text{xc}}^{\text{LDA}}[n_{\uparrow}, n_{\downarrow}] + \sum_{\sigma} \int d\mathbf{r} \frac{k_{\text{F}\sigma}}{48\pi^2} \left(\frac{\chi_{L\sigma}}{\chi_{L\sigma}^0} - 1 \right) n_{\sigma}(\mathbf{r}) \left| \nabla \times \frac{\mathbf{j}_{p\sigma}(\mathbf{r})}{n_{\sigma}(\mathbf{r})} \right|^2. \quad (\text{A.9})$$

Here, $k_{F\sigma}$ is the Fermi momentum, and $\chi_{L\sigma}^{(0)}$ the spin- σ contribution to the orbital-magnetic susceptibility of the (non-)interacting electron gas (calculated within the RPA; Sec. 3.1). The second term contains the current-current interaction resulting from its coupling to the external electromagnetic field, the contributions of which are contained in the susceptibility (this is somewhat analogous to the Eqs. (A.31) and (A.33) for the current-current interaction in QED), and its form is in compliance with gauge invariance. The current-current interaction serves to restore causality (i.e., it incorporates the retardation effects), which is broken by only taking into account charge density and instantaneous Coulomb interaction along with coupling of the spin density to the external magnetic field [Kle09; Vig06]. The result is valid for slowly varying currents, that is, $|\nabla \times \mathbf{j}_{p\sigma}|/|\mathbf{j}_{p\sigma}| \ll k_{F\sigma}$ (cf. Eq. (2.31)).

The results could have been obtained in the non-relativistic limit from the full relativistic QED Hamiltonian (e.g., by a Foldy-Wouthuysen transformation, cf. Appx. A.2) containing the interaction part

$$\hat{H}_{\text{ext}} = \int d\mathbf{r} \hat{j}_\mu(\mathbf{r}) V_{\text{ext}}^\mu(\mathbf{r}), \quad \hat{j}^\mu(\mathbf{r}) = \hat{\psi}(\mathbf{r}) \gamma^\mu \hat{\psi}(\mathbf{r}). \quad (\text{A.10})$$

In principle, the electromagnetic field has to be treated classically to prevent electron-positron annihilation, and their subsequent recombination into the QED vacuum. As always in the relativistic context, one has the possibility for manifest causality and gauge invariance, for example, the $\mathbf{V}_\sigma^2(\mathbf{r})$ term would not appear in the Hamiltonian. However, the disadvantage is the need for renormalization procedures to treat the divergencies appearing in four-dimensional PT.

A.2 Relativistic DFT

As mentioned in the introduction (Chpt. 1), condensed matter systems can in the most general context be described by bound-state QED. QED is the merger of special relativity and quantum field theory for (U(1)-)charged particles interacting via the electromagnetic field. Considering the interacting system in QED at zero temperature, we know that this many-body system in its GS can be described (at least formally) completely by DFT. Within this section we closely follow the exposition of RDFT in Ref. [Eng02]. As the present section contains only the results needed to understand causality, and eventually the emergence of the SOC from the relativistic context, the reader is referred to Ref. [Eng02] and the references therein for more details on RDFT.

The Lagrangian for the electrons reads

$$\mathcal{L}_e(x) = \hat{\psi}(x) (ic\gamma_\mu \partial^\mu - mc^2) \hat{\psi}(x), \quad (\text{A.11})$$

and the one for the electromagnetic field

$$\mathcal{L}_\gamma(x) = -\frac{1}{16\pi} \hat{F}_{\mu\nu}(x) \hat{F}^{\mu\nu}(x) - \frac{\lambda}{8\pi} \left(\partial_\mu \hat{A}^\mu(x) \right)^2, \quad \hat{F}_{\mu\nu}(x) = \partial_\mu \hat{A}_\nu - \partial_\nu \hat{A}_\mu. \quad (\text{A.12})$$

The interaction between the two is

$$\mathcal{L}_{\text{int}}(x) = -e\hat{j}^\mu(x)\hat{A}_\mu(x), \quad \hat{j}^\mu(x) = \hat{\psi}(x)\gamma^\mu\hat{\psi}(x), \quad (\text{A.13})$$

and the electrons are subject to some classical time-independent external potential,

$$\mathcal{L}_{\text{ext}}(x) = -e\hat{j}^\mu(x)V_\mu(\mathbf{r}). \quad (\text{A.14})$$

The fields $\hat{\psi}(x)$ in this section denote Dirac spinor fields, and γ^μ , $\mu = 0, \dots, 3$, are the Dirac gamma matrices. For comparability to the non-relativistic limit, m , c , e have been reintroduced in this section, but $\hbar = 1$ is retained. Einstein summation is employed with metric signature $(+, -, -, -)$, and $x = (t, \mathbf{r})$ (written opposite to the non-relativistic notion (\mathbf{r}, t)). If the external potential arises from positive charges (e.g., ions), one may equivalently describe them with their own Lagrangian, and let them interact with the electrons via their own coupling to the photon field. We shall follow the viewpoint of Eq. (A.14), where the electrons move in the classical external electromagnetic potential of the (spatially fixed) ions (Born-Oppenheimer approximation), and perhaps some other time-independent external fields. For example, the spatial part of the four-potential V^μ may include the ionic magnetic moments. The second term in Eq. (A.12) is the gauge-fixing term within the Gupta-Bleuler quantization approach of the photon field (λ being the gauge-fixing parameter) [Ble50; Gre96; Gup50]. This term is needed for the canonical quantization procedure, that is, for the definition of equal-time commutation relations between $A^\mu(x)$ and its conjugate momenta $\pi^\mu(x)$. The classical Lorentz gauge condition $\partial_\mu A^\mu(x) = 0$ cannot be satisfied as an operator equation (a quantum anomaly), only its expectation values are admitted to obey that condition, that is, $\langle \partial_\mu \hat{A}^\mu(x) \rangle = 0$. But this is sufficient to eliminate the unphysical time-like and longitudinal polarization components of the photon field.

The invariance of the Lagrangian with respect to local gauge transformations of the photon field yields the current conservation,

$$\partial_\mu \hat{j}^\mu(x) = 0, \quad (\text{A.15})$$

from which follows the conservation of the total charge

$$\hat{Q} = \int d\mathbf{r} \hat{j}^0(x) = \int d\mathbf{r} \hat{\psi}^\dagger(x)\hat{\psi}(x). \quad (\text{A.16})$$

The canonical energy-momentum tensor follows from Noether's theorems via invariance of the QED action under spatio-temporal translations, and it has the form

$$\begin{aligned} \hat{\Theta}_{\mu\nu}(x) = & \hat{\psi}(x) [ic\gamma_\mu\partial_\nu - g_{\mu\nu} (ic\gamma^\rho\partial_\rho - mc^2)] \hat{\psi}(x) \\ & - \frac{1}{4\pi} \left\{ \hat{F}_{\mu\rho}(x)\partial_\nu\hat{A}^\rho(x) + \lambda \left(\partial_\rho\hat{A}^\rho(x) \right) \partial_\nu\hat{A}_\mu(x) \right. \\ & \left. - g^{\mu\nu} \left[\frac{1}{4}\hat{F}_{\rho\sigma}(x)\hat{F}^{\rho\sigma}(x) + \frac{\lambda}{2} \left(\partial_\rho\hat{A}^\rho(x) \right)^2 \right] \right\} \end{aligned}$$

$$+ g_{\mu\nu} e \hat{j}^\rho(x) \left(\hat{A}_\rho(x) - V_\rho(\mathbf{r}) \right). \quad (\text{A.17})$$

The energy-momentum tensor in this form is neither symmetric nor gauge-invariant, but we do not need the symmetrized Belinfante-Rosenfeld version for our purposes [Gre96]. From Eq. (A.17) one derives the continuity equation for the energy-momentum tensor,

$$\partial^\mu \hat{\Theta}_{\mu\nu}(x) = e \hat{j}^\rho(x) \partial_\nu V_\rho(\mathbf{r}). \quad (\text{A.18})$$

The inhomogeneity on the right-hand side tells that the external potential acts as a source field. Its time-independence yields the equation

$$\partial^\mu \hat{\Theta}_{\mu 0}(x) = 0, \quad (\text{A.19})$$

and performing a spatial integral yields the energy conservation and the definition of the Hamiltonian in the Feynman gauge with $\lambda = 1$,

$$\hat{H} = \hat{H}_e + \hat{H}_\gamma + \hat{H}_{\text{int}} + \hat{H}_{\text{ext}} \quad (\text{A.20})$$

$$\hat{H}_e = \int d\mathbf{r} \hat{\psi}^\dagger(x) (-i c \boldsymbol{\alpha} \boldsymbol{\partial} + \beta m c^2) \hat{\psi}(x) \quad (\text{A.21})$$

$$\hat{H}_\gamma = e \int d\mathbf{r} \left[\left(\partial^0 \hat{A}_\mu(x) \right) \left(\partial^0 \hat{A}^\mu(x) \right) + \boldsymbol{\partial} \hat{A}_\mu(x) \cdot \boldsymbol{\partial} \hat{A}^\mu(x) \right] \quad (\text{A.22})$$

$$\hat{H}_{\text{int}} = e \int d\mathbf{r} \hat{j}^\mu(x) \hat{A}_\mu(x) \quad (\text{A.23})$$

$$\hat{H}_{\text{ext}} = e \int d\mathbf{r} \hat{j}^\mu(x) \hat{V}_\mu(\mathbf{r}). \quad (\text{A.24})$$

Here, $\beta = \gamma^0$, $\boldsymbol{\alpha} = \gamma^0 \boldsymbol{\gamma}$, and the usual nabla is denoted in this section by a bold partial because nabla in the relativistic context denotes the covariant derivative. As often the case in quantum field theories, renormalization procedures are needed due to the appearances of divergencies in the perturbation expansion based on the Hamiltonian in Eq. (A.20). Here, renormalization includes the subtraction of negative-energy contributions leading to divergent **vacuum expectation values (VEVs)** (within interacting **QED** without the external field), and the removal of **ultraviolet (UV)** divergencies, which includes the redefinition of the parameters of the theory, such as the electronic charge, and leads to the appearance of counterterms. The total **GS** energy and **GS** current are then given by

$$E_{\text{tot}} = \langle \Psi_0 | \hat{H} | \Psi_0 \rangle - \langle 0 | \hat{H}_e + \hat{H}_\gamma + \hat{H}_{\text{int}} | 0 \rangle + \Delta E_{\text{tot}} \quad (\text{A.25})$$

$$j^\mu(\mathbf{r}) = \langle \Psi_0 | \hat{j}^\mu(x) | \Psi_0 \rangle + \Delta j^\mu(\mathbf{r}). \quad (\text{A.26})$$

Here, the **VEV** $\langle 0 | \dots | 0 \rangle$ in Eq. (A.25) subtract the divergencies due to the negative-energy states in interacting **QED** without the external field. The ones with the external field have the form of **UV** divergencies, and are included in the counterterms ΔE_{tot} and $\Delta j^\mu(\mathbf{r})$. $|\Psi_0\rangle$ is the interacting **GS** with the external field.

Already the non-relativistic spin-DFT does not fulfil the uniqueness property of the **HK**

theorem I, so that two different external potentials may lead to the same **GS** [Cap01]. For example, an external magnetic field which already fully polarizes a material will not change the charge and spin density if it becomes stronger. The probable invalidity of the **HK** theorem I, however, does not prevent the construction of a unique **GS** energy functional depending on the **GS** current density (**HK** theorem II). Important is the unique definition of the **GS** in terms of the current density, $|\Psi_0\rangle = |\Psi_0[j]\rangle$, up to a static (i.e., due to its time-independence non-dynamical) gauge transformation of the external potential (i.e., $V'_\mu(\mathbf{r}) = V_\mu(\mathbf{r}) + \partial_\mu \Lambda(x)$ with $\Lambda(x) = \text{const} \cdot t + \lambda(x)$ and $\square \lambda(x) = 0$). Fixing the gauge, a **GS** energy functional can be constructed on the basis of renormalization, which has subtracted the negative-energy contributions and thus renders the energy bounded from below,

$$E_{\text{tot}}[j] = \langle \Psi_0[j] | \hat{H} | \Psi_0[j] \rangle - \langle 0 | \hat{H}_e + \hat{H}_\gamma + \hat{H}_{\text{int}} | 0 \rangle + \Delta E_{\text{tot}}. \quad (\text{A.27})$$

What remains is the expression of the results obtained from the variational principle in terms of **relativistic KS (RKS)** particles $\phi_k(\mathbf{r})$ (here indexed by k instead of α (cf. Eq. (2.16))). Their kinetic energy is given by

$$T_s[j] = \sum_k \Theta_k \int d\mathbf{r} \phi_k^\dagger (-ic\boldsymbol{\alpha}\boldsymbol{\partial} + \beta mc^2) \phi_k(\mathbf{r}) + T_{s,v}[j], \quad (\text{A.28})$$

where

$$\Theta_k = \begin{cases} 0 & \text{for } \varepsilon_k \leq -mc^2 \\ 1 & \text{for } -mc^2 < \varepsilon_k \leq \varepsilon_F \\ 0 & \text{for } \varepsilon_f < \varepsilon_k, \end{cases} \quad (\text{A.29})$$

and $T_{s,v}[j]$ encompass vacuum contributions and counterterms. The energy from the coupling of the current density to the external potential retains the classical expression

$$E_{\text{ext}}[j] = e \int d\mathbf{r} j_\mu(\mathbf{r}) V^\mu(\mathbf{r}), \quad (\text{A.30})$$

with the current density as in Eq. (A.26). The Hartree energy is given in terms of the free photon propagator [Dre03]

$$\begin{aligned} D_{\mu\nu}^{(0)}(x-y) &= \langle 0_0 | \text{T} \hat{A}_\mu^{(0)}(x) \hat{A}_\nu^{(0)}(y) | 0_0 \rangle \\ &= g_{\mu 0} g_{\nu 0} \frac{e^2}{|\mathbf{r} - \mathbf{r}'|} \delta(t - t') + D_{\mu\nu}^{(0),\text{T}}(x-y), \quad (y = (t', \mathbf{r}')), \end{aligned} \quad (\text{A.31})$$

(with T the time ordering operator, and T denoting transversality) as

$$E_{\text{H}}[j] = \frac{1}{2} \int d\mathbf{r} d^4y j^\mu(\mathbf{r}) D_{\mu\nu}^{(0)}(x-y) j^\nu(\mathbf{r}'), \quad (\text{A.32})$$

which, using $j^\mu(\mathbf{r}) = (n(\mathbf{r}), \mathbf{j}(\mathbf{r})/c)$, can be decomposed into the Coulomb contribution as

seen in Eq. (2.10), that is, the classical Hartree term, and the transverse contribution (in the stationary case)

$$E_{\text{H}}^{\text{T}}[\mathbf{j}] = -\frac{e^2}{2c^2} \int d(\mathbf{r}, \mathbf{r}') \frac{\mathbf{j}(\mathbf{r}) \cdot \mathbf{j}(\mathbf{r}')}{|\mathbf{r} - \mathbf{r}'|}. \quad (\text{A.33})$$

The transverse part of the photon propagator $D_{\mu\nu}^{(0),\text{T}}(x-y)$ (which is space-like) contains retardation and magnetic effects. In the weakly relativistic limit, without the transverse part one obtains the so-called Dirac-Coulomb approximation, and with the transverse part the Dirac-Coulomb-Breit approximation. The **XC** term $E_{\text{xc}}[j]$, finally, is defined by the decomposition $E_{\text{tot}}[j] = T_s[j] + E_{\text{ext}}[j] + E_{\text{H}}[j] + E_{\text{xc}}[j]$. For a thorough discussion of the **XC** functional $E_{\text{xc}}[j]$ the reader is referred to Refs. [Dre03; Eng02]. One may note here that it can be approximately constructed analogously to the non-relativistic limit, but with this analogy already hampered by the fact that the relativistic homogeneous electron gas (RHEG) does not exhibit any currents, $\mathbf{j}^{\text{RHEG}}(x) = \mathbf{0}$.

In the non-relativistic current- and spin-DFT (Appx. A.1), the current-current interaction contained in the **XC** energy (Eq. (A.9)) is due to the presence of the external potentials, and do not originate from the **QED** electron-photon coupling. From the latter only the Coulomb part is taken into account in \hat{H}_0 , cf. Eq. (A.1). We will give a short account of that at the end of the present section. The inclusion of the current-current interaction in the transverse contribution to the Hartree energy, Eq. (A.33), leads to the full restoration of causality missing in the usual non-relativistic approaches [Kle09]. **RDFT** contains both current-current interactions, but the transverse contribution from the electron-photon coupling is of order $1/c^2$ and thus neglected in the non-relativistic approximation [Eng02].

Having set up the **RKS** system and the energy functional, one is now able to obtain the **RKS** equation from the minimum principle,

$$[-i c \boldsymbol{\alpha} \boldsymbol{\partial} + \beta m c^2 + \alpha_{\mu} V_{\text{RKS}}^{\mu}[j](\mathbf{r})] \phi_k(\mathbf{r}) = \varepsilon_k \phi_k(\mathbf{r}), \quad (\text{A.34})$$

with the **RKS** potential

$$V_{\text{RKS}}^{\mu}[j](\mathbf{r}) = e V_{\text{ext}}^{\mu}[j](\mathbf{r}) + V_{\text{H}}^{\mu}[j](\mathbf{r}) + V_{\text{xc}}^{\mu}[j](\mathbf{r}), \quad (\text{A.35})$$

where

$$V_{\text{H}}^{\mu}[j](\mathbf{r}) = e^2 \int d\mathbf{r}' \frac{j^{\mu}(\mathbf{r}')}{|\mathbf{r} - \mathbf{r}'|}, \quad V_{\text{xc}}^{\mu}[j](\mathbf{r}) = \frac{\delta E_{\text{xc}}[j]}{\delta j_{\mu}(\mathbf{r})}. \quad (\text{A.36})$$

The **RKS** equation describes the system of non-interacting Dirac particles in the presence of the effective **RKS** potential $V_{\text{RKS}}^{\mu}[j](\mathbf{r})$.

Having set up the **RKS** equation, it is now time to consider the physics it contains in some limits. As in most systems there is no external magnetic field applied, one may consider $\mathbf{B}_{\text{ext}}(\mathbf{r}) = \nabla \times \mathbf{V}(\mathbf{r}) = \mathbf{0}$. The external part of the **QED** Hamiltonian in Eq. (A.24)

thus assumes the form

$$\hat{H}_{\text{ext}} = e \int d\mathbf{r} \hat{j}^0(x) V^0(x) = \int d\mathbf{r} \hat{n}(\mathbf{r}) V_{\text{ext}}(\mathbf{r}). \quad (\text{A.37})$$

According to the **HK** theorem I, there now exists a unique correspondence between the external potential $V_{\text{ext}}(\mathbf{r})$, the **GS** $|\Psi_0\rangle$, and the **GS** density $n(\mathbf{r})$. The **XC** energy functional $E_{\text{xc}}[n]$ now depends on the charge and spin density only, and the transverse component of the Hartree energy $E_{\text{H}}^{\text{T}}[\mathbf{j}[n]]$ depends implicitly on the densities. As mentioned in Subsec. 2.1.3 (on spin-DFT), there might still be a magnetization present in the system also without an external magnetic field applied. Thus, a non-vanishing current density $\mathbf{j}[n] = \langle \Psi_0[n] | \hat{\mathbf{j}} | \Psi_0[n] \rangle$ might still exist because the magnetic moment does *a-priori* vanish only in closed-shell systems. It is this purely electrostatic case together with the so-called no-sea approximation (the neglect of all radiative corrections due to vacuum contributions) which is standardly used in quantum chemistry [Dre03].

Another approximation starts with the Gordon decomposition of the four-current density,

$$\begin{aligned} \bar{\psi}(x) \gamma^\mu \psi(x) &= \frac{i}{2mc} [\bar{\psi}(x) \nabla^\mu \psi(x) - (\nabla^\mu \bar{\psi}(x)) \psi(x)] \\ &\quad - \frac{e}{mc^2} \bar{\psi}(x) \psi(x) V^\mu(\mathbf{r}) + \frac{1}{2mc} \partial_\beta \bar{\psi}(x) \sigma^{\alpha\beta} \psi(x), \end{aligned} \quad (\text{A.38})$$

with ∇^μ the covariant derivative containing the gauge (electromagnetic) potential, and $\sigma^{\alpha\beta} = \frac{i}{2}[\gamma^\alpha, \gamma^\beta]$. The space-like component gives the current density in terms of its orbital/paramagnetic part, its diamagnetic part (describing the centre-of-mass motion), and the curl of the magnetization density

$$\frac{1}{c} \mathbf{j}(x) = \frac{1}{c} \mathbf{j}_p(x) - \frac{e}{mc^2} \bar{\psi}(x) \psi(x) \mathbf{V}(\mathbf{r}) - \frac{1}{e} \boldsymbol{\partial} \times \mathbf{m}(x), \quad (\text{A.39})$$

where the magnetization density is given by $\mathbf{m}(x) = -\mu_{\text{B}} \bar{\psi}(x) \boldsymbol{\Sigma} \psi(x)$, with $\boldsymbol{\Sigma} = \text{diag}(\boldsymbol{\sigma}, \boldsymbol{\sigma})$. The time-like component contains the spin densities (i.e., the charge and the spin density), the coupling to the external electric potential, and the divergence of the electric moment (polarization) density [Str98]. The Gordon decomposition here may be compared with Eq. (A.3), the one in the current- and spin-DFT (Appx. A.1), which contains the centre-of-mass motion only. The curl of the magnetization density in the collinear formulation is shifted within the Hamiltonian in Eq. (A.1) (the implicit term $\frac{1}{2}[n_\uparrow(\mathbf{r}) - n_\downarrow(\mathbf{r})][V'_\uparrow(\mathbf{r}) - V'_\downarrow(\mathbf{r})]$), in contrast to the non-collinear extension where the physical current density exhibits the curl of the magnetization density directly: it is the spin-current density [Str98; Vig88]. See also Ref. [Sun05] for a more thorough discussion of the various components contained in the four-current density (in particular, there are “linear” and angular parts describing translational and rotational (precessing) motions of the vectorial part). Spin-DFT itself neglects the orbital current and the gauge term, and the coupling of the curl of the magnetization density to the external vector field within the Hamiltonian yields by partial integration and $\mathbf{B}_{\text{ext}}(\mathbf{r}) = \boldsymbol{\partial} \times \mathbf{V}(\mathbf{r})$ the relativistic generalization of the Zeeman term $-\mu_{\text{B}} \mathbf{m}(\mathbf{r}) \mathbf{B}_{\text{ext}}(\mathbf{r})$. The variables for relativistic spin-DFT are given by n and \mathbf{m} .

Yet other approximations are given by the weakly relativistic and the non-relativistic limits. The first one is obtained by application of the Foldy–Wouthuysen transformation [Gre00], which is designed as to decouple the two bispinors within a Dirac spinor (which are coupled in the Dirac basis), because for a fixed sign of the energy one of them becomes larger than the other. The transformation is performed by an expansion up to certain orders of $1/mc^2$, and the result is

$$\begin{aligned} \hat{H} = \int d\mathbf{r} \hat{\psi}^+(x) & \left\{ \left[\frac{1}{2m} \left(\hat{\mathbf{p}} - \frac{e}{c} \left(\hat{\mathbf{A}}(x) + \mathbf{V}(\mathbf{r}) \right) \right)^2 + mc^2 - \frac{1}{8m^3c^2} \left(\hat{\mathbf{p}} - \frac{e}{c} \hat{\mathbf{A}} \right)^4 \right] \beta \right. \\ & + e \left(\hat{A}_0(x) + V_0(\mathbf{r}) \right) - \mu_B \boldsymbol{\Sigma} \left(\hat{\mathbf{B}}(x) + \boldsymbol{\partial} \times \mathbf{V}(\mathbf{r}) \right) \beta \\ & \left. + \frac{\mu_B}{4mc} \boldsymbol{\Sigma} \left(\hat{\mathbf{p}} \times \hat{\mathbf{E}}(x) \right) - \frac{\mu_B}{2mc} \boldsymbol{\Sigma} \left(\hat{\mathbf{E}}(x) \times \hat{\mathbf{p}} \right) - \frac{\mu_B}{4mc} \boldsymbol{\partial} \hat{\mathbf{E}}(x) \right\} \hat{\psi}(x). \end{aligned} \quad (\text{A.40})$$

Here, $\mathbf{p} = -i\boldsymbol{\partial}$, $A^\mu(x) = (A_0(x)/c, \mathbf{A}(x))$, and $V^\mu(\mathbf{r})$ analogously. The term in the first squared brackets is the expansion of the relativistic energy $[(\mathbf{p} - e(\mathbf{A} + \mathbf{V})/c)^2 + m^2]^{1/2}$ and describes the relativistic mass enhancement. Not all terms are shown. There follow the electrostatic energies, the Zeeman terms, the coupling between the spin and the rotation of the electric field \mathbf{E} (which, by the Maxwell equations, is the time derivative of the magnetic field \mathbf{B}), the SOC, and at last the Darwin term. The commonly known form of the SOC can be obtained for spherical potentials with $\mathbf{E} = -(\partial V/\partial r)\mathbf{r}/r$. The equation does not mix the two bispinors anymore. For the upper two-spinor, by neglecting all terms outside of the squared brackets of order $1/c$, while retaining inside the squared brackets only the first term, one obtains the non-relativistic Pauli equation for an electron in the presence of the electromagnetic and external fields. It is also by the Foldy–Wouthuysen transformation and its decoupling that the Hamiltonian of current- and spin-DFT in Eq. (A.1) can be obtained (just Eq. (A.40) additionally contains the electromagnetic field).

B The PAW formalism and the SOC

In view of the physics to be captured by **DFT**, the condensed matter system can be divided into three main parts: the nuclei of the ionic lattice, the core electrons located at the nuclei, and the valence and conduction electrons. The chemical bonding is mostly performed by the valence electrons, which thus are responsible for the geometric structure of the system, but also for its electronic and magnetic properties. The core electrons can be combined with the nuclei to form the ionic lattice, thus setting up an effective **pseudopotential (PP)** in which the valence and conduction electrons move [Sch13]. The combination of core electrons and nuclei into frozen cores greatly reduces the computational demands, which are now set by the **DFT** description of the valence and conduction electrons only.

The **PP** definition depends on the choice of which orbitals are treated as core and which as valence. In any case, the valence orbitals will be orthogonal to the core orbitals, which is mathematically realized by rapid oscillations and thus the many nodes of the valence **WFs**. These oscillations need to be near the localized core electrons, and are therefore less important for the chemical bonding. As they are also difficult to treat numerically, one can just define pseudo-**WFs**, which replace the original **KS-WFs** by some smoother and nodeless **WF** inside some augmentation sphere around the nuclei, but which are identical to the **KS-WFs** outside that sphere.

This simple construction results in problems with the transferability of the **PPs** and the just gained computational power [Kre99]: The transferability needs a sufficiently small core radius, for otherwise the usability of the augmentation spheres for the various condensed matter systems become too limited; but still the core radius must be at least around the outermost maximum of the **KS-WF**, for only then the charge distribution and moments are well-reproduced. But the reduced space for the strongly localized orbitals lead to large basis sets for the expansion of the **WFs** into **PWs**, which now increases again the computational demands. The basis set size can be reduced by increasing the core radius, but this would reduce again the transferability. Vanderbilt solved this problem by dropping the norm-conservation imposed on the **PPs**, but at the same time introducing localized atom-centred augmentation charges to balance the charge deficit [Van90].

In the **PAW** approach developed by Blöchl [Blö94], the **KS-WFs** are obtained from the computationally more convenient pseudo-**WFs** by the linear transformation

$$|\Psi_n\rangle = |\tilde{\Psi}_n\rangle + \sum_i (|\phi_i\rangle - |\tilde{\phi}_i\rangle) \langle \tilde{p}_i | \tilde{\Psi}_n \rangle. \quad (\text{B.1})$$

The index i comprises site and orbital indices. To make the computational results more sophisticated, one can include several **PWs** for the same site and orbital having different reference energies (also addressed by the index i). The **PWs** ϕ_i for the **KS-WF** are obtained for corresponding reference atoms, and the so-called projector functions \tilde{p}_i are defined via the orthogonality relation $\langle \tilde{p}_i | \tilde{\phi}_j \rangle = \delta_{ij}$, with $\tilde{\phi}_i$ the **PWs** for the pseudo-**WFs**. All **PWs** are

once and for all times fixed for both, **KS**- and pseudo-**WFs**, and the pseudo-**WFs** now become variational. The **PAW** transformation in Eq. (B.1) can be abbreviated by the operator $\hat{T} = 1 + \sum_{\mathbf{R}} \hat{T}_{\mathbf{R}}$, so locally one has within the augmentation spheres $|\phi_i\rangle = (1 + \hat{T}_{\mathbf{R}})|\tilde{\phi}_i\rangle$. The variational quantities are now the pseudo-**WFs** $|\tilde{\psi}_n\rangle$. – The **PAW** approach is used in **VASP** [Kre96], which was used throughout all projects reported on in the present thesis.

This formalism can naturally be extended to include non-collinear magnetism (Subsec. 2.1.3). Within the non-collinear formalism the density is a 2×2 matrix given by Eq. (2.36). A **KS** formalism can be written down as usual (with taking care of the complications mentioned in Subsec. 2.1.3), and the pseudo-**WFs** now acquire an additional spin index α , that is, $|\tilde{\psi}_n^\alpha\rangle$ [Hob00]. The **PAW** formalism then becomes appropriate for the inclusion of the **SOC**, Appx. A.2. The **SOC** Hamiltonian in **DFT** has the form [Ste16a]

$$\hat{H}_{\text{SOC}}^{\alpha\beta} = \frac{\hbar^2}{(2mc)^2} \frac{K(r)}{r} \frac{dV(r)}{dr} \hat{\sigma}^{\alpha\beta} \hat{\mathbf{L}}, \quad (\text{B.2})$$

with $K(r) = 1/[1 - V(r)/2mc^2]^2$, and $V(r)$ the spherical part of the **KS** potential (Sec. 2.1). This form of the **SOC** Hamiltonian can be transferred into

$$\hat{H}_{\text{SOC}}^{\alpha\beta} = \frac{\hbar^2}{(2mc)^2} \sum_{ij} |\tilde{p}_i\rangle R_{ij} \hat{\sigma}^{\alpha\beta} \hat{\mathbf{L}}_{ij} \langle \tilde{p}_j|, \quad R_{ij} = 4\pi \int_0^{r_c} dr R_i(r) \frac{K(r)}{r} \frac{dV(r)}{dr} R_j(r). \quad (\text{B.3})$$

One may see from this equation that the **SOC** parameter $\propto R_{ij}$ has a more complicated meaning in **DFT** as it becomes orbitally dependent (but only on l , not m , because the radial functions $R_i(r)$ do not depend on m). Furthermore, its physical meaning is actually reduced by the necessity to choose the **PP**, so one may say that the **SOC** parameter is even “gauge-dependent”. However, in the realistic **AIM** approach beyond **DFT** (with parameters determined from **DFT** without **SOC**), one can still extend the **AIM** by the **SOC** Hamiltonian with the **SOC** parameter as determined from **DFT**, because both, the **AIM** and **SOC** parameters, are eventually determined with the same **PP** and within the same **PAW** basis set.

As the **SOC** is effective locally, the corresponding modifications of the **AIM** can be assessed within its impurity part [Dai08]. In principle, the complicated multi-orbital structure will lift all degeneracies between the **ME** eigenstates. However, the **SOC** parameter is small, and quantum-mechanical **PT**, see Ref. [Sch13], shows that degeneracies may survive the **SOC** up to second order. Indeed, at first order one can see that the **SOC** Hamiltonian does not change the **GS** energies: their change is given by the matrix element $\lambda \langle g\mu | \hat{\mathbf{L}} \hat{\mathbf{S}} | g\mu' \rangle$, with g denoting the **GS** and μ counting its degeneracy d , and $\hat{\mathbf{L}}$ always maps to excited states, while $\hat{\mathbf{S}}$ maps to states within the same spin multiplet only. At second order the energies are modified via the Hamiltonian

$$\hat{H}_{\text{SOC}}^{(2)} = \lambda^2 \sum_{ab}^{\{x,y,z\}} \sum_{\mu\mu'=1}^d \hat{S}_a |g\mu\rangle \Lambda_{ab}^{\mu\mu'} \langle g\mu' | \hat{S}_b, \quad (\text{B.4})$$

where

$$A_{ab}^{\mu\mu'} = \sum_{i \neq g} \sum_{\nu=1}^{d_i} \frac{\langle g\mu | \hat{L}_a | i\nu \rangle \langle i\nu | \hat{L}_b | g\mu' \rangle}{\varepsilon_b - \varepsilon_i}, \quad (\text{B.5})$$

with ε_g and ε_i the ground and excited state energies, respectively. Knowing that the spin operator maps to states within a multiplet only, the GS Hamiltonian in Eq. (B.4) can be rewritten as a matrix product in the d -dimensional GS multiplet,

$$\underline{H}_{\text{SOC}}^{(2)} = \lambda^2 \sum_{ab}^{\{x,y,z\}} \underline{S}_a \underline{A}_{ab} \underline{S}_b \quad (\text{B.6})$$

Often it appears possible to focus on the diagonal directional components, and in this approximation one can read off the commonly known MAE parameters, $\underline{H}_{\text{SOC}}^{(2)} = E(\underline{S}_x^2 - \underline{S}_y^2) + D\underline{S}_z^2 - \frac{D}{3}\underline{S}^2$.

As mentioned in the introductory part to the present section, the SOC might lead to a modified Kondo scenario based on the MAE term in Eq. (B.4) [Ter09], and to the step-like appearance of the dI/dV as seen in Fig. 4.1. If the in-plane MAE parameter E is small, one can observe, for example, for a $S = 3/2$ system that the $S_z = \pm 1/2$ states are still degenerate, while they become energetically decoupled from the states with $S_z = 3/2$. If a tunnelling current with a bias equal to their energy difference is applied, an inelastic tunnelling channel opens up, and is seen as additional steps in the corresponding dI/dV spectra. This situation might apply to the case of the Co adatom at the central part of the chain, where according to the diagonalization of the local Hamiltonian the GS has $S = 3/2$ (Subsec. 4.6.8). As the states with $S_z = \pm 1/2$ are still degenerate, a Kondo resonance appears at the Fermi energy, which is decorated by the steps away from the Fermi energy. In the other configurations with $S = 1$, there is either not Kondo resonance any more, or only the orbital Kondo effect contributes, because one GS with $S_z = 0$ alone does not provide any degeneracy. – The situation becomes more complicated to discuss in case the other, or even all (Eq. (B.4)), MAE parameters are important. In principle, for a Kondo effect to surface, the diagonal components should be dominant, for otherwise the lifting of the degeneracies becomes too strong.

Another important ingredient in the theory is how the experiments are actually performed: the adatom-substrate system is put into subject to an external magnetic field, which additionally lifts the remaining degeneracies due to spin. In this way, the MAE and its magnetic-field dependence in different directions can be investigated. A further restructuring of the dI/dV spectrum can then be observed accordingly, for example, the splitting of the central Kondo peak in case of $S = 3/2$, in case the external magnetic field has a component perpendicular to the surface. The importance of an external magnetic field can theoretically be understood from its appearance at first order in quantum-mechanical PT. However, Eqs. (B.4) and (B.5) reveal that there is already a SOC already due to pure geometric reasons, that is, due to CF effects, which in certain systems might be comparable in strength as the energy separations between the eigenstates of the unperturbed local

Hamiltonian. This situation might apply to the $\text{CoCu}_n/\text{Cu}(111)$ systems, and a more detailed study would analyse the interplay between the [MAE](#) term and the symmetry breaking due to the different coordination environments.

C Luttinger-Ward functional and the DC correction

C.1 Exact DC correction

Having outlined the transition from **DFT** to the **AIM** to account for the local electronic correlations (Subsec. 3.2.1), there remains the issue of the **DC** problem to be clarified, that is, its general relevance. The **DC** term is needed to subtract the correlations already present in **DFT**, but which are fully accounted for by the post-**DFT** treatment as, for example, within **DFT+U** (Sec. 2.1.4). **DFT+U** still lies within the realm of **DFT**, that is, it is a static and **MF** approach, and describes the correlations between static deviations of orbital occupations from their **MF** values. For these the **DC** term can be computed as given in Eq. (2.51) for the **FLL-DC** (the **AMF-DC** is contained in Eq. (2.43)), and in nearly all other approaches to correlations beyond **DFT**, such as the **AIM** for correlated adatoms, molecules, or other nanosystems, or **DMFT** for the local correlations in bulk systems, one uses the same or related formulas. An overview of common **DC** approaches can be found in Ref. [Kar13].

Recently, Haule provided a nice mathematical representation of the **DC** problem by means of the **LW** functional approach [Hau15]. To know what the **LW** functional is and what it is good for, we neglect its possible convergence problems at strong interactions in some models (to which, however, the **AIM** belongs) [Koz15], and show it to be the Legendre transform of the free energy with respect to the **GF** [Ren16]. Let us start with the path integral containing a set of external sources \underline{J} (a real matrix) to which the operators \mathbf{c} (organized in a vector) couple,

$$Z[\underline{J}] = \int \mathcal{D}[\mathbf{c}, \mathbf{c}^+] e^{-S[\mathbf{c}, \mathbf{c}^+] + \mathbf{c}^+ \underline{J} \mathbf{c}}. \quad (\text{C.1})$$

$Z = Z[0]$ is the partition function which contains all closed diagrams (also the ones with disconnected components) in terms of the bare (non-interacting) **GF** and the bare vertex, and from the path integral with sources (i.e., from Eq. (C.1)) one can obtain the N -point **GF** via functional derivation,

$$G_{i_1 j_1 \dots i_N j_N} = -\langle c_{i_1} c_{j_1}^+ \dots c_{i_N} c_{j_N}^+ \rangle = -\frac{1}{Z[0]} \frac{\delta^N Z[\underline{J}]}{\delta J_{j_1 i_1} \dots \delta J_{j_N i_N}} \Big|_{\underline{J}=0}. \quad (\text{C.2})$$

The effective action is defined by

$$W[\underline{J}] = \ln(Z[\underline{J}]). \quad (\text{C.3})$$

Physically it amounts to the sum of all closed and connected (zero-particle irreducible) diagrams, and mathematically to the generating functional for the connected **GFs**, that is, it eventually subtracts from the N -point **GF** in Eq. (C.2) the diagrams with disconnected com-

ponents. The Legendre transform of the effective action with respect to $G = -\delta W[J]/\delta J^T$ yields the **Kadanoff-Baym (KB)** functional [Bay61] given by

$$\Gamma[\underline{G}] = -W[\underline{J}] - \text{Tr}(\underline{J}^T \underline{G}), \quad \underline{J} = \underline{J}[\underline{G}]. \quad (\text{C.4})$$

The **KB** functional is the two-particle irreducible effective action, and evaluated at the stationary point (i.e., at the physical **GF**) it becomes the grand potential Ω [Blö13]. Subtracting its non-interacting part, one obtains the **LW** functional,

$$\Phi[\underline{G}] = \Gamma[\underline{G}] - \Gamma_0[\underline{G}] = \Gamma[\underline{G}] - \text{Tr}[\log(-\underline{G})] - \text{Tr}[(\underline{G}^{-1} - \underline{G}_0^{-1})\underline{G}], \quad (\text{C.5})$$

which is the sum of all two-particle irreducible diagrams in terms of the bold (interacting) **GF** and the bare vertex, also named as skeleton expansion. The first functional derivative of the **LW** functional yields the self-energy,

$$\frac{\delta \Phi[\underline{G}]}{\delta \underline{G}} = \underline{\Sigma}. \quad (\text{C.6})$$

We obviously cannot go further beyond this simple derivation of the **LW** functional, but mention its unifying perspective and ability to provide a framework from which different conserving approximations can be derived (see for example Ref. [Kot06] and references therein; Ref. [Kot06] is a review on realistic **DMFT** calculations, in particular **DFT+DMFT**, and provides a **LW** functional approach to both, **DFT** and **DMFT**, which is only rudimentary outlined below).

The **LW** functional is universal, that is, it does not depend on material-specific data being included in the **KB** functional (Eq. (C.5)). Following Haule in Ref. [Hau15], we denote the **LW** functional by $\Phi_{V_C}[G]$, where V_C denotes the bare Coulomb interaction (like some other references, Haule assumed the **KB** as the **LW** functional, and $\Phi_{V_C}[G]$ as “its interacting part”, but we take the **LW** functional as the interacting part of the **KB** functional). In particular, the **LW** functional for **DFT** has the form $\Phi_{V_C}^{\text{DFT}}[G] = E_H[\rho] + E_{\text{XC}}[\rho]$, that is, it is the sum of Hartree and **XC** energy (functional derivative w.r.t. the density yields the **DFT** self-energy, i.e., the sum of Hartree and **XC** potential, cf. Eq. (C.6)). **DFT** is a static approximation to the correlations, so the variable of the **LW** functional, the **GF** $G(\mathbf{r}, \tau, \mathbf{r}', \tau')$, has to be truncated to its diagonal component, that is, to the density $\rho(\mathbf{r}, \tau)$. Yet the Coulomb interaction is still the same. For the **DMFT** approach (for the **AIM** the discussion is the same, see below) the **LW** functional is given by $\Phi_{V_C}^{\text{DMFT}}[G] = \Phi_U[G_{\text{local}}]$, where U is the screened Coulomb potential and G_{local} the (still dynamical) **GF** of the impurity coupled to a self-consistent bath. Here, the **GF** has been truncated by “localization”, which may be denoted with help of a projection operator, $G_{\text{local}}(\mathbf{r}, \mathbf{r}') = \hat{P}G(\mathbf{r}, \mathbf{r}') = \sum_{\alpha, \alpha'} \langle \mathbf{r} | \alpha \rangle \langle \alpha | \hat{G} | \beta \rangle \langle \beta | \mathbf{r}' \rangle$, where $\alpha = (n, l, m)$ and $\langle \mathbf{r} | \alpha \rangle = u_{nl}(r) Y_{lm}(\mathbf{r})$ (radial **WFs** times spherical harmonics). (At this point we may note that the already discussed **HF** theory and **GWA** follow from the **LW** functional by truncations in the space of Feynman diagrams within its skeleton expansion rather than from a truncation of its variable). $G_{\text{local}}(\mathbf{r}, \mathbf{r}')$ is actually the **GF** of the **AIM** impurity with discrete states (coupled to a self-consistent bath) embedded into (unfolded to) the lattice model. The **DC** problem now becomes rather clear: **DFT** relies on an

auxiliary system, which is the uniform electron gas defined on a continuum, while **DMFT** refers to lattice models, such as the Hubbard model, together with the mapping to a local model, such as the **AIM**. The quantum numbers of the **DFT** auxiliary system are given by the continuous momenta of the solid, while the ones of the **AIM** by discrete orbital states. One may say in more mathematical, category theoretical terms that the two systems are living in two different categories. Furthermore, it is known that the **DFT** self-energy has no diagrammatic representation, while **DMFT** admits such a representation (indeed, the same as the one of the exact **LW** functional, only with G and V_C replaced by G_{local} and U), so it is *a priori* unclear what the relation between the two is, and how (and if at all) physical processes may be mutually represented. The link, however, can be established within the **LW** functional approach (or, again more mathematically, by some functorial mapping between the two). In particular, the Hartree term in **DFT** looks like

$$E_{V_C}^{\text{H,DFT}}[\rho] = \frac{1}{2} \int d(\mathbf{r}, \mathbf{r}') \rho(\mathbf{r}) \rho(\mathbf{r}') V_C(\mathbf{r} - \mathbf{r}'), \quad (\text{C.7})$$

which in terms of **DMFT** variables can be expressed as

$$E_U^{\text{H,DMFT}}[\hat{P}\rho] = \frac{1}{2} \int d(\mathbf{r}, \mathbf{r}') (\hat{P}\rho(\mathbf{r})) (\hat{P}\rho(\mathbf{r}')) U(\mathbf{r} - \mathbf{r}'), \quad (\text{C.8})$$

where $U(\mathbf{r} - \mathbf{r}')$ is the screened Coulomb potential. This term is the exact **DC** arising from the Hartree interaction, and one may observe that it results from successive variable truncations. Indeed, again mathematically, one has a commutative diagram of truncation mappings, that is, one could also have performed first the **DMFT** truncation, followed by the one of **DFT**. The physical result for the Hartree term is a uniform electron gas, now given by the localized charge $\hat{P}\rho(\mathbf{r})$, and interacting via the screened Coulomb potential $U(\mathbf{r} - \mathbf{r}')$. Doing the same for the **XC** energy, one obtains the **LW** functional for the **DC** correction,

$$\Phi^{\text{DC,DFT+DMFT}}[\hat{P}\rho] = E_U^{\text{XC,DMFT}}[\hat{P}\rho] + E_U^{\text{H,DMFT}}[\hat{P}\rho]. \quad (\text{C.9})$$

In conclusion, one obtains the exact **DC** correction by a continuum representation of **DMFT**.

C.2 Relation between DMFT and the AIM via the Luttinger-Ward functional

We finally give a short presentation of the relation between the Hubbard model as solved by **DMFT** and the underlying **AIM**. A short account of the computational procedure within **DMFT** has been provided in Subsec. 3.2.1, while we will give here its relation to the **AIM** as expressed by the **LW** functional approach [Pot06]. As mentioned, the **KB** functional as defined in Eq. (C.5) yields the grand potential if evaluated at the stationary point. The grand potential is an expansion in the bare vertex with particle lines given by the bare (non-interacting) **GF**, so the **KB** functional itself depends parametrically on the bare vertex and its variable is the bare **GF**, $\Gamma_U[G_0]$, and one has $\Gamma_U[G_{\underline{t},0}] = \Omega_{\underline{t},U}$. Here, \underline{t} denotes the one-particle parameters, such as the hoppings, and \underline{U} the interaction parameters. The bold

(interacting **GF**) depends on both these parameters, $\underline{G}_{t,U}$, and via Eq. (C.6) so does the self-energy, $\underline{\Sigma}_{t,U}$. By the nature of the **KB** functional, its functional derivation evaluated at the bare **GF** yields the bold **GF**,

$$\left. \frac{\delta F_U[\underline{G}_0]}{\delta \underline{G}_0} \right|_{\underline{G}_0 = \underline{G}_{t,0}} = \underline{G}_{t,U}. \quad (\text{C.10})$$

The functional on left-hand side, being universal, is sufficient for the definition of a functional $\underline{G}_U[\underline{\Sigma}]$ with $\underline{G}_U[\underline{\Sigma}_{t,U}] = \underline{G}_{t,U}$.

Now, from Eq. (C.6) one may see that \underline{G} and $\underline{\Sigma}$ are conjugate variables, and the Legendre transform of the **LW** functional is then defined by $\Phi_U[\underline{G}] = F_U[\underline{\Sigma}_U[\underline{G}]] + \text{Tr}(\underline{\Sigma}_U[\underline{G}]\underline{G})$ (cf. Eq. (C.4)). Using the Legendre transform $F_U[\underline{\Sigma}]$, one may define the **KB** functional in terms of the self-energy, $\Gamma_{t,U}[\underline{\Sigma}] = F_U[\underline{\Sigma}] + \text{Tr}[\log(\underline{G}_{t,0}^{-1} - \underline{\Sigma})^{-1}]$ (cf. Eq. (C.5)). Again comparing with Eq. (C.5), the Legendre transform is given by $F_U[\underline{\Sigma}] = \Gamma_U[\underline{G}_U[\underline{\Sigma}]^{-1} + \underline{\Sigma}] - \text{Tr}[\log(\underline{G}_U[\underline{\Sigma}])]$. One thus finally arrives at the **KB** functional in terms of the self-energy,

$$\Gamma_{t,U}[\underline{\Sigma}] = \Gamma_U[\underline{G}_U[\underline{\Sigma}]^{-1} + \underline{\Sigma}] - \text{Tr}[\log(\underline{G}_U[\underline{\Sigma}])] + \text{Tr}[\log(\underline{G}_{t,0}^{-1} - \underline{\Sigma})^{-1}]. \quad (\text{C.11})$$

Obviously, evaluated at the physical self-energy $\underline{\Sigma}_{t,U}$, one observes the consistency of the construction $\Gamma_{t,U}[\underline{\Sigma}_{t,U}] = \Gamma_U[\underline{G}_{t,0}]$. Functional derivation of the Legendre transform $F_U[\underline{\Sigma}]$ of the **LW** functional yields the bold **GF** \underline{G} (the variable conjugate to $\underline{\Sigma}$). Thus, functional derivation of Eq. (C.11) yields the stationarity condition

$$\frac{\delta \Gamma_{t,U}[\underline{\Sigma}]}{\delta \underline{\Sigma}} = -\underline{G}_U[\underline{\Sigma}] + (\underline{G}_{t,0}^{-1} - \underline{\Sigma})^{-1} = 0. \quad (\text{C.12})$$

The equation $\underline{G}_U[\underline{\Sigma}] = (\underline{G}_{t,0}^{-1} - \underline{\Sigma})^{-1}$, which is to be solved by finding the physical $\underline{\Sigma}_{t,U}$, applies to the lattice model as well as to the **AIM**, because the **LW** functional $\Phi_U[\underline{G}]$ is the same for both. If the **AIM** has single-particle parameters \underline{t}' , the equation (with $\underline{t} = \underline{t}'$) is solved for $\underline{\Sigma} = \underline{\Sigma}_{t',U}$, and one obtains the bold **GF** $\underline{G}_U[\underline{\Sigma}_{t',U}] = \underline{G}_{t',U}$. In **DMFT** one approximates the exact bold **GF** by the one of the **AIM**, but Eq. (C.12) is obeyed locally only at the correlated site which has been represented by the **AIM**, and one obtains

$$\underline{G}_{t',U}|_{\text{local}} = (\underline{G}_{t,0}^{-1} - \underline{\Sigma}_{t',U})^{-1}|_{\text{local}}, \quad (\text{C.13})$$

which is just the **DMFT** self-consistency condition for the single-particle parameters \underline{t}' (describing the self-consistent bath, to which the local correlated orbitals couple).

Publications

1. A. Lichtenstein, M. Valentyuk, **R. Mozara**, and M. Karolak: ‘Electronic Structure and Magnetism of Correlated Nanosystems’. *Atomic- and Nanoscale Magnetism*. NanoScience and Technology. Springer International Publishing, 2018.
2. **Mozara, R.**, M. Valentyuk, I. Krivenko, E. Şaşıoğlu, J. Kolorenč, and A. I. Lichtenstein: ‘Cobalt adatoms on graphene: Effects of anisotropies on the correlated electronic structure’. *Phys. Rev. B* (2018), vol. 97(8): p. 085133.
3. **Mozara, R.**, A. Kamlapure, M. Valentyuk, L. Cornils, A. I. Lichtenstein, J. Wiebe, and R. Wiesendanger: ‘Atomically thin oxide layer on the elemental superconductor Ta(001) surface’. *Phys. Rev. Materials* (2019), vol. 3(9): p. 094801.
4. Kamlapure, A., L. Cornils, R. Žitko, M. Valentyuk, **R. Mozara**, S. Pradhan, J. Fransson, A. I. Lichtenstein, J. Wiebe, and R. Wiesendanger: ‘Investigation of the Yu-Shiba-Rusinov states of a multi-impurity Kondo system’. *arXiv:1911.03794*. arXiv e-prints. 2019. Published as ‘Correlation of Yu-Shiba-Rusinov States and Kondo Resonances in Artificial Spin Arrays on an s-Wave Superconductor’. *Nano Lett.* (2021), XXXX, XXX, XXX-XXX

Acknowledgments

I thank Prof. A. I. Lichtenstein and Prof. R. Wiesendanger for giving me the opportunity to write this PhD thesis at the University of Hamburg. In particular, I thank Prof. A. I. Lichtenstein for his professional advise, his optimism, and for his patience.

I thank the collaborators with whom I was working on during the years, for their guidance, their accompany, and for sharing their insights and knowledge. In particular, I thank Prof. R. Berndt for the collaboration, for giving me the opportunity to perform theoretical studies along the experiments performed in his group, for the invitation to a talk at the CAU in Kiel, and for the fruitful discussions; J. Kolorenč for the collaboration and the invitation to the Academy of Sciences in Prague, for sharing his insights into many-body physics, and his guidance; A. Weismann for the fruitful collaboration and long discussions, for sharing his encompassing knowledge on Kondo physics, and for his guidance; J. Wiebe for giving me the opportunity to perform theoretical studies along the experiments performed in his group; Prof. A. B. Shick for the fruit- and helpful dicussions, and for his advises; Prof. Antropov for the fruit- and helpful discussions, and for his insights; M. Valentyuk for the still on-going collaborations, for her optimism and endurance, and for sharing her insights into real materials; Igor Krivenko for being my office mate for the first years, for providing the best instructions to the codes which he himself has developed or contributed to, and for sharing his sophisticated knowledge on many-body physics; A. Kamlapure for the fruitful collaborations, for the informative and helpful discussions; Lasse Cornils for the fruitful collaboration and the discussions, Neda Noei for the fruitful collaboration and the discussions; T. Bučko for his helpful explanations and advises; Bodo Krause-Kyora, Michael Vedmedenko, and Martin Stieben for the many help with the local cluster.

I thank the research team of Prof. A. I. Lichtenstein who readily and willingly provided information at any time and for sharing their PhD time. In particular, I thank Hristiana Atanasova, Sergey Brener, Mikhail Danilov, Malte Harland, Daniel Hirschmeyer, Arthur Huber, Michael Karolak, Friedrich Krien, Oleg Kristanovski, Patryk Kubiczek, Yusuf Mohammed (my second office mate), Burkhard Sachs, Viktor Valmispild, Aljoscha Wilhelm. I thank Prof. R. Wiesendanger, Elena Vedmedenko, and Kolja Them who initiated this PhD work with a prior collaboration. I thank Prof. F. Lechermann for the helpful discussions and his advises, and his (former) team members Malte Behrmann, Lewin Boehnke, and Christoph Piefke for helpful discussions. I thank Benjamin Baxevanis for providing his code, and for the helpful discussions; Mohammad Sayad for the long and helpful discussions; and Agnieszka Kozub and Vladislav Pokorný for the discussions, and for sharing the working time in Prague.

I would also like to thank all people who supported me in writing this thesis. In particular, I thank Antje Brockmüller for her guidance in life, all my friends, of whom each have so much meaning, and my family for their love and support.

